Physico-Chemical study of the Focused Electron Beam Induced Deposition Process

Tristan Bret

▶ To cite this version:

HAL Id: tel-00182533

https://theses.hal.science/tel-00182533

Submitted on 26 Oct 2007

PHYSICO-CHEMICAL STUDY OF THE FOCUSED ELECTRON BEAM INDUCED DEPOSITION PROCESS

THESE N°3321 (2005)

PRESENTEE A LA FACULTE SCIENCES ET TECHNIQUES DE L'INGENIEUR

SECTION MICROTECHNIQUE

ECOLE POLYTECHNIQUE FEDERALE DE LAUSANNE

POUR L'OBTENTION DU GRADE DE DOCTEUR ES SCIENCES

PAR

Tristan BRET

Ingénieur, Ecole Supérieure de Physique et Chimie Industrielles, Paris, France
et de nationalité française

Acceptée sur proposition du jury :

Dr. P. Hoffmann, directeur de thèse

Prof. P. Kruit, rapporteur

Dr. J. Cleaver, rapporteur

Prof. P. Stadelmann, rapporteur

Prof. H. Bleuler, président du jury

Lausanne, EPFL

2005

Abstract

The focused electron beam induced deposition process is a promising technique for nano and micro patterning. Electrons can be focused in sub-angström dimensions, which allows atomic-scale resolution imaging, analysis, and processing techniques. Before the process can be used in controlled applications, the precise nature of the deposition mechanism must be described and modelled. The aim of this research work is to present a physical and chemical description of the focused electron beam induced deposition process.

As an introduction, a review of the literature, up to the present day, shows how this process was first identified as the origin of contamination in electron microscopes. Then the modifications made to a scanning electron microscope for deposition experiments are described. Gas supply systems and gas cryo-trapping devices were set up. Electrical and optical systems were constructed for an *in-situ* monitoring of the process. The experiment procedure was carried out in several phases, with the first being the deposition of flat films of carbon, copper-containing carbon composites, and pure gold for the study of the physics of the process. By measuring the fraction of the probe current that was absorbed in the sample, an accurate description could be made of the propagation of electrons. The backscattered electrons clearly influenced the deposition rate of Cu-containing films. A physical model for scanning deposition was created. The second phase is the deposition of metal-matrix composite tips from a stationary beam. Forward electron scattering was discovered to be responsible for tip formation and shape. A physical model of electron trajectories is included. The third phase is the construction of three-dimensional micro-structures by moving the beam during deposition. The deposited shapes result from an electron range that is larger than the structure size.

Further investigation into the chemistry of the process involved the analysis of carbon films by micro-beam techniques. Regardless of the precursor used, the resulting films had a composition as $C_9H_{2\pm x}O_{1\pm x}$ (x<1). The C phase hybridization was 90% sp^2. The elements H, N, O, F, and Cl were volatilized from the precursor during precursor fixation. Further parameters of deposition rate, temperature of the sample, vapour pressure, and the dipole moment of the precursors were examined. Electrically conductive metal-containing focused electron beam induced deposits were used for constructing micro-devices, a nanotube-based contact and a magnetic field sensor with 500x500 nm^2 active area.

R é s u m é

La technique de croissance assistée par faisceau focalisé d'électrons offre des perspectives attrayantes pour la nano et micro-fabrication en trois dimensions. Les faisceaux d'électrons peuvent être focalisés sur des dimensions inférieures à 1 Å, ce qui permet l'observation, l'analyse et la modification d'objets à l'échelle atomique. De nombreuses applications peuvent être envisagées, mais supposent une description précise des mécanismes physico-chimiques mis en jeu.

Une étude bibliographique montre d'abord que cette technique est dérivée du phénomène de contamination observé en microscopie électronique. Puis, afin d'en faire un outil expérimental efficace, un microscope électronique à balayage a été muni de systèmes d'approvisionnement en gaz précurseur et de condensation. De nouvelles méthodes électriques et optiques ont été mises au point pour le suivi *in-situ* du procédé. La démarche scientifique s'est déroulée en deux phases. La physique du phénomène a d'abord été étudiée, en déposant des films minces de carbone, d'un composite cuivre-carbone, puis d'or pur. La propagation des électrons dans ces films a été décrite grâce à la mesure en continu de la fraction du courant de sonde absorbée dans l'échantillon. Les effets des électrons diffusés sur le taux de croissance ont été étudiés. Un modèle physique a été développé pour rendre compte des résultats. La deuxième phase a été la croissance de pointes composites sous un faisceau immobile. La forme des pointes est déterminée par la diffusion des électrons. Un modèle physique décrivant les trajectoires des électrons à l'intérieur et autour des pointes a été mis au point. La troisième phase a été la construction de micro-structures tridimensionnelles, dont la forme illustre les effets de la profondeur de pénétration des électrons, qui est plus grande que l'épaisseur des dépôts.

Pour comprendre la chimie du phénomène, les dépôts de carbone obtenus ont été analysés par plusieurs techniques de micro-sonde. Tous les dépôts obtenus à partir de précurseurs pourtant différents avaient la composition $C_9H_{2\pm x}O_{1\pm x}$ (x<1). La fraction d'hybridation sp^2 de la phase carbone amorphe est de 90%. Le taux de croissance augmente avec la pression de vapeur, le moment dipolaire et la masse moléculaire du précurseur. Il diminue avec la température de l'échantillon. La réaction de fixation du précurseur adsorbé est une ionisation, suivie de la perte des éléments volatils H, N, O, F et Cl. L'analyse des dépôts composites de métaux a montré qu'ils peuvent être conducteurs. Des micro-dispositifs ont été démontrés, comme un contact électrique à un nanotube et un capteur de champ magnétique présentant une surface active de 500 x 500 nm^2.

Table of contents

Chapter 4 – Electron range effects in focused electron beam induced deposition

Chapter 5 – Chemical analyses of focused electron beam induced deposits

Chapter 1 – Introduction

Focused Electron Beam induced deposition is a nanofabrication method using a local, site-selective chemical vapour deposition process. Adsorbed molecules are decomposed under the focused probe of an electron microscope. The beam, which can be as narrow as 1 Å in modern electron microscopes, deposits nano- to micrometer-wide structures. Thin over-layers are continuously fixed on to existing shapes resulting in two and three-dimensional nanostructures. Micro-devices can be rapidly prototyped. The location of the deposit on the substrate is precisely chosen because the deposition machine is also a high-resolution imaging tool. Understanding how the deposition process works opens the way to a variety of advances in the fields of microelectronics, physics, chemistry, and engineering. Applications have already been found as a quality control tool for finding and repairing defects in computer chips and lithography masks. Other applications are electrical contacts between single bio-molecules or nano-wires for basic research, and fabricating miniaturized 3D devices and high-resolution contact scanning probes.[1-6]

Chapter 2 is a survey of the relevant literature and history. Electron-induced contamination was first observed as a problem in electron beam systems. Residual gas-phase hydrocarbons were fixed on to the samples under electron microscopic observation. The physical origins of contamination were first studied with the aim of reducing it. Researchers then used it for micro patterning processes, and optimised it for larger growth rates by deliberately injecting precursor gases on to substrates in vacuum chambers. New materials were deposited at nano-scale, but without an understanding of the deposition process. More research was needed

to answer such questions as: Is the process thermal? Is it directly triggered by the incident high-energy electrons, or by secondary processes? Is the adsorbed layer replenished by the gas phase or by surface diffusion? What are the effects of temperature, electron flux, or precursor pressure? How can pure elements, such as metals, be deposited? If the deposited material is not a pure crystalline element, what is it and how can it be characterized? What is the resolution limit? What can the process be used for? Can functional nano-devices be designed and constructed? Numerous researchers have studied the process and have attempted to answer these questions. Interdisciplinary investigations from neighbouring research fields such as electron-beam lithography, scanning probe microscopy, and focused ion beam induced processing, have also provided new information about the process.

The experimental setup is described in Chapter 3. Several modifications and improvements were made on a Cambridge S100 Scanning Electron Microscope for its use as an efficient deposition machine. The improvements to the continuous *in-situ* monitoring of the process included physical, electrical, and optical measurement setups.

The effects of electron range on the deposition process are presented in Chapter 4. The incident electrons cross the adsorbed precursor layer and penetrate into the underlying solids, and become scattered by atoms. The number of electrons that cross the interfaces and decompose the precursor molecules depends on the scattering processes that take place in the bulk of the solids. The scattering effect was first demonstrated on large-area deposits, and incited the following questions: What is the relation between film thickness and deposition rate? Does the composition of the film have an influence on the deposition rate? To answer these questions I used the beam to deposit low, intermediate and high atomic number elements, at several electron energies, and on different substrates. Thus I was able to describe the effects of electron scattering. In order to control the process precisely, an *in-situ* monitoring method was developed. This showed that the propagation of electrons in the growing films was quantitatively revealed by the backscattering yield and the collected sample current.

When the electron beam is kept at the same place, vertical tips are deposited. Why do tips form? Is electron scattering responsible? And if the electrons are scattered, then how does deposition take place in the surrounding environment? The effects of several parameters were investigated: precursor composition, tip diameter, accuracy of focusing, nature of the substrate, role of obstacles on the substrate, and acceleration voltage. Through this research I was able to develop a physical model of electron scattering in and around deposited tips.

A higher deposit complexity was reached by moving the beam during deposition. Is it possible to deposit any 3D structure? Electron scattering in the growing structures is shown to have consequences on the final structure shape. The effects of electron scattering were measured and interpreted through a series of 3D model microstructures.

The challenging question of how to chemically characterize such small deposits is addressed in Chapter 5. If the composition of the deposits is measurable, then it may be possible to manipulate the process in order to deposit different ratios of elements, nanostructures, and crystalline states. First, deposition from purely organic precursors is described. From the wide range of compounds available, a few were selected for their deposition efficiency in order to discover the exact composition of the deposited materials. Through several micro-beam analysis techniques, slight variations were seen in the composition of the deposits. The deposited material was found to be hydrogenated amorphous C, with some incorporated oxygen. Given the difference between the crystalline and amorphous states of C, is it possible to locally deposit diamond under FEB-induced growth conditions?

Organometallic compounds contain both metals and ligands, most of which contain carbon. In the search for a way to deposit a pure metal, the composition of the deposits from organometallic precursors was analysed. Selected experiments showed that, depending on the nature of the precursor and on the electronic interactions with the adsorbed layer and the growing structure, the deposits had a varying atomic content of metal. Examples of micro-devices based on electrical conduction in these metal-containing deposits were developed and are described.

In Chapter 6, the study is summarized and future directions of research are proposed. Solutions for successful focused electron beam induced deposition of diamond are discussed. The optical properties of deposited nano-composites also offer a promising route for future applications. The conclusions drawn from the analysis of the deposition mechanism will allow developing new focused electron beam induced processes, with possible applications for high-resolution metal etching.

C h a p t e r   2   –   L i t e r a t u r e   s u r v e y

*Mais il ne faut pas toujours tellement épuiser
un sujet, qu'on ne laisse rien à faire au lecteur.
Il ne s'agit pas de faire lire, mais de faire penser.*

Montesquieu, de l'Esprit des Lois, ch. XX, livre XI

The aim of this chapter is to present the context in which the present study was undertaken. In Section 2-1, electron-induced contamination is described. This side effect of electron interactions on surfaces, observed since the early studies of 'cathodic rays', was satisfactorily understood in the 1960s. When applied in electron microscopes, it found applications to 2D and 3D micropatterning. In Section 2-2, its evolution in the 1980s into "focused electron beam induced deposition" is described. The deliberate introduction of gases in electron microscopes turned contamination into a versatile nanofabrication process. In Section 2-3 the mechanisms of electron-beam induced chemistry in solids and at surfaces are commented on. A formal parallel exists between electron-beam lithography and electron-beam induced deposition. Finally, the possibilities offered by alternative nanofabrication methods are discussed in Section 2-4. This literature overview proved very helpful in the design and interpretation of the experiments presented in the next chapters, and resulted in a physical understanding of the focused electron beam induced deposition process.

2-1 Electron-induced contamination

2-1-1 Nature of the phenomenon

2-1-1-A) Observation of electron-induced contamination

Reports in literature of electron-induced surface deposition occurred as early as 1913, and intermittently until 1939.[1-6] A solid deposit formed when an electron beam crossed a rarefied vapour of a room-temperature-condensable element and impinged upon a screen. When the rarefied medium contained a gaseous carbon compound, the gas molecules were decomposed by collisions with the electrons, leaving a surface contamination of C. Between 10 eV and 1 MeV, the contamination rate decreased with increasing beam acceleration. This was attributed to the decreasing ionizing power of the primary beam.[7-10] The phenomenon was used to pseudo photographically record the electron beam distribution on metallic substrates. The exposed areas resisted acid etching and electroplating.[10, 11] The insulating deposited films were made conductive by heating *in vacuo*.[12, 13] After the construction of the first electron microscopes in the 1930's and improvements in the 1940's, it was reported that the examination of carbon black particles in a TEM increased their diameters (by ~100 Å in 3 minutes), which was attributed to electron-induced contamination.[14-16] 3D replicas of template particles were built by contamination (see fig. 2-1-1).[17-19] The shells remained stable upon annealing in a vacuum at 500°C, but were burnt away in air.
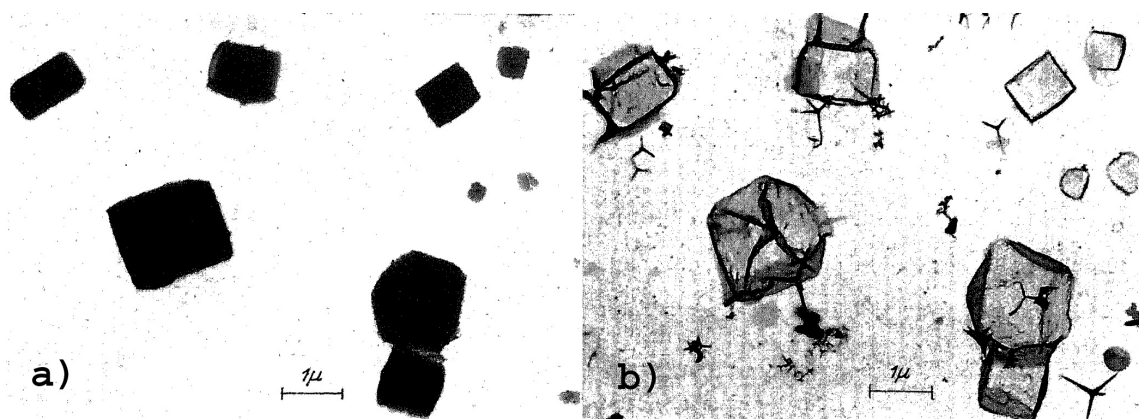
Figure 2-1-1. Contamination in electron microscopy. a) NaCl crystals irradiated in TEM. b) After dissolution in water, only contamination shells remained. ZnO needles were added for scaling.[18]

2-1-1-B) Understanding and reducing contamination

Contamination was understood as a beam-induced polymerization of carbon.[20] Free organic radicals form in an adsorbed layer and polymerize into stable long-chain molecules with occasional H atoms.[21-23] The adsorbed layer sources were diffusion pump oil, hot vacuum grease, rubber gaskets, and dirty metal surfaces.[24] A specimen bias up to $\pm$ 1000 V, or a magnetic beam deflection close to the substrate, did not affect the process. It was inversely proportional to the spot size and slightly increased with the atomic number of the substrate.[25-28] The process was not thermal because it left heat-sensitive samples unchanged.[29] Contamination films were shown to change the electronic properties of surfaces.[30-34] 40 keV electrons yielded 400x smaller contamination rates than 40 kV Li ions, each of which fixed ~9 C atoms at RT.[35-39] Between 6 and 25 eV the growth rate was acceleration voltage-dependent and the deposits were electrically photosensitive.[40] X-Ray analyses indicated a deposit composition of $C_{19}O_1Si_{0.5}H_1$ (from silicone oils), confirmed by IR absorption spectra (see fig. 2-1-2a).[9, 41]
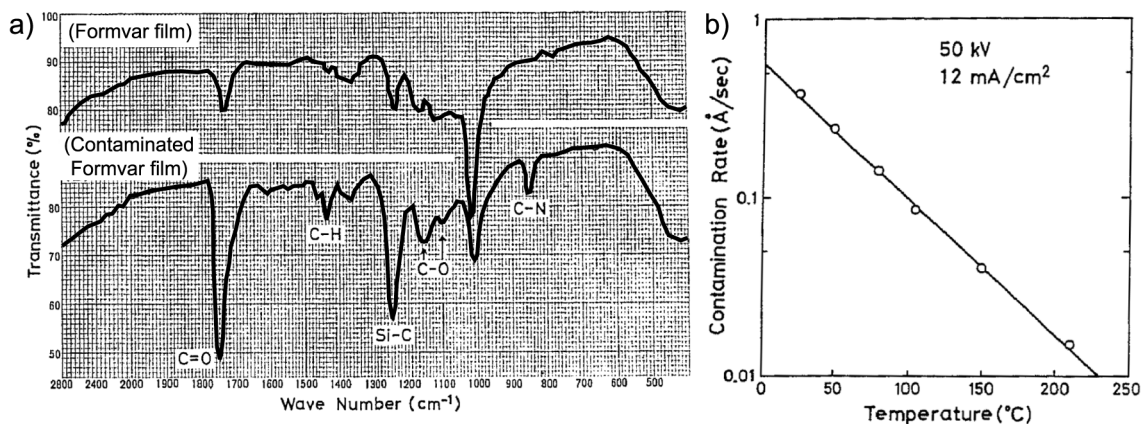
Figure 2-1-2. a) FTIR analysis of contaminated films. b) Contamination *vs.* temperature.[9]

Heating the sample at 250°C eliminated contamination (see fig. 2-1-2b).[9, 23] A gentle flow of air towards the bombarded area reduced the contamination rate and even etched previously deposited carbon.[42-47] During the 1960's using liquid N_2 cold traps reduced contamination.[48-52] The contamination rate in TEM was determined by the time the sample spent in the vacuum outside the cryo-pumped regions.[53] At 10^{-5} Torr, the vacuum chamber residual gases were composed of water vapour (8.10^{-6} Torr), CO, N_2 and O_2 (5.10^{-7} to 10^{-6} Torr each). All carbon species reached 10^{-6} Torr.[54-56] The residual gases could be fixed to the chamber walls by a glow

discharge.[57] Fomblin oil (a perfluoro-polyether) was recommended for reducing contamination as it fragments without polymerizing.[58, 59] The sample could also be "electron-flooded" with a large spot size before observation.[60-65] In 1979, all these methods were still not capable of avoiding contamination completely and routinely in X-ray chambers.[66]

2-1-2 Rationalizations and applications

2-1-2-A) Theoretical models and physical observations

By the early 1960s, contamination was no longer considered a negative side effect, but a new area of research. Applications were found for micro patterning.[67, 68] Christy proposed a model based on the electron-induced fixation of adsorbed molecules, as shown in fig. 2-1-3.[69]
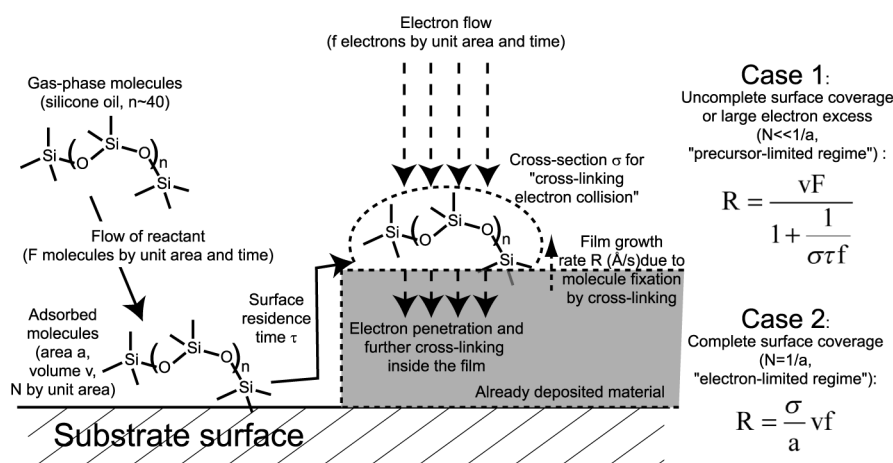
Figure 2-1-3. Christy's model of electron-beam-induced deposition.[69]

R: deposition rate. v: molecular volume. F: precursor flow. σ: cross-section of electron-induced fixation. τ: precursor residence time at the surface. f: electron flow. a: molecule area. N: precursor surface density.

This model described correctly the experiments made at different temperatures (T) and current densities (f). At high f or at low T (when $\sigma\tau f \gg 1$), the growth rate was vF. The oil vapour pressure was determinant. At very low f or at high T, the growth rate was approximately $\sigma\tau f v F$. It depended on current density and temperature, through τ and F (as shown in eq. 2-1).

$$F = \frac{\alpha p}{\sqrt{2\pi m k_B T}} \qquad (2\text{-}1)$$

Precursor flow F *vs.* temperature T. α : fraction of the incident molecules that stick to the surface. p : local pressure; *m* : molecular mass; k_B : Boltzmann's constant.

Fixing one silicone oil molecule required ~100 electrons.[70] Ageing in air increased the resistivity (about 10^4 Ω.cm for contamination deposits) and reduced the dielectric constant, indicating the presence of free radicals.[71-76]

Interesting results were obtained when weighing contamination *in-situ* on a Ni-coated quartz crystal microbalance.[77] Between 10 eV and 4 keV, the contamination rate and the SE emission depended similarly on the PE energy, reaching a maximum at 200 eV (compare fig. 2-1-4a and b) and having a similar evolution during deposition (see fig. 2-1-4c). Recapturing or pushing away the low-energy SE did not alter the growth rate. A subtle mechanism was proposed: the PE ionized the adsorbed molecules as efficiently as they ejected SE from the substrate, so that the process was similar to SE emission in all aspects, but the SE themselves were not involved. Although the recollected SE probably played a role by cross-linking the deposited films, this interpretation was satisfactory.[22, 78]

a) Growth rate vs. PE energy, residual oil contamination

b) Compared SE yields vs. PE energy, for 3 qualities of Ni surfaces

c) Compared SE yield η and film growth rate W during growth on Ni (Silicone oil precursor)
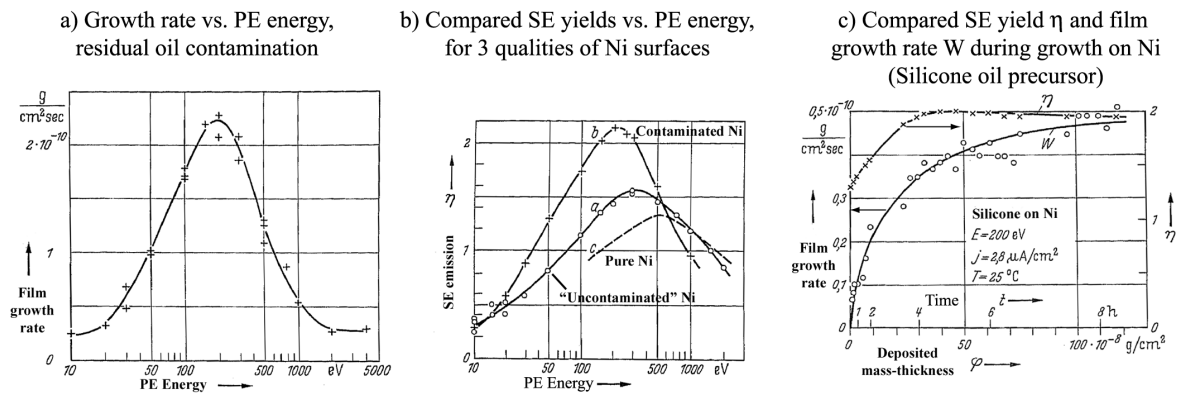
Figure 2-1-4. a,b) Contamination rate and SE yield dependence on PE energy. c) Evolution of growth rate and SE yield during film growth.[77]

2-1-2-B) Role of surface diffusion

Some complex spot profiles were obtained (see fig. 2-1-5a,b).[53, 79, 80] The scan frequency influenced contamination rates.[81] Were these effects due to the surface diffusion of adsorbates?

a) Fourie, 1975:

60 kV, beam diameter 1.5 µm,
200 nA on specimen,
"homogeneous" beam, exposure 5 min.
Contamination rate depends on
time t_{pv} spent in pre-chamber

$t_{pv} = 0$;

$t_{pv} = 8$ min.

$t_{pv} = 20$ min.

Densitometer profiles   TEM pictures

b) Reimer & Wächter, 1978: 100 kV

Effect of anti-contamination device (ACD)

Effect of increased current density

Effect of gaussian beam

----------- Current density (j) distributions
——— Deposit thickness distributions

Figure 2-1-5. Experimental contamination spot profiles.[53, 80]

Müller introduced a surface diffusion component into Christy's model.[82, 83] The balance of contributions to the local concentration of reactive species N(r, t) was summarized in the following differential equation (retaining Christy's symbol names):

$$\frac{\delta N}{\delta t} = F - \frac{N}{\tau} + \lambda.\Delta N - \frac{f}{e_0}.\sigma N \qquad (2\text{-}2)$$

λ: diffusion constant; $e_0 = 1.6 \ 10^{-19}$ C.

In equilibrium the balance was at zero. Solving the equation with a homogeneous circular beam with current f_0 and diameter D, led Müller to:

$$\overline{N_{irradiated}} \approx \frac{const.}{f_0.D^2} \qquad (2\text{-}3)$$

This relation agreed with his experimental results. The qualitative theoretical profiles showed a depletion of the adsorbed layer coverage under irradiation, as shown in fig. 2-1-6a-d.
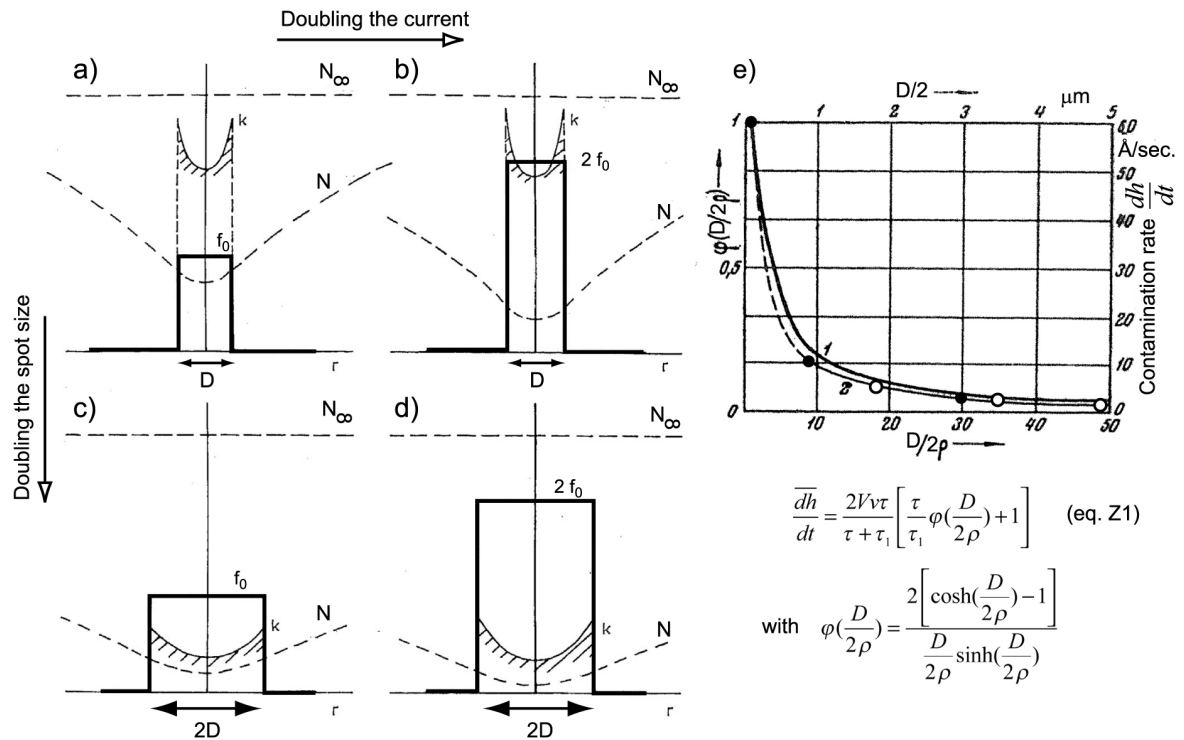
Figure 2-1-6: a-d) Qualitative contamination rate k and precursor concentration profiles (cylindrical symmetry).[82] e) Growth rate vs. spot size. On the left scale, φ(D/2ρ) is the probability for a molecule of being hit by an electron. Curve 1, calculated dependence. Curve 2, experimental values.[84]

The average time τ_1 between two adsorbate-electron collisions was estimated as 10% of the residence time τ (at f=0.1 A/cm^2).[84] The reduced diffusion length ρ was defined as:

$$\rho = \sqrt{\frac{a\upsilon\tau\tau_1}{4(\tau+\tau_1)}} \qquad (2\text{-}4)$$

τ_1 is defined by $\tau_1 = \dfrac{e}{\sigma f}$. At the surface, molecules "hop" from one adsorption site to

another during time τ : a is the average hop distance and υ the average speed.

The contamination rate was a function of the ratio D/ρ (see eq. Z1 in fig. 2-1-6e). Physically, if the beam radius was smaller than ρ the molecules rapidly diffused to the beam, so its exact

dimension had no effect. From ρ to 10ρ, the contamination was significantly reduced because the molecules were fixed on the edge of the beam. Above 10ρ, the effects of surface diffusion were less pronounced while the effects of temperature became important. A value of $\rho\sim0.1$ μm fitted the experiments. The same value was obtained by another approach. The average time spent on the surface by an adsorbed molecule was calculated as 3 μs, during which the molecule travelled on average 2 μm distance in a random walk.[85] This corresponds to an area of 0.1 μm diameter. As a conclusion, the range of surface migration of 100 nm was too short to explain the spot profiles shown in fig. 2-1-5.[9] Other effects are involved, such as electron-flux-dependent density of the deposited material or beam-induced heating, as shown in the next paragraph.

2-1-2-C) Two-dimensional applications: deposition and etching

Examples of 2D applications of contamination deposits are shown in the next figures. Using the deposits as etch masks, the 80 Å line resolution (see fig. 2-1-7b) was not limited by the electron-beam process but by the grain size of the supporting metal film.[86-88]

a) Customized deposits for absolute scaling of 3D objects (for instance, bio-objects such as erythrocytes)

b) Contamination lithography for micro-contacts

c) High-resolution data storage
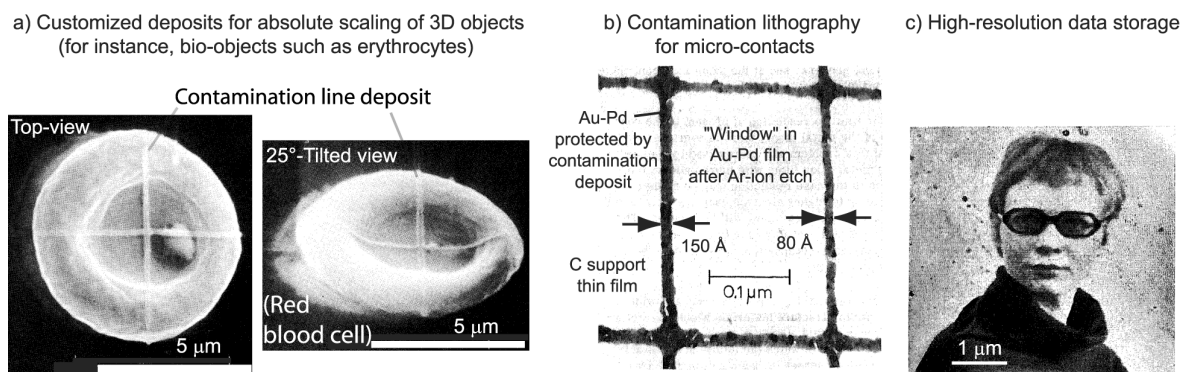
Figure 2-1-7. 2D applications of contamination (1970's).[83, 86, 89]

A grayscale picture with pixel size of 300 Å on a 5 x 5 μm^2 area was recorded in 10 minutes (see fig. 2-1-7c).[83] The performances were improved (10 x 10 μm^2 in 16 s, with pixel size 250 Å) by using fluxes of volatile organics.[90-94] Carbonaceous spots served as pattern stitching marks. Contamination "darning" was used to repair hole defects in lithography masks.[95]

Cooling the sample reduced contamination. The condensed water etched C away when activated by the electron beam, as shown in fig. 2-1-8c.[96, 97]
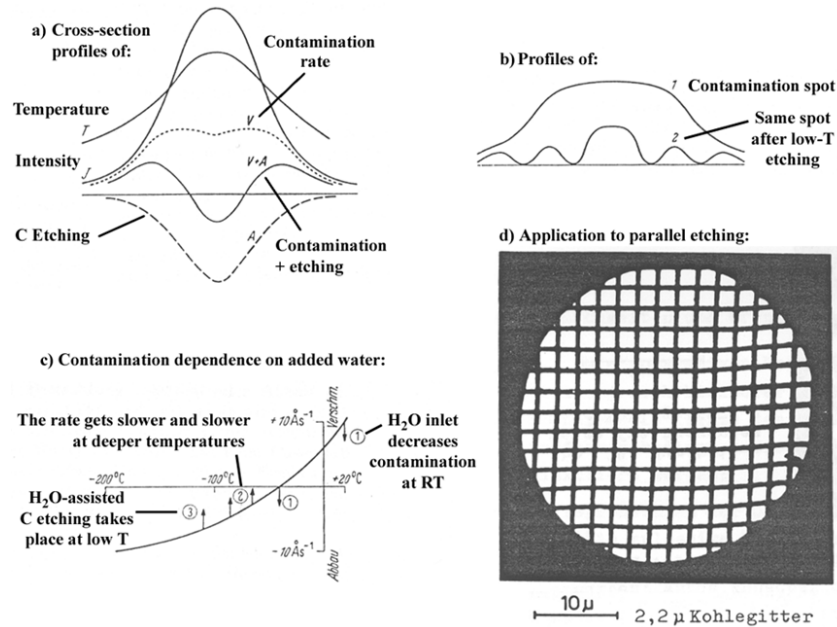
Figure 2-1-8. a, b, c) Schematic single-spot contamination possible profiles and residual water effects. d) 2.2 µm-pitch array in C film by H_2O-assisted parallel e-beam etching.[98]

Competing with C build-up and temperature effects, it yielded complex deposit cross-sections (see fig. 2-1-8a,b), offering an interpretation to the profiles shown in fig. 2-1-5.[80]. Grids were etched in C films down to 0.1 µm pitch, by parallel 20 kV irradiation (see fig. 2-1-8d).[98]

2-1-3 Three-dimensional micro-deposits

2-1-3-A) Contamination tips

By reducing the spot size, the deposits developed 3-dimensionally (see fig. 2-1-9a). Heights of 1 µm were reached in minutes.[99-102] Observing the deposits from a side view revealed a conical shape grown on both sides of thin films (see fig. 2-1-9b).[103] The lower part of the deposit was rounded due to PE scattering in the upper part. The cone sharpness depended on focusing accuracy.[104]
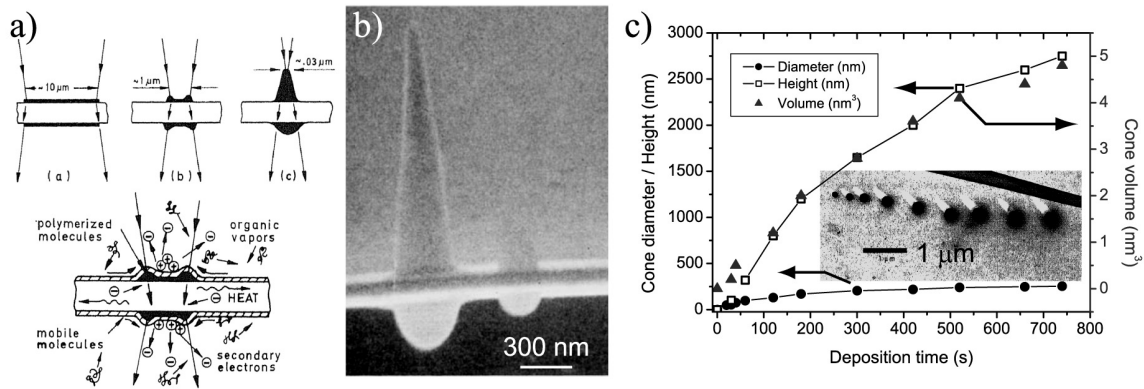
Figure 2-1-9. From large spot deposits to 3D contamination cones with a narrow beam. a) Schematic transition and graphical summary of some involved effects.[99] b) Tilted-view of 4 pA, 25 kV contamination spots on a thin film.[104] c) Diameter and height vs. time.[105]

The growth rate decreased beyond 1 μm height (see fig. 2-1-9c).[105] Material was also deposited around the main deposits, in regions that were not exposed to the beam.

2-1-3-B) Contamination rods and fingers

In 1965, freestanding carbonaceous rods were built by moving the beam across a metallic edge at 30 nm/s in the presence of added organic vapours.[106] Isolated 3 μm-long rods were as fine as 65 nm, but gratings showed proximity effects attributed to secondary, Auger, and scattered primary electrons (see fig. 2-1-10).[107]

a) 45° tilted view of isolated contamination rod

b) Edge widening by deposition of a new perpendicular rod

c) Widening of an array by deposition of a new parallel rod
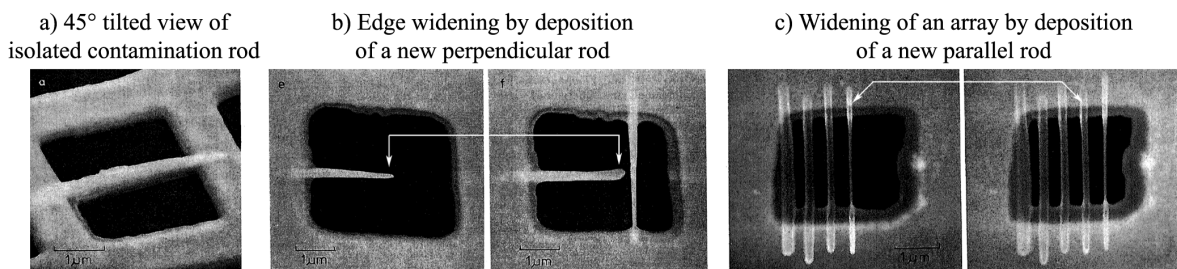
Figure 2-1-10. Freestanding contamination rods and proximity effects.[107]

Side effects were observed during rod deposition. At 50°C the incident beam simultaneously deposited several thin, parallel, separated filaments.[108, 109] Deposits were formed on a metal wire when a 1 nm diameter FEB was spotted in the vacuum up to 35 nm away (see fig. 2-1-11b).[110]
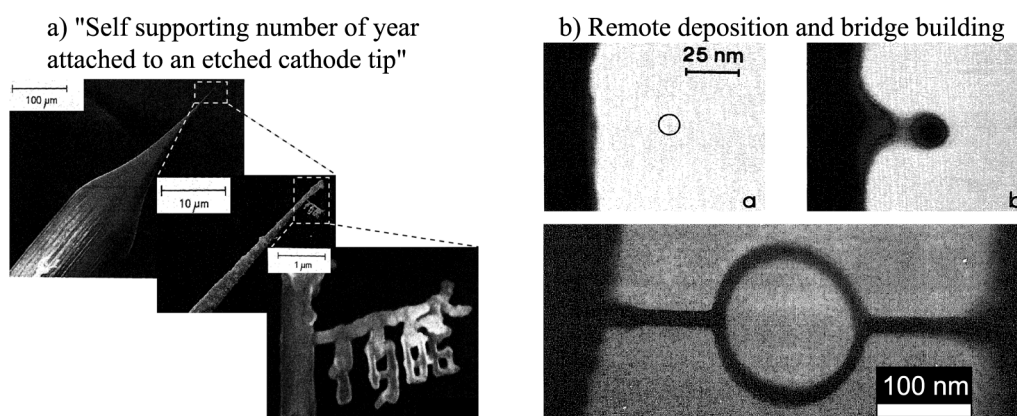
Figure 2-1-11. Freestanding contamination deposits by single-slow-scanning.[108, 110, 111]

This long-range interaction was assigned to 18 eV plasmons, remotely excited at the substrate surface by the passing electron beam. Rods grew more rapidly when the beam intersected a solid material, and were used as 3D templates for evaporation of metallic nanowires.[63, 111-113] Electrodes with sub-5 nm spacing were produced with this template method.[114]

2-1-3-C) Applications

Contamination deposits are used as supertips for scanning probe microscopy (also see below, fig. 2-2-3).[115-118] They penetrate into deep groves with less angular limitations than standard Si tips.[119, 120] The small apex diameters allow supertips to have a 10 nm resolution.[121, 122] They were sharpened in O_2 plasmas for higher resolutions.[123] They have low enough resistivities to be used in STM, but can also be metal-coated.[124-127] High-resolution contact lithography with such probes was demonstrated.[128-131] For high deposition rates, it was advised to place a piece of carbon adhesive tape in a microscope chamber, but "C blocks" (~50 mm^3) and paraffine traces were also satisfactory.[132, 133] Supplying oil vapors to the reaction site allowed the deposition of C markers as reference points for AFM imaging studies of surface modifications.[134, 135] Contamination "soldering" was used to join C nanotubes in a TEM.[136]

Carbon fibers deposited by a 10 kV FEB can be used as field emission tips. Higher growth rates than "natural" contamination are obtained from methane-hydrogen mixtures but give conducting deposits only above 50% CH_4.[137] The nature of the carbonaceous deposits obtained at 30 kV was investigated by Raman spectroscopy, revealing a typical spectrum of

amorphous C.[138] This material was used as an insulator in diodes,[139] in single-electron-transistors,[140] and as a mask for 60 nm planar electrode gaps.[141] A "diamond-like carbon" spectrum reported from a contamination deposit obtained at 5 kV, was actually a spectrum of a-C, with a different D/G ratio.[142] FEB-induced deposition of a diamond phase was claimed from a 1% CH_4 in H_2 mixture with a high-current probe, but from a noisy Raman spectrum.[143]

2-1-3-D) Electrical effects

Electrostatic effects under the electron beam and their consequences on contamination are controversial subjects. The intense electric fields generated around the impingement point of the FEB on the substrate were claimed to enhance the surface diffusion of molecules towards the contaminating spot by induced polarization.[144] Most authors did not share this opinion because of poorly reproducible results,[80] or did not see a need to add electrical effects in their interpretations ([65], p.19; [63, 97]). Yet charge effects seemed to take place when deliberately contaminating with large beams on insulating samples like BN.[145] In this case, fractal filament growth took place (see fig. 2-1-12a,b). This "Laplacian" growth was of a non-diffusion-limited type, hinting at an electrostatic origin.[146] These results were reproduced on polymers, metals and ceramics, even from organometallic compounds.[147-150]
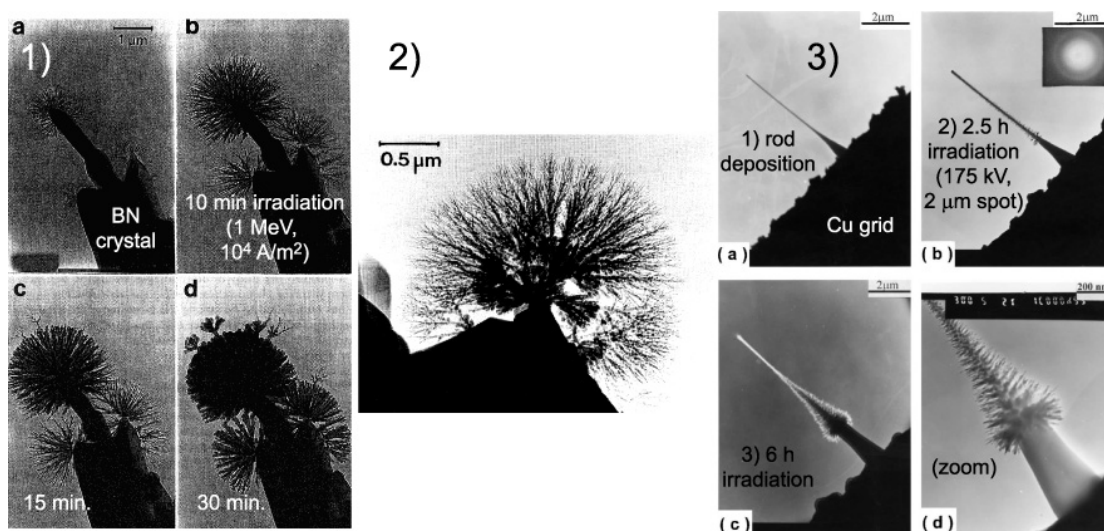
Figure 2-1-12. Charging effects lead to fractal contamination growth modes. 1) Growth sequence on BN. 2) Detail of morphology, from compact (centre) to fractal (borders) aggregate. 3) Growth sequence on a contamination freestanding rod.[145, 146, 149]

2-1-4 Summary

The contamination process is an electron-assisted cracking of hydrocarbons at an interface. The probable mechanism is the ionization of an adsorbed hydrocarbon layer by inelastic collisions with the primary electrons. The reactant is supplied mainly by the gas phase. The range of the surface migration of adsorbed species is on the order of 100 nm. Heating and charging effects are involved. The deposited material is amorphous and contains mostly (>80%) carbon. The process allows for deposition of a wide range of customized 2D and 3D nanostructures. Despite side effects it is satisfactory from an engineering point of view. Its speed was remarkably increased by the deliberate introduction of fluxes of volatile hydrocarbons. However, mostly partial characterizations were reported, and many properties of the deposited materials (mechanical, chemical, optical or electrical properties…) are still unknown.

2-2 Focused electron beam induced deposition

Instead of "contaminating" under an electron beam from the residual hydrocarbons, the process can be used for 2D or 3D construction of functional nanostructures. Organometallic precursors containing the desired chemical elements were deliberately introduced in the chamber and decomposed by an electron beam.

2-2-1 Historical development

As early as 1961, vapors of volatile tin derivatives ($Sn(CH_3)_4$, $Sn(C_4H_9)_4$, $SnCl_2$) were fixed on substrates by large electron beams with energies ranging from 50 eV to 1 keV.[151-153] Highly reflective superconducting Sn films were obtained. Good film quality and large metal content required low growth rates and a heated substrate (> 50°C).

The volatile metal carbonyls were then used for deposition. $W(CO)_6$ led to resistive deposits with a composition of $W_{11}C_6O_3$.[154-156] Carbonyls of Mo, Re, Cr, and Fe, and ferrocene also deposited carbides.[157-163] At 125°C autocatalytic effects were observed.[164-166] The actual deposition mechanism is complex. Mass spectrometry indicated incomplete electron-induced fragmentations and mixtures of decarboxylated ions (see fig. 2-2-1).[167-176] Direct electron-

induced CO desorption was observed from adsorbed $W(CO)_6$.[177] The total ionization cross-sections σ by electron impact, determined for simple gases, reached a maximum σ_{max} between 100 and 300 eV and decreased by a factor 2 until 1 keV.[178] They were larger when the gases contained larger amounts of heavier elements. For instance, $\sigma_{max}(NO_2)=4.10^{-16}$ cm^2, while $\sigma_{max}(CCl_2F_2)=8.10^{-16}$ cm^2, and $\sigma_{max}(CCl_4)=16.10^{-16}$ cm^2.[179-181]
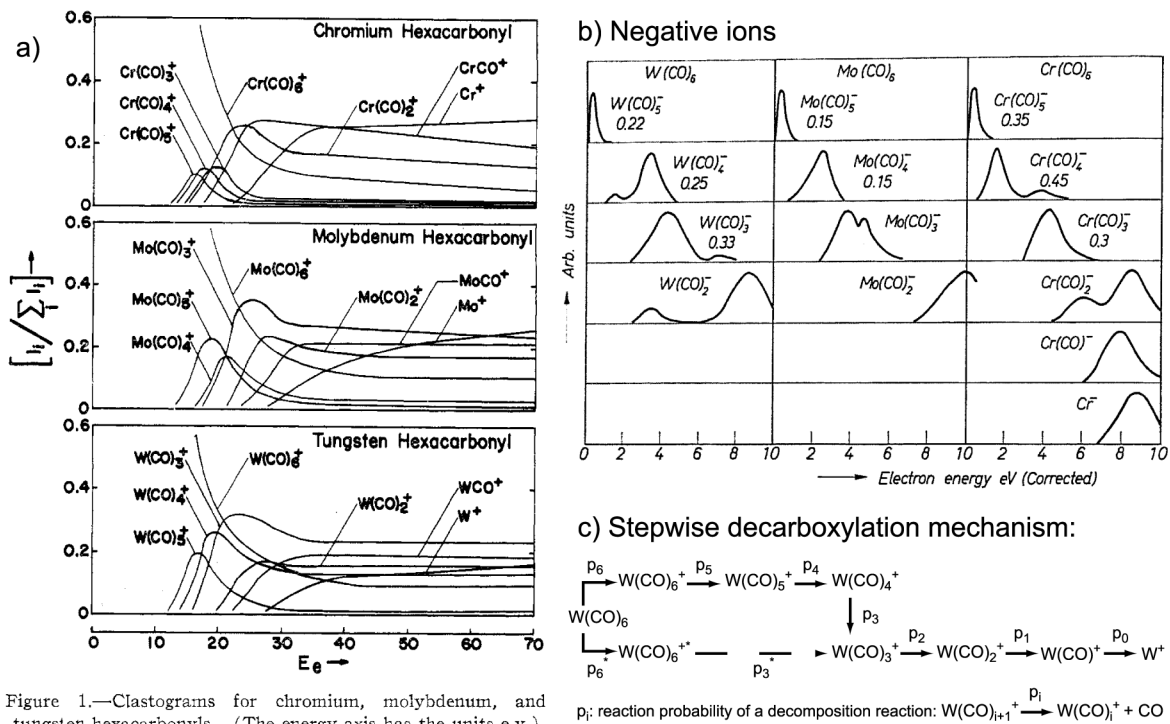
Figure 1.—Clastograms for chromium, molybdenum, and tungsten hexacarbonyls. (The energy axis has the units e.v.)

Figure 2-2-1. Mass spectrometry studies of the electron-induced fragmentations of metal-carbonyls. a) "Clastograms" of positive ions. Notice the successive energy thresholds.[167] b) Simultaneously produced negative ions.[168] c) Mechanism inferred.[169]

New applications, such as high-resolution deposition without contact masks, renewed the interest in the process when using the focused beams from modified electron microscopes (see fig. 2-2-2a).[182, 183] Heating the precursor reservoir and optimizing the gas supply increased the growth rate to 15 nm/s (see fig. 2-2-2b).[184, 185] 3D structures were built in reasonable time frames.[186, 187] A 15 nm wide W-containing rod with crystalline clusters was constructed in a TEM (see fig. 2-2-2c).[188, 189] A 150 nm wide line containing Cr was deposited in a SEM.[182] The nano-deposits were smooth.
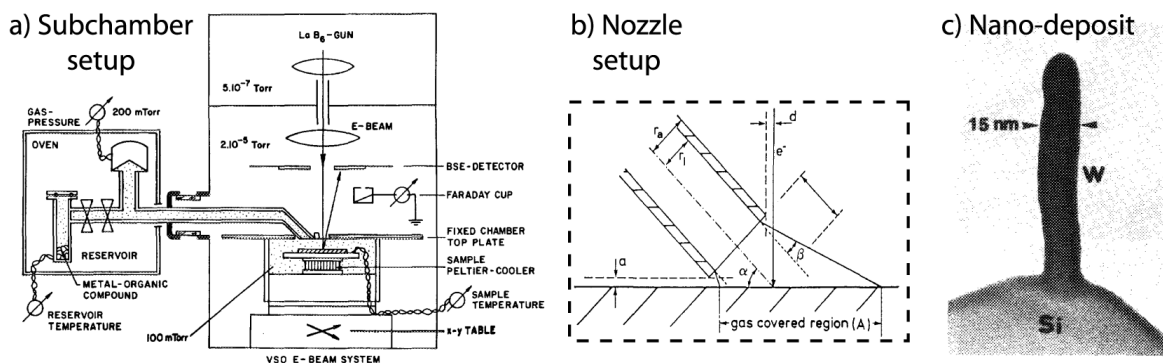
Figure 2-2-2. Focused electron beam induced deposition. a) Detailed setup.[155] b) Precursor supply by an optimized gas nozzle.[184] c) Constructed 3D nano-rod.[188]

The halogenides WF_6, WCl_6, SiH_2Cl_2, $SnCl_4$ or $TiCl_4$ appeared promising for FEB-induced pure element deposition, but at low temperatures halogen atoms were co-deposited.[190-195] Upon substrate heating, F was liberated and etched the Si substrate. Post-deposition electron irradiation incompletely desorbed Cl.[194, 196] Auger analysis revealed impurity incorporation from residual gases (WCl_6 deposited $W_7Cl_2C_1O_2$ while $Cr(C_6H_6)_2$ deposited $Cr_2C_9O_3$, H not measured). Parallel deposition was achieved by masking the wide beam from a TEM. The decomposition of a $Ru_3(CO)_{12}$ molecule required 280±110 electrons at 40 keV. The decomposition cross-section, 0.2±0.15 $Å^2$, was similar to the molecular inelastic scattering cross-section.[183] At high electron flux, the precursor was thermally decomposed into pure metal, but without area selectivity.[197]

2-2-2 Improvements and applications

New FEB-induced chemistries appeared with new CVD precursors. $Al(Me)_3$ deposited Al:C alloys.[198] $Ga(Me)_3$-AsH_3 mixtures deposited GaAs:C.[199, 200] Heating the substrates lowered the C content.[201] Smooth deposits with 25 to 40% Au content but low conductivity were obtained from $Me_2Au^{III}(tfac)$. These were used as etch resists and X-ray absorbers,[155, 202] as well as for customized AFM and STM supertips (see fig. 2-2-3).[203-206] The principle was the same as with contamination supertips (see §2-1-3C), but the growth rates were higher.
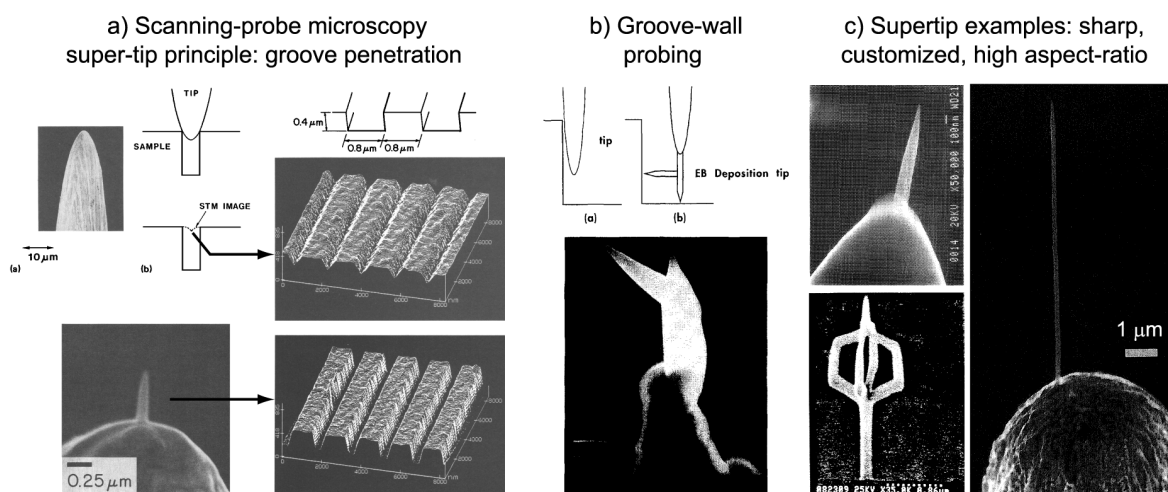
Figure 2-2-3. FEB deposited SPM supertips. a) Principle of penetration in deep narrow grooves.[124] b) Principle of STM scanning of vertical walls.[125] c) Customized tips.[121, 126, 204]

During the 1990's, the deposition mechanism was studied in depth. Pulsing the beam to 5 kHz brought a twofold increase by letting the adsorbed layer "refresh".[207] Tip geometry was similar to that of contamination tips, i.e. a cone on top of a cylinder. The conical tip shape was attributed to PE scattering. The fraction of energy deposited as heat in the tips was usually less than 20%.[211, 212] The apex curvature radii decreased with increasing beam energy.[208] The growth rate decreased with tip height, affecting the growth of nano-coils.[209, 210] In spite of previous results (see fig. 2-1-4), the emitted SE were proposed to play the major role in precursor fixation because the energy dependence of the dissociation cross-section of small molecules overlaps the SE spectrum (see fig. 2-2-4a).[213] Controlling the primary beam energy showed a maximum deposition yield from $W(CO)_6$ at 100 eV, but the lowest resistivity obtained (6.10^{-4} Ω.cm) was still 100 times larger than that of pure W.[214] *In-situ* sample cleaning (O_2 plasma + 300°C anneal) and deposition from WF_6 reproducibly led to 300 $\mu\Omega$.cm.[215] Deposits with low resistivities (3.6 $\mu\Omega$.cm, twice the value of bulk Cu) were created from (hfac)Cu(VTMS), despite low (~10%) Cu contents.[216] In an attempt to deposit tunnel junctions for single electron transport devices, higher growth rates were obtained at constant dose by slow scanning.[217-219] Because the calculated heat was too low to account for the phenomenon, it was attributed to SE emission at the deposit walls.[220] The number of molecules fixed from each electron (the deposition "yield") depends on the geometry of the 3D structures on which the beam impinges.[221]
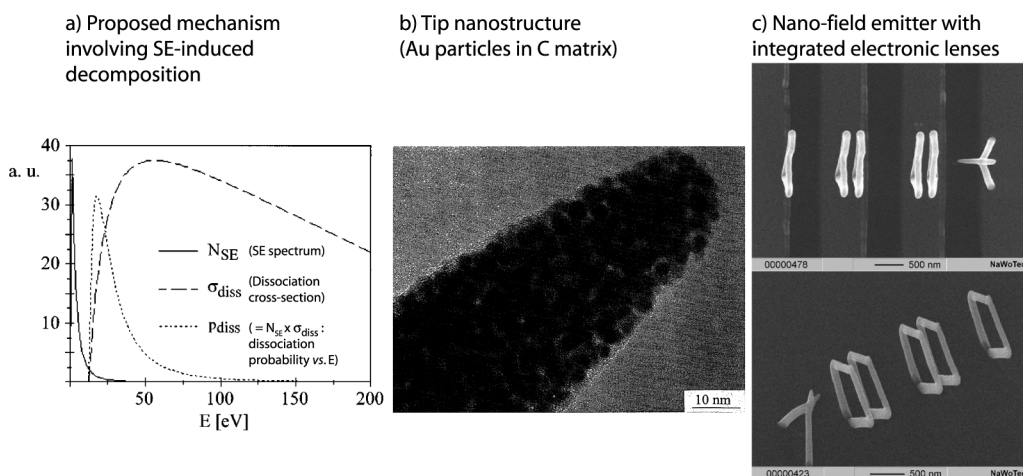
Figure 2-2-4. Advances in electron-beam induced deposition. a) Proposed mechanism.[213] b) TEM shows the deposit nanostructures.[222] c) Functional 3D device grown by FEBID.[223]

Functional nanodevices such as electrical contacts, field-emission tips,[224] sensors,[222], and photonic crystals,[225, 226] required a detailed knowledge of the deposit composition and nanostructure. TEM observation (see fig. 2-2-4b) revealed that 2 to 10 nm metallic clusters were embedded in a carbonaceous matrix. The metallic content in the deposits was increased by up to 75 % through depositing with larger beam currents,[227] on heated substrates,[228] or in reactive environments (H_2O, O_2).[229, 230] "Hopping" electrical conduction between the percolating clusters accounted for the electrical properties.[231] Annealing produced efficient, and bright, cold field emission tips.[232-234] Designs of miniature electrical devices appeared soon after these discoveries (see fig. 2-2-4c).[223, 235-242]

Two strategies were developed to improve the purity of the deposits. The use of simple precursors like Si_2H_6 or Ge_2H_6 yielded crystalline, partially hydrogenated Si or Ge films.[243-245] Insulating SiO_2 was obtained by adding O_2.[246] "Smart" precursor choice allowed purer deposits. FEB deposition from (ethyl)Au(PMe$_3$) in a TEM, between 125 and 200°C, produced crystalline Au films.[247] Depositing from the carbon-free inorganic precursor AuPF$_3$Cl, at room temperature, yielded pure Au films with facetted grains and low resistivity (down to only 10 times the value for bulk Au, partially due to grain boundaries).[248-250] With C-containing precursors, only smooth deposits were obtained, with a polymeric matrix between the grains, although Au optical plasmon effects were observed.[251] Adding water vapor led to polycrystalline Au cores,[252] which allowed for local soldering.[253, 254] Replacing the C-containing ligands by

phosphines did not allow direct pure metal deposition, as shown in the case of Rh.[255] Deposition from [RhCl(PF$_3$)$_2$]$_2$ led to a Rh-P nanocomposite[256] with 60% Rh content, 19% P and 7% Cl, according to Auger spectroscopy.[257]

Recently, the deposition of magnetic materials, mainly from cobalt-containing precursors, has attracted some attention.[258, 259] An application was found in super-tips for magnetic contact probe sensing ("magnetic force microscopy"[260]). As the probe size in electron microscopes continues to shrink,[261] the final process resolution became a relevant issue.[262, 263] W-containing dots, as small as 1 nm, were produced in TEMs with 0.8 nm probe size,[264-267] as well as Fe-Si nanorods.[268]

2-2-3 Summary

The deliberate introduction of organometallic vapors into electron microscopes turned contamination into a versatile nanofabrication process. The principles of both processes are similar. A wide choice of chemical elements can be deposited thanks to the numerous CVD precursors available. The deposits usually contain C, either because organometallic precursors are incompletely decomposed at low temperatures, or because C incorporation from the background gases takes place. Numerous applications of the process were found in 3D micro-patterning. It is widely used but its mechanism is still under investigation.

2-3 Electron beam induced chemistry

I found useful to summarize here results from the well-documented field of electron-induced chemistry. The technologically important field of electron beam lithography has attracted a wide scientific interest.

2-3-1 Electron beam induced bulk processes – "Radiation damage"

Electron beams damage organic and inorganic compounds.[269-272] There are two ways a reaction may be provoked by electron beam interaction with a sample: electron excitation or direct atomic displacement. The cross-section of electron excitation decreases with the square

root of the electron velocity. Direct atomic displacement can occur in materials when the kinetic energy transferred to each atom exceeds an energy threshold.[273, 274] Beam damage usually involves mass loss by removing the volatile elements (H, N, O, F, Cl), loss of crystalline structures and clustering of the remaining atoms.[275] Electron-induced dissociation and desorption require low electron energies (a few eV only).[276] Knock-on momentum transfer can sputter unvolatile elements, especially the lighter of them.[277-280]

2-3-2 Applications to nanometer-scale lithography

Electron-beam lithography is based upon the chemical transformation of a "resist" layer, which is then developed. In "positive" resists the developer solvent removes the exposed area, which is made more soluble. In "negative" resists the exposed area is cross-linked and only unexposed areas are dissolved. The resolution, sensitivities and chemistries of numerous resists were studied and reviewed.[281-287] In PMMA used as a positive resist, the sensitivity at 50 keV is $10 \, \mu C/cm^2$ and the resolution is between 5 and 10 nm. It is not limited by the electron beam diameter but by the electron interaction range and the polymer chain size. The exposure mechanism involves the formation of radicals. Competing chain breakage and cross-linking occur. The thickness of the resist can be reduced down to a single monolayer.[288-294]

Direct-write lithography processes were developed on inorganic compounds. Selected compounds used as inorganic resists are listed in table 2-3-1. This table shows that removal of a volatile element (H, N, O, F, Cl) and clustering of non-volatile elements are usual phenomena under electron beams. The high-resolution studies were made at high electron energy and may have involved knock-on mechanisms, but the phenomena occurred similarly at the lower electron energies, indicating that momentum transfer was not the only mechanism involved. In many of these experiments, atomic ionization due to inelastic collisions is the rate-limiting step.

Electron-beam contamination and deposition are actually "dynamic" lithographic processes. They involve the exposure of a renewing adsorbed layer. Depending on the precursors used, electron-induced volatile element removal and cross-linking of fragments occur in the same way as in thick resist layers.

Inorganic compound	Electron energy	Result	Resolution	Dose	Proposed mechanism	Investigation method	Ref.
Silicones, siloxanes	20 keV	Etch resists, SiO_2	100 nm	10 $\mu C/cm^2$	Cross-linking	SEM	[295-297]
Oxides (SiO_2, Al_2O_3, MgO, ZrO_2, Y_2O_3, WO_3, $YBa_2Cu_3O_y$)	30-100 keV	Holes and lines	1 nm	$10^{-2} – 100$ C/cm^2	Electron-induced O desorption, bulk defect formation, cation diffusion	TEM	[298-309]
Halogenides (NaCl, AgCl, $CdCl_2$, LiF, AlF_3, $10\%AlF_3$:LiF, MgF_2, CaF_2, BaF, SrF_2, $RbAg_4I_5$, $CsAgBr_{3-x}I_{2+x}$, FeF_2, CoF_2)	100 keV	Holes and lines	1 nm holes	$10^{-2} – 100$ C/cm^2	Halogen vaporization, knock-on metal displacement	TEM+EELS	[310-321]
	1-30 keV	Metal clusters and halogen loss	<10 nm	10–200 mC/cm^2	Halogen desorption, "F-center" formation and metal diffusion	SEM, Auger, XPS, AFM	[322-329]
Hydrides ($NaAlH_4$, AlH_3, MgH_2, LiH, NaH, $NaBH_4$, CuH, Si:H, $(SiH_2)_n$, BeH_2, C:H, solid H_2O)	100 keV	Metallic particles	5 nm	-	H evolution and metal particle formation	HRTEM, EDX, selected area diffraction	[330-334]
	3-25 keV	H-depleted compounds	100 nm-5 μm	10-500 mC/cm^2	Electron-induced H desorption	Auger, RHEED, SEM, FTIR, area-selective CVD	[335-340]
Alkoxides, carboxylates, dicetonates (Y, Ba, Cu, Pd, Bi, Ti, Zr, Ta, Pb, Sr)	25-40 keV	Oxide lines after annealing (superconductors, ferroelectrics)	100 nm	1.2 mC/cm^2	Cross-linking	SEM, sheet resistance, Auger, RBS	[341-352]
Alkyls, carbonyls, phosphines (Au, Pd, Ir, Ru, Fe, Co)	5-30 keV	Conductive lines, functional ceramics	100 nm	10-200 mC/cm^2	Metal clustering	SEM, AFM, XPS, sheet resistance, TEM	[353-357]
Colloids (Au, Pd, Pt)	30 keV	Conductive Au lines	250 nm	0.4 mC/cm^2	Cross-linking	SEM+sheet resistance	[358-363]

Table 2-3-I: Inorganic resists used in electron-beam lithography

2-4 Alternative direct nanofabrication techniques

2-4-1 Light-induced chemical vapour deposition

Laser beams decomposed organometallic compounds.[364, 365] The decomposition processes were thermal or photolytic depending on the photon energy and substrate temperature. Films and 3D objects were directly deposited from focused beams or by image projection.[366-371] The best lateral resolutions obtained were typically 0.5 μm. The resolution was limited by the wavelength. Among the shorter wavelengths used was synchrotron radiation, but on large areas.[372-377] Photoelectrons and secondary electrons cracked the adsorbed species.[378, 379] Under photolytic decomposition conditions, the compositions were similar to those obtained by FEB deposition.

2-4-2 Scanning probe deposition

10-nm metal-containing features were deposited under STM tips.[380-387] The mechanism of deposition from the adsorbed precursor (hfac)CuVTMS involved fragmentation upon impact with low-energy tunnel electrons and field-induced dissociation.[388, 389] Deposition occurred simultaneously on the STM tip,[390] which was used to deposit self-aligned supertips.[391] Other mechanical surface modifications involved ploughing resists or depositing from the liquid phase.[128, 129, 392] Parallel versions were developed.[131]

2-4-3 Focused ion beam induced deposition

Precursors supplied in vacuum chambers were decomposed by focused ion beams (FIBs) similarly as by FEBs.[393, 394] The main used ions were protons, ionized noble gases, and especially Ga^+ because of the high brightness liquid metal ion sources available.[395] The larger ions had higher energy deposition rates. The resolution was thought to be limited by the emitted SE (10 nm) and elastic recoil ion ranges (30 nm).[396] The smaller 3D deposits from 10 nm probe diameters were typically 100 nm.[397, 398] The main deposited materials were Au, Pt and Cu.[399-407] The metal contents and the growth rates were usually higher than by FEB. Sputtering by nuclear

collisions removed the lighter elements. Carbon was deposited as contamination or from deliberately injected organics.[408-413]

2-4-4 New methods

New nanofabrication methods are under development.[414] Among them, parallel imprint lithography is promising for mass replication at the sub-micrometer scale.[415] Many of these methods involve the replication of a micro- or nanopatterned structure, still making the pattern generation by conventional methods necessary. Most of the developments in these fields are driven by the microelectronics industry. Its famous "Moore's law" states that the computer performances should be able to double on average every 18 months. Pushing towards smaller feature sizes and cheaper lithography processes is required in this competitive and rapidly renewing context.

Chapter 3 – Setup description

(…) A cette cause, le commerce des hommes y est merveilleusement propre, et la visite des pays étrangers, pour en rapporter principalement les humeurs de ces nations et leurs façons, et pour frotter et limer notre cervelle contre celle d'autrui.

Montaigne, De l'éducation des enfants, *Essais*, ch. 26

A previously modified Cambridge Stereoscan 100 (fabrication date 1980) was used for our focused electron beam induced deposition experiments.[1] The main features of this apparatus are described in Section 3-1. Several technical improvements are presented. Several *in-situ* analysis procedures for the monitoring of deposition are detailed. The external characterizations techniques are described in Section 3-2.

3-1 Electron microscope S100

3-1-1 Setup overview

The organization of the laboratory is shown in figure 3-1-1.
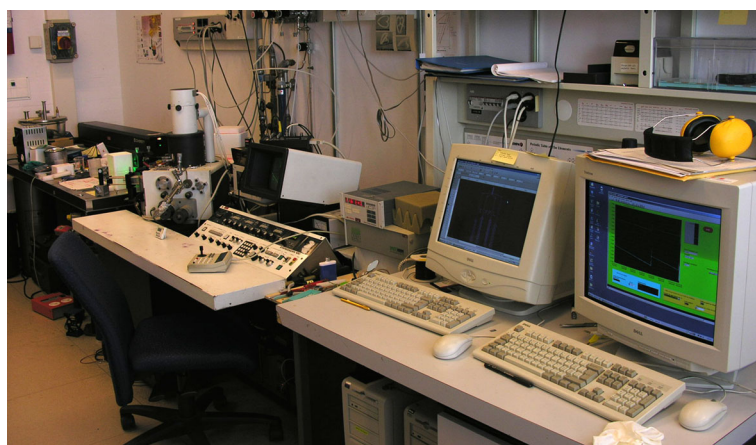
Figure 3-1-1. Complete setup overview. From left to right: optical table, electron microscope and control board, and computers used for the controlled beam scanning and monitoring

A detailed view of the electron microscope is shown in fig. 3-1-2.
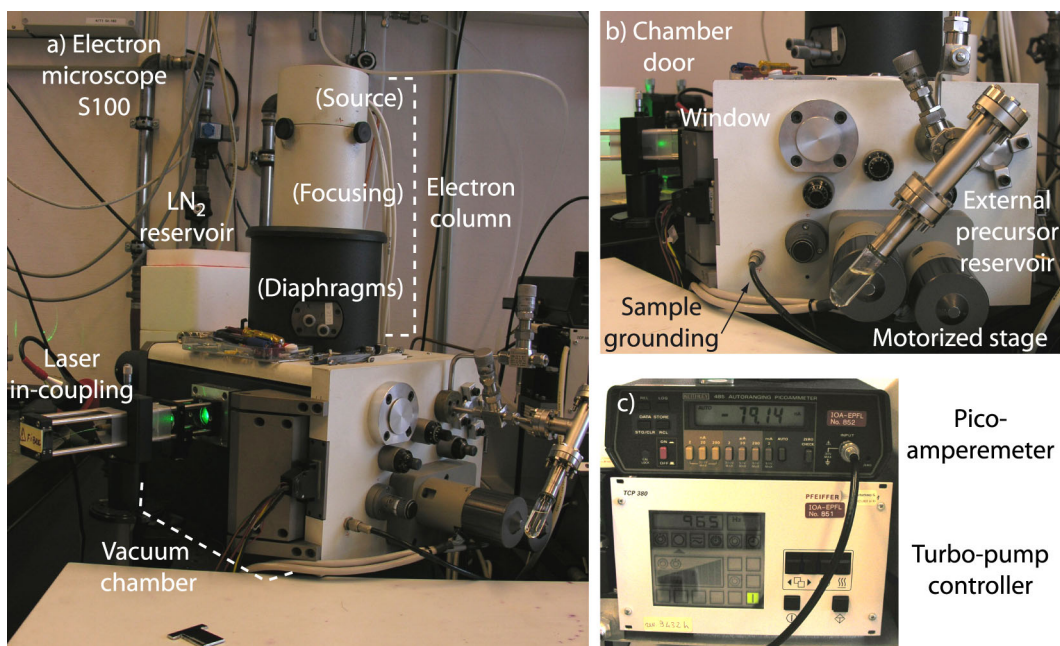
Figure 3-1-2. Outer view of the S100. a) Complete system. b) Front door. c) Controls.

The electron column and vacuum chamber are under a secondary vacuum. The background pressure was 10^{-6} mbar. The higher pressure allowed in the chamber for stable electron emission was 5.10^{-4} mbar. An oil-free membrane pump, fitted with a cold trap for condensing all organic vapours, backed the turbo-pump (see fig. 3-1-3a).
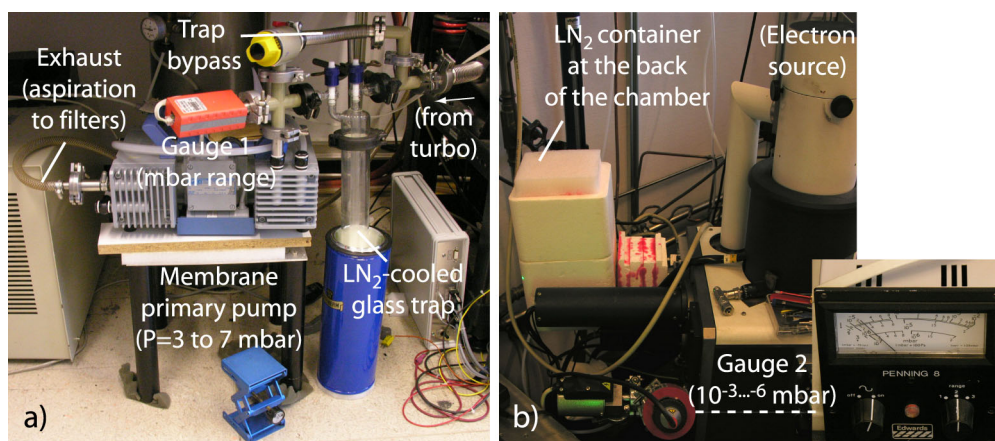
Figure 3-1-3. Pumping system. a) Primary pump setup. b) Rear-view of the microscope, with pressure gauge and homemade liquid N_2 container.

At the rear of the microscope, a liquid N_2 container (see fig. 3-1-3b) was connected to a thermally isolated 2-tube vacuum feed-through. A cryo-shielding tube was built in the chamber for condensing the effusing precursor vapours (see fig. 3-1-4a). When using for instance formic acid as precursor, with this system the working pressure was reduced from 10^{-3} to 8.10^{-5} mbar.
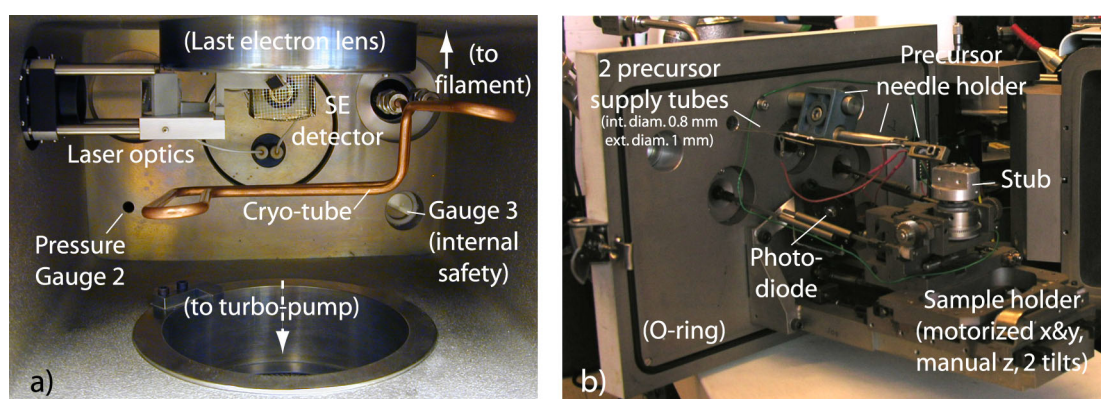
Figure 3-1-4. Inside the vacuum chamber. a) Front-view. b) Inner side of the front door.

The holder for the precursor needle keeps the supply tubes in place (see fig. 3-1-4b). Once the chamber door is closed, the needle is fixed with respect to the FEB (see fig. 3-1-5a,b). The needle must be positioned so that precursor effusion takes place at 100 μm of the centre of the image (see fig. 3-1-5c). The angle between the needle direction and the FEB was 45° to 60°.
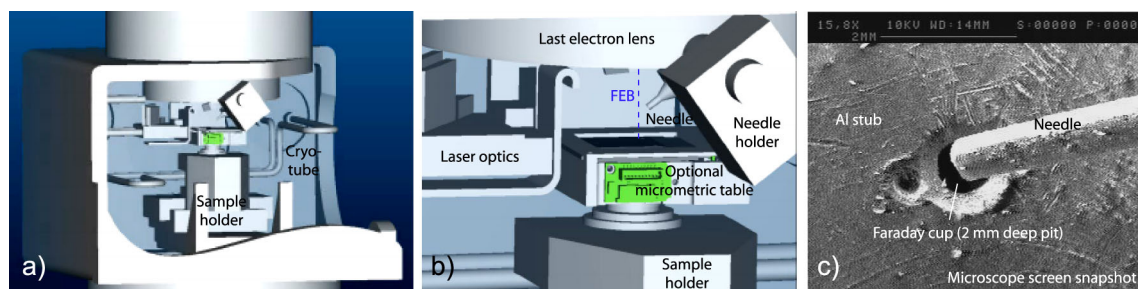
Figure 3-1-5. a,b) Internal organization in the closed chamber. c) S100 screen snapshot showing an overview of the needle alignment.

3-1-2 Precursor supply

Internal reservoirs were built from surgical stainless steel pieces, purchased from Unimed SA, Lausanne (see fig. 3-1-6). They were filled by liquid or solid precursors under N_2 in a glove box. The reservoirs were weighed before and after effusion. Typically, 50 mg of (hfac)CuVTMS evaporated in 6 h. The average flux was obtained by dividing the corresponding number of evaporated molecules by the effusion time and the needle area. The organometallics were purchased from Strem, ABCR, or Schumacher, or were synthesized by a partner research team.[2]
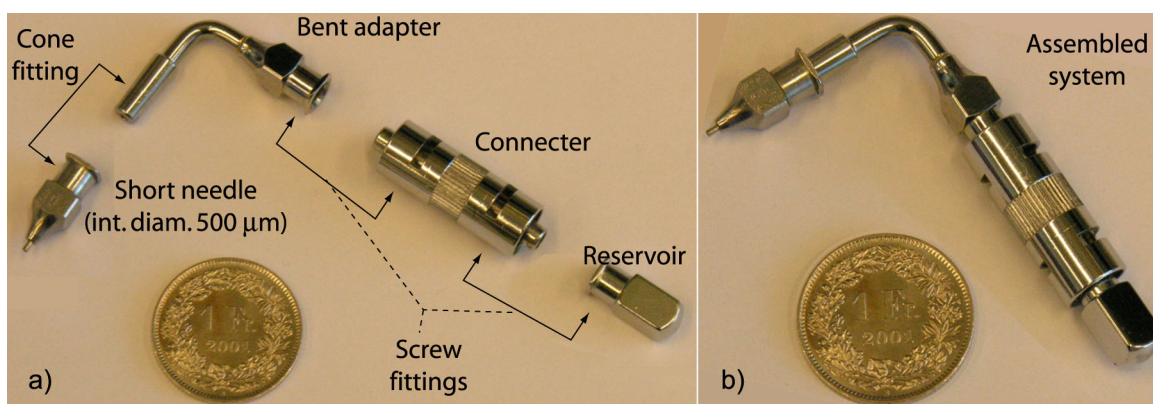
Figure 3-1-6. Internal precursor reservoir system. a) Separate pieces. b) Assembled system.

The external precursor supply (see fig. 3-1-2b) was used for compounds with vapour pressures at RT larger than 1 mbar (they evaporated too quickly from the internal reservoir). The reservoir was surrounded by a beaker of water at room temperature in order to avoid evaporative cooling. The organic compounds were purchased from Sigma-Aldrich.

3-1-3 Sample and holder; specimen movement control

The main substrate used was naturally oxidized p-doped silicon. Pieces were cut from a wafer down to 6x6 mm². They were laid horizontally and held to the Al stub by thin flexible Cu lamellas. The sample height was controlled with $100\,\mu$m resolution. The sample tilt was manually adjustable with 10° accuracy. A motorized stage allowed rapid horizontal (x and y) movements of the sample under the fixed needle and the FEB (see fig. 3-1-2b). The length of manual steps was 5 μm. The slower continuous speed available was 2.5 μm/s. A customized x-y micrometric table using stick-slip piezoelectric actuation was constructed for the S100 (see fig. 3-1-5b).[3, 4] The step resolution was 100 nm and the slower continuous speed measured was 140 nm/s. A compact resistively heating sample holder was obtained from the flat W filament of a halogen light bulb, on which the sample and a ceramic plate were directly laid. This setup heated the sample up to 120°C.

3-1-4 Electron beam deflection control

Among the microscope built-in TV scans, only the standard rate was used for large-area exposure. It consisted of a standard 50 Hz TV scan, with 625 lines per frame, and aspect ratio 1.27 at all magnifications (from 25x to 240000x at 25 kV and 15 mm working distance, in 15 coarse steps). To deposit tips the beam scan was switched off and the beam was spotted. The spot position was manually chosen. It was usually at the centre of the screen at 4000x (4kx).

A beam control software was adapted to this microscope. Named NPGS for Nanometer Pattern Generation System (version 7.6), it was developed for electron lithography and commercially available from J.C. Nabity, Bozeman, MT59717, USA. The design of complex

beam patterns was possible with this system. To define the scan speed, continuous lines were interpreted as series of points. The smaller distance d allowed by the program hardware, typically 4.8 Å at magnification 4 kx, was used to separate the points. The points were exposed for a "dwell time" τ. For a scan speed of 30 nm/s, τ=16000 μs. It was checked experimentally that as long as the point-to-point spacing was below 10% of the electron probe diameter, the structures obtained at a given speed (ratio d/τ) were independent of the exact value of d or τ. Beam alignment on patterned marks before deposition was possible with NPGS.

3-1-5 Image quality and recording

The image was formed in a standard Everhart-Thornley secondary electron (SE) detector, behind a +400 V biased grid. No backscattered electron (BSE) imaging was available. A computer acquired screen snapshots through a Mirovideo DC20 image acquisition card (see fig. 3-1-7). This feature was limited to coarse geometries. In the S100, observing at higher resolution required using lower probe currents, which decreased the signal-to-noise ratio (SNR). Satisfactory images could be taken only above 100 pA probe current. At 10 pA, the SNR was so low that even focusing was difficult. Structures could be deposited but not observed.
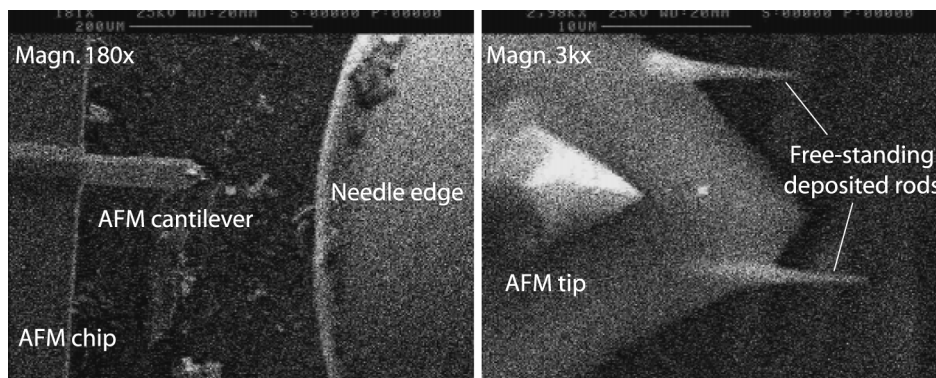
Figure 3-1-7. Imaging quality in the S100 at two magnifications (500 pA, screen snapshots).

3-1-6 Focused Electron Beam parameters

The electron source was a W filament heated to 2500-2800 K. The typical filament lifetime was one week, occasionally less when using certain precursors. The filaments were routinely replaced and realigned. They were slowly heated to saturation in 20 min before each first use. As acceleration energies 2, 3, 5, 10, 15, and 25 keV were available. Using one of the three lower energies required changing the anode in the electron extraction system. The working distance was imposed by the size of the precursor reservoir. It was at least 15 mm. The diameter of the diaphragm at the end of the electron column was either 50 or 70 μm.

The electron probe diameter was measured at 25 keV, at a working distance (WD) of 17 mm, with a diaphragm of 50 μm diameter, by imaging an Au on C resolution standard and applying Rayleigh's criterion.[1] The probe current and the probe diameter at 4σ varied together:

$$i_p = 2.10^{-6} d_{p,4\sigma}^{2.547} \tag{3-1}$$

Probe current i_p (in nA) as a function of the probe diameter $d_{p,4\sigma}$ (in nm).

According to this formula, at 500 pA probe current the probe diameter at 4σ was 132 nm. A knife-edge profiling method was applied to measure the electron distribution and convergence angle (see fig. 3-1-8a).
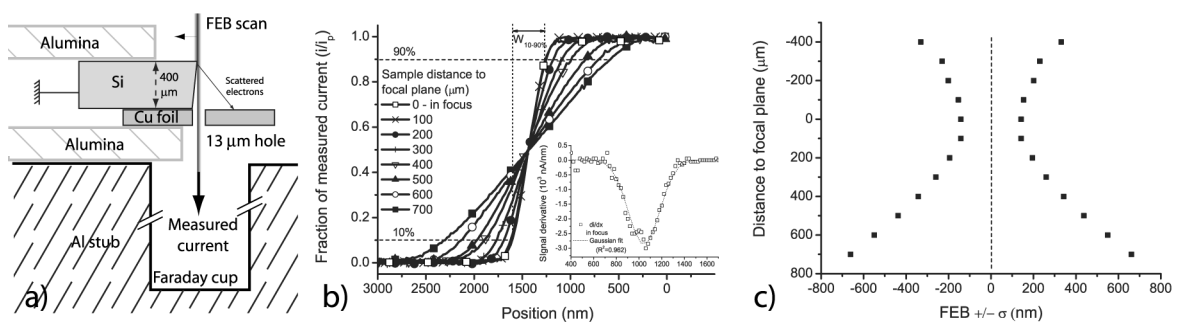
Figure 3-1-8. Knife-edge profiling. a) Experimental principle. b) Results. c) σ vs. height.

The conditions used were 25 keV, WD 45 mm, 70 μm diameter diaphragm, 430 pA. The beam was scanned at 20 nm/s across the edge of a cleaved Si sample. The un-intersected probe was

collected and measured in a Faraday cup through a 13 µm diameter opening in a Cu foil placed 400 µm below the Si edge. The electrons laterally scattered into angles larger than 16 mrad hit the grounded Cu foil and were not measured. The knife-edge curves were symmetrical, and their derivative showed the Gaussian beam distribution (see inset of fig. 3-1-8b). The beam profile was defined as:

$$I(r) = \frac{i_p}{2\pi\sigma^2} \exp\left(-\frac{r^2}{2\sigma^2}\right) \qquad\qquad \textbf{(3-2)}$$

The parameter σ was calculated from the knife-edge curves by the formula 3-3, in which $W_{10\text{-}90\%}$ was the width, defined graphically in fig. 3-1-8b, between the points where the signal reached 10 and 90% of its full value.[5]

$$\sigma = 0.39 W_{10-90\%} \qquad\qquad \textbf{(3-3)}$$

The beam convergence angle was 0.8 ± 0.2 mrad (see fig. 3-1-8c). The values obtained at this sample height were larger (see fig. 3-1-8c) than those measured previously by using Rayleigh's criterion (eq. 3-1). The shorter working distance and the smaller diaphragm conditions were chosen in the deposition experiments.

3-1-7 *In-situ* sample current monitoring during deposition

During operation of the S100, the sample was grounded through a Keithley 485 autoranging pico-amperemeter (shown in fig. 3-1-2c), which measured continuously the current absorbed by the sample. A computer acquired the measured value through a DAQ card and a Labview (v6.1, National Instruments) visual interface (see fig. 3-1-9). It was possible to acquire simultaneously either the SE detector signal, which modulated the intensity on the CRT screen of the electron microscope, or the photodiode signal (see below, §3-1-8). During deposition the sampling rate was 20 Hz. The values were averaged on 1 or 2 s. The actual number of electrons emitted by the filament could not be measured. In all the presented results where the sample current changed during deposition, the initial and final values of the probe current were checked

to be equal, either on the bare substrate or in the Faraday cup. As a consequence, the measured variations corresponded to a modification of the electron absorption efficiency of the sample.
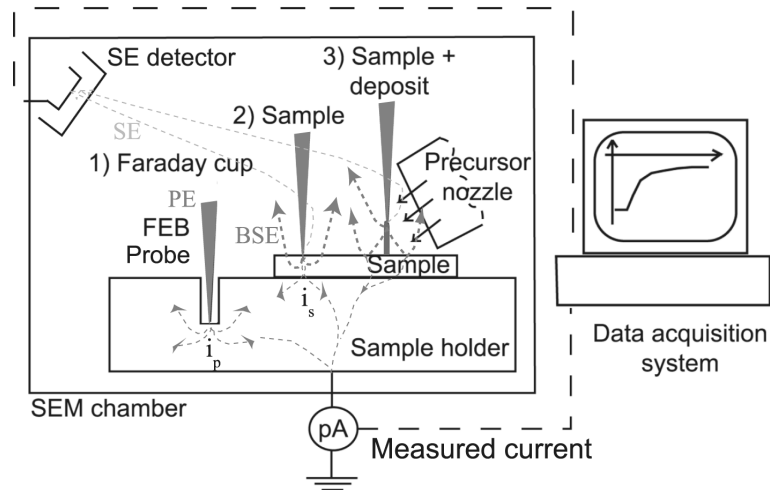
Figure 3-1-9. Principle of the *in-situ* monitoring of signals.

For clarity, only the absolute measured values, with their sign, are reported in the entire text. The sample current was usually negative at 25 keV, but positive sample currents were occasionally measured.

3-1-8 Co-focused laser beam

An Ar^+ ion laser emitting at 514 nm was co-focused with the FEB. The saturated SE scintillator was switched off while operating the laser inside the chamber. Coupling the laser into a monomode optical fibre (core diameter 4 μm) brought 40% of the laser power at a fixed point in front of a focusing optical system mounted across the chamber wall (see fig. 3-1-10a). The alignment was stable. The divergent beam exiting the optical fibre was made parallel by passing through Lens 1 (focal length f_1=2 cm). Lens 2 (focal length f_2=5 cm) focused it onto the sample (see fig. 3-1-10b). The beam on the sample was the image through a telescope of the beam at the fibre exit. A knife-edge measurement across the sharp edge of a Cr film on quartz revealed an elliptical laser spot with lateral dimensions 50 x 70 μm². The beam incidence angle on the substrate was 45°.
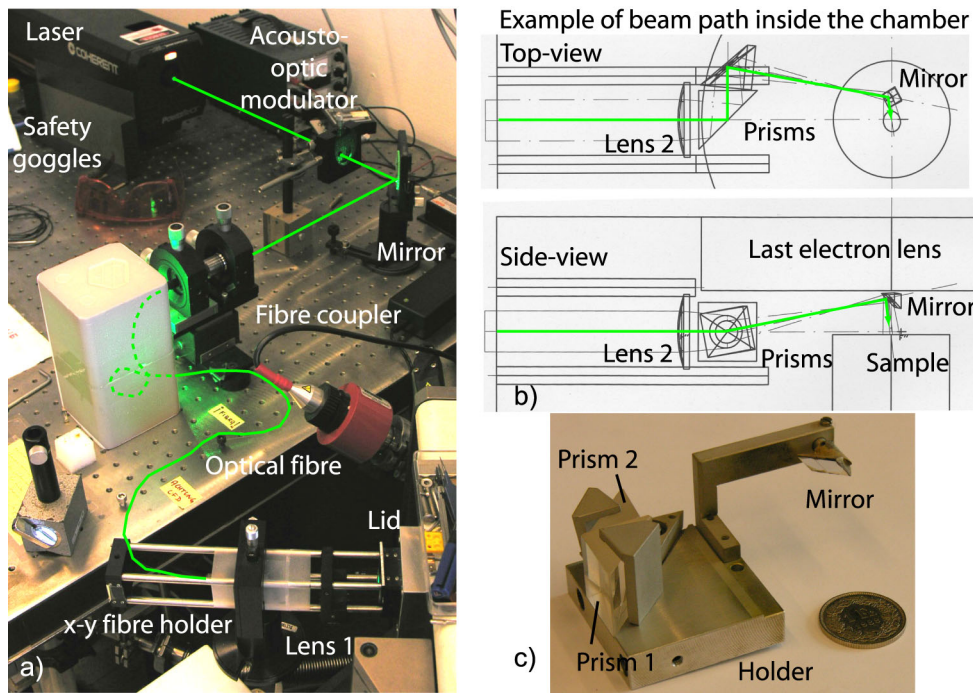
Figure 3-1-10. Laser co-focusing setup. a) Beam path outside the chamber. b) Example of beam path inside the chamber. c) Home-made holder for optical parts.

The fine co-focusing was achieved by marking the sample with red or black pen spots (2-3 mm wide). At 1 W power, the laser locally melted the thick (~200 μm) ink marks, resulting in a small pit visible in the SEM. The x-y fine positioning of the fibre exit moved the laser beam to the right horizontal position on the SEM screen. The vertical position was adjusted by moving the sample up or down. After reflection on the sample, the beam was sent to a photodiode (see fig. 3-1-4b) by a reflection on a horizontal mirror fixed to the last electron lens. The reflectivity of large growing deposits (at magnification 1 kx) was monitored in-situ with usually 200 mW laser power. The power incident on the sample was 10 mW due to the coupling and the multiple reflections. The temperature increase induced by the relatively large spot was at most 5°C.[6]

3-1-9 *In-situ* resistance measurements

Resistivity measurements were performed on deposited lines. To avoid oxidation effects and electrical breakdowns upon contacting, the resistance was monitored *in-situ* during the deposition of conductive deposits. The principle of the measurement is shown in fig. 3-1-11a.

The gain of the operational amplifiers varies with the resistance to be measured. A miniaturized electrical system was designed and realized for use in the S100 chamber (see fig. 3-1-11b,c).[7] Typically, U_s=0.1V and R_d=1 MΩ were measured with R_1=120 kΩ, R_2=620 Ω, and V_b=1V.
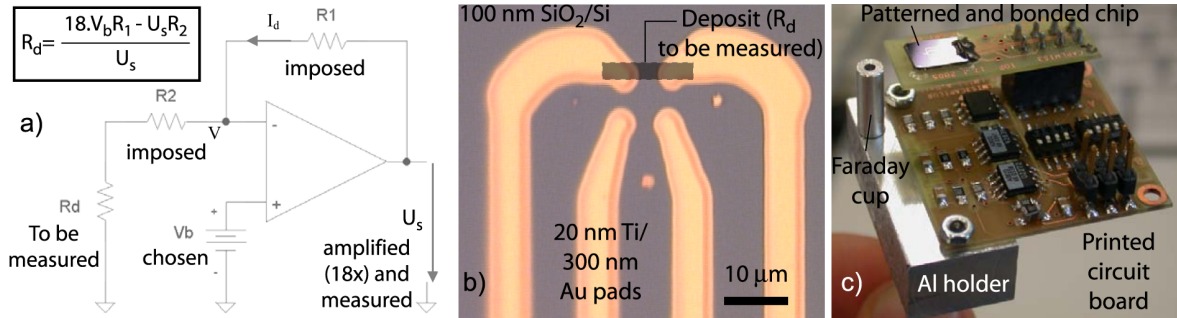
Figure 3-1-11. *In-situ* resistance measurement. a) Electrical scheme. b) Optical micrograph of the electrode pattern used. c) Ready-to-use system.

3-2 *Ex-situ* characterization

After deposition the samples were taken out of the S100 chamber. No precautions were taken against air exposure. They were imaged in a field-emission-gun Philips XL30 scanning electron microscope (FEG-SEM). This SEM was equipped for SE and BSE imaging, and had an Oxford LEAP detector for electron dispersive X-ray spectroscopy (EDXS) microanalysis. Routine transmission electron microscopy (TEM) analyses were made in a Philips CM-20 operated at 200 kV. Higher-resolution TEM, scanning TEM and EELS analyses were performed in a Hitachi HF-2000 operated at 200 kV, with the help of an operator. TEM analyses with a heated sample holder were performed in a Philips EM-430 TEM operated at 300 kV. All electron microscopy observations were made at CIME, EPFL.

Optical imaging was performed up to magnification 500x in an optical microscope (Zeiss Axiotech Vario 25 HD) equipped with a CCD camera for image acquisition (see fig. 3-1-12a). A system was constructed for micro-spectrophotometry by coupling the light from this microscope into an Optical Spectrum Analyzer (Ando AQ-6315B) through an optical fibre (see fig. 3-1-12b).[8] A compromise was made between resolution and signal-to-noise ratio by

selecting a 380 µm diameter fibre. Spectral information in the 400 to 800 nm wavelength range was available on spots of 10 µm diameter with this system.
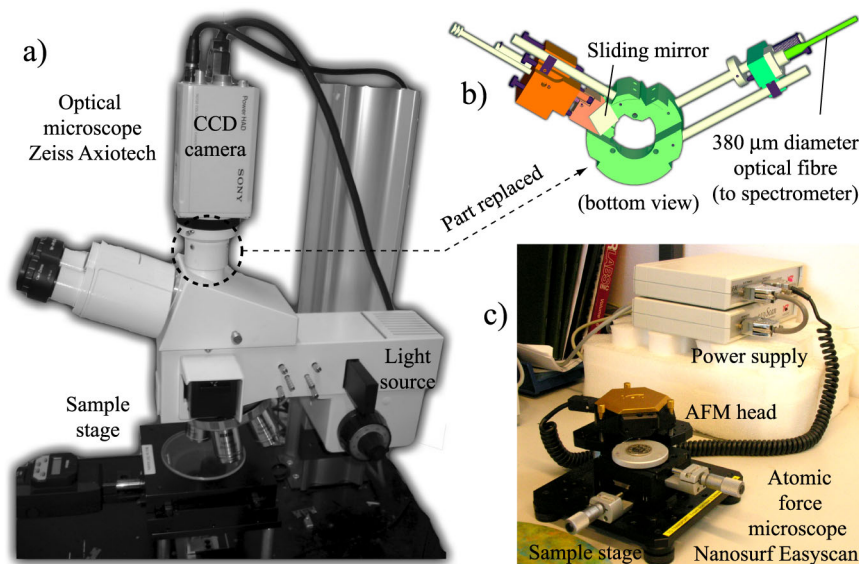
Figure 3-1-12. *Ex-situ* optical microscopy and AFM. a,b) Optical microscope used and part modified for micro-spectrophotometry. c) Compact AFM system used.

The sample profile was measured along lines by profilometry using a Tencor Alphastep. The stylus diameter was 50 µm. The smaller lateral range was 80 µm. For 2D mappings at higher resolution, a Nanosurf Easyscan atomic force microscope (AFM) was used (see fig. 3-1-12c). The larger lateral range was 80 µm. The samples were aligned with micrometric screws.

Microscopic Fourier Transform Infrared Spectroscopy (µ-FTIR) was performed in a Perkin-Elmer Spotlight 300 infrared microscope (LTP, DMX, EPFL). The deposits on Si substrates were analyzed in transmission. Square window areas with 20 µm side length were selected. The signal transmitted through the bare Si substrate was defined as background. The measured spectra were averaged on 64 to 1024 scans. Microscopic Raman spectroscopy (µ-Raman) was performed in a Renishaw RM1000 spectrometer with a 50x objective (IPS, UNIL). The excitation wavelength was 514 nm. The measured spectra were averaged on 2 to 10 scans.

Chapter 4 – Electron range effects in focused electron beam induced deposition

Il n'est pas de brouillards, comme il n'est point d'algèbres,
Qui résistent, au fond des nombres ou des cieux,
A la fixité calme et profonde des yeux.

Victor Hugo, la Légende des Siècles, 0, 40

In the usual beam energy range used for electron microscopes (1-50 keV in SEMs, 30 keV-a few MeV in TEMs), the penetration of electrons into solids takes place at larger scales (typically > 100 nm) than the lateral beam diameter (down to ~1 nm in SEMs, ~1 Å in TEMs). This chapter presents the propagation of electrons in materials and its evolution during Focused Electron Beam induced deposition (FEBID). The deposition process, which consists of a surface reaction, is linked to the scattering of electrons that takes place in bulk matter. Three types of deposits are considered, in an increasing order of complexity. In Section 4-1, the simple case of deposition of large-area films is presented. The principle of *in-situ* monitoring of the sample current, and to a lesser extent of the SE detector signal, is demonstrated. Several beam energies and deposit compositions are investigated and interpreted to show the scope of the method. Monte-Carlo simulations illustrate the physical origin of the phenomenon. A relation is defined between the growth rate and the numbers of electrons through interfaces. In Section 4-2, the deposition of sharp tips is studied. Systematic *in-situ* sample current monitoring allowed developing a more detailed model of electron scattering. In Section 4-3, the electron range effects during deposition of complex 3D microstructures are presented. Fundamental aspects of the deposition process were discovered and interpreted during this study.

4-1 Large-area deposits

Numerous parameters are involved in the focused electron beam induced deposition process (see fig. 4-1-1). Several parameters are linked together by physical relations. During deposition of a simple structure like a large-area flat film on a substrate, the target upon which the electron beam impinges is modified. This section shows how electron propagation evolves during deposition, and what are the consequences on the film deposition rate.
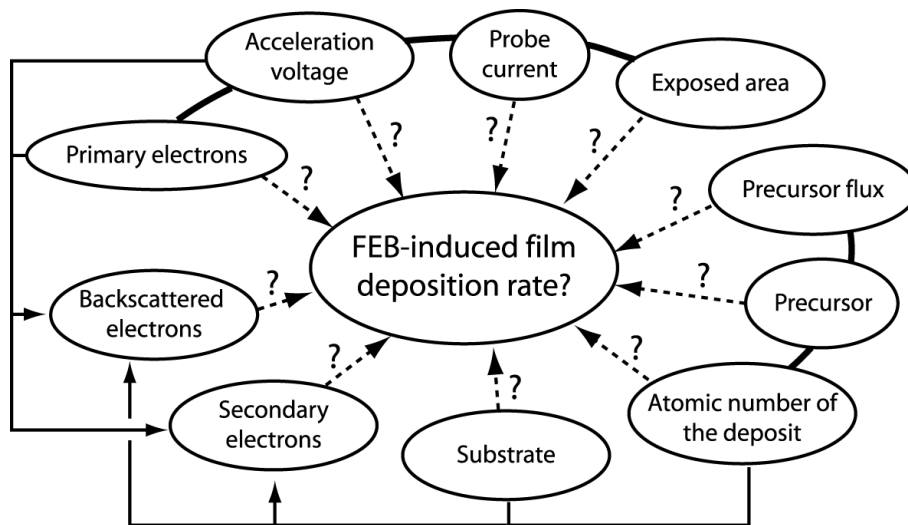
Figure 4-1-1. Schematic diagram of the process parameters

The deposition of low-atomic number (carbonaceous) films is first addressed. The effects of several experimental parameters are studied, namely the deposition substrate, acceleration voltage, probe current, exposed area, and distance to the gas effusion needle. Then the deposition of an intermediate atomic number material, a Cu-containing carbonaceous film, is described at several acceleration voltages and on two different substrates. The deposition of high atomic number Au films is then studied. In the discussion of the results, Monte-Carlo simulations describe common features of the three deposited materials. Finally, physical interpretations of the results are proposed.

4-1-1 Definition

A "large-area deposit" has lateral dimensions that exceed the electron backscattering range (see fig. 4-1-2a) and the electron probe diameter, as shown in fig. 4-1-2b.
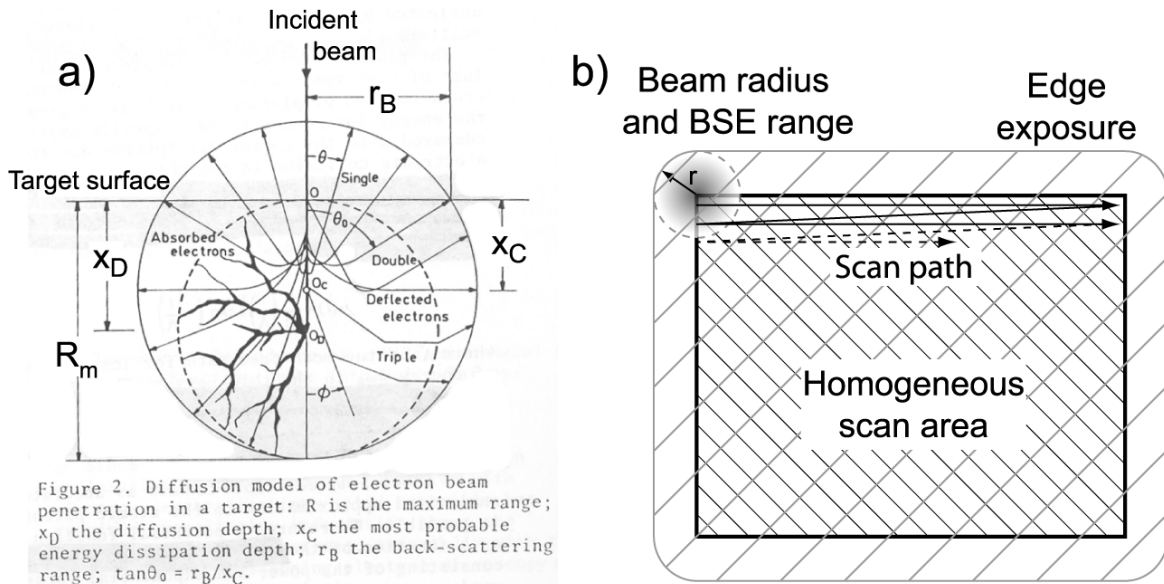
Figure 4-1-2. "Large-area deposit" definition. a) Graphical definition of electron ranges in a solid target (R_m: maximum range; r_B: backscattering (BSE) range; $x_{C, D}$: characteristic depths).[1] b) Large-area deposit writing sequence. r: edge radius.

The backscattering range r_B is the larger distance from the incidence point up to which a backscattered electron (BSE) can exit a solid target after a series of collisions (see fig. 4-1-2a).[1] r_B increases with the beam energy and decreases with the target atomic number. It ranges from 30 nm in Au at 3 keV to 2.5 µm in C at 25 keV (see Annexes 1 and 2 for further details). The larger probe diameter d_p used was 1.05 ± 0.1 µm at 100 nA probe current. Both d_p and r_B convolute the rectangular beam scan (see fig. 4-1-2b). The scan areas were considered "large" when the central areas exposed by both primary electrons (PE) and BSE were at least equal to the exposed edge areas. In the presence of a precursor, the scans resulted in the local deposition of films having large lateral dimensions as compared to their thickness.

4-1-2 Low atomic number deposits

The deposition of C films on light (Si) and heavy (Au) substrates is compared at several beam energies. The film thicknesses were measured by profilometry. The SE and BSE contrasts of *ex-situ* SEM images were compared to the *in-situ* evolutions of the SE and sample current monitored during deposition. The sample current indicated the amounts of BSE with a small SE contribution. The monitoring made thickness and growth rate information available during deposition. It was used to study the effect of several parameters of the process. The results are interpreted in paragraphs 4-1-5 and 4-1-6.

Large-area C films were deposited from acrylic acid (H$_2$C=CH-COOH) as a precursor. The precursor flux, estimated by a volume reduction of 0.2 mL in 6 h through a 600 μm diameter needle, was $(3 \pm 1).10^{19}$ molecules/cm^2.s. The PE energy was varied from 5 to 25 keV, at a probe current of 100 nA. At magnification 2 kx, the 50 Hz TV scan exposed a 50x60 μm^2 area at a constant distance of 100 μm from the needle. The sample was naturally oxidized p-doped Si. Deposition was performed across the edge of a 500 nm thick Au film evaporated prior to deposition, in order to measure the effect of the substrate in strictly identical conditions.

4-1-2-A) Intermediate acceleration energy – 10 keV

The thickness of large-area deposits increased linearly with the deposition time.
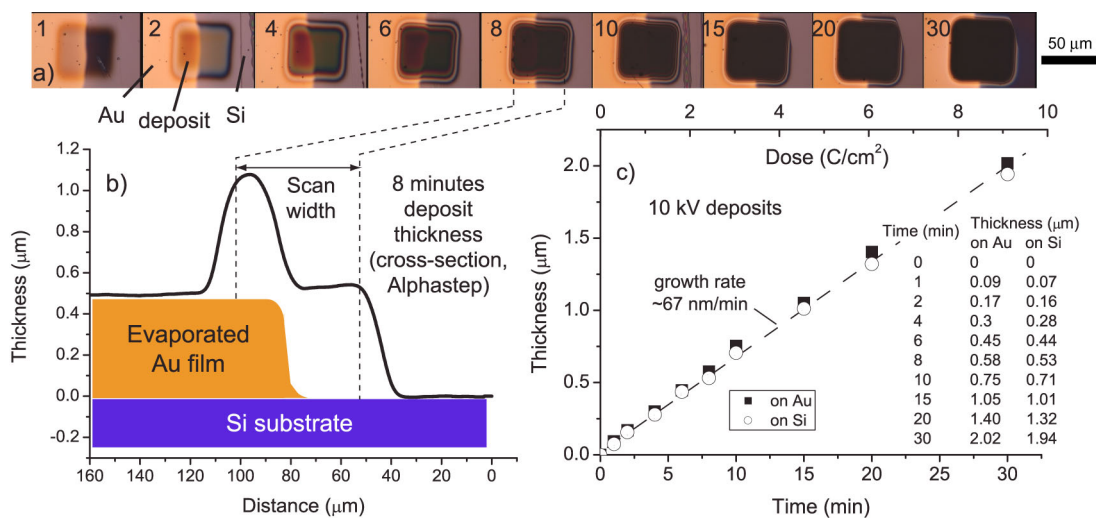
Figure 4-1-3. *Ex-situ* characterization of large-area deposits from acrylic acid, TV scan at magnification 2 kx across a Si-Au film edge, 10 keV, 100 nA. a) Optical micrographs

(reflection, bright field) with deposition times (minutes). b) Example of measured cross-section (Alphastep; note the different scales). c) Measured deposit thickness on Si and Au *vs.* deposition time and electron dose.

Interference colors were seen in the optical micrographs of films thinner than 1 µm (see fig. 4-1-3a). They clearly showed the homogeneous thickness in the central part of the scanned rectangles, as compared to their edges. The film thicknesses (at most 2 µm) were always smaller than their lateral dimensions (see fig. 4-1-3b). The constant growth rate of 67 ± 3 nm/min was independent of the substrate (see fig. 4-1-3c).

The deposited films were observed *ex-situ* in a higher-resolution SEM (XL30 SFEG) at 10 kV (see fig. 4-1-4a). Both the SE and BSE signals from the films decreased with increasing thickness before saturating after 8 minutes (see fig. 4-1-4b,c). The variations were larger on Au than on Si but the final values were identical.
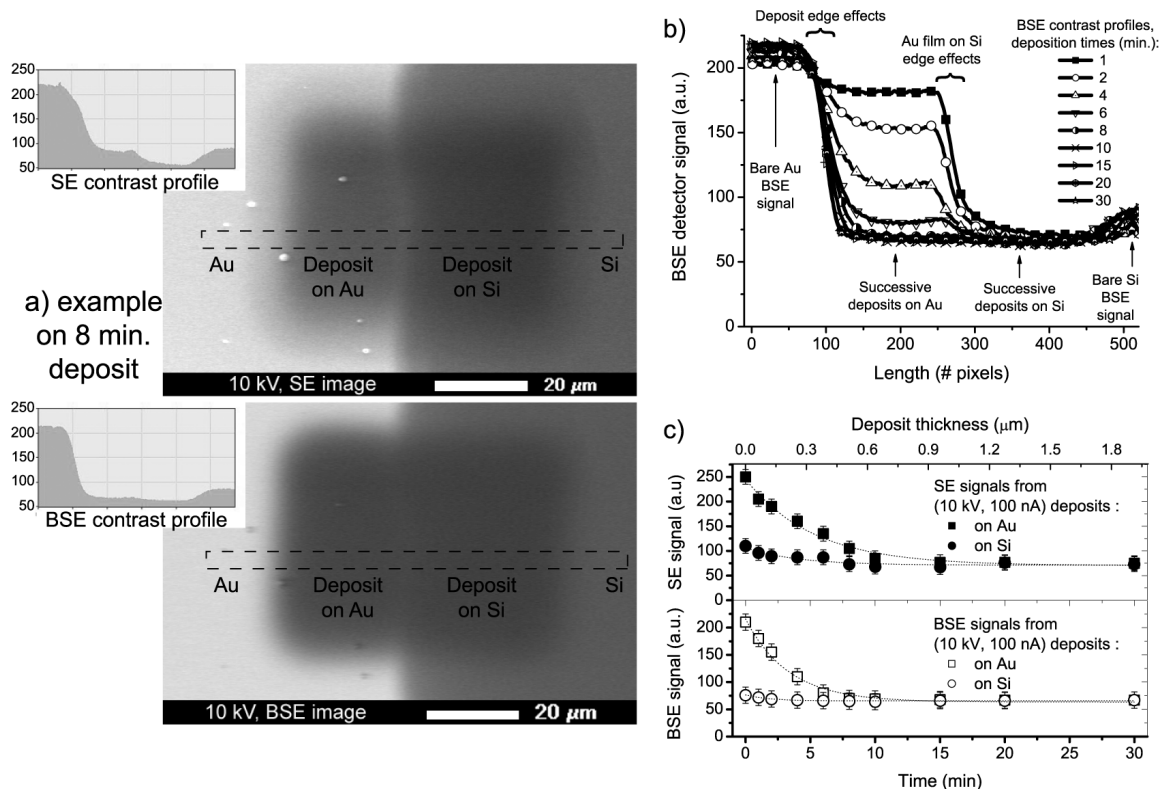
Figure 4-1-4. *Ex-situ* 10 kV SEM pictures. a) SE and BSE images of the 8 min. deposit. Insets: contrast profiles. b) BSE contrast profiles on successive deposits. c) Evolution of SE and BSE contrasts of successive deposits on Si and Au. Dotted lines are first-order exponential fits (see below, §4-1-5B,C).

During deposition of the films shown in figs. 4-1-3 and 4-1-4, the sample current and SE signal of the SEM used for deposition were monitored and recorded by a computer. The recorded signals are shown in fig. 4-1-5.
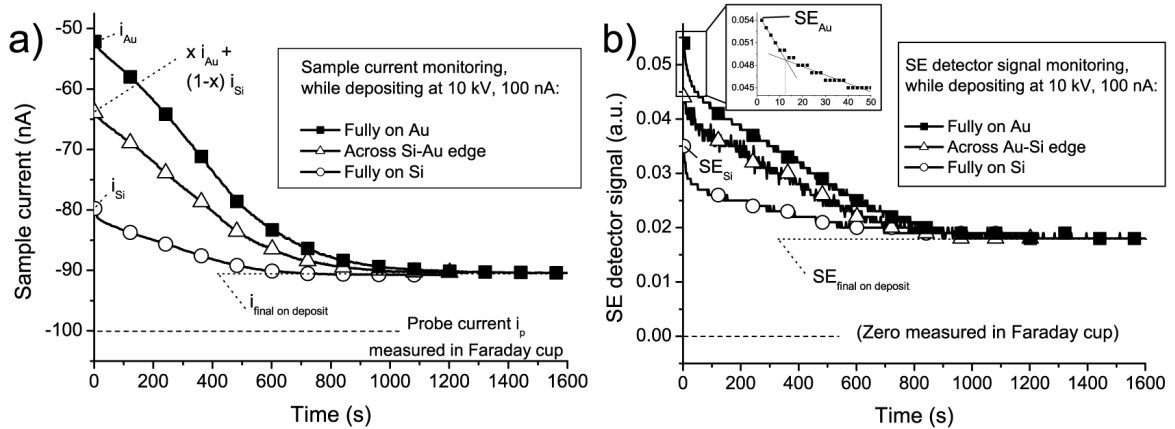
Figure 4-1-5. *In-situ* monitoring of signals from acrylic acid at 10 kV, 100 nA, TV scan at magnification 2kx. a) Sample current *vs.* time (2 s per point). b) SE detector signal *vs.* time. Inset, close-up on the beginning of the process on Au.

The *in-situ* monitored SE signals decreased with the same time constants as the *ex-situ* SEM contrasts, but they offered continuous information. Slope variations occurred at 13 ± 3 nm deposit thickness, then the signals decreased linearly (see inset in fig. 4-1-5b). Saturation occurred after 900 ± 90 s, on a 1 ± 0.1 μm thick deposit, to a substrate-independent value, which corresponded to reductions of 67% and 50% from the signals on Au and Si, respectively (see fig. 4-1-5b). The absolute values of the negative sample currents were initially imposed by the substrates (see fig. 4-1-5a). They linearly increased in correspondence to the film thickness. Saturation occurred at 91% of the probe current after 900 ± 90 s, on all substrates. After saturation was reached, no more information on film thickness or growth rate was obtained. The signals across the Si-Au edge were weighted sums of the evolutions on Si and Au. The sample current had two advantages over the SE signal. First, it was less noisy. Second, the indicated value was absolute, while only relative variations were measured with the SE detector.

The following hypothesis was formulated: the variation of the sample current could be due mainly to the evolution of the BSE yield, because they were linked by a simple relation:

$$i = i_p \left(1 - \eta - \delta\right) \tag{4-1-1}$$

Sample current balance from probe current i_p, BSE yield η, and SE yield δ.

At 10 keV η is larger than δ (see Annexes 3 and 4). The fraction of incident electrons absorbed in the sample increased when η decreased. In order to test by experimental proofs, deposition was performed at different beam energies with a systematic monitoring of the signals.

4-1-2-B) Lower acceleration energy – 5 keV

The films deposited at 5 keV on Au were similar in optical microscopy (not shown). The successive thicknesses measured by profilometry showed that the growth rate was not constant (see fig. 4-1-6). It decreased from 53 to 41 nm/min after 8 min.
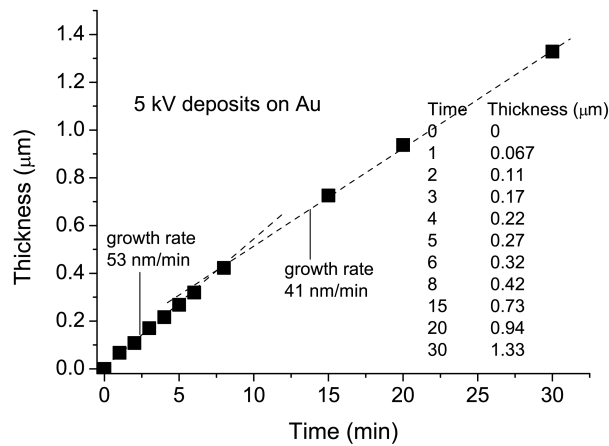
Figure 4-1-6. *Ex-situ* profilometry measurements of large-area deposit thickness *vs.* time from acrylic acid on Au, TV scan at magn. 2 kx, 5 keV, 100 nA.

During deposition the sample current and SE were monitored *in-situ*. After a slope variation at 9 ± 2 s (see inset in fig. 4-1-7b), the SE signal lost 60% of its value and saturated (see fig. 4-1-7b). A slope variation also occurred at 9 ± 2 s on the sample current curve (see inset in fig. 4-1-7a), then the absolute value of the sample current increased and saturated at 95% of the probe current (see fig. 4-1-7a). Both saturations occurred in 8 minutes, when the film was 350 nm thick, coinciding with the time at which the growth rate decreased.
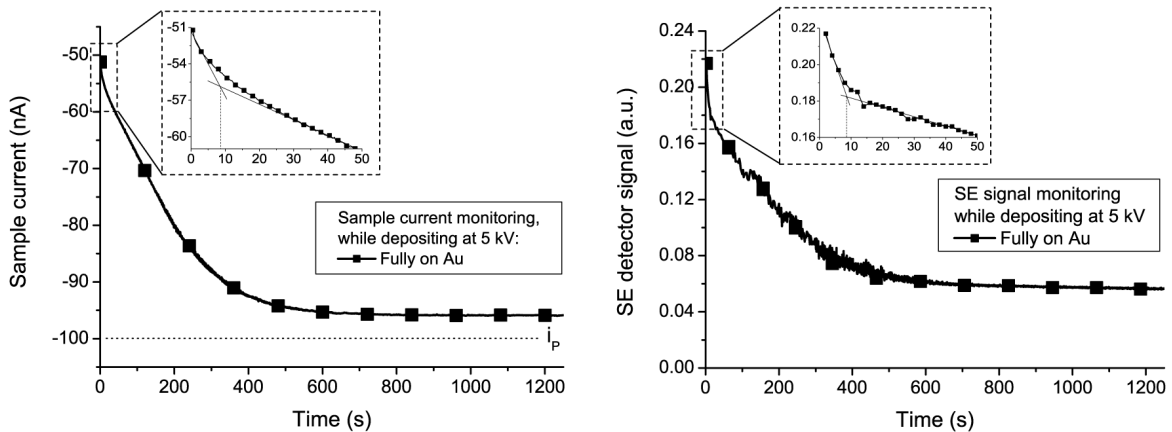
Figure 4-1-7. *In-situ* monitoring of signals from acrylic acid at 5 keV, 100 nA, TV scan at magn. 2 kx. Left, sample current *vs.* time. Right, SE detector signal *vs.* time. Insets, close-ups on the beginning of the process.

The initial slope variations (see insets in fig. 4-1-7a,b) were due to a change in SE emission properties of the sample. The beam current was lowered to 10 nA, which lowered the growth rate to 7.5 ± 2 nm/min. Detailed initial slope variations reproducibly occurred (see fig. 4-1-8a) at 12 ± 3 nm film thickness, which is of the order of the SE escape depth.[2] By recollecting the SE in the substrate with a +9 V sample bias, the initial slope variations disappeared from the sample current and were strongly attenuated in the SE curve (see insets in fig. 4-1-8b).
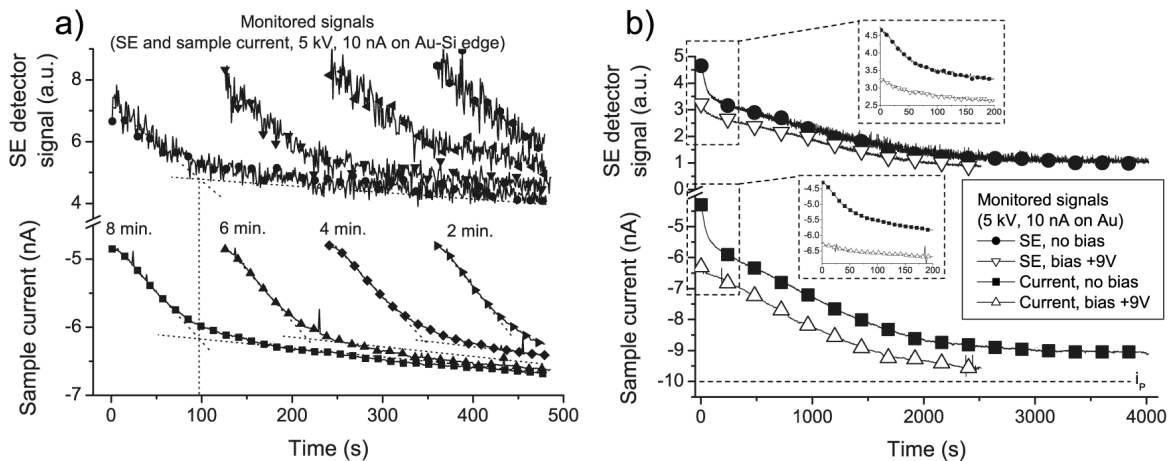
Figure 4-1-8. Detailed *in-situ* observation of the initial slope variation from acrylic acid at 5 keV, 10 nA. a) Monitoring across an Au-Si edge (repeated on several deposits, 2 to 8 min.; curves shifted for comparison). b) Monitoring on Au with and without +9 V sample bias.

With the bias the signals evolved at the same rate, but the sample current was 10 % larger and the SE signal 10 % smaller (see fig. 4-1-8b). The sample recollected all the SE emitted from the sample at energies lower than 9 eV. Although by definition all electrons emitted at energies below 50 eV are called "secondary", most of the SE emission spectrum is contained below 10 eV.[3-8] The remaining SE signal was probably due to third-generation SE, emitted by the BSE on the chamber walls. The initial slope variation in the sample current curve indicated a partial SE contribution to this signal.

The rapid initial SE decrease with film thickness was confirmed by SEM imaging at 5 kV (see fig. 4-1-9a). The successive SE intensities showed a quick initial decrease on the thinner films, while the BSE initial decrease was linear (see fig. 4-1-9b and compare to fig. 4-1-8b).
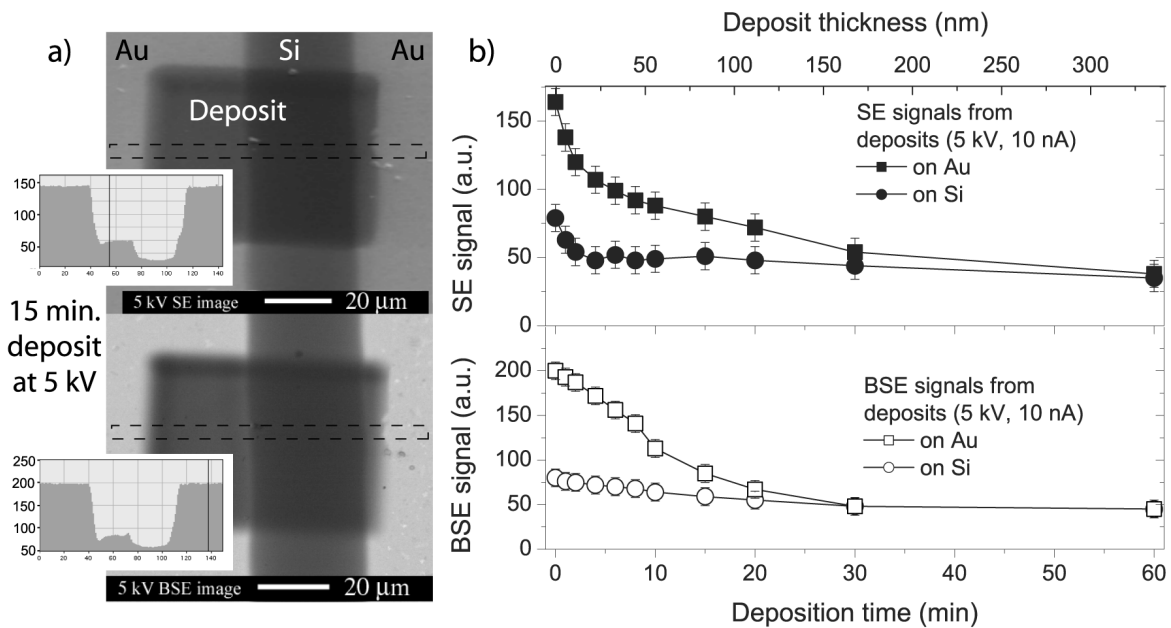
Figure 4-1-9. *Ex-situ* 5 kV SEM imaging confirms the SE contribution to initial slope variation. a) 5 kV SE (top) and BSE (bottom) images of a deposit across an Au-Si(-Au again) edge. Insets, contrast profiles. b) Successive SE and BSE intensities, on Au and Si.

These measurements confirmed the hypothesis: the sample current depended mainly on the BSE yield. The SE, BSE and sample current evolved in correspondence to the film thickness, with a higher sensitivity in the first deposited nanometers. After 10 nm thickness, the SE emitted from the sample decreased the measured sample current by only 10%. The

simultaneous sample current and BSE evolutions occurred on thinner films than at 10 keV due to lower electron penetration.

4-1-2-C) Higher acceleration energy – 25 keV

At 25 keV the average growth rate of 25 nm/min was halved as compared to the lower energies. The substrate had almost no effect on the growth rate, which had an inflexion point at 15 min (375 ± 50 nm, see fig. 4-1-10b).
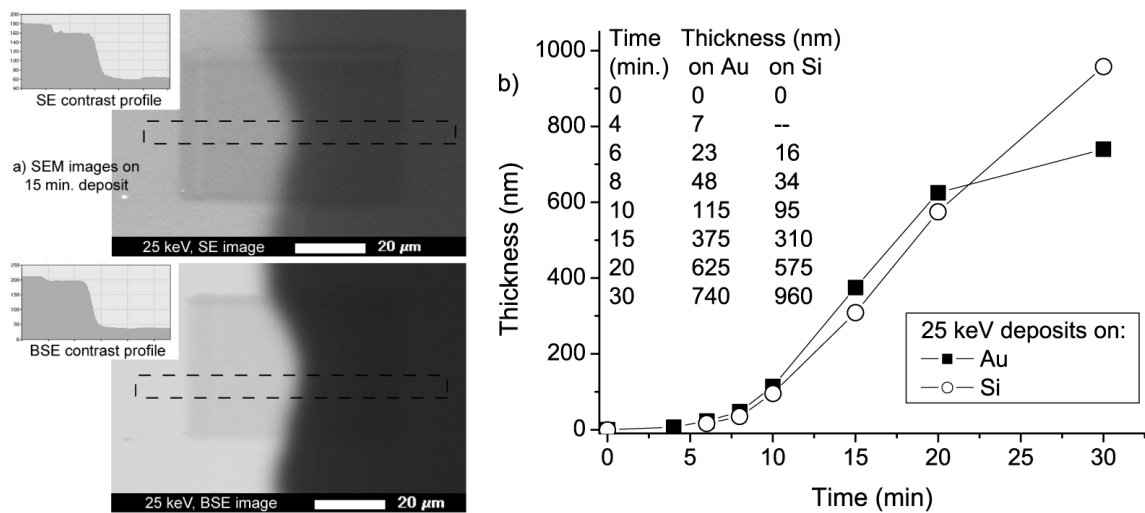
Figure 4-1-10. Films deposited at 25 keV, 100 nA. a) *Ex-situ* 25 keV SEM images (SE and BSE). Insets, contrast profiles. b) Film thickness *vs.* time (Alphastep), on the two substrates.

The 25 keV SEM contrasts between the film and the substrates were low (see fig. 4-1-10a). The monitored signals (not shown) evolved much more slowly (from 66 to 72 nA in ½ h for the sample current) and did not saturate during the investigated time span. Saturation was reached by depositing on smaller areas (see §5-1-3). The slow decrease of the BSE yield and sample current were due to the larger electron penetration, which makes the electron probe less sensitive to surface layers. As a conclusion, 25 keV energy was not recommended to study the dependence of the deposition rate on the process parameters, as compared to lower energies.

4-1-2-D) Growth rate dependence on process parameters and mapping

The sample current was a useful tool to monitor the film deposition rate, since it was less noisy than the SE signal. Monitoring was used to investigate the effect of several process parameters on the deposition rate. A compromise had to be made between the higher sample current sensitivity to film thickness at lower beam energy and the higher growth rate at intermediate beam energy. The deposition conditions were chosen as 10 keV and 100 nA on Au.

When keeping the exposed area constant, the growth rate (R) depended on the probe current (i_p). The relative growth rates were deduced by scaling the time bases so that the monitored curves superimposed on one another, as shown in fig. 4-1-11a.
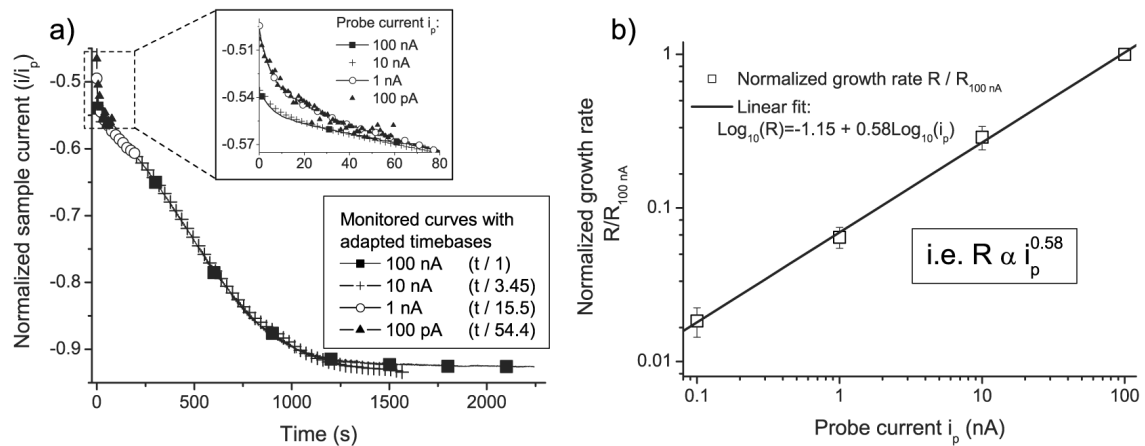
Figure 4-1-11. Growth rate (R) *vs*. probe current (i_p) from acrylic acid on Au, 10 keV, TV scan at magn. 2 kx. a) Curves superimposed by adapting the time bases. b) Log-log plot of the relative growth rates, normalized at 100 nA, and deduced power law.

All curves were superimposed on the same values around saturation, or around the initial slope variation (see inset in fig. 4-1-11a) if, for technical reasons, saturation was not possible. Each reduction of the probe current by a factor of 10 decreased the growth rate by 3.5. The growth rate varied as the power 0,58 of the probe current (see fig. 4-1-11b).

By following the same time base scaling procedure, monitoring was used to study the growth rate dependence upon the scan area (S). The large-area deposits obtained at different magnifications are shown in fig. 4-1-12a. The effective surfaces on which the deposits formed were measured from the optical micrographs.
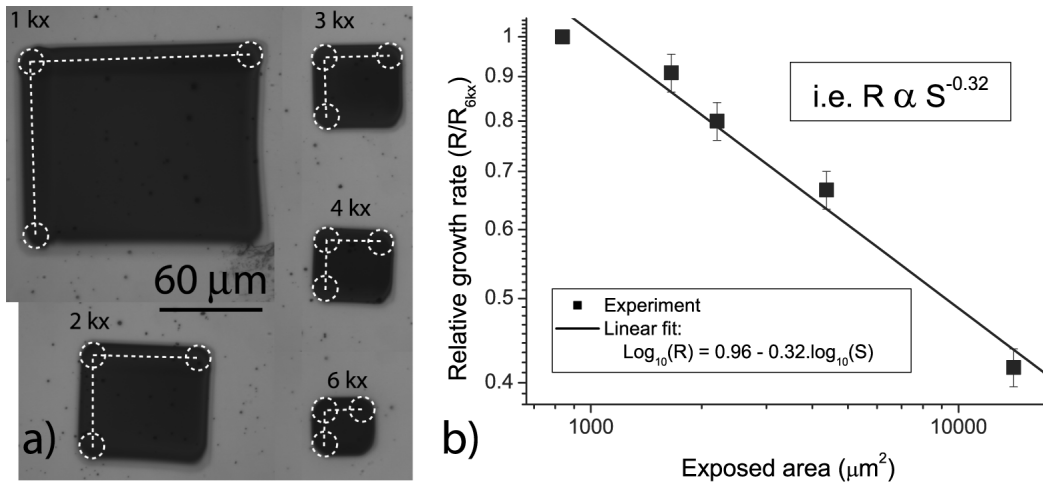
Figure 4-1-12. Growth rate *vs.* exposed area from acrylic acid on Au, 10 keV, 100 nA, TV scan. a) Optical micrographs (dotted lines: schematic beam size and path). b) Log-log plot of the relative growth rate, normalized at 6 kx, and deduced power law.

Each reduction of the exposed area by a factor of 3 increased the growth rate by 30% (see fig. 4-1-12b). The growth rate varied as the inverse power 0,32 of the surface. The two power laws give information on the deposition rate dependence on the electron flux, as shown in §4-1-7.

Monitoring was used to map the relative growth rate decrease *vs.* distance to the needle.
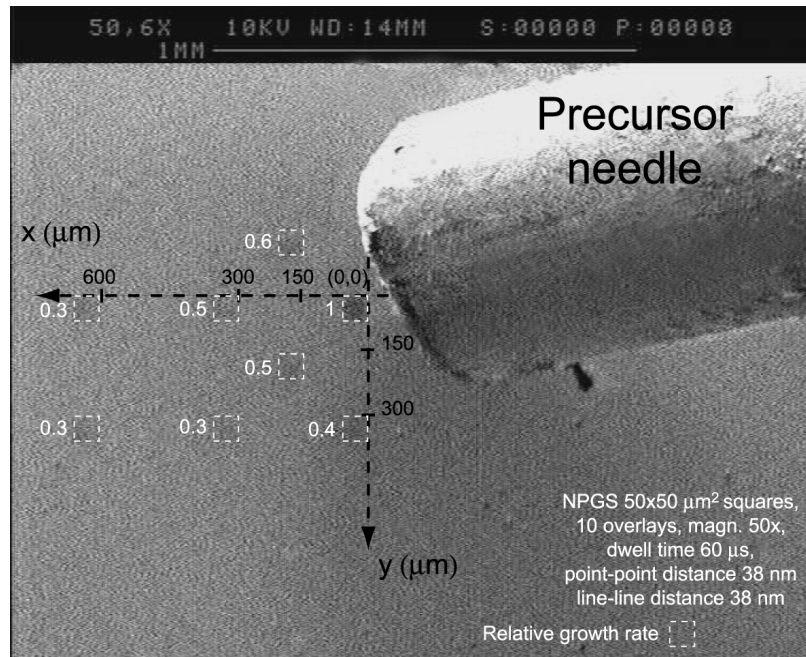
Figure 4-1-13. *In-situ* growth rate mapping (acrylic acid on Au, 10 keV, 100 nA). S100 screen snapshot after deposition. Deposit positions and relative growth rates highlighted.

In the direction of effusion, a 70% deposition rate decrease occurred at 600 μm (see fig. 4-1-13). The lateral reduction was 60% at only 300 μm. Both were due to a lower local precursor supply.[9, 10] At the needle exit, the gaseous precursor flux was 3.10^{19} molecules/cm^2.s. According to the kinetic theory of gases, the corresponding local pressure was 0.4 mbar, i.e. 10% of the precursor vapor pressure of 3.8 mbar.[11] The collision mean-free-path was 50 μm. The gas then expanded and its internal pressure dropped down to the pressure in the vacuum chamber, measured as $1.3.10^{-5}$ mbar with this precursor. This agreed with Monte-Carlo simulations of the gaseous flow in the molecular regime.[12] The deposition regime was thus precursor-limited.

To study the effects of the three parameters, the advantage of monitoring was a rapid, precise and continuous access to the growth rates. Profilometry or AFM would have required several deposits, thus been more time-consuming and not as accurate.

4-1-2-E) Summary of the results

- The SE and BSE contrasts of C films deposited on Si and Au, observed *ex-situ* by SEM at the same energy, decreased and saturated at substrate-independent values with similar time constants. Saturation occurred on thinner films at lower energies.

- Similar and simultaneous variations were continuously monitored during deposition in the signals of the emitted SE and of the sample current.

- The larger growth rate was measured at 10 keV. It was constant with deposition time. The 30% lower growth rate measured at 5 keV on Au decreased when the sample current saturated. A much lower growth rate with a complex evolution during growth was measured at 25 keV.

- Initial slope variations occurred in the monitored signals at 12 nm deposit thickness due to the emitted SE. A +9 V sample bias suppressed them without affecting the growth rate. The SE contribution to the sample current was limited to 10%. During deposition, the sample current variation was due mainly to a change in BSE yield of the structure on which the electron probe impinges.

- The substrate had no important effect on the growth rate, contrary to what was observed by contamination.[13]

- Monitoring of the sample current was used to study the effects of the process parameters. The growth rate was mapped as a function of the distance to the needle. It varied as the power 0,58 of the probe current at constant exposed area, and as the inverse power 0,32 of the exposed area at constant probe current.

In order to observe the dependence of sample current on the average atomic number of the deposit, monitoring was applied when depositing films with heavier elements, Cu and Au.

4-1-3 Intermediate atomic number deposits

Deposition was performed from the copper CVD precursor hexafluoro-acetylacetonato-copper(I)-vinyltrimethylsilane ((hfac)CuVTMS, CAS n°[139566-53-3]) at several accelerations. A probe current of 10 nA was used in order to avoid heating. As determined by EDX, all the film deposits showed the same composition, $Cu_1C_3O_1F_1$ (see §5-2-2).
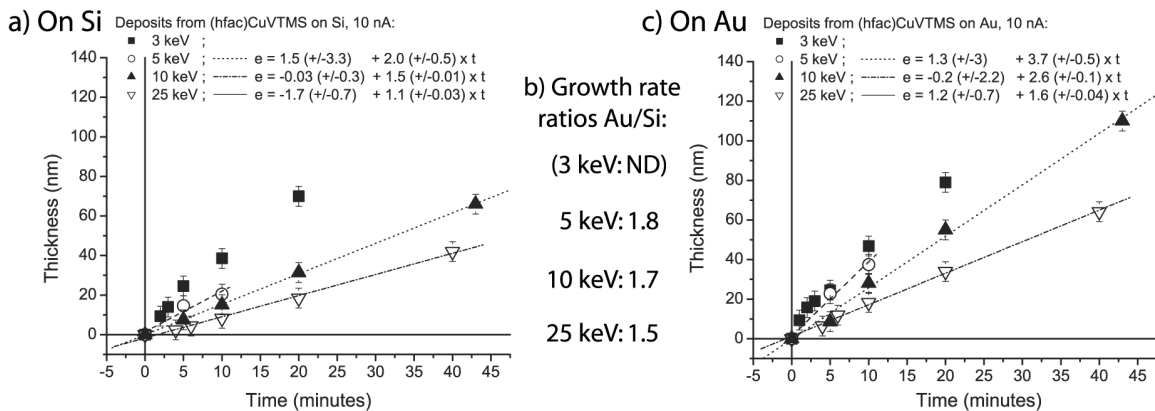
Figure 4-1-14. Deposition from (hfac)CuVTMS at several energies, 10 nA, TV scan, 2 kx. a) Thicknesses (Alphastep) on Si *vs* time t. b) Ratios of the linear growth rates (ND: not defined at 3 keV; see below, fig. 4-1-15). c) Thicknesses on Au, plotted at the same scale as in (a).

The growth rates increased with the decreasing beam energy (see fig. 4-1-14a,c). During deposition all growth rates were constant except at 3 keV, and were higher on Au than on Si by a factor 1.5 to 1.8 (see fig. 4-1-14b). Only the 3 keV films BSE contrasts saturated at 40 ± 5 nm

thickness in *ex-situ* SEM imaging at the same energy as deposition (see fig. 4-1-15). Due to the high C content in the films the contrasts were very similar to those of the previous section (compare figs. 4-1-15 and 4-1-9).
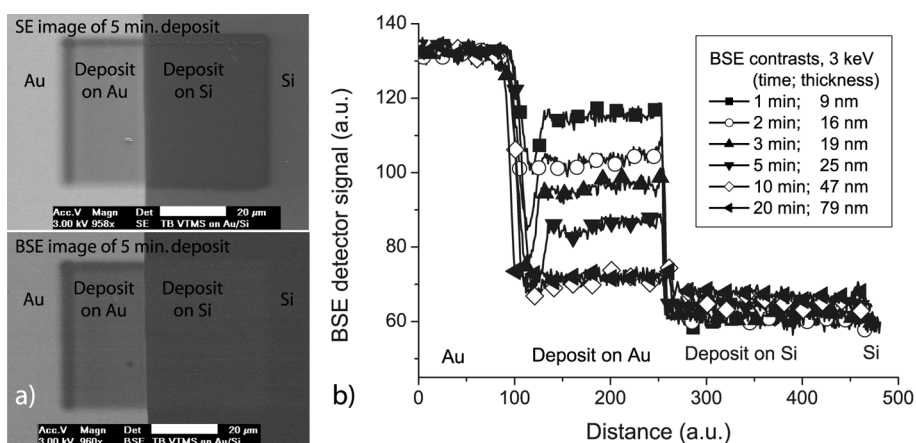
Figure 4-1-15. a) *Ex-situ* 3 keV SEM images of films deposited at 3 keV. The thicker left and upper deposit lines were due to the built-in TV scan .b) Successive BSE profiles.

The initial growth rate variations seen in fig. 4-1-14c at deposition energy 3 keV coincided with a decrease in BSE and SE (see fig. 4-1-16a).
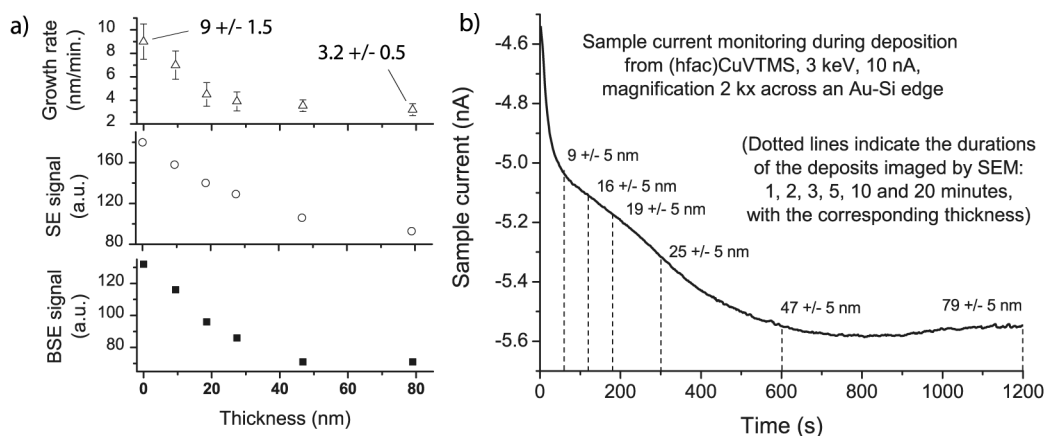
Figure 4-1-16. Simultaneous evolutions from (hfac)CuVTMS on Au at 3 keV. a) Growth rate, *ex-situ* SE and BSE contrasts *vs.* deposit thickness. b) *In-situ* sample current monitoring.

A simultaneous decrease in the absorbed sample current was measured, after a sharp slope variation at 7 ± 2 nm deposit thickness (see fig. 4-1-16b). The sample current saturated at 56% of the total probe current on a 45 ± 5 nm thick film, following the same trend as the BSE yield.

As a conclusion, the deposition regime for this precursor was substrate-dependent. The growth rate evolved at the same speed as the numbers of electrons passing through the interface.

4-1-4 High atomic number deposits

Most precursors used for FEB-induced deposition contained C, which was also present in the deposits. In order to deposit on a Si substrate a film with a much higher average atomic number, the inorganic precursor $AuPF_3Cl$ was used. This is the only compound that had been reported to deposit a pure crystalline metal by FEB.[14] Lines with only half the conductivity of bulk Au had been deposited. Au has atomic number $Z_{Au}=79$, in comparison to $Z_{Si}=14$. The experimental conditions for pure Au deposition were similar as those used in the last paragraphs: at room temperature, without any other gas. At 5 keV, the growth rate was constant and remained at 1 ± 0.2 nm/min (see fig. 4-1-17a). SEM showed 50 nm pure Au grains and the AFM roughness was 10 nm (see fig. 4-1-17b).
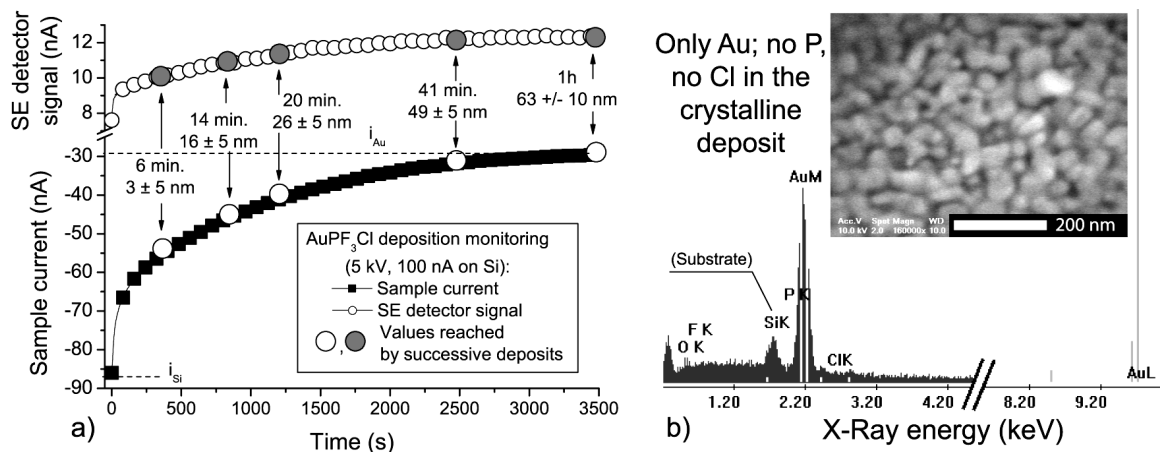
Figure 4-1-17. Au film on Si. a) *In-situ* monitoring from AuPF₃Cl on Si, at 5 kV, 100 nA, 2 kx. b) 10 keV EDX spectrum. Inset, e*x-situ* SEM top view of the film (scale bar 200 nm).

During deposition, the monitored SE increased by 50% (see fig. 4-1-17a). The sample current increased and saturated to 25% of the probe current when the film was 50 nm thick. Initial slope variations were probably due to the nucleation of islands. Since the substrate on which the film was being deposited changed from Si to pure Au as the film got thicker, but the growth rate remained constant, this precursor led to a substrate-independent growth rate, contrarily to the

organometallic Cu precursor (see §4-1-3) but in the same way as the purely organic precursor did (see §4-1-2).

At 10 keV the growth rate was still constant during growth but at a slightly higher value, at 1.3 ± 0.2 nm/min (see fig. 4-1-18a).
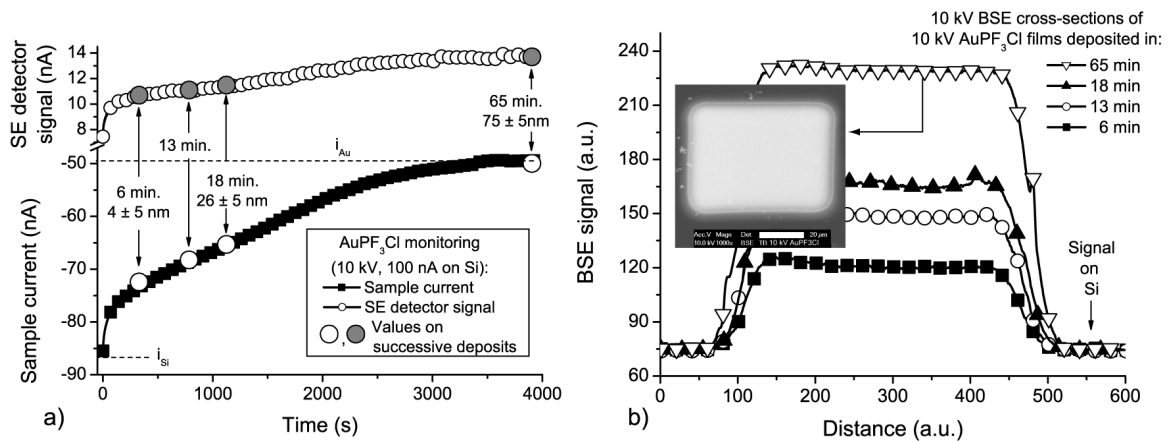
Figure 4-1-18. Au deposition from $AuPF_3Cl$ on Si at 10 keV, 100 nA, 2 kx. a) *In-situ* monitoring. b) *Ex-situ* BSE contrasts from 10 kV SEM images (Inset, BSE top view of 1 h deposit, scale bar 20 µm).

The initial slope variations still occurred. Saturation was reached on 60 nm thick films, at 50% of the probe current and twice the initial SE signal, respectively (see fig. 4-1-18a). The *ex-situ* BSE and SE signals on the deposits in 10 kV SEM images simultaneously increased (see fig. 4-1-18b).

These results confirmed that the measured sample currents evolved in the opposite way as the BSE yields did, since these were much higher on heavy films than on the C-containing deposits. The value reached at saturation depended on the chemical compositions of the films. The film thickness, at which the saturation was reached, was also linked to the film composition. When the films contain heavier elements, saturation occurs on thinner films than if the deposits contain light elements.

4-1-5 Discussion of the results

4-1-5-A) Monte-Carlo simulations

Electron trajectories were simulated with the Monte-Carlo algorithm Mocasim (L. Reimer, Plano GmbH, 1999) developed for electron microscopy. This program computes series of individual trajectories of electrons scattered in solids by using elastic and inelastic cross-sections (see Annex 1). It counts the numbers of BSE or SE from customized 2D or 3D structures. It gave satisfactory results for the BSE yields of bulk substrates (BSE yields measured in previous works are summarized in Annex 3). The BSE from a large-area deposit were computed using the film thickness, its composition, and the PE energy as parameters. For the pictures 100 trajectories were used. For the absolute BSE yield calculations 10000 trajectories were used. The statistical uncertainty was 3%. The electron range in Au is at most 260 nm at 10 kV (see Annex 1), so the 500 nm thick Au film used in the experiments was modeled as bulk Au.

4-1-5-A-α) Illustrated electronic trajectories

The composition of the amorphous deposit from acrylic acid was $C_9H_2O_1$ (see chp. 5). It was modeled as pure C. The deposit from (hfac)CuVTMS, approximately Cu_1C_7, led to similar results. Selected simulation results are shown in the following figures.
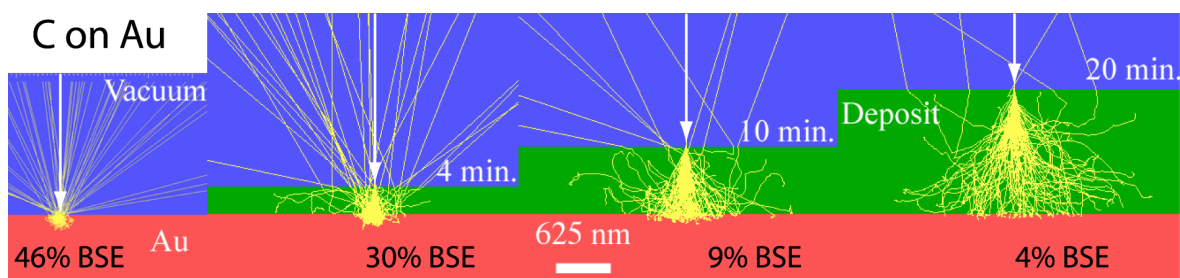
Figure 4-1-19. Monte-Carlo simulations of 100 electronic trajectories (C film on Au, 10 keV).
Selected deposit thicknesses during 10 kV exposures on Au (see fig. 4-1-2), increasing from
left to right. The white arrow represents the punctual primary beam.

Electron penetration in C was deeper than in Au. The electrons were transmitted through thin C films (see fig. 4-1-19). Most of the backscattering occurred from the substrate. Scattering and energy loss increased in thicker C films. More electrons reflected at the interface were absorbed.

The computed BSE yield decreased from the value on bulk Au (46 ± 2%), and became independent upon C film thickness and equal to the value on bulk C (5 ± 2%) above 1 μm.

The picture was different when considering C films on a Si substrate. Electron penetration was not as different between C and Si as between C and Au. The trajectories were hardly affected at the interface (see fig. 4-1-20). The excitation volume slightly increased when the electrons propagated in thicker films. The computed BSE yields decreased from the value on bulk Si (16%) to the bulk C (5%), with saturation above 1 μm C film thickness.
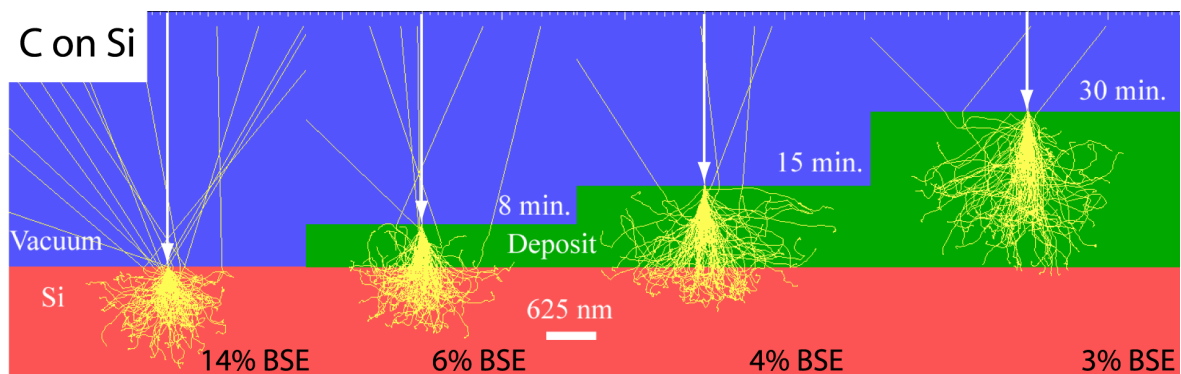
Figure 4-1-20. Monte-Carlo simulations of 100 electronic trajectories (C film on Si, 10 keV). Selected thicknesses from 10 kV exposures on Si (see fig. 4-1-2), increasing from left to right.

Trajectories at increasing acceleration voltages E_0 were compared on a 375 nm thick film.
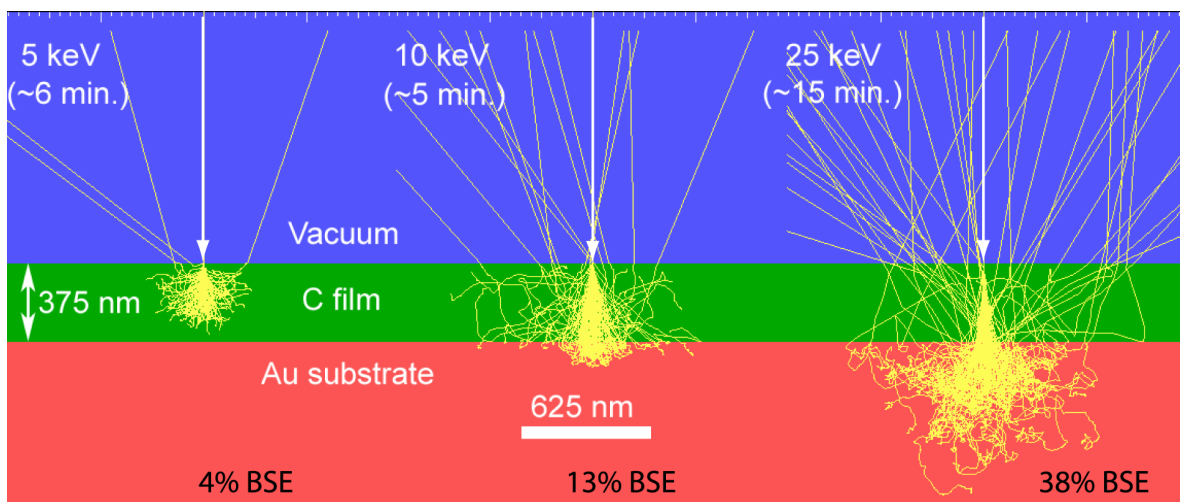
Figure 4-1-21. Monte-Carlo simulations at several energies (C on Au, 5, 10 and 25 keV from left to right). Legend: experimental deposition times required for 375 nm C film thickness and computed numbers of BSE.

The interaction volume and the BSE yield increased with E_0. (see fig. 4-1-21) At 5 keV the film contained the whole interaction volume and the BSE yield was that of bulk C. At 10 keV the thickness was still intermediate. At 25 keV the electron transmission through the C film was still quantitative and the BSE yield was not far below that of bulk Au.

In the case of a high-Z material deposited on a lighter substrate (Au on Si), the interaction volume was much smaller in the depositing film than in the substrate (see fig. 4-1-22).
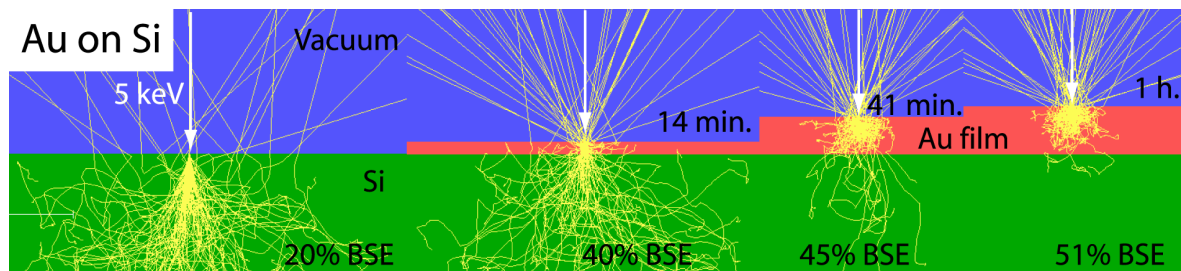
Figure 4-1-22. Monte-Carlo simulations of 100 electronic trajectories in model structures. Selected deposit thicknesses during 5 kV deposition of Au on Si (see fig. 4-1-17), increasing from left to right. The white arrow represents the punctual primary beam.

The electrons that reached the substrate had a low probability to cross the heavy film again. The BSE yield increased as the interaction volume was increasingly restricted to the film.

4-1-5-A-β) Quantitative results

The evolutions of the computed BSE yields of the deposits matched the successive BSE contrasts measured in SEM. The BSE yield of C films saturated at 5% independently of the substrate (see fig. 4-1-23a). The film thickness at saturation scaled with the electron range R_m. At 5 keV, saturation at 250 nm occurred at 60% of R_m (418 nm, see Annex 2). At 10 keV, saturation at 900 nm thickness occurred at 64% of R_m (1322 nm). The increase in BSE yields in the case of deposition of Au on Si was also predicted correctly (see fig. 4-1-23b). In this case, the thicknesses of the Au films at saturation (30 nm at 5 keV and 80 nm at 10 keV) were only 30% of the corresponding electron range in Au (83 and 263 nm, respectively).
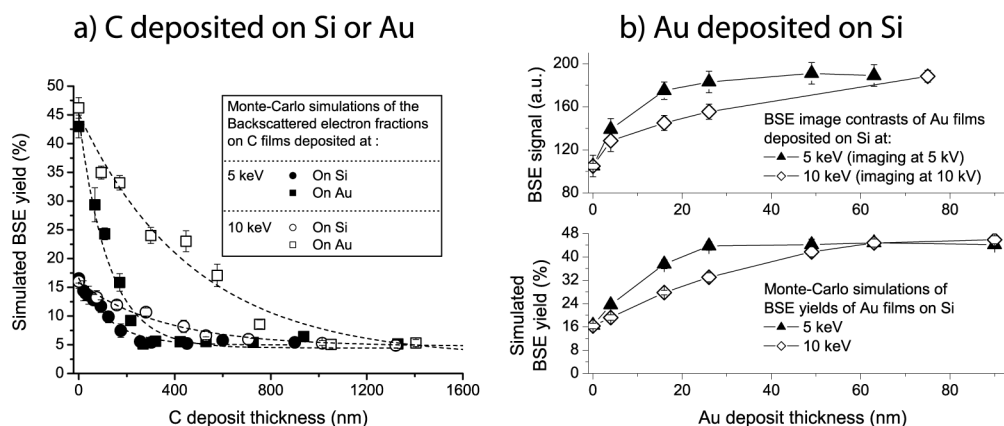
Figure 4-1-23. Quantitative BSE simulation results (10000 electronic trajectories per point).
a) Simulated BSE yields *vs.* film thickness (C on Si or Au, at 5 and 10 keV). b) Simulated BSE
yields *vs.* Au film thickness on Si (5 and 10 keV) and experimental contrasts.

The BSE contrasts and the simulations could not be quantitatively compared because the image settings (contrast and brightness in the imaging SEM) converted the absolute signal, measured by the BSE detector, into a non-linear scale. Both the angular distributions and the energies of the exiting BSE depended on the analyzed element.[15] The detector collected different fractions of these distributions.([16], p. 138) Absolute measurements would require a device optimized for the collection of all BSE.

In conclusion, an illustrated view of the varying electron propagation was obtained. The simulations satisfactorily described the experimental BSE contrasts and agreed with published BSE yields on bulk materials (see Annex 3). The BSE fractions during deposition of the films were predicted correctly in all cases (C on Au or Au on Si, at different electron energies). The results agreed with previous works from several authors.[17-19]

4-1-5-B) Secondary electrons

The SE contributed to 10% of the measured sample current, as shown in fig. 4-1-8b. This is in agreement with the SE yields for C at 10 keV measured in previous works (see Annex 4). The slope variations in the initial stages of deposition (see fig. 4-1-8 for the case of C on Au, fig. 4-1-16 for Cu-C on Au, and fig. 4-1-17,18 for Au on Si) corresponded to changes in SE

emission. This was similar to a result obtained during 20 kV electron-beam induced contamination of Al surfaces.[20] The SE emission changed once the thickness of the over-layer was larger than the SE escape depth, which was typically 50 Å.[2] Once this thickness was deposited, the SE emission originated from the deposit only, depending upon the number of rapid electrons that crossed the film surface. These were the constant number of incident PE (n_{PE}), plus the variable number of BSE (n_{BSE}), as shown by eqs. (4-1-2) to (4-1-4).[21]

$$n_{SE} = \delta_{substrate}\left(n_{SE} + \beta n_{BSE}\right) \qquad \textbf{(4-1-2)}$$

Deposit thickness t < λ, $\qquad n_{SE} = \delta_{substrate}(1 + \beta_{substrate}\eta_{substrate})n_{PE} \qquad \textbf{(4-1-3)}$

t > λ $\qquad n_{SE} = \delta_{film}(1 + \beta\eta_{film+substrate})n_{PE} \qquad \textbf{(4-1-4)}$

SE emission from the depositing film. λ: SE escape depth; n_{SE}: number of emitted SE.
$\delta_{substrate, film}$: intrinsic SE yields (in the absence of BSE, as measured on a thin film) of the substrate and deposit, respectively; η: backscattering yields. β: see text below.

The parameter β in eq. (4-1-2) integrates the effects of the BSE energy spectrum and angular distributions on SE emission. Its value goes from 3 to 5 depending on the substrate.[5] Equation (4-1-4) explains why the variations in BSE and SE yields were simultaneous once the first 10 nm were deposited.

4-1-5-C) Monitored sample current

4-1-5-C-α) Weighing of the SE and BSE contributions

As already stated in eq. 4-1-1, the same time constants of the BSE contrasts and sample current signals were due to a simple relationship ([16], p. 256):

$$i_{Sample} = \underbrace{i_{PE}}_{\substack{\text{Incident} \\ \text{electrons}}} - \underbrace{\eta \cdot i_{PE}}_{\substack{\text{Backscattered} \\ \text{electrons}}} - \underbrace{\delta_{PE} \cdot i_{PE}}_{\substack{\text{SE emitted} \\ \text{by the PE}}} - \underbrace{\delta_{PE} \cdot \beta \cdot \eta \cdot i_{PE}}_{\substack{\text{SE emitted} \\ \text{by the BSE}}} \qquad \textbf{(4-1-5)}$$

Sample current balance from probe current i_{PE}, BSE yield η, SE yield δ_{PE}, and parameter β.

The sample current is the probe current diminished by the BSE and SE yields. The SE contribution to all the monitored sample currents was observed in the initial stages of growth as a slope variation. Once it was suppressed by a substrate bias, the simulated BSE yields then correctly described the evolution of the monitored signal (see fig. 4-1-24).
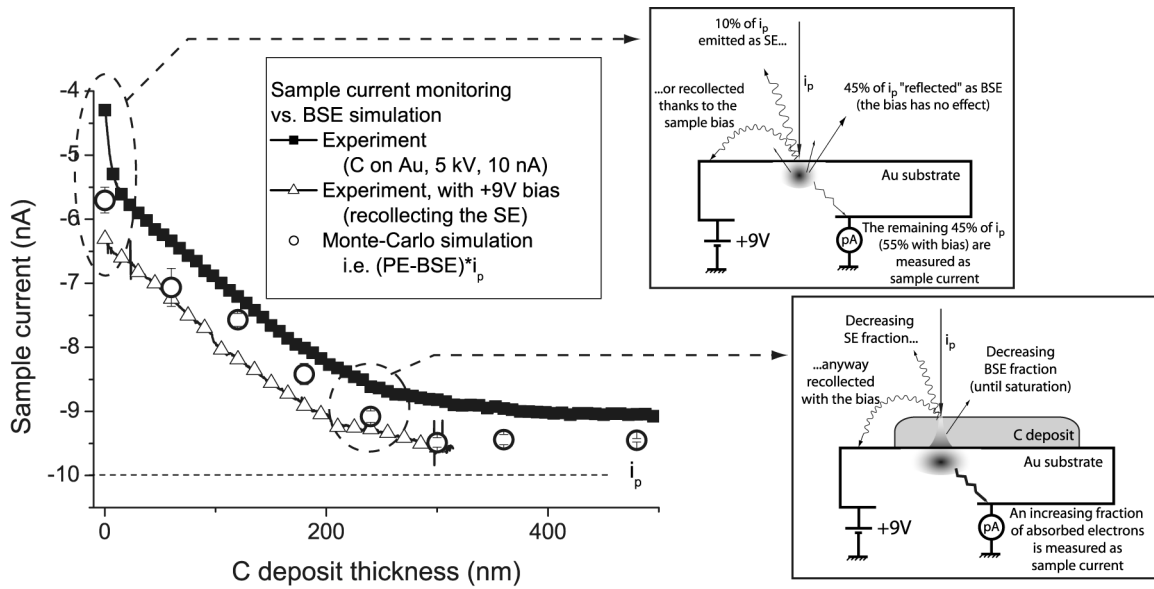
Figure 4-1-24. Comparison of the monitored sample current with Monte-Carlo simulations. Left, experimental curves from acrylic acid, at 5 keV, 10 nA, 2 kx on Au, with and without +9 V sample bias, compared to computed BSE yields. Right, schematic effects of BSE and SE on the sample current, on the bare substrate and at saturation.

Lower BSE yields corresponded to larger sample currents. At 5 keV, the SE were responsible for a decrease of the measured sample current of 10% of the probe current on Au and 5% on C.

4-1-5-C-β) Mathematical curve fitting

The sample current offered a direct measurement of the instantaneous BSE yield. The curves in fig. 4-1-5 were fitted by a second-order exponential function.[18]

$$i(t) = i_p \left(1 - \delta(t) - \eta_{film+substrate}(t)\right), \qquad (4\text{-}1\text{-}6)$$

$$\text{with } \delta(t) = \left(1 + \beta\eta_{film+substrate}(t)\right)\delta_{film} \qquad (4\text{-}1\text{-}7)$$

and $\eta_{film+substrate}\left(t\right)=\eta_{substrate}\eta_{tr}\left(t\right)+\eta_{film}\left[1-\eta_{tr}\left(t\right)\right]$ (4-1-8)

where $\eta_{tr}\left(t\right)=e^{-bt-ct^2}$, with b and c = constants > 0 (4-1-9)

Here η_{tr}(t) is the fraction of electrons transmitted through the film of thickness t. The linear exponent originates from Lenard's law of electron transmission through a thin film.[22] The second-order term was required for satisfactory fittings. δ_{film} is the "intrinsic" SE yield of the considered material, as in eq. (4-1-3). The function used for the mathematical description of the sample current curves was:

$$i\left(t\right)=i_p\left[1-\delta_{film}-\left(1+\beta\delta_{film}\right)\left(\eta_{substrate}\left(\exp^{-bt-ct^2}\right)+\eta_{film}\left(1-\exp^{-bt-ct^2}\right)\right)\right]$$ (4-1-10)

As the growth rate from acrylic acid at 10 keV was constant with time, the thickness increased linearly so the curve of current *vs.* time was fitted directly. The results are as follows:
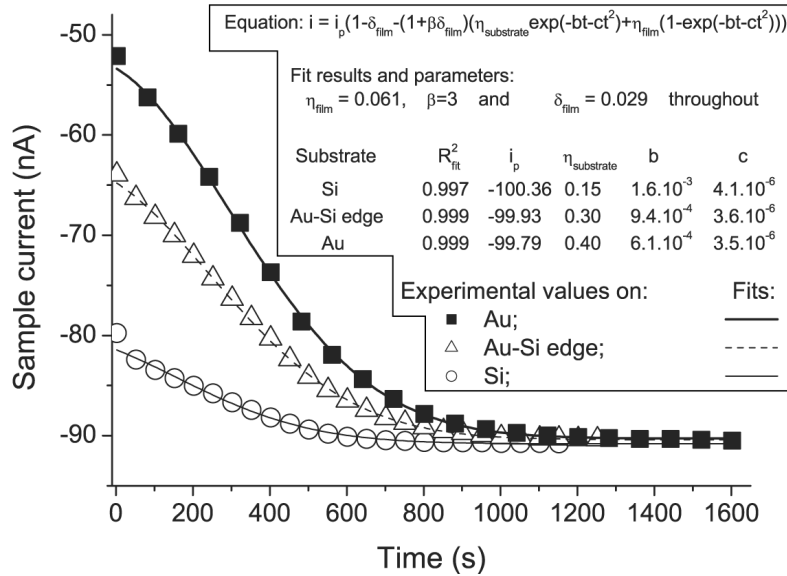
Figure 4-1-25. Mathematical fits of the sample current curves monitored in-situ from acrylic acid, at 10 keV, 100 nA, TV scan at magn. 2 kx.

The parameters η_{film} and δ_{film} were kept constant for all three fittings since they represent the properties of a single type of deposited film. The other parameters i_p, b and c showed a small dispersion. Only the parameter η_{sub}, which represented the BSE yield of the substrate, varied

significantly between Si, Au and the Si-Au edge (see fig. 4-1-25). The values correspond to those shown in Annex 3. For the low values of time (t), the almost linear variation observed in the experiment agreed with the mathematical description proposed here.

The results from the two other precursors used were also fitted (see fig. 4-1-26).
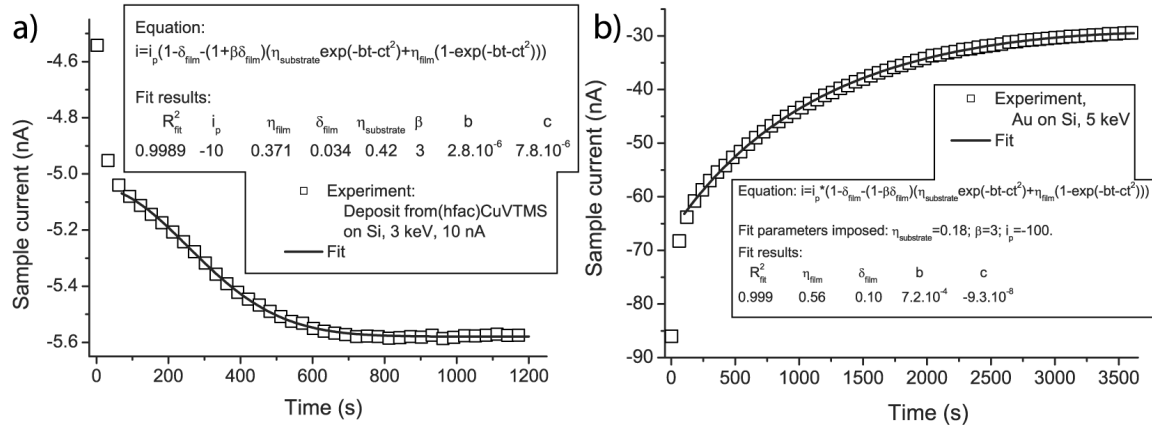
Figure 4-1-26. Fits of the sample current curves monitored in-situ from a) (hfac)CuVTMS, at 3 keV, 10 nA, magn. 2 kx on Si; and b) AuPF$_3$Cl, at 5 keV, 100 nA, magn. 2 kx on Si.

The initial slope variations were deliberately excluded from the fits. In the deposition from (hfac)CuVTMS, the saturation occurred at a larger fraction of the sample current because at 3 keV the deposit BSE yield and SE emission were larger (see fig. 4-1-26a). For the curve of Au on Si, the saturation value was larger than the value obtained on the flat evaporated Au films (see fig. 4-1-26b). The high film roughness, as compared to the electron range, probably enhanced both the BSE yield and SE emission.

4-1-5-C-γ) Generalization

Thanks to eq. (4-1-10), the sample current evolution can be predicted during deposition of films on substrates as is shown in fig. 4-1-27. Only films thicker than the SE escape depth (~10 nm) were considered. The saturation thicknesses, 60% of R_m on C films and 30% of R_m on Au films, allowed for an estimation of the parameter b. By solving $\exp(-bt)=10^{-3}$ in the two cases, it was found $b_C=5/R_m$ (=3.8.10^{-3} at 10 keV) and $b_{Au}=10/R_m$ (=0.038 at 10 keV). For the intermediate elements, the values $b_{Ti}=7/R_m=8.3.10^{-3}$ nm^{-1} and $b_{Cu}=1.3.10^{-2}$ nm^{-1} were used.
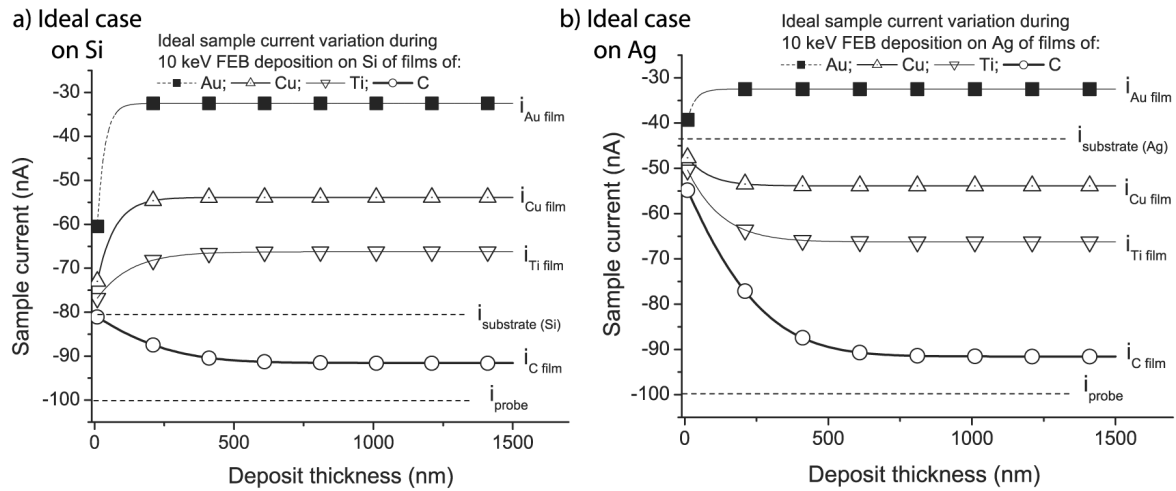
Figure 4-1-27. Ideal variations of the monitored sample current when depositing films of 4 different pure elements, at 10 keV, on a) Si and b) Ag substrates.

In an ideal experiment, the saturation values and the thicknesses at which they are reached depend on the pure material deposited. The amplitude of current variation until saturation depends on the difference in atomic number between the substrate and the film (compare fig. 4-1-27a and b). When depositing mixtures of elements, the relevant parameter is the average atomic number. The primary beam energy determines the saturation thickness. The physics of electron backscattering provide thickness information on the depositing films. No more information is available when the film thickness reaches between 30 and 60% of the electron range, depending on the deposited material.

4-1-6 Deposition regimes

The previous paragraph interpreted the electrons propagation in the bulk of the depositing films, without considering the deposition rate. Two different regimes were observed. The substrate-dependent growth rate from the Cu precursor is commented on in §4-1-6-A. The substrate-independent growth rate from acrylic acid and the more detailed study of the growth rate dependence on the deposition conditions is interpreted in §4-1-6-B. The elementary electron-induced precursor fixation step is modeled.

4-1-6-A) From the Cu precursor

The growth rate from (hfac)CuVTMS increased with decreasing beam energy and was higher on heavier substrates (see fig. 4-1-14). During deposition on Au at 3 keV, the growth rate decreased with film thickness at the same rate as the total electron flux $\varphi(t)$ through the film surface decreased (see fig. 4-1-16). The BSE contributed to the electron flux on the whole central area of the deposit (see fig. 4-1-28). Each point at the surface was exposed by the entire BSE fraction coming from the neighboring points.
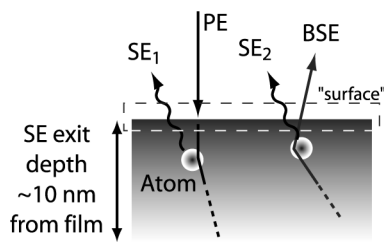
Total electron flux through the surface:

$$\varphi(t) = i_p \left(1 + \delta(t) + \eta(t) \right) \qquad \text{(4-1-11)}$$

Figure 4-1-28. Surface electron flux

The following hypotheses were made:

-   The precursor decomposition cross-section σ depends on electron energy. For deposition, the three electronic fluxes through the surface (PE, SE, BSE) must be weighed by their respective decomposition cross-sections (σ_{PE}, σ_{SE}, σ_{BSE}). The resulting growth rate is:

$$R = \alpha i_p \left(\sigma_{PE} + \delta(t)\sigma_{SE} + \eta(t)\sigma_{BSE} \right) \qquad \text{(4-1-12)}$$

-   The value of σ is independent of the direction in which the electron crosses the interface: into the solid (PE) or outwards (SE, BSE).

-   The BSE energies are close enough to E_0, so that $\sigma_{BSE} \sim \sigma_{PE}$ at normal incidence.

-   The probability for the SE and BSE to decompose a molecule depends on their exit angle θ through the surface ($\sigma_{SE, BSE} = \sigma_{SE, BSE}(\theta)$). Precursor decomposition and SE generation are supposed to be influenced similarly by the electron exit angle. The effective SE and BSE fluxes increase by the factor β (defined in eq. 4-1-4):

$$\sigma_{SE} = \int_\theta \delta(t,\theta)\sigma_{SE}(\theta)d\theta \quad \Rightarrow \quad \overline{\sigma_{SE}} = \delta_{film}\left(1+\beta\eta(t)\right)\sigma_{SE} \qquad \text{(4-1-13)}$$

$$\sigma_{BSE} = \int_\theta \eta(t,\theta)\sigma_{BSE}(\theta)d\theta \quad \Rightarrow \quad \overline{\sigma_{BSE}} = \beta\eta(t)\sigma_{BSE,\perp} \qquad \text{(4-1-14)}$$

The precursor decomposition rate is thus deduced as:

$$R(t) = \alpha \cdot i_p \left(\sigma_{PE} + \delta_{film}\left(1+\beta\eta(t)\right)\sigma_{SE} + \beta\eta(t)\sigma_{PE}\right) \qquad \text{(4-1-15)}$$

which simplifies into $R(t) = \alpha \cdot i_p \left[\left(1+\beta\eta(t)\right)\cdot\left(\sigma_{PE} + \delta_{film}\sigma_{SE}\right)\right]$ (4-1-16)

Once the deposit thickness reaches 10 nm, precursor molecules are adsorbed on the same surfaces, regardless of the substrate. SE are emitted entirely from the deposit. The growth rates ratios on the substrates depend only on the backscattering yields of the bulk solids:

$$\frac{R_{Au}}{R_{Si}} = \frac{1+\beta\eta_{Au}}{1+\beta\eta_{Si}}, \qquad \text{(4-1-17)}$$

With the values η_{Au}=0.48 and η_{Si}=0.18, values for β between 2 and 4 led to growth rate ratios between 1.5 and 1.8. This described perfectly the 5 to 25 keV experimental results in fig. 4-1-14. It also explained the variation of the growth rate during deposition at low energy (see figs. 4-1-14 and 4-1-16a). The deposition rate depended on the BSE yield. The SE and BSE contributions, however, could not be separated by this approach.

The deposition yield was estimated as follows. At 10 nA, the primary electron flux integrated over the whole area of 50x60 μm^2 was $2.1.10^{15}$ e$^-$/cm^2.s. The growth rate of 1 to 4 nm/min over this area corresponded to the fixation of a volume of $\sim 1.6.10^{-2}$ nm^3/e$^-$. In amorphous C, which is the main constituent of the deposited mixture of elements, the nearest neighbors are at 1.45 and 2.5 Å.[23] A lower limit of the C atomic volume was estimated as ~ 4.9 Å^3/atom. With an atomic radius of 1.28 Å, the atomic volume of Cu was estimated as 6.8 Å^3. The yield was deduced as 3 atoms/e$^-$. Each (hfac)CuVTMS molecule had 33 atoms, but only 5 to 8 of the atoms present in the molecule were non-volatile (1 Cu + 3 C + 1 Si plus the

O, H and F measured by microanalysis) and remained, the others were desorbed upon further electron exposure. So it was as if every 2 electrons fixed one precursor molecule.

4-1-6-B) From acrylic acid

The deposition rate when using acrylic acid as the precursor was substrate-independent and constant with film thickness. At 10 keV and 2 kx the growth rate (R) depended on the power 0.58 of the probe current (i_p): $R \alpha i_p^{0.58}$ (see fig. 4-1-11b). The growth rate at 100 nA also depended on the inverse power 0.26 of the exposed area (S): $R \alpha S^{-0.32}$ (see fig. 4-1-12). In the case of static exposure, Christy's model predicted a linear dependence between the growth rate and the electron current density (f, see §2-1-2A).[24] The current density depends on the power ¼ of the probe current, as shown in fig. 4-1-29 and eqs. (4-1-18) to (4-1-20). The results of the experiment were that the growth rate was proportional neither to f (the power law would have been $R \alpha i_p^{0.25}$), nor to the electron dose integrated over the complete exposed area (the power law would have been $R \alpha i_p/S$). Christy's model was adapted to the case of a scanning beam.
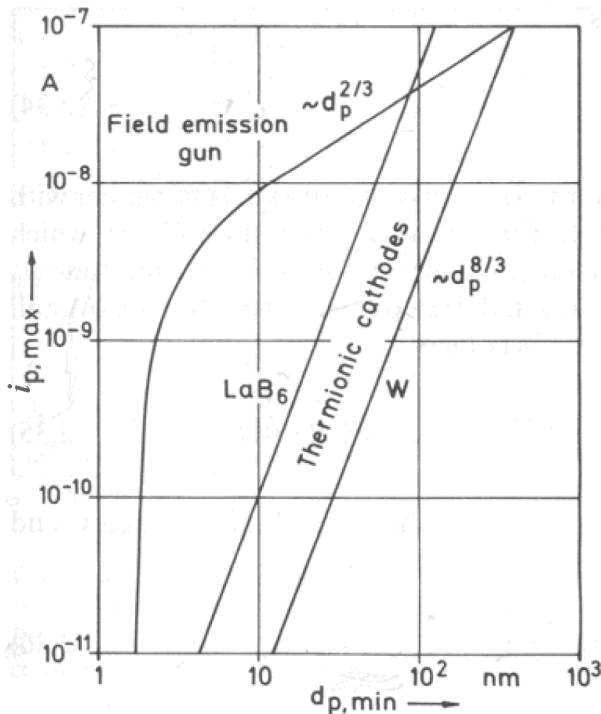
$$f = \frac{4}{\pi} \frac{i_p}{d_p^2} \qquad \text{(4-1-18)}$$

f: current density;
i_p: probe current; d_p: probe diameter

In thermionic effect electron microscopes, i_p and d_p are linked by:

$$i_p = C d_p^{8/3} \qquad \text{(4-1-19)}$$

Hence, the current density increases as the ¼th power of the probe current:

$$f = \frac{4C}{\pi} d_p^{2/3} = \frac{4C^{3/4}}{\pi} i_p^{1/4} \qquad \text{(4-1-20)}$$

Figure 4-1-29. Electron probe current (i_p) vs. probe diameter (d_p), for different electron sources.[16]

The following model is proposed for scanning deposition:

- At each point the growth rate followed Christy's model, and was proportional to the current density f and to the adsorbed precursor concentration (see fig. 2-1-3);

- On each individual scan line the time τ_p, during which a point was exposed, depended on the beam size (see fig. 4-1-30a). The number n of successive lines, by which each point was exposed, depended upon the beam size and upon the magnification. The TV scan consisted of a 50 Hz image rate. Each image was scanned in 20 ms and had 625 lines. Each line was scanned in 32 µs;

- During the exposure of each point on the sample, the balance between precursor depletion and replenishment exponentially decreased the growth rate with the time constant τ_1 (see fig. 4-1-30b).
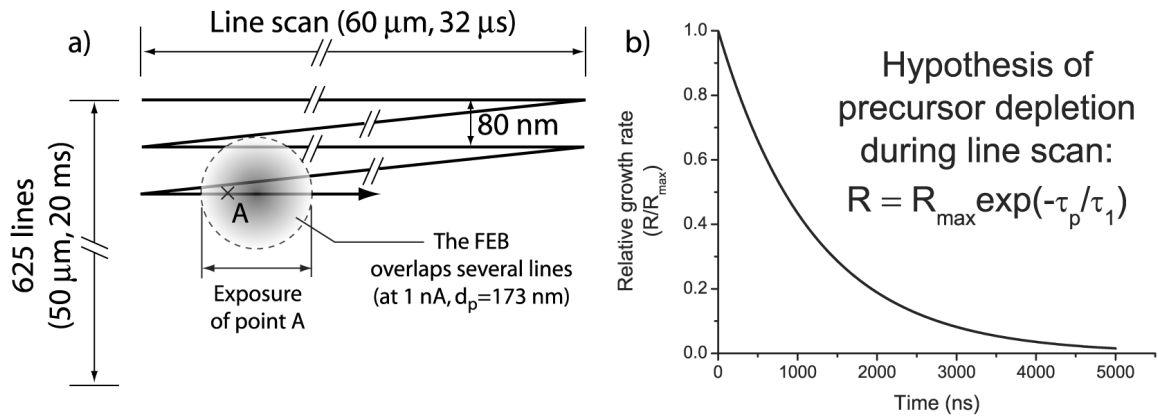
Figure 4-1-30. TV scan model. a) Successive line distances vs. beam size (in the case of 2 kx, 1 nA). b) Plot of the effect of the hypothesis of precursor depletion during line scan.

The last hypothesis was derived from the adsorbed precursor balance (see eq. (4-1-21) and compare it to eq. (2-2) in §2-1-2-B), by not taking into account surface diffusion:

$$\frac{dN}{dt} = F - \frac{N}{\tau} - \frac{f}{e}\sigma N \qquad (4\text{-}1\text{-}21)$$

N: adsorbed precursor concentration; F: precursor flux; τ: residence time; f: electron flux; σ: fixation cross-section; e=1.6.10^{-19}C.

The concentration of adsorbed precursor is:

$$N = N_0 \exp\left(\left(F - \frac{1}{\tau} - \frac{f}{e}\sigma\right)t\right)$$

(4-1-22)

So the growth rate under a stationary beam decreases exponentially with the exposure time:

$$R = \frac{f}{e}\sigma N = R_{max} \exp\left(-\frac{t}{\tau_1}\right)$$

(4-1-23)

Where $\tau_1 = \dfrac{1}{F - \dfrac{1}{\tau} - \dfrac{f}{e}\sigma}$

(4-1-24)

During scanning, the growth rate at each point resulted from the exposure by n overlapping lines, each time during the time τ_p, and with the current density f:

$$R = n \times f \times \left(R_{max} \exp\left(-\frac{\tau_p}{\tau_1}\right)\right)$$

(4-1-25)

τ_p was calculated as $32\,\mu s*$(line length)$/d_p$. The scan parameters during all the experiments were summarized as follows.

Probe current i_p (nA)	Probe diameter d_p (μm) at 10 keV	Current density $f=4i_p/\pi d_p^2$ (nA/μm^2)	Number n of overlapped lines at 2 kx	Integrated exposure time τ_p of each point in a line (ns)
0.1	0.070	26.0	0.87	37
1	0.173	42.6	2.16	92
10	0.427	69.9	5.3	227
100	1.05	115.5	12	560

Table 4-1-I. Scan parameters at different probe currents (magnification 2 kx).

Magnification	Distance between two successive lines (nm)	Number n of lines overlapped by a 100 nA beam	Integrated exposure time τ_p of each point in a line (ns)
1 kx	163	6.4	245
2 kx	96	10.9	461
3 kx	68.5	15.3	654
4 kx	62	16.9	758
6 kx	41	25.6	1031

Table 4-1-II. Scan parameters at different magnifications (probe current 100 nA).

The growth rates variations with the probe current and the exposed area were calculated from the data shown in tables 4-1-I and 4-1-II. The values obtained by calculating them with different characteristic times τ_1 were fitted as power laws, as shown in the next figure.

a) R *vs.* i_p at constant magnification (2 kx)   b) R *vs.* exposed area at constant i_p (100 nA)
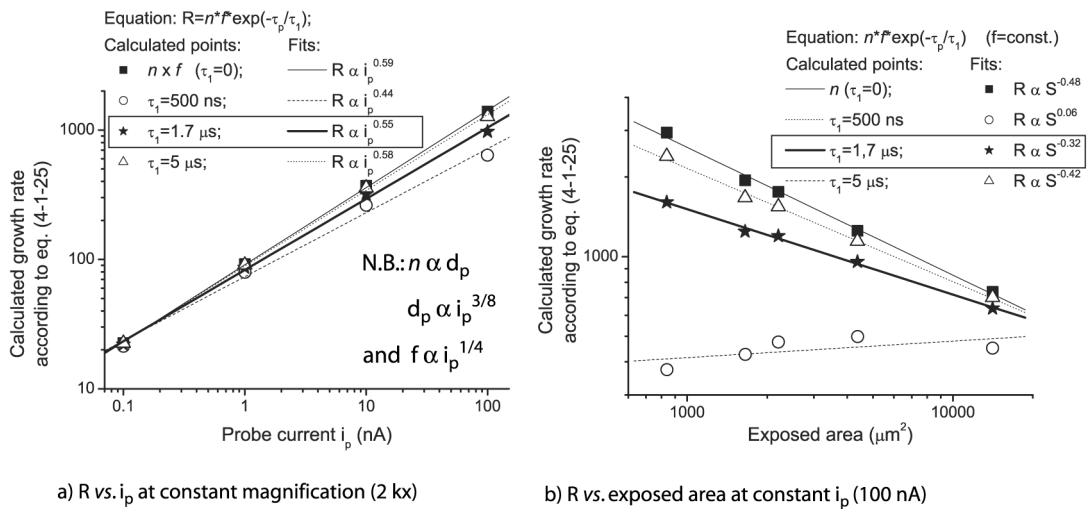
Figure 4-1-31. Model of growth rate variations with scan parameters, from acrylic acid at 10 keV. a) Calculated relative growth rate vs. probe current at magnification 2 kx. b) Calculated relative growth rate vs. magnification at probe current 100 nA.

τ_1 had little effect on the growth rate dependence on the probe current, which was already well described by the product $n * f$ (see fig. 4-1-31a). This is due to the power dependence of both parameters upon i_p. With n proportional to $i_p^{3/8}$ and f proportional to $i_p^{1/4}$, then $n * f$ is proportional to $i_p^{5/8}$. The exponent 5/8 (=0.62) is close to the experimental value of 0.58. At constant i_p, the current density f was constant. The exponent of the power laws obtained with τ_1=1.7 μs fitted the experimental result correctly (see fig. 4-1-31b). By taking into account only

the variation of *n*, R would have depended on the inverse of the square root of the area, i.e. the scan length (see fig. 4-1-31b). τ_1 was required to obtain the correct power law. Physically, $\tau_1 \sim 2$ μs was similar to the precursor residence time at the surface (also see §4-3-4-C and §5-1-4).

The modified scanning deposition model offered a satisfactory explanation of the observed power law dependences. However, the reason why the growth rate can be simultaneously substrate-independent and proportional to the current density remains unclear. Whatever the physical origin of precursor fixation, a SE- or high-energy-electron induced reaction, the BSE contribute to the total current density, as seen above in the case of the Cu precursor. An alternative mechanism is a deposit-assisted precursor fixation (see fig. 4-1-32a).[25, 26] Radicals or ions formed in the carbonaceous material by the incoming beam (see fig. 4-1-32b for the case of a di-radical formation from a conjugated double bond) are mobile and reactive with the double bond of the acrylic acid precursor (see fig. 4-1-32c). They could be more efficient in precursor grafting than direct primary-beam-induced fixation.
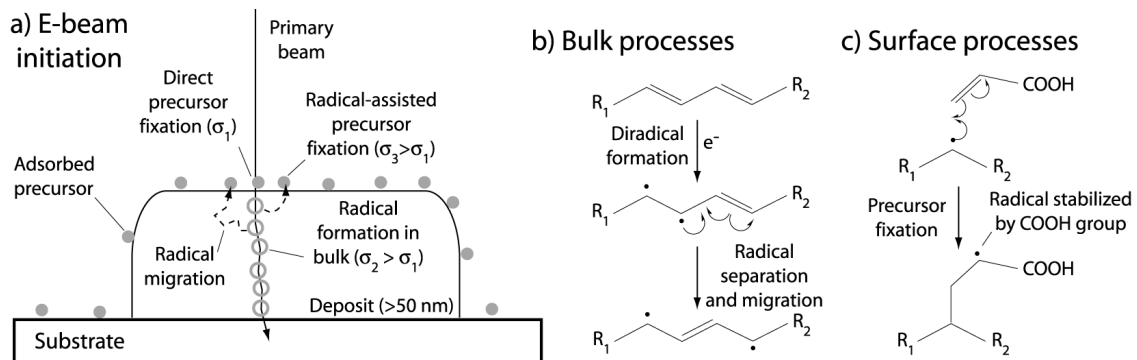
Figure 4-1-32. Schematic radical-assisted mechanism in carbonaceous material. a) Overview.
b) Electron-induced radical formation. c) Radical-assisted precursor fixation.

The advantage of this mechanism is to explain why the growth rate is higher, at 25 keV, on an already deposited thin film than on the bare substrate (see fig. 4-1-10b). A non-linear radical formation dependence on the concentration of electrons (the current density) could explain why the growth rate depends mainly on the current density of the primary electrons, and not on the more diffused BSE. Resistance measurements were another hint at beam-induced formation of radicals or ion pairs and gave information on the charge carrier mobility and decay (see §5-2-3).

The deposition yield was estimated as follows. At 100 nA, the electron flux integrated over the whole area of 50x60 μm^2 was $2.1.10^{16}$ e$^-$/cm^2.s. The growth rate of 63 nm/min over this area corresponded to the fixation of a volume of $4.7.10^{-3}$ nm^3/e$^-$. With a C atomic volume of ~4.9 Å^3/atom, the yield was deduced as 0.96 atom/e$^-$. Each molecule had 9 atoms, but only 3 C atoms per molecule were non-volatile (plus O and H up to 20% atomic content, see §5-1). This was as if every 3 electrons fixed one precursor molecule. However, the fraction of fixed molecules was small. The precursor flow at the needle exit was 3.10^{19} molecules/cm^2.s, and at the deposition site it was around 10 times smaller, 3.10^{18} molecules/cm^2.s. A growth rate of 63 nm/min (~1 nm/s) corresponded, taking into account a volume of ~15 Å^3/molecule, to the fixation of 60 molecules/nm^2.s, which was 6.10^{15} molecules/cm^2.s. Only one out of 500 incoming molecules was thus fixed under the electron beam.

4-1-7 Summary

Electron interactions with bulk samples were shown to evolve during large-area film deposition. The variations of the BSE yield and SE emission were accessed both by *in-situ* (sample current and SE detector monitoring) and *ex-situ* (SEM imaging) measurements. Extreme systems were selected for large variations (pure C on Au, and pure Au on Si) but the principle was also demonstrated in intermediate cases (Cu-C mixture on Si and Au). The scope of the sample current monitoring method (only used occasionally for imaging[27-30]) was extended to the *in-situ* control of deposition. Excellent agreement was found between experimental measurements, previously reported BSE measurements, and Monte-Carlo simulation results. The dual use of the depositing focused-electron-beam as an analysis tool was applied to fundamental studies of the FEB-induced process. The parameters accessed by this method were the growth rate and, to some extent, the chemical compositions of the deposited films.

4-2 Tip deposits

In this section, the tip deposits obtained by keeping the focused electron beam at the same place are described. Three successive growth regimes are encountered, which are clearly observed by *in-situ* monitoring. Electron scattering follows a different behaviour due to the small tip diameters compared to the electron range. The effect of several deposition parameters on the monitoring was investigated. The results are synthesized in a physical model. The origin of the tip shape is attributed to the distribution of scattered electrons.

4-2-1 Definition

Tip deposits were formed under a narrow stationary beam. Tall tips were created by continuously fixing the precursor in a given place, so that the deposit grew vertically and coaxially. Tips grew faster from organometallic than from purely organic compounds.

4-2-2 Growth sequence

A typical tip growth sequence from (hfac)CuVTMS is shown in fig. 4-2-1.
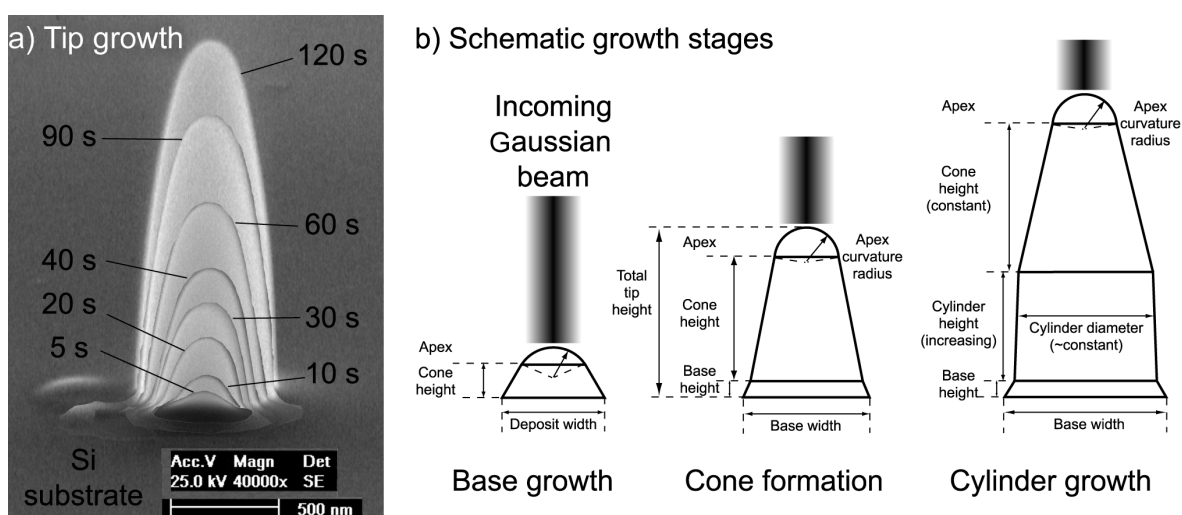
Figure 4-2-1. Typical tip growth sequence (from (hfac)CuVTMS on Si, 25 keV, 500 pA). a) Superposition of *ex-situ* SEM pictures (tilt 73°) of deposits obtained from 5 to 120 s deposition times. b) Schematic growth stages: base, cone, and cylinder growth mode.

Three growth modes were observed. The base growth mode showed a hill-like structure with lateral dimensions similar to that of the primary Gaussian beam. In the cone growth mode, the deposits grew upwards from a short base. The curvature radius at the top of the cone maintained the same width as the incoming beam (130 nm). The cone profile was described by a polynomial in which the main parameters involved were of order 2 and 4 (see fig. 4-2-2).
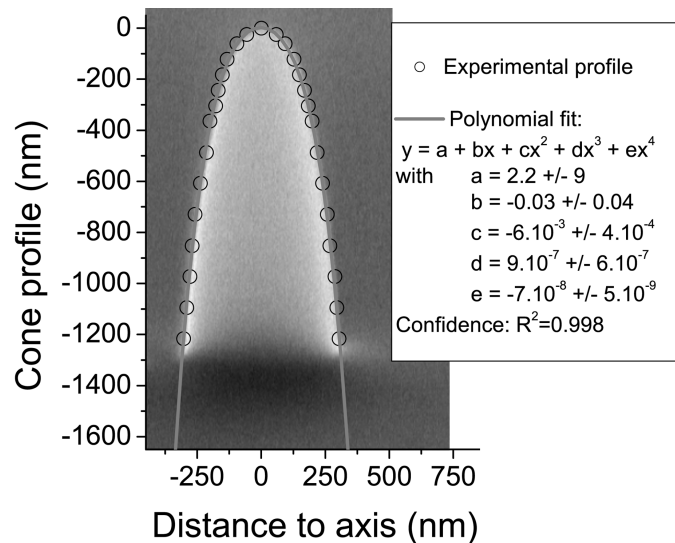
Figure 4-2-2. 4th order polynomial fit of experimental cone profile.

No other fit, including Gaussian functions, matched the entire cone profile as perfectly. The Gaussian incident beam distribution was not solely responsible for the deposit profile.

The third growth mode, or cylinder growth mode, occurred after a transition from the cone shaped deposit to a cylindrical form topped by a cone (see fig. 4-2-3). It started once the cone reached 1,8 μm. The cylindrical part of the deposit grew in height, even though deposition occurred on the cone-shaped top. The cylinder diameter was 600 nm. Higher deposits were obtained by depositing for longer periods of time. As the deposit height increased the vertical growth rate decreased. After 10 μm the growth rate was reduced by a factor of five. The cone-cylinder transition did not have any effect on the growth rate decrease. Similar reductions were reported in electron-beam contamination and when depositing from organometallic compounds of Au and Cu.[31-33] Thin layers were also visible around the bases of the higher tips.[34, 35] The higher cylinder had a rough aspect, which will be described later (see §5-2-2).
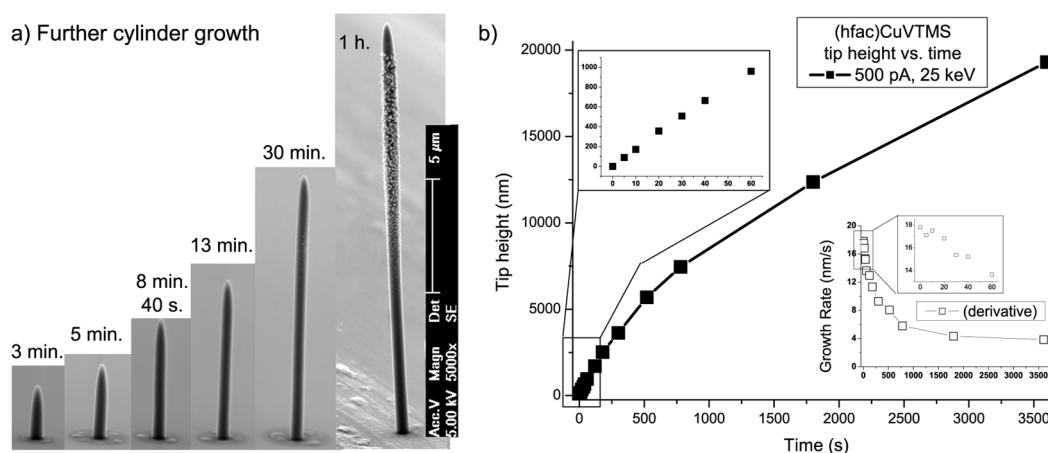
Figure 4-2-3. Cylinder growth mode. a) *Ex-situ* SEM pictures (tilt 73°) of tips deposited at increasing intervals (3 to 60 min). b) Plotted heights and growth rates.

The rate at which the tip volume increases per time unit was calculated from the SEM pictures:
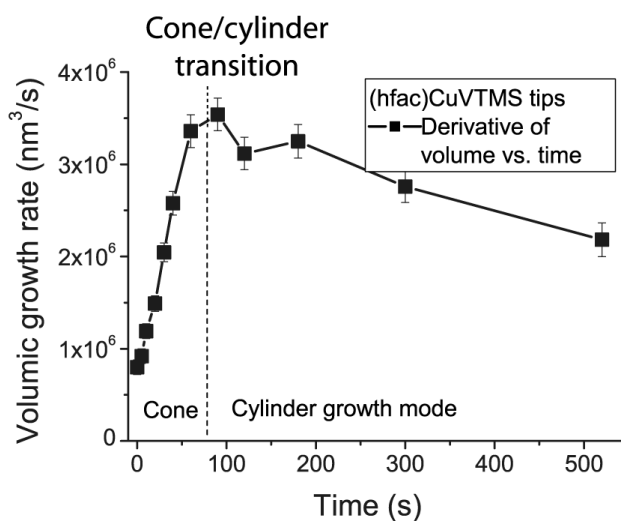
Figure 4-2-4. Volume growth rate *vs.* time elapsed, from figs. 4-2-1 and 4-2-3.

Not only did the tip volume increase during cone growth, but also the volume deposited per time unit, which was maximal when the cone was complete (see fig. 4-2-4). As the cylinder grew, less and less volume was deposited per time unit as the vertical growth rate decreased. From a constant probe current, the incident electrons fixed ~4 times more precursor molecules when impinging on the complete cone, than on the flat substrate or on the same cone on top of a high cylinder.

4-2-3 *In-situ* monitoring

4-2-3-A) Observation of the phenomenon

The sample current and SE detector signals were monitored while depositing the consecutive tip series (see fig. 4-2-5).
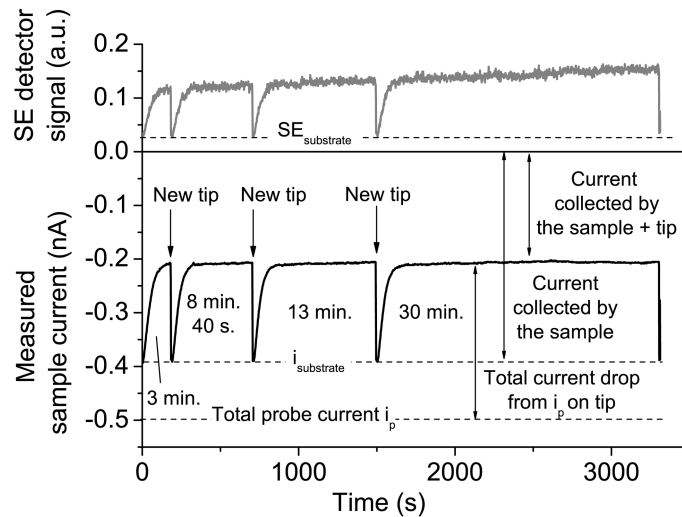
Figure 4-2-5. *In-situ* monitoring of sample current and SE detector signal during deposition of 4 consecutive tips shown in fig. 4-2-3 (except the 5 min. tip).

The signals followed simple first-order decays, as shown in fig. 4-2-6.
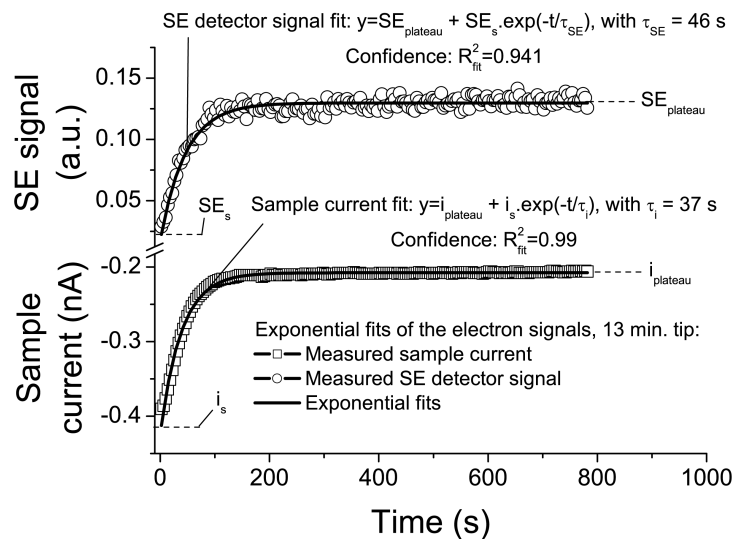
Figure 4-2-6. First-order exponential fits of the *in-situ* monitored electron signals during deposition of the 13 min. tip in fig. 4-2-3 (precursor (hfac)CuVTMS on Si, 25 keV, 500 pA). i_s, current measured on the bare substrate. SE_s, SE signal on the substrate.

These results were summarized as follows:

$$i(t) = i_s \left[1 - \exp\left(-\frac{t}{\tau_i} \right) \right] + i_{plateau} \qquad \textbf{(4-2-1)}$$

$$SE(t) = SE_s \left[1 - \exp\left(-\frac{t}{\tau_{SE}} \right) \right] + SE_{plateau} \qquad \textbf{(4-2-2)}$$

Empirical formulas for first-order evolutions of the monitored sample current and SE.

Slight deviations were noticed at the very beginning of the sample current curve and in the 90-120 s region, just before saturation. The confidence value on the SE curve was lower due to noise. The apparent time constants were almost identical. The sample current decreased in absolute value and the SE signal increased during deposition. The curves presented characteristic features:

a) The substrate values i_s and SE_s were detected at all new deposition sites (see fig. 4-2-5). Electron emission was stable during the series of experiments.

b) The current saturated in ~3 min. at a reproducible plateau value (see fig. 4-2-6). Only slightly more than 40% of i_p were then collected by the sample.

c) In a similar time span, the noisier SE detector signal increased and saturated at a value representing a 300% increase with respect to the signal on the substrate.

d) The signals saturated shortly after the beginning of the cylinder growth mode.

e) Once saturation was reached, the evolutions of the signals did not transmit more information on tip height. In particular, no growth rate decrease was noticed.

4-2-3-B) Role of the precursor and focus accuracy

Deposition from the Rhodium precursor $[RhCl(PF_3)_2]_2$ at 25 keV was monitored.[36] The growth rates were higher than from the Cu precursor. The deposited material has been

examined previously.[37] With a probe current of ~100 pA, narrower cylinders were produced during a more detailed consecutive tip series. The similar SE evolutions were omitted for clarity.
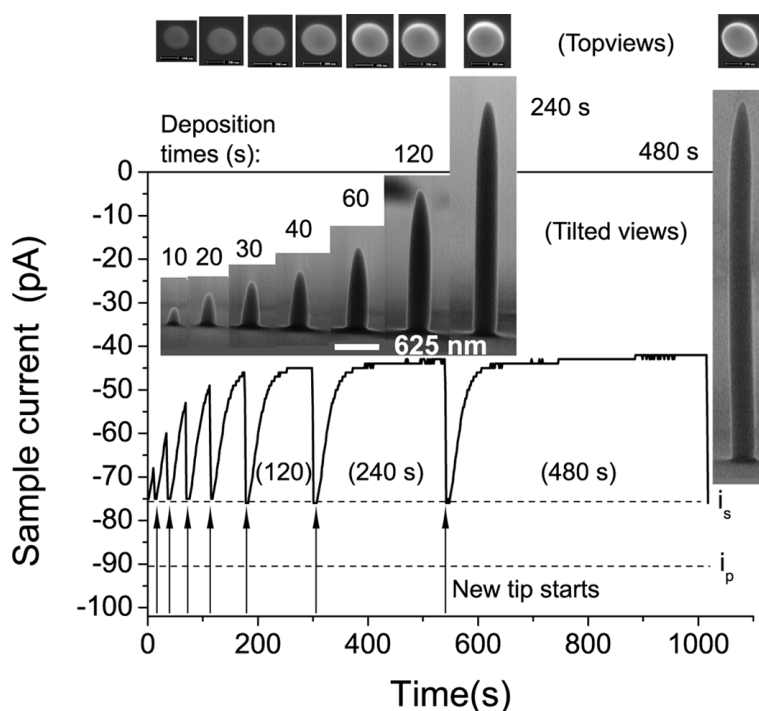
Figure 4-2-7. Detailed *in-situ* sample current monitoring (from [RhCl(PF₃)₂]₂ on Si, 25 keV, 91 pA). Top, corresponding *ex-situ* SEM pictures (top views, scale 200 nm; tilted views 75°).

The vertical growth rate was 20 ± 4 nm/s, and 7 pA were "lost" in 10 s on a 200 nm high cone: the initial current decrease rate vs. tip height was 0.035 pA/nm (see fig. 4-2-7). The picoamperemeter had a resolution of only 1 pA. A more precise device may monitor the deposition from the first nanometers on. After 60 s, saturation occurred at 45% of the probe current. The cone diameter reached a constant value and cylinder growth began. The SE detector signal (not shown) also increased during deposition, with a similar time constant. In the SEM top-views of the successive tips, in which a perfect cylindrical symmetry was observed, increasingly bright contrasts were obtained until the cone was completely formed. This indicates that saturation of the signals and cone formation were closely linked.

The monitored signals evolved more slowly when the beam was un-focused. Large blunt tips were produced by stepwise un-focusing (see fig. 4-2-8).
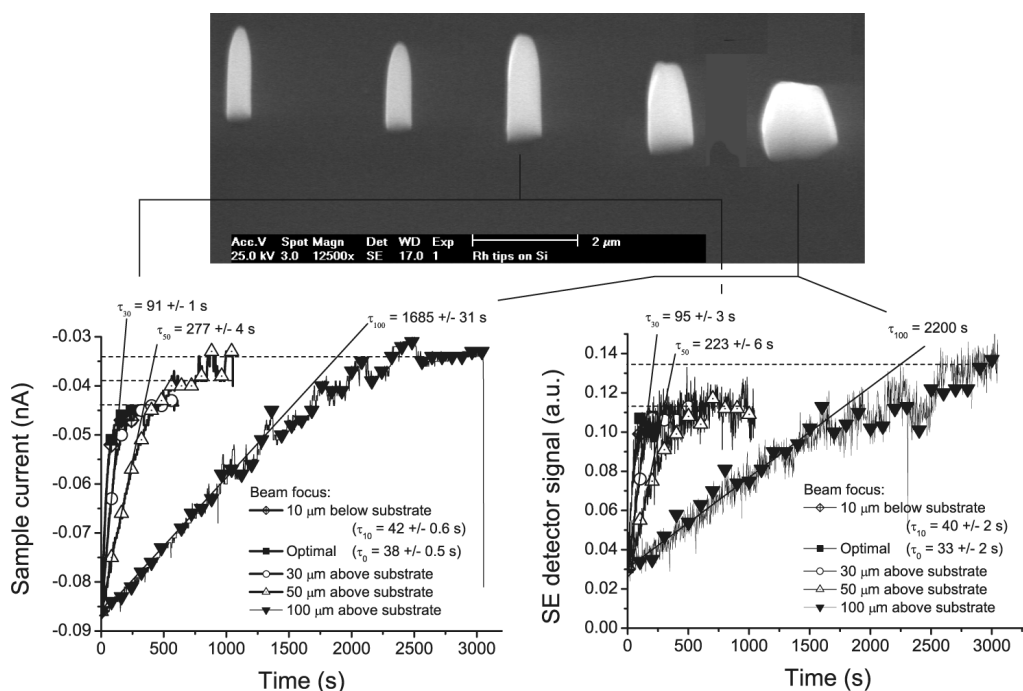
Figure 4-2-8. Monitoring of deposition with un-focused beams ([RhCl(PF$_3$)$_2$]$_2$ on Si, 25 keV, 100 pA). Top, SEM tilted views (75°) of the obtained tips. Increasing defocus from left to right. Bottom, monitored signals (left, sample current; right, SE) and time constants from exponential fits.

Bigger current drops at saturation were observed on the larger deposits. Although the top-right tip in fig. 4-2-8 was longer to deposit and had a larger volume than the top-left one, it appears as a short blunt cone. The signals still saturated when the cylinder growth mode began. The value depended on the shape of the cone and the cylinder diameter. From a practical point of view, monitoring was useful to check for focus accuracy.

4-2-3-C) Quantitative role of the deposit chemical composition and diameter

Systematic series of tips were deposited from several precursors and at several probe diameters. The current drop depended on tip composition and cylinder diameter. For each condition the results were averaged on 2 to 5 tips.
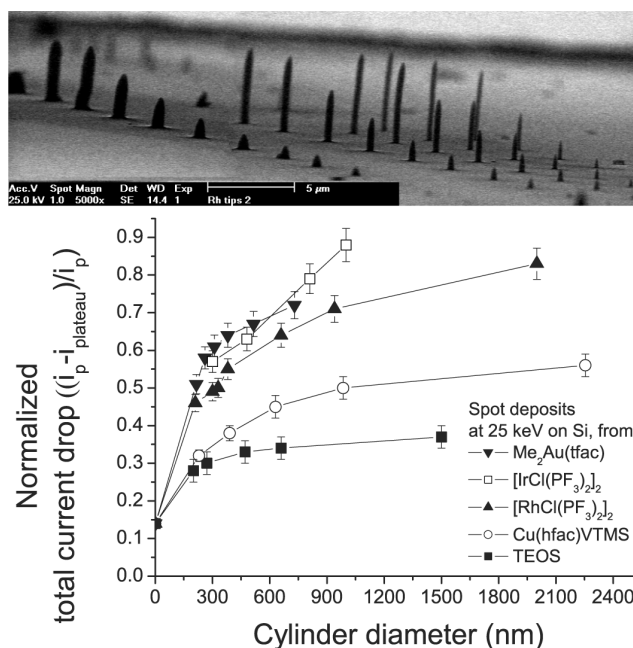
Figure 4-2-9. Total current drop at saturation *vs.* cylinder diameter and precursor used. Top, tilted (85°) SEM overview of a series of Rh tips with varying diameters. The value extrapolated at 0 cylinder diameter is that measured on the bare substrate (Si, at 25 keV).

From a given precursor, the current drop was larger when depositing tips with larger diameters (see fig. 4-2-9). The comparison of 330 nm diameter tips obtained at 90 pA is as follows:

Precursor	Total current drop (pA)	τ_i (s)	Growth rate (nm/s)	Cone height (nm)	Precursor flux (#/cm².s)	EDXS deposit composition
TEOS	27 ± 2	43 ± 3	6 ± 0.5	900 ± 60	10^{18}	$Si_{0.15}C_{0.45}O_{04}$
(hfac)CuVTMS	29 ± 2	29 ± 2	16 ± 3	860 ± 50	10^{18}	$Cu_{0.1}C_{0.5}O_{0.1}Si_{0.3}$
[RhCl(PF$_3$)$_2$]$_2$	46 ± 4	16 ± 2	20 ± 4	800 ± 50	2.10^{17}	$Rh_{0.66}P_{0.33}$
[IrCl(PF$_3$)$_2$]$_2$	57 ± 4	31 ± 3	14 ± 2	780 ± 50	7.10^{16}	$Ir_{0.25}P_{0.25}Cl_{0.25}F_{0.25}$
Me$_2$Au(tfac)	61 ± 5	65 ± 5	4 ± 0.5	700 ± 40	7.10^{17}	$Au_{0.2}C_{0.8}$

Table 4-2-I. Tip monitoring vs. precursor and deposit properties (25 keV, 90 pA on Si). All deposit cylinder and apex diameters were 330 ± 30 nm and 80 ± 10 nm, respectively.

At constant diameter, the current drops were larger on tips with heavier elements (Ir, Au) or higher metal contents (Rh). The time constants were shorter for the precursors with the higher growth rates. Sample current monitoring allows monitoring the cone growth rate.

4-2-3-D) Partial physical interpretation based on Monte-Carlo simulations

TEM micrographs of tips from $[RhCl(PF_3)_2]_2$ revealed tip structures of Rh nanocrystallites in an amorphous P matrix (see fig. 4-2-10), as observed in a previous work.[38]
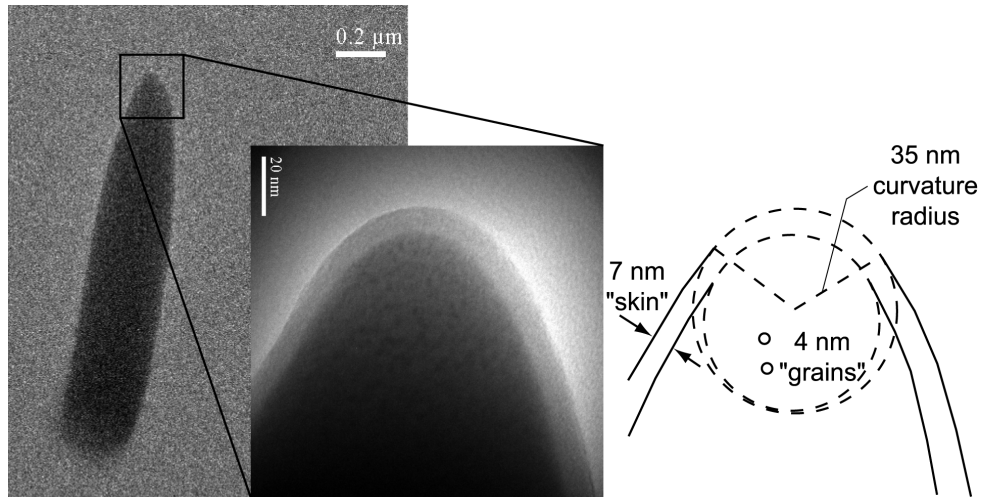
Figure 4-2-10. Nanostructure of a tip deposit. TEM micrographs of a tip on a membrane (Precursor $[RhCl(PF_3)_2]_2$ on 70 nm thich Si_3N_4 film, 25 keV, 20 pA, 60 s; tilt 30°).

The thin and smooth "skin", possibly due to air exposure before observation, was not taken into account. The tip material was considered as homogeneous since the crystallites were smaller than the collision mean-free-path at 25 keV (see Annex 1). An average density of 8.8 was calculated from the measured EDX compositions. The tip structures were modeled (see fig. 4-2-11a) and used for Monte-Carlo simulations of the electronic trajectories (see fig. 4-2-11b).
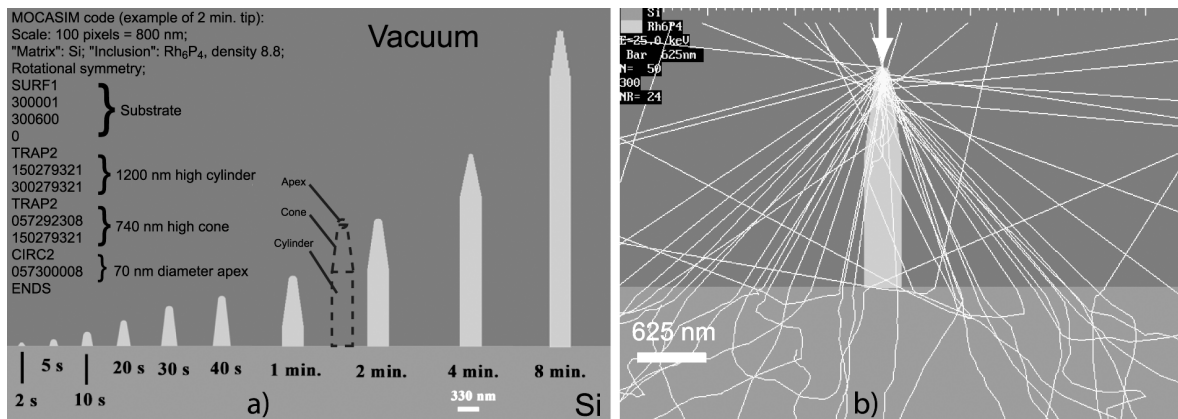
Figure 4-2-11. Monte-Carlo simulations in tips. a) Overview of successive simulated tip structures (cylinder-cone-apex, from fig. 4-2-7, with MOCASIM code). b) 50 electron trajectories (25 keV), at abscissa 300, on the 2 min. model tip.

Electrons were not absorbed in the tips because the diameters are narrower than the electron range (see fig. 4-2-11b). They were scattered in the cone and escaped through its sides. Some were directly backscattered. Most electrons were still oriented towards the substrate with an angle (fig. 4-2-11b is a planar projection of the 3D simulation). Their BSE yield was higher than at normal incidence. The SE emission increase during tip growth was qualitatively explained by an "edge effect". As a forward scattered PE crossed each interface, SE were liberated, thus increasing the SE emission beyond the level found at normal incidence on the substrate surface.

The numbers of BSE and SE were computed from all tips. The sample current being taken as the probe current and diminished by the escaping electron currents (see eq. 4-1-5), the simulations were compared with the experiments. The results were in excellent agreement (see fig. 4-2-12). The evolutions were predicted at the right times and at correct values.
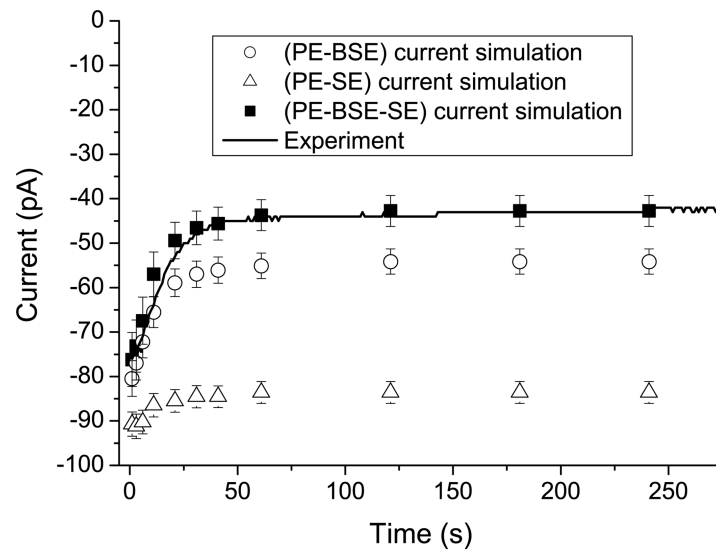
Figure 4-2-12. Comparison of the Monte-Carlo simulations with the experiment.

The current drop and SE increase were due to the tip geometries. This was checked after deposition. The SE and sample current were monitored during a top-view line scan across a deposited tip. The bright contrast seen in *ex-situ* SEM observation was also due to the increased SE emission.
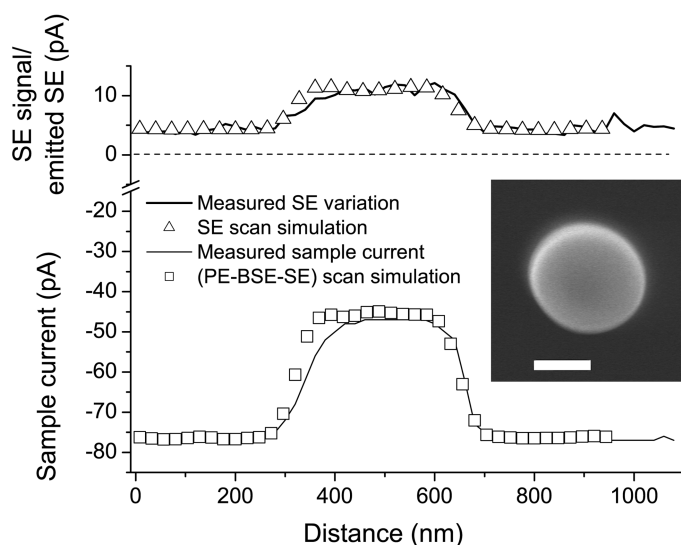
Figure 4-2-13. Measured and simulated signals during a line scan of the 2 min tip. Inset, FEG-SEM 25 keV top-view (scale bar: 200 nm).

The SE contrast in *ex-situ* imaging (see fig. 4-2-13) corresponded to a lower sample current.

Electrons reached the substrate at increasingly grazing incidences when scattered by heavy elements. The precursor $[IrCl(PF_3)_2]_2$ fortuitously led to a direct experimental proof:
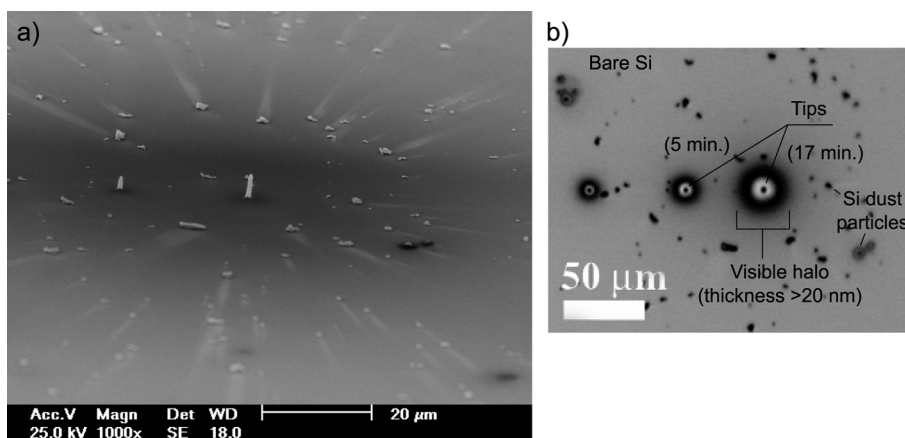
Figure 4-2-14. "Electronic shadow effects" around a tip from $[IrCl(PF_3)_2]_2$, 25 keV, 500 pA, on Si, 17 minutes. a) SEM tilted view (50°). b) optical micrograph, topview.

Deposition was performed in the centre of a substrate area covered by small Si particles. Radial bright-contrasted "shadows" appeared behind them in SEM observation (see fig. 4-2-14a). A dark area extended several tenths of μm around the tip. Optical microscopy revealed an

interferentially-colored halo (see fig. 4-2-14b). This was due to a thin Ir-containing film, formed by the forward-scattered electrons that reached the substrate at high angles and large distances. This explained the shadows behind the particles, and proved that many widely deflected electrons escaped the tips. The film thickness decreased with distance, as the substrate contrast was gradually recovered. Only thicknesses above 20 nm were optically visible, so only a thin layer of deposited material was responsible for the SEM contrast.

This observation and the early interpretation of the sample current evolution during tip deposition have been reported and published.[39, 40]

4-2-3-E) Role of the substrate

A special sample was constructed to study the role of the substrate when depositing from a given precursor, without varying other parameters such as beam focus or needle distance. This "multi-stub" consists of stacked, 10 to 100 μm thick metal sheets, held together and polished on the side, as shown in fig. 4-2-15. Deposition was carried out successively on each of the metals.
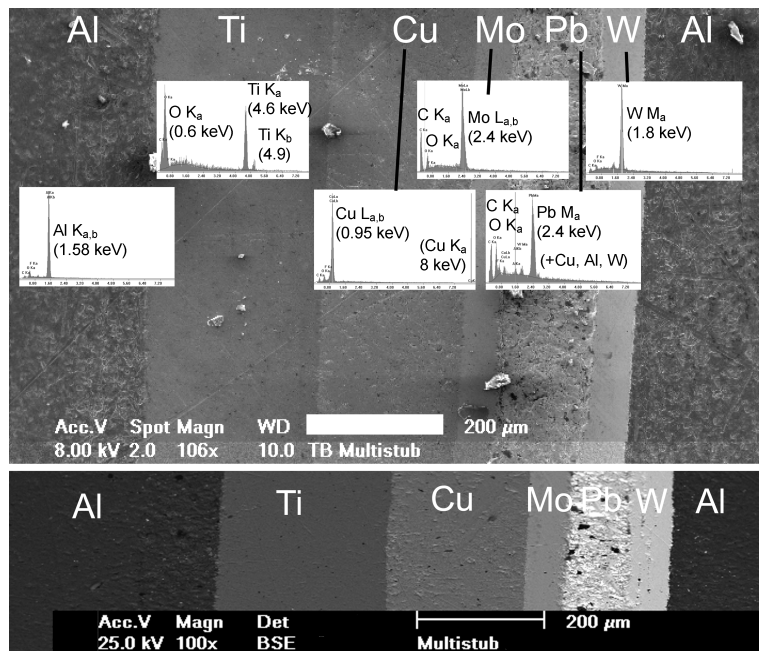
Figure 4-2-15. Multistub sample. Top, SEM top view (SE, 8 kV), identification of the materials and corresponding EDX spectra (excitation at 8 kV). Bottom, 25 keV BSE image.

Smooth and homogeneous surfaces and quantitative EDXS purities, were obtained for all metals except Pb, which was probably damaged due to its softness as compared to the neighboring harder metals Mo and W. The BSE contrasts increased monotonically with the atomic number (see Annex 3).[18]

4-2-3-E-α) - Low atomic number tips from (hfac)CuVTMS

In the investigated ranges, deposition occurred identically on all these materials (as well as on Si, shown in fig. 4-2-3). Tips deposited in 15 min had similar growth rates and morphologies.
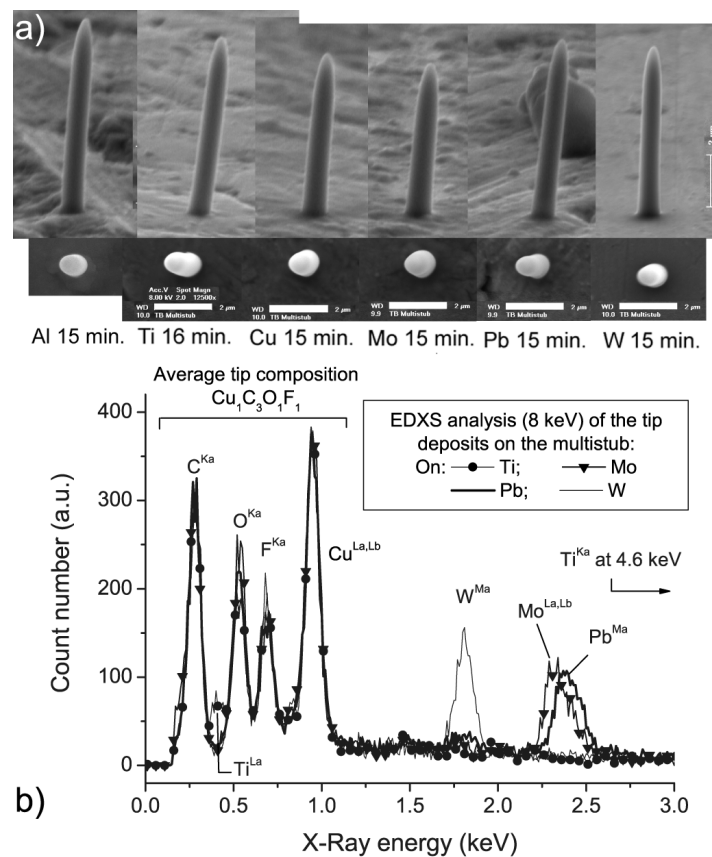
Figure 4-2-16. Analysis of tips deposited on different substrates. a) *Ex-situ* SEM views (70° tilt, and top-views, scale bars 2 μm). b) EDXS analyses, normalized on the Cu^L peak.

Slight height differences between the tips (shown here in chronological order of deposition) were due to a slight focus drift during the experiment, which became apparent and was corrected only when reaching Pb (see fig. 4-2-16a). All the measured compositions (excluding the tip on Cu, where the substrate peak overlapped) corresponded to $Cu_1C_3O_1F_1$ (see fig. 4-2-

16b). Only slight variations in the relative content of oxygen were noticed, which could be due to the substrates. For further details on the positions of X-Ray peaks, see Annex 5.

The signals were monitored during deposition. To mimic the absence of a substrate, deposition was performed on 30 nm thick Si_3N_4 commercial membranes (Agar Ltd.). These membranes do not contain C and are chemically similar to naturally oxidized Si. The films were held above a Faraday cup for quantitative collection of the transmitted electrons.
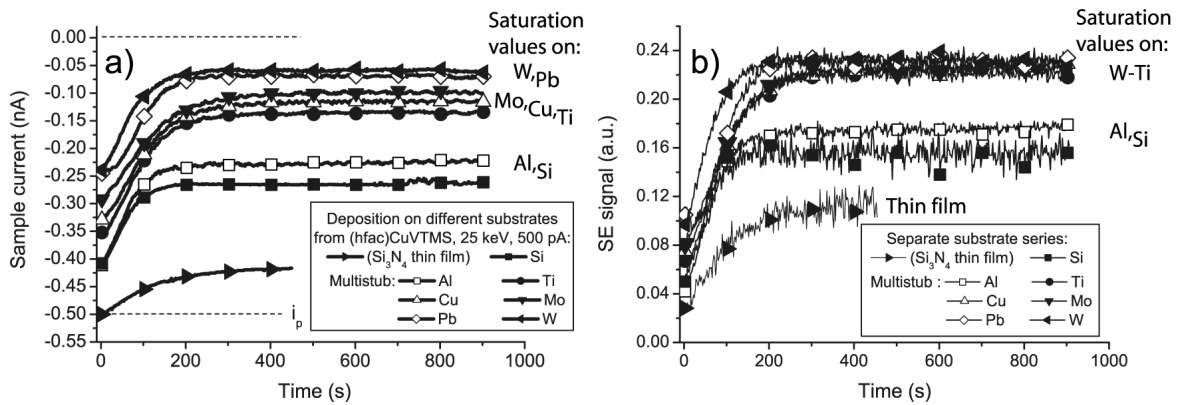
Figure 4-2-17. *In-situ* monitoring of the signals on the different substrates. a) Sample current monitoring. b) Simultaneous monitoring of the SE detector signal.

Substrate	$i_{substrate}$ (pA)	$i_{tip\ saturation}$ (pA)	$SE_{substrate}$ (a.u.)	$SE_{tip\ saturation}$ (a.u.)
30 nm membrane	-500	-420	0.025	0.112
Al	-410	-232	0.042	0.174
Ti	-350	-139	0.065	0.222
Cu	-330	-120	0.075	0.223
Mo	-297	-103	0.081	0.223
Pb	-246	-70	0.092	0.232
W	-246	-63	0.095	0.233

Table 4-2-II. Measured sample current and SE detector signal values, initial and at saturation, during 500 pA, 25 keV deposition from (hfac)CuVTMS on the multistub.

The monitored signals evolved with similar time constants but between substrate-dependent values (see fig. 4-2-17a). The initial sample current values increased with the increasing BSE yields of the substrates. At saturation the currents followed the same order. On W, the collected sample current at saturation was only 12% of the probe current (see Table 4-2-II). On the

transparent film it was 84% of the probe current. The evolutions of the detected SE are similar. These signals increase between 2.4 (W) and 4 (Al) times until saturation (see fig. 4-2-17b).

To compare the SE and BSE yields from the tips, SEM images were taken with constant contrast and brightness settings (instead of looking for well-balanced images as in fig. 4-2-16):
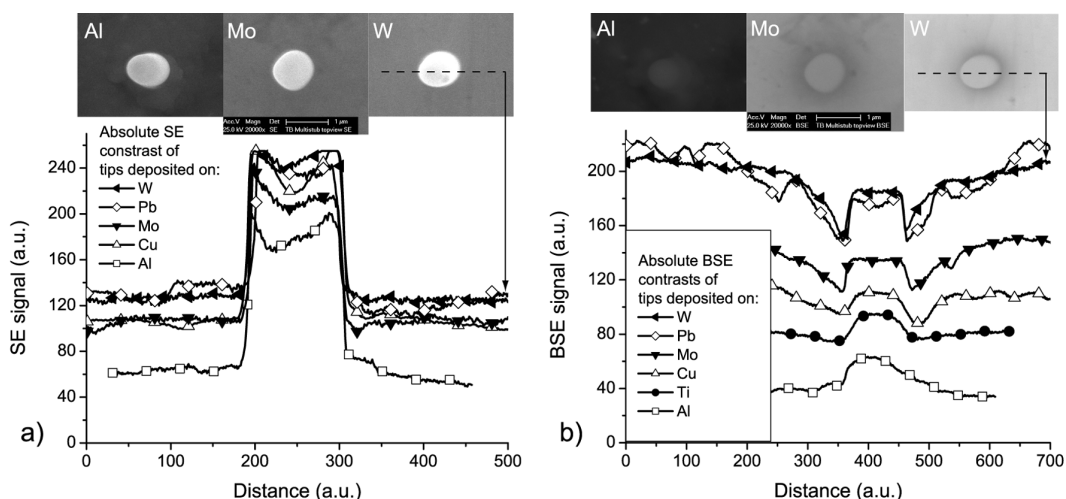
Figure 4-2-18. Absolute *ex-situ* SEM contrasts of tips at 25 keV. a) SE detector. b) BSE detector. Top: two selected series of images.

The difference in SE signals between the tip and substrate was constant (see fig. 4-2-18a). On the heavier substrates, the BSE signals from the tips were less than the values on the substrate. Dark BSE contrasts appeared around the tips (see fig. 4-2-18b). For this precursor, most of the current drop on heavy substrates seemed to be due to the SE increase.

4-2-3-E-β) - High atomic number tips from [IrCl(PF₃)₂]₂

Tips with large amounts of the heavy element Ir (Z_{Ir}=77) were deposited on the multistub from the non-commercial precursor $[IrCl(PF_3)_2]_2$.[36, 41] The composition measured by EDX was IrClPF (see fig. 4-2-19a). All spectra were comparable but they overlapped with substrate peaks, on all substrates but Ti, either in the 1.5 to 3 keV range or around 9 keV (see fig. 4-2-19a). The high-energy $Ir^{La,Lb}$ peaks were present in all tips. The Ir^{Ma} peak overlapped the P^{Ka} peak and entailed a large uncertainty on the Ir/P ratio. All the deposited tips had similar aspects (see fig.

4-2-19b). The substrate thus had little influence on the tip growth rates, compositions, and geometries.
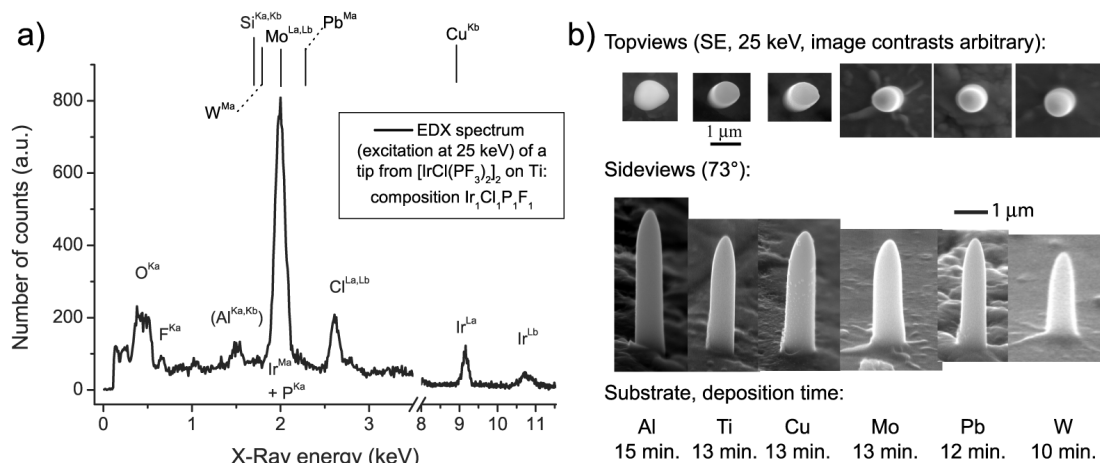
Figure 4-2-19. Deposition from Ir precursor (25 keV, 500 pA). a) EDX spectrum on Ti. b) *Ex-situ* SEM images of the tips on the different metals.

The monitored sample current had larger variations than from the Cu precursor.

Substrate	$i_{substrate}$ (pA)	i_{tip} saturation (pA)	$SE_{substrate}$ (a.u.)	SE_{tip} saturation (a.u.)
Al	-420	-90	0.05	0.28
Ti	-320	-50	0.08	0.34
Cu	-315	-30	0.11	0.36
Mo	-290	-19	0.12	0.37
Pb	-216	-20	0.14	0.32
W	-248	+7	0.12	0.33
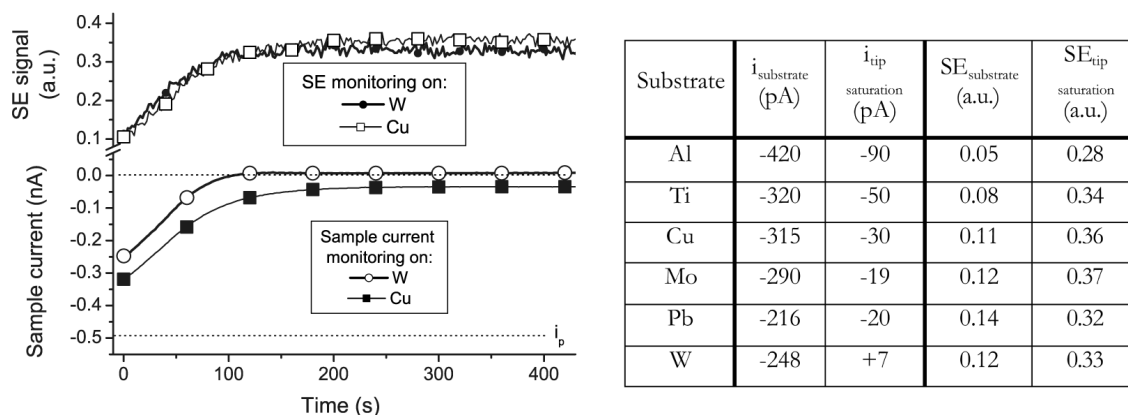
Figure 4-2-20. Examples of *in-situ* monitoring from Ir precursor (25 keV, 500 pA) on Cu and W.

Table 4-2-III. Initial and final monitored values from Ir precursor on the multistub.

The saturation current on W was positive (see fig. 4-2-20). This demonstrated that the SE contributed to the sample current during tip deposition, since the BSE yield cannot be above 1. On all other substrates it was negative but close to zero. The SE signals increased between 2.7 (W) and 5.6 times (Al). As was observed on Si, the "current drop" was larger when the tips contained heavier elements (see Table 4-2-III).

The vapor pressure of the Ir precursor was measured as a function of temperature. It was 2.10^{-2} mbar at RT and obeyed the relation $\log(P_{vap})=5.8-1.5.10^3 T$, showing a sublimation enthalpy of 28.7 kJ.mol^{-1}. Its flux was lower than from the Cu precursor, due to a lower vapor pressure $(P_{vap}((hfac)CuVTMS)=0.1$ mbar). However, the cone growth rates remained close (20 nm/s from (hfac)CuVTMS and 14 nm/s from [IrCl(PF$_3$)$_2$]$_2$). The compensation was due to a larger electron decomposition cross-section, because with its molecular weight of 807 g.mol^{-1} the bimetallic Ir compound was heavier than (hfac)CuVTMS (370 g.mol^{-1}).

4-2-3-F) Role of distant obstacles on the substrate

Until now, no information on the tip growth rate was available after saturation had been reached. Experiments were designed, so that monitoring would yield information on the height of the growing cylinders. From the Monte-Carlo simulations (see fig. 4-2-11), it was postulated that electrons were forward scattered between the angles Φ_{min} and Φ_{max} and followed a diffused conical distribution (see 4-2-21a). Tips were deposited on patterned substrates.
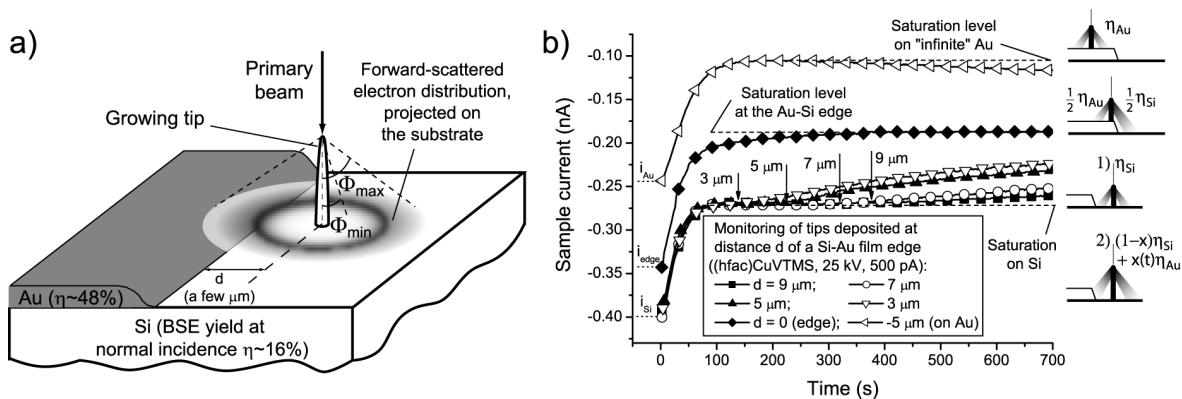
Figure 4-2-21. Forward-scattered electron cone on a patterned substrate. a) schematic principle. b) Current monitoring of tips deposited at different distances d from film edge. Arrows indicate inflexion points on the curves and recall the corresponding distances.

The deposition site was at a given distance from the edge of a 400 nm thick Au film. A plateau was reached once the tip cone was formed and the cylinder growth mode began. The BSE yield increased when the cone of forward-scattered electrons intersected the Au film, from a tip height that depended on the distance to the edge (see fig. 4-2-21b). An inflexion point then

appeared on the current curve. The curve asymptotically tended towards the constant value obtained from the tip deposited *on* the edge. The inflexion times were converted into heights as seen in the previous series in fig. 4-2-3. The ratio of edge distance to tip height was $\tan(\Phi_{max})$. This gave $\Phi_{max}=60\pm5°$ (1030$\pm$70 mrad).

Cone obstacles, prepared by the deposition process, were used to evaluate Φ_{min}:
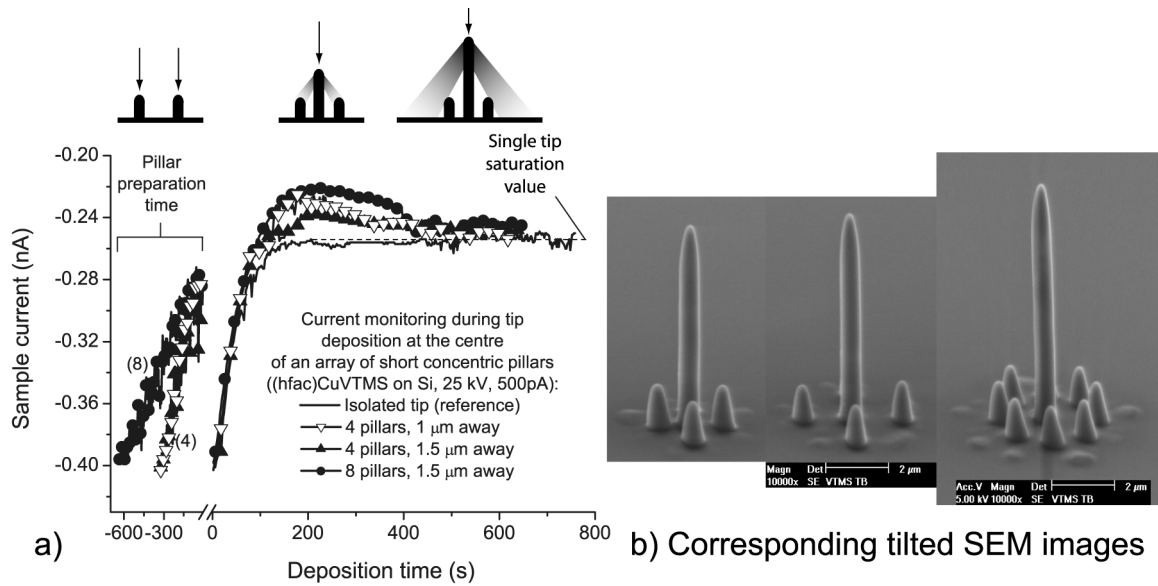
Figure 4-2-22. Tips deposited at the center of pre-deposited cones. a) Sample current monitoring. b) Corresponding tilted (64°) SEM images (scale bars 2 μm).

The measured sample current first decreased beyond the single tip saturation value, and then returned (see fig. 4-2-22a). The overshoot was larger when the cones were closer (1 μm vs. 1.5), or with more cones (8 vs. 4). This was due to the interaction of the forward-scattered electrons with the pillars, which was more important (and results in more BSE, thus lower sample current) when the pillars occupied larger solid angles (see fig. 4-2-22b). The signals turned back to the single tip value ($\sim$500 s) when the whole forward-scattered cone reached the substrate beyond the pillars. The corresponding height ($\sim$5.5 μm) gave $\Phi_{min}=15\pm5°$ (260$\pm$80 mrad).

4-2-3-G) Role of the acceleration voltage

The effect of the acceleration voltage on the current drop was studied in another deposition machine, a commercial FEI Dual-beam system, in which smaller spots were obtained at lower energies. This also demonstrated that the current dropped similarly when depositing from a field emission gun (FEG). Deposition was performed from the organometallic precursor Methylcyclopentadienyl-trimethyl-Platinum ($MeCpPtMe_3$), from a reservoir heated at 45°C. The growth rates were higher than in the S100. Only the deposition of tip arrays allowed for reliable measurements:
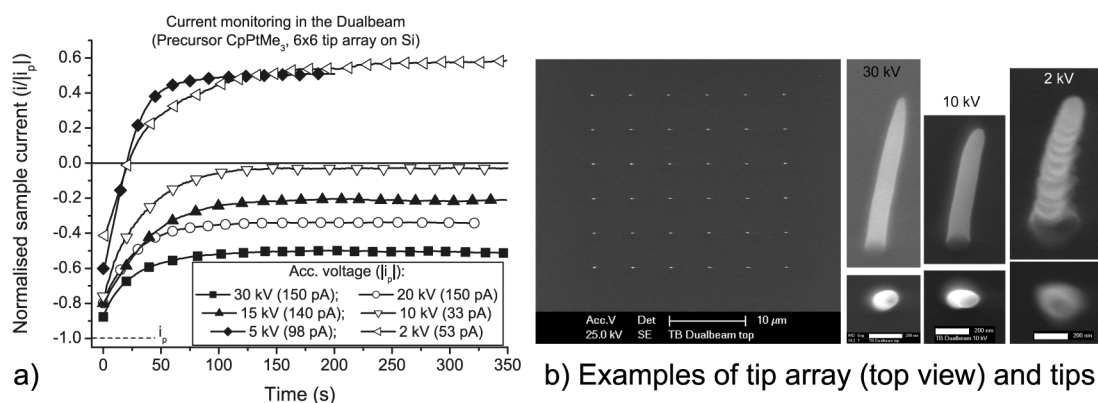
Figure 4-2-23. Effect of acceleration voltage on sample current monitoring in a FEG-SEM.
a) *In-situ* monitoring. b) Selected top and tilted (30°) *ex-situ* SEM views (scale bars 200 nm).

At all accelerations, the currents were selected to produce tip-like deposits in SEM tilted view. Higher accelerations gave sharper tips (see fig. 4-2-23b).[35, 42] The monitored curves saturated in the same way as in the S100 (see fig. 4-2-23a). Only tips with similar cylinder diameters (130 to 200 nm) were compared. EDX analysis revealed compositions close to $Pt_2C_7O_1$ for all tips, although the morphologies were sometimes different. At the lower acceleration voltages (2 and 5 kV) positive sample currents were routinely measured on thin tips due to the increased SE emission at lower electron energy.[21] The tips bent during SEM observation. These structures can probably still change shape, morphology and composition under the analysis probe.

A series of Monte-Carlo simulations was computed on these tips. The forward-scattered electron cone widens at decreasing energy (see fig. 4-2-24). Under 5 keV, most electrons are backscattered or absorbed directly in the tips.
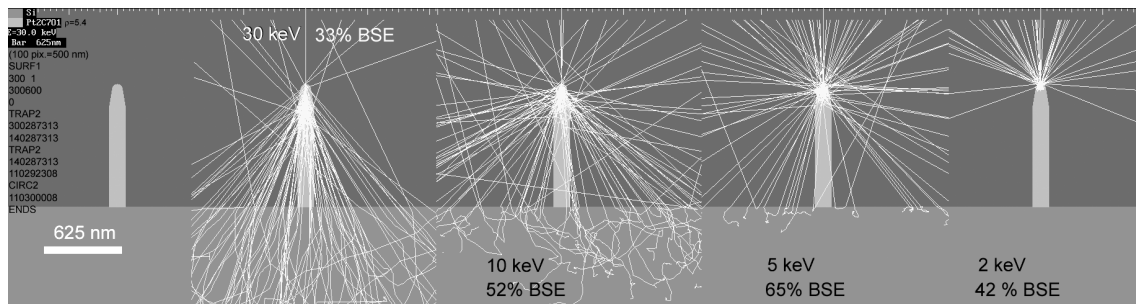
Figure 4-2-24. Monte-Carlo simulations of electron trajectories in 130 nm diameter tips deposited at different energies. From left to right: model tip with code, and 100 trajectories at 30, 10, 5, and 2 keV.

4-2-3-H) Summary of the influence of the parameters in the monitoring

Tip growth occurred through three successive regimes: base, cone, and cylinder. The monitored sample current and SE saturated at the transition between the cone and cylinder growth modes.

The saturation values were more distant from the probe current when:

    a)   the tips consisted of heavier elements,

    b)   the cylinder diameters were larger,

    c)   the substrate was heavier, and

    d)   when the beam had lower energy.

Even positive sample currents were occasionally measured at saturation. Monte-Carlo simulations indicated that the electrons were forward scattered by the tips. The electron distribution escaping from the tips had a conical shape. Information on the tip height was obtained by intersecting the forward-scattered electron distribution with scattering obstacles.

4-2-4 Physical model

4-2-4-A) Qualitative tip scattering model for a single electron

The incidence of a single electron on a tip with a complete cone was considered. The principles of electron scattering by atoms, used in this model, can be found in Annex 1. In the FEB-deposited carbonaceous mixtures, the collision mean-free-paths were typically 5 to 10 nm.
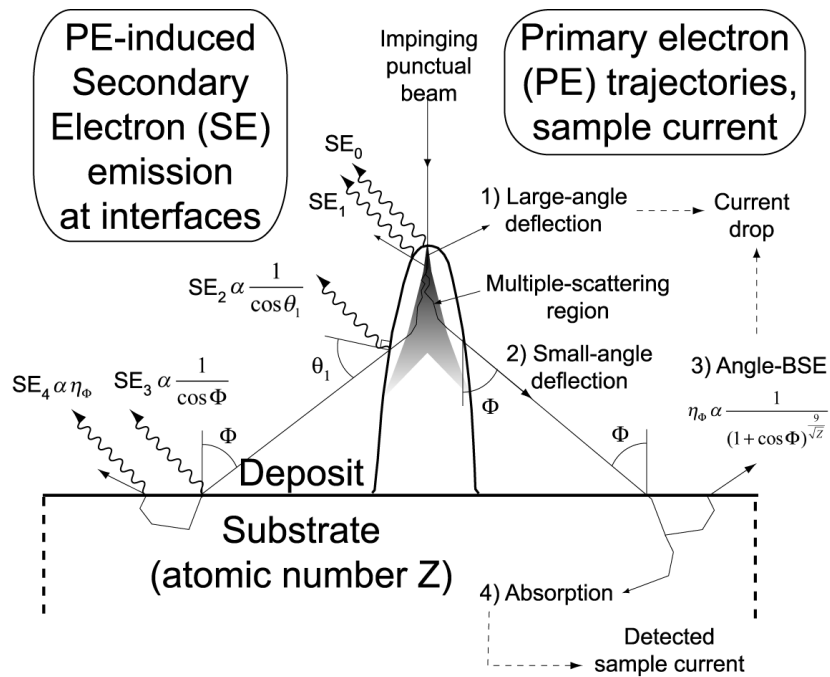
Figure 4-2-25. Schematic physical model of the sample current drop and SE emission increase during deposition. Right-hand side, trajectory of a single primary electron. Left-hand side, resulting SE emission at each crossed interface.

If the electron was not submitted to a large-angle scattering event that rapidly drove it out of the tip (see 1, at the right of fig. 4-2-25), it reached a tip sidewall after M collisions (2). The escape angle in relation to the vertical axis of the tip, named Φ, is the numerical result of all the collisions. Φ is also the incidence angle on the substrate (3). If θ_{av} represents the most probable scattering angle for each initial scattering process, then Φ would be statistically close to $M*\theta_{av}$. According to Arnal's formula (see eq. 4-2-3), the probability $\eta_{Z,\Phi}$ of being backscattered by the substrate increases with Φ.[43] This empirical law was recognized to quantitatively describe experimental measurements:[18]

$$\eta_{Z,\Phi} = \left(\frac{2}{1 + \cos(\Phi)} \right)^{\frac{9}{\sqrt{Z}}} \eta_{Z,\perp} \qquad\qquad \textbf{(4-2-3)}$$

Arnal's formula: $\eta_{Z,\Phi}$ is the backscattering yield under the angle of incidence Φ on a
substrate with atomic number Z.

The probability of electron absorption by the substrate (4, in fig. 4-2-25) is lower than at normal incidence. This explained the measured drop in the sample current when the electron impinged on the tip. The increased SE emission is the result of the PE crossing several interfaces before getting absorbed or backscattered, instead of generating SE only from the substrate (see SE_{1-4} on the left side of fig. 4-2-25). For a quantitative calculation, each interface crossed was weighed by an angular factor. SE emission was almost Lambertian, even when the primary beam crossed interfaces with angles as high as 60°.[44] The substrate collected roughly half of the SE emitted from the tip walls.

The formation of the cylinder is due to the lateral escape of the electron through the cone surface. Statistically, no electron could travel deep enough inside the deposit, to reach the surface and fix precursor at the level of the cylinder. The signals saturated for the same reason: once the cone was formed, the angular distribution of the laterally scattered electrons was constant. This is also why the growth rate was maximal at complete cone formation, as observed in fig. 4-2-4. The cone was the shape from which all electrons escaped laterally, meaning that each electron crossed more interfaces than ever before, and at each interface had the same probability of decomposing adsorbed precursor. This had been already observed, but was attributed to SE generation for smaller structures.[45] The efficiency of deposition then decreased due to tip heating, as discussed later (see §5-2).

At each interface the electrons decomposed the adsorbed precursor molecules. The surface layers, which generated the SE, were rapidly formed from deposited material. The absorbed sample current was expressed by the following equation.

$$i_{sample} = i_p - \eta_\Phi i_p - \delta i_p \qquad\qquad \textbf{(4-2-4)}$$

Expressing the BSE and SE currents according to fig. 4-2-25 leads to:

Total probe current

Back-scattered electrons $(\eta_\Phi \cdot i_p)$

$$i_{sample} = i_P - \left(\frac{2}{(1+\cos\Phi)}\right)^{\frac{9}{\sqrt{z}}} \eta_\perp i_p \qquad\qquad\text{(4-2-5)}$$

$$-\delta_{tip}i_p - \frac{1}{2}\left(\frac{1}{\sin\Phi}\right)\delta_{tip}i_p - \left(\frac{1}{\cos\Phi}\right)\delta_{tip}i_p - \beta\left(\frac{2}{(1+\cos\Phi)}\right)^{\frac{9}{\sqrt{z}}} \eta_\perp\delta_{tip}i_p$$

SE_0 SE_2 (assuming $\theta_1 \sim \pi/2 - \Phi$ in fig. 4-2-24) SE_3 SE_4

Secondary Electrons leaving the sample

Collected sample current according to fig. 4-2-25. First approach, supposing all electrons escape the tip identically. $\eta_\perp$: BSE yield of the substrate at normal incidence; δ_{tip} : SE yield of the deposited material; β: SE generation efficiency of the BSE.

A thin layer (> 10 nm) of deposited material was assumed to cover each interface crossed by the PE, so all SE were emitted from the deposit. Physically, at energies above 10 keV the BSE term was predominant over the SE terms, since $\eta > \delta$ (see Annexes 3 & 4). The sample current predicted by eq. (4-2-5) was plotted as a function of Φ in fig. 4-2-26.

Figure 4-2-26. Plot of the collected sample current as a function of single electron exit angle Φ, according to eq. 4-2-5. Parameters used for calculation: δ_{tip}=0.05, β=3.

Beyond exit angles of 0.4 rad on the solid substrates, the electron balance increased towards positive currents with increasing **Φ**, and was positive beyond substrate-dependent values. This explained its dependence on the tip parameters:

- More collisions occurred in tips with larger diameters. The resulting **Φ** was larger and less current was absorbed in the sample (as shown in fig. 4-2-9).

- In tips with identical diameters, the higher average atomic numbers gave rise to larger average deflection angles θ_{av}. The resulting angles **Φ** and the current drops were larger.

- On tips deposited on different substrates, the BSE yields followed the order of the BSE yields of the substrates, increasing with the atomic number (see figs. 4-2-17, 4-2-20).

- At lower electron energies, the elementary deflection angles were larger: the resulting **Φ** and current drops were also larger, as long as the electrons were scattered forward (see figs. 4-2-23 and 4-2-24).

This single-electron model was satisfactory, but to accurately describe the actual phenomenon, the angular distribution of the forward-scattered electrons needed to be determined.

4-2-4-B) Physical effects of the angular electron distribution

The cone shape resulted from the convolution of several factors (see fig. 4-2-27). The angular electron distribution N(**Φ**) at the surface of the existing cone, weighed by its decomposition efficiency dependence on the on escape angle $\zeta(\theta)$, decomposed the local precursor concentration W(r,h,t) (see inset in fig. 4-2-27). The cone geometry was stable under the conditions of the experiment. In principle, this schematic drawing was valid for both the electron- or precursor-flux-limited regimes. The final tip profile may depend upon the regime. If the PE density was high then a regime transition may have occurred between the PE incidence site (precursor-limited) and the tip sidewalls (electron-limited).
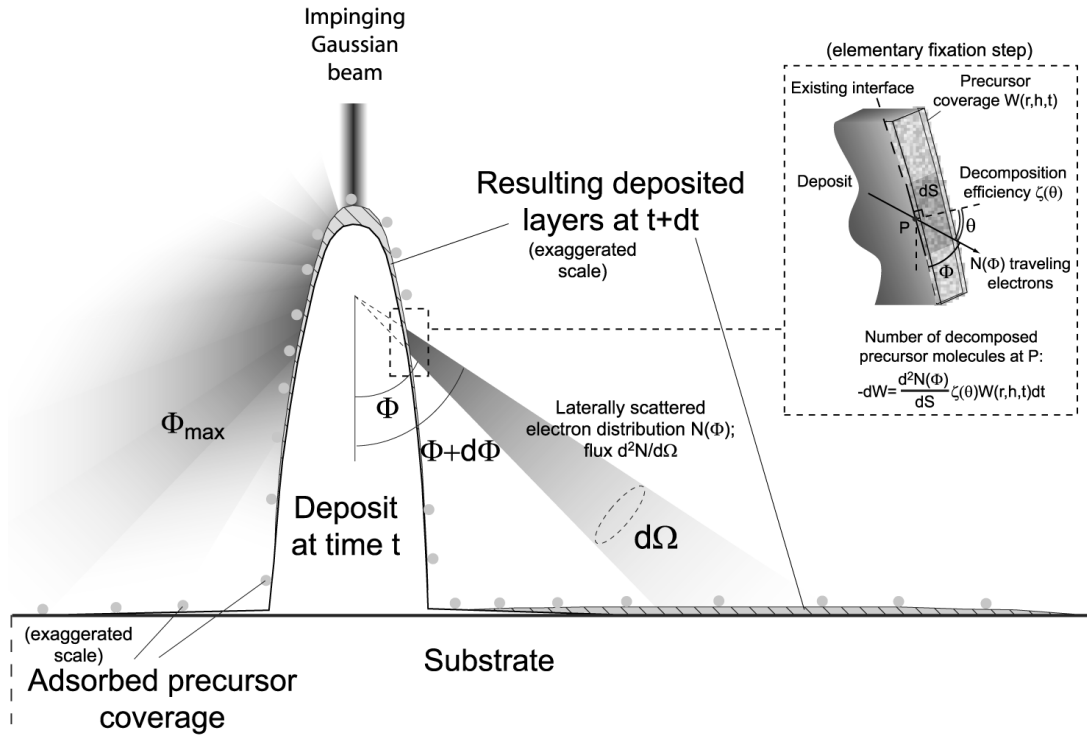
Figure 4-2-27. Schematic relation between cone shape and scattered PE distribution. N(Φ): angular distribution of forward-scattered electrons; Φ$_{max}$: angle at which N(Φ) is larger. ζ(θ): efficiency of decomposition of a precursor molecule by an electron crossing the interface at an angle θ. W(r,h,t): precursor coverage at radius r, height h and time t.

This explained why the tip shapes and compositions were similar when depositing on the multistub. Soon after starting deposition, precursor adsorption and fixation occurred on the smooth layer of decomposed precursor. Equation (4-2-5) was refined by including N(Φ):

$$i_{sample} = i_P(1-\eta_{dir})\left(1-\eta_\perp \times \int_\Phi \left(\frac{2}{(1+\cos\Phi)}\right)^{\frac{9}{\sqrt{Z}}} N(\Phi)d\Phi\right)$$
$$-\left[1+\eta_{dir}+(1-\eta_{dir})\int_\Phi \left(\frac{1}{2\sin\Phi}+\frac{1}{\cos\Phi}+\beta\left(\frac{2}{(1+\cos\Phi)}\right)^{\frac{9}{\sqrt{Z}}}\eta_\perp\right)N(\Phi)d\Phi\right]\delta_{tip}i_p$$

(4-2-6)

Collected sample current – complete approach. η_{dir}: Fraction of electrons exiting the tip with angles Φ larger than 90°.

The multistub experiments (figs. 4-2-16 to -20) showed a variation between η and Z, while η_{dir}, δ_{tip}, and N(Φ) remained constant. To simplify, β was supposed to be independent of Φ and Z.

4-2-4-C) Derivation of an analytical expression for the forward scattered electron distribution

Multiple scattering resulted in broadening the beam but initially created little electron absorption, so that the total number of traveling electrons was constant.[46] When an electron beam passes through a flat film, the large numbers of randomly oriented collisions create a Gaussian distribution of the transmitted electrons.[47-50] The root-mean-square width increases with the power 3/2 of the film thickness.[51] The following dependency on the material parameters was found to agree with measurements obtained on Cu, Ag, and Au:[46]

$$\sigma^2 = 0.44.10^3 \left(\frac{Z}{E}\right)^{\frac{3}{2}} \frac{\rho}{A} t^3 \qquad (4\text{-}2\text{-}7)$$

Spatial beam broadening. Parameter σ (in nm) of the Gaussian distribution of an electron
beam of energy E (in eV) transmitted by a slab of thickness t (in nm) of a material with
density ρ (in g.cm⁻³), atomic mass A (in g.mol⁻¹), and atomic number Z. a: scaling constant.

This equation was interpreted as a probabilistic law, which applied to individual electronic trajectories in the scattering film. The mathematical shape of all trajectories in the scattering medium was r=aCh³/². The scaling constant a was given by writing eq. (4-2-7) as $\sigma^2=at^3$. The parameter C follows a normal Gaussian distribution ($\mathcal{N}(0,1)$, see fig. 4-2-28a).
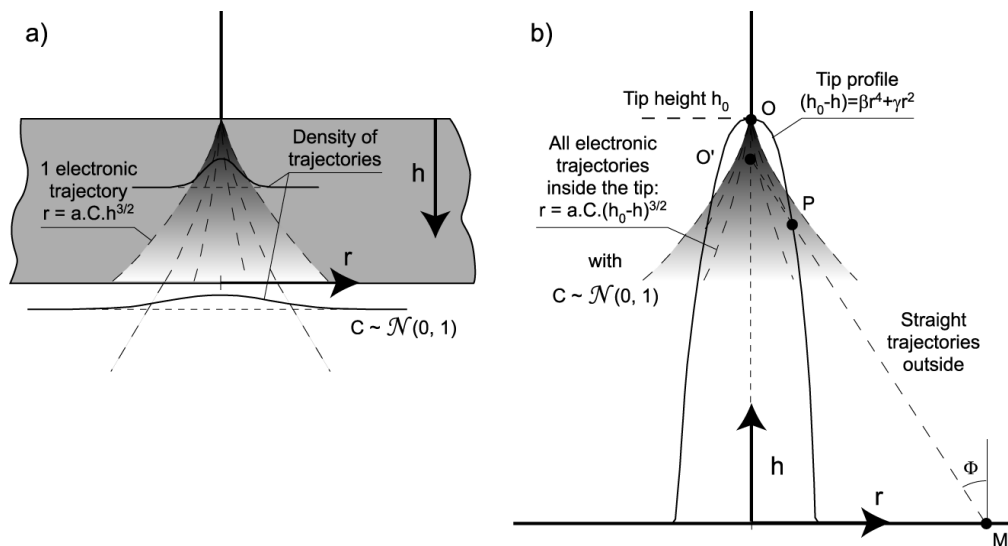
Figure 4-2-28. Analytical electron trajectories in solids. a) Beam broadening by scattering through a thin film (probabilistic approach). b) Application to the case of a tip.

In order to determine the distribution N(Φ), the outline of the calculation was as follows: the number dN of electrons, which impinged on the substrate at point M (see fig. 4-2-28b) between r and r+dr, was evaluated by expressing r_M as a function of the parameter C. Inverting the obtained relation yielded C(r). The desired 2D distribution was obtained by inserting C(r) in:

$$dN = \frac{1}{2\pi} \exp\left(-\frac{C^2}{2}\right) dC \qquad (4\text{-}2\text{-}8)$$

As can be seen, this gave the correct result for a thin film.

The expression of the electron trajectory in the tip is given in fig. 4-2-28. At each point and at the exit point P, the tangent to the trajectory is given by:

$$\tan\Phi = \left(\frac{dr}{dh}\right)_P = \frac{3}{2}\left(r_P a^2 C^2\right)^{\frac{1}{3}} \qquad (4\text{-}2\text{-}9)$$

The radius r_P was calculated by taking P as the intersection of the electron trajectory with the tip surface, expressed analytically by the polynomial in fig. 4-2-2:

$$\text{The system} \begin{cases} h_0 - h_P = \beta r_P^4 + \gamma r_P^2 \\ aC(h_0 - h_P)^{\frac{3}{2}} = r_P \end{cases} \qquad (4\text{-}2\text{-}10)$$

$$\text{leads to: } C = \frac{1}{a r_P^2 \left(\beta r_P^2 + \gamma\right)^{\frac{3}{2}}} \qquad (4\text{-}2\text{-}11)$$

The tip surface was not reasonably described by a purely 2nd order or 4th order polynomial. But the 2nd order term was dominant at small r_P (the tip apex), while the 4th order dominated at large r_P: these two regions were treated separately. The dependence of C on r_P was thus made simpler.

$$\text{Hence,} \begin{cases} \text{for } r_P \gg \sqrt{\dfrac{\gamma}{\beta}} : C \simeq \dfrac{1}{a\beta^{\frac{3}{2}} r_P^5} \\[4mm] \text{for } r_P \ll \sqrt{\dfrac{\gamma}{\beta}} : C \simeq \dfrac{1}{a\gamma^{\frac{3}{2}} r_P^2} \end{cases} \qquad (4\text{-}2\text{-}12)$$

In both regions, the coordinate r_P remained a simple function of C after inversion.

The electron impinged on the substrate at M, the coordinates of M are given by trigonometry:

$$r_M = r_P + h_P \tan\Phi \qquad\qquad \textbf{(4-2-13)}$$

An exact solution required numerical inversion (see below). For now, an approximate but analytical solution was derived. As soon as the cone was complete, or at large a Φ, the distance OP was small compared to PM. The points O, P and M were considered as aligned (O'~O).

$$\text{Approximating } \overrightarrow{OM} \parallel \overrightarrow{OP}: \quad r_M = h_{O'} \tan\Phi \simeq h_0 \tan\Phi \qquad \textbf{(4-2-14)}$$

Combining equations (4-2-14), (4-2-12), and (4-2-9) led to r_M:

$$\text{With } C_{\lim} = \frac{\beta}{a\gamma(2\gamma)^{\frac{3}{2}}} \left\{ \begin{array}{l} \text{for } C \ll C_{\lim} : r_M \equiv r \simeq \dfrac{3h_0}{2}\dfrac{(aC)^{\frac{3}{5}}}{\beta^{\frac{1}{10}}} \\[4mm] \text{for } C \gg C_{\lim} : r_M \equiv r \simeq \dfrac{3h_0}{2}\dfrac{\sqrt{aC}}{\gamma^{\frac{1}{4}}} \end{array} \right. \qquad \textbf{(4-2-15)}$$

These expressions were inverted:

$$\text{With } r_{\lim 1,2} = \frac{3h_0}{2}\frac{\sqrt{\beta}}{\gamma^{\frac{3}{2}} 2^{\frac{9}{10},\frac{3}{4}}} \left\{ \begin{array}{ll} \text{for } r \ll r_{\lim 1} : C \simeq \dfrac{\beta^{\frac{1}{6}}}{a}\left(\dfrac{2r}{3h_0}\right)^{\frac{5}{3}} \equiv K_1 r^{\frac{5}{3}} & \textbf{(4-2-16)} \\[5mm] \text{for } r \gg r_{\lim 2} : C \simeq \dfrac{\gamma^{\frac{1}{2}}}{a}\left(\dfrac{2r}{3h_0}\right)^{2} \equiv K_2 r^{2} & \textbf{(4-2-17)} \end{array} \right.$$

The constants K_1 and K_2 depended on the tip height, composition and profile. By differentiation and insertion into (4-2-8), the following relations were obtained:

$$\begin{cases} for \ r \ll r_{\lim 1} : dN \simeq \dfrac{5K_1}{6\pi} r^{\frac{2}{3}} \exp\left(-\dfrac{K_1^2 r^{\frac{10}{3}}}{2}\right) dr & \textbf{(4-2-18)} \\[3em] for \ r \gg r_{\lim 2} : dN \simeq \dfrac{K_2}{\pi} r \exp\left(-\dfrac{K_2^2 r^4}{2}\right) dr & \textbf{(4-2-19)} \end{cases}$$

From a practical point of view, these distributions were similar to one another. The following parameters were used for plotting, in the case of a 600 nm diameter tip from (hfac)CuVTMS at two successive heights. The averaged atomic number (Z_{av}) and atomic mass (A_{av}) of the deposits, according to the EDXS measurements, were used to calculate the scaling constant *a*. The values Z_{av}=11 and A_{av}=22 g.mol^{-1} did not take into account the possible H content in the deposits. The density ρ=3.3 g.cm^{-3} was used, and the acceleration energy was at 25 keV.

$$\left.\begin{array}{l} \beta = 7.10^{-8} \ nm^{-3} \\ \gamma = 6.10^{-3} \ nm^{-1} \end{array}\right\} from \ fig.4\text{-}2\text{-}2$$

$$a = \sqrt{0.44.10^3 \left(\frac{Z}{E}\right)^{\frac{3}{2}} \frac{\rho}{A}} \quad from \ eq.(4\text{-}2\text{-}7)$$

$$\equiv \sqrt{0.44.10^3 \left(\frac{11}{25.10^3}\right)^{\frac{3}{2}} \frac{3.3}{22}} = 2,6.10^{-2} \ nm^{-\frac{1}{2}}$$

$$\text{Hence} \quad \begin{cases} r_{\lim 1}(h_0 = 1,5\,\mu m) = 685 \ nm; \quad r_{\lim 2}(1,5\,\mu m) = 758 \ nm \\ r_{\lim 1}(h_0 = 3\,\mu m) = 1371 \ nm; \quad r_{\lim 2}(3\,\mu m) = 1524 \ nm \end{cases}$$

The expression from eq. (4-2-18) was plotted in figure 4-2-29. The second part of the curves, given by eq. (4-2-19), represents only a slightly faster decay, and was omitted for simplicity. The forward-scattered electron distributions reached maxima at different distances on the substrate. This confirmed the existence of the most probable electron exit angle Φ_{max} postulated in paragraph 4-2-3-F. The maximum widened and went away from the centre as the tip height increased. When the tip reached a height of 3 μm, the electrons were forward scattered up to a distance of 5 μm, creating the flat disk that surrounds the tip (see fig. 4-2-3).
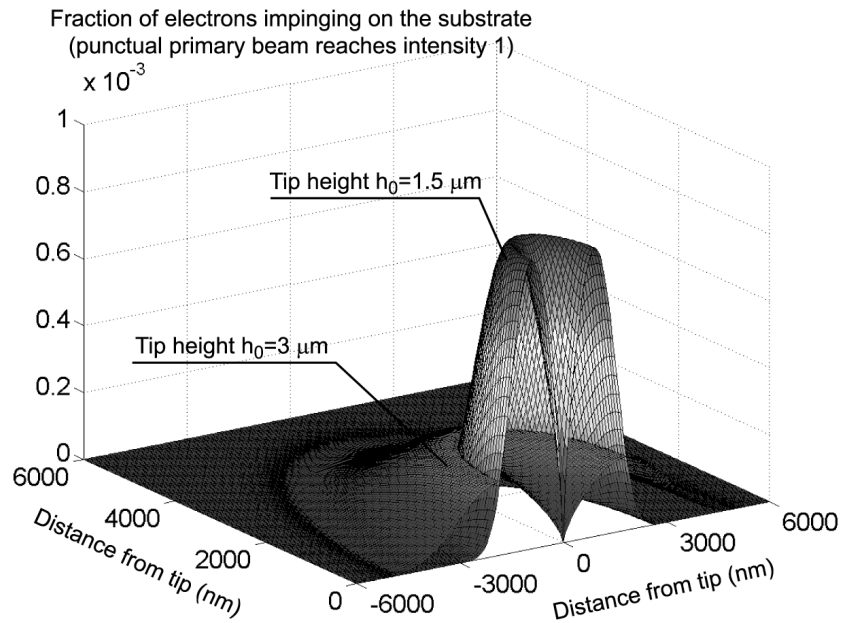
Figure 4-2-29. Analytical electron distributions impinging on the substrate after forward scattering in the tips, according to eq. (4-2-18). Position (0,0) is the tip center.

The angular distribution N(Φ) was obtained from equations (4-2-14) and (4-2-18). Taking into consideration only the 4th order term of the tip profile, yielded the following law:

$$dN = \frac{5K_3}{6\pi}\left(1+\tan^2\Phi\right)\left(\tan\Phi\right)^{\frac{2}{3}}\exp\left(-\frac{K_3^2\left(\tan\Phi\right)^{\frac{10}{3}}}{2}\right)d\Phi \qquad \textbf{(4-2-20)}$$

$$\text{(by writing } K_3 = K_1 h_0^{\frac{5}{3}} = \left(\frac{2}{3}\right)^{\frac{5}{3}}\frac{\beta^{\frac{1}{6}}}{a}\text{)}$$

4-2-4-D) Numerical inversion

The expression in eq. (4-2-11) was inverted numerically, without the simplifying approximations (eqs. 4-2-12 and 4-2-14).

The function g was introduced as: $C = \dfrac{1}{ar_P^2\left(\beta r_P^2 + \gamma\right)^{\frac{3}{2}}} \equiv g\left(r_P\right)$ \qquad \textbf{(4-2-21)}

g is a monotonous, decreasing function of r_p, and could thus be inverted.

$$\text{Hence } \tan\Phi = \frac{3}{2}\left(r_p a^2 C^2\right)^{\frac{1}{3}} = \frac{3}{2}\left(g^{-1}(C) a^2 C^2\right)^{\frac{1}{3}} \equiv f(C) \qquad \textbf{(4-2-22)}$$

The function g^{-1} was monotonous and increasing. f was also inverted and differentiated:

$$C = f^{-1}(\tan\Phi) \qquad \textbf{(4-2-23)}$$

$$dC = \left(1 + \tan^2\Phi\right)\left(\frac{df^{-1}(\tan\Phi)}{d\Phi}\right)d\Phi \qquad \textbf{(4-2-24)}$$

The expression (4-2-8) was evaluated numerically thanks to these relations.

4-2-4-E) Comparison with Monte-Carlo simulations

The obtained results were checked against the Monte-Carlo approach. The designed structures consisted of "free-standing tips", without a substrate, as shown in fig. 4-2-30a. The number of electrons scattered from this structure into successive annular regions were computed. The angular distributions predicted by the three approaches (analytical inversion, numerical inversion, and simulations) were compared in fig. 4-2-30b.
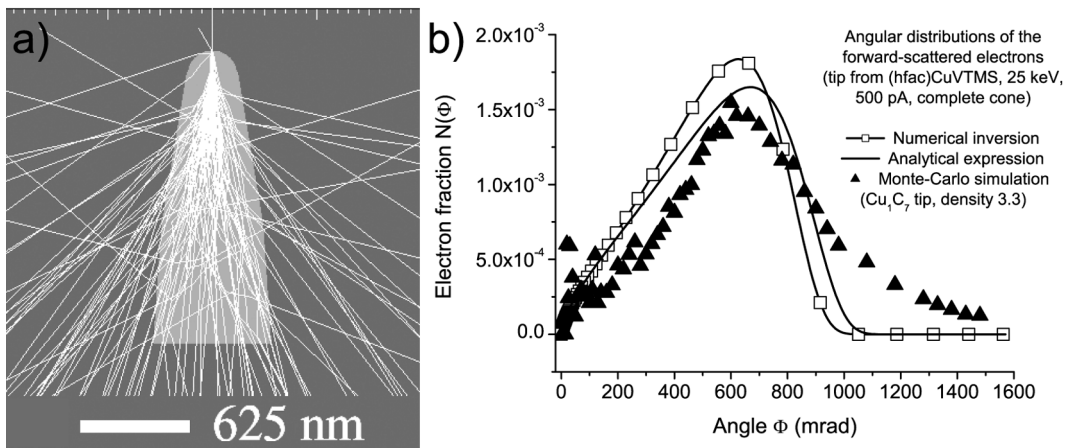
Figure 4-2-30. Forward angular distributions of electrons scattered in tips. a) Example of Monte-Carlo simulation used for the transmitted electron distribution (planar projection of 100 trajectories from a cylindrically symmetrical "free-standing tip" with no substrate). b) Compared results from the numerical inversion of eq. (4-2-24), the analytical eq. (4-2-20), and simulations (10000 trajectories per point).

A good agreement was found. The simplified analytical expression slightly overestimated the position of the density maximum and the electron fraction behind it, as compared to the numerical inversion. Both approaches underestimated the numbers of electrons scattered at high angles, as compared to the Monte-Carlo simulation. This was probably due to large-angle single scattering (see the resulting trajectories in fig. 4-2-30a). The multiple-scattering regime, which was responsible for the Gaussian beam broadening, was valid only after the electrons crossed a deposit with a mass-thickness of $125\,\mu g/cm^2$.[46] This fails to take into account the electrons which escaped from the tip after a single large-angle scattering event. However, the discrepancy was small, confirming that the approximations made in the analytical derivation were justified.

The advantage of the Monte-Carlo approach is its versatility concerning the shapes of the structures. Exact structures were designed based on the experimental results. This allowed visualization of the evolution of the transmitted angular distribution during cone formation:
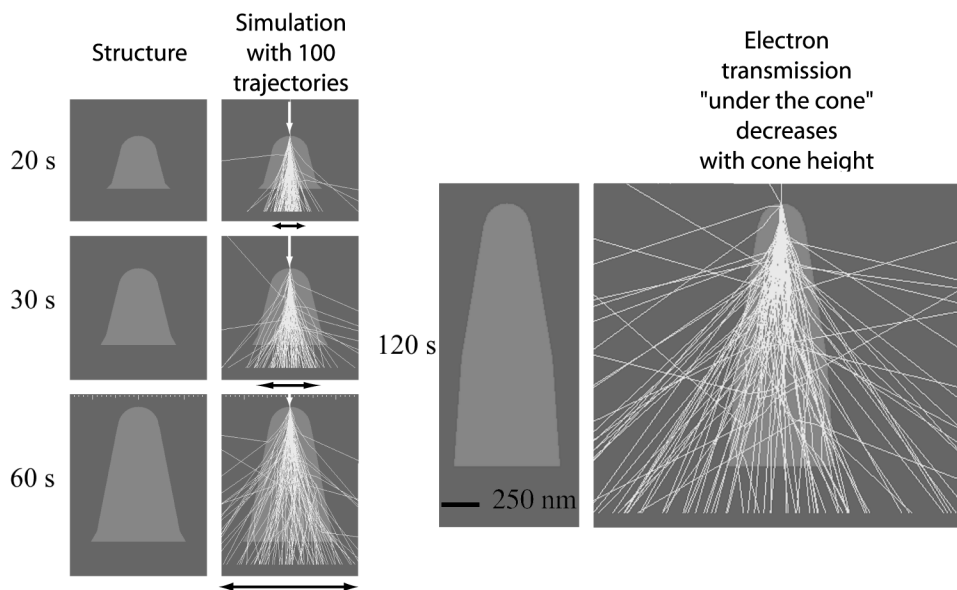
Figure 4-2-31. Monte-Carlo simulations of the evolution of electron angular distributions during tip growth (Cylindrical symmetry, Cu_1C_7, density 3.3, 25 keV, no substrate).

The angular distribution widened as the tip grew (see fig. 4-2-31). Quantitative results were computed but software artifacts arose on thin structures (<500 nm). They were compared with the results of the numerical inversion, obtained by determining separately the "transmitted" (through the cone base) and "laterally scattered" distributions, as shown in fig. 4-2-32.
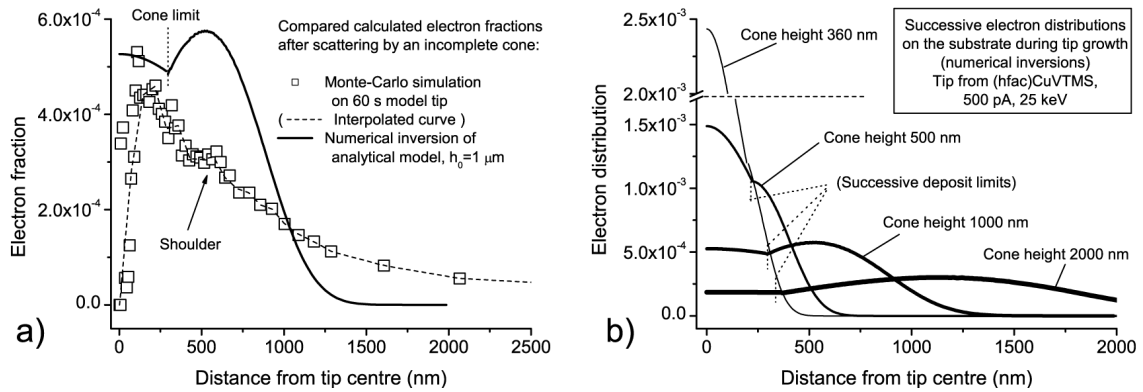
Figure 4-2-32. Comparisons of predicted distributions during cone growth. a) Simulation results on the 60 s tip, as compared to the numerical inversion results on a 1 μm cone. b) Evolution of numerically inverted angular distributions during tip growth.

For the 1 μm high cone, the Monte-Carlo simulations predicted a shoulder where the analytical model indicated a peak (see fig. 4-2-32a). The analytical model underestimated the fractions of electrons scattered at wide angles. The evolutions of the smoother numerically inverted distributions were comparable to the Monte-Carlo results.

4-2-4-F) Calculation of the absorbed sample current

The following integrals can now be numerically evaluated:

$$I_Z = \int_{\Phi=0}^{\frac{\pi}{2}} \left(\frac{2}{1+\cos(\Phi)} \right)^{\frac{9}{\sqrt{Z}}} dN(\Phi) \qquad (4\text{-}2\text{-}25)$$

$$F = \int_{\Phi=0}^{\frac{\pi}{2}} \frac{dN(\Phi)}{2\sin(\Phi)} \qquad (4\text{-}2\text{-}26)$$

$$G = \int_{\Phi=0}^{\frac{\pi}{2}} \frac{dN(\Phi)}{\cos(\Phi)} \qquad (4\text{-}2\text{-}27)$$

The complete equation of the sample current as a function of N(Φ) (eq. 4-2-6) was rewritten as:

$$i_{sample} = i_P (1 - \eta_{dir})(1 - \eta_\perp I_z) - \left[1 + \eta_{dir} + (1 - \eta_{dir})(F + G + \beta \eta_\perp I_z)\right] \delta_{tip} i_P \qquad \textbf{(4-2-28)}$$

The parameters of the calculation and the obtained results were compared with the multistub experiment results in fig. 4-2-33. For the tip from (hfac)CuVTMS, the scattering factor *a* was low. The electrons escaped the tip mainly from the lower part of the cone and eq. (4-2-18) was applied to calculate dN. Conversely, on the tip containing Ir, factor *a* was larger due to the heavy atom content. The electrons escaped the cone mainly through the upper part and hit the substrate at wide angles, as seen in fig. 4-2-14. The relevant expression is eq. (4-2-19).

Substrate	Tips from (hfac)CuVTMS (a=0.026; F+G=2.58)			Tips from [IrCl(PF$_3$)$_2$]$_2$ (a=0.064; F+G=2.36)		
	I_Z	$i_{calculated}/i_p$	i_{exp}/i_p	I_Z	$i_{calculated}/i_p$	i_{exp}/i_p
Membrane	NA	0.670	0.84	NA	NA	NA
Al	1.47	0.442	0.464	3.27	0.203	0.18
Ti	1.33	0.335	0.278	2.47	0.136	0.1
Cu	1.28	0.266	0.24	2.19	0.068	0.06
Mo	1.23	0.163	0.206	1.92	0.015	0.038
W	1.16	0.120	0.126	1.63	-0.024	-0.014
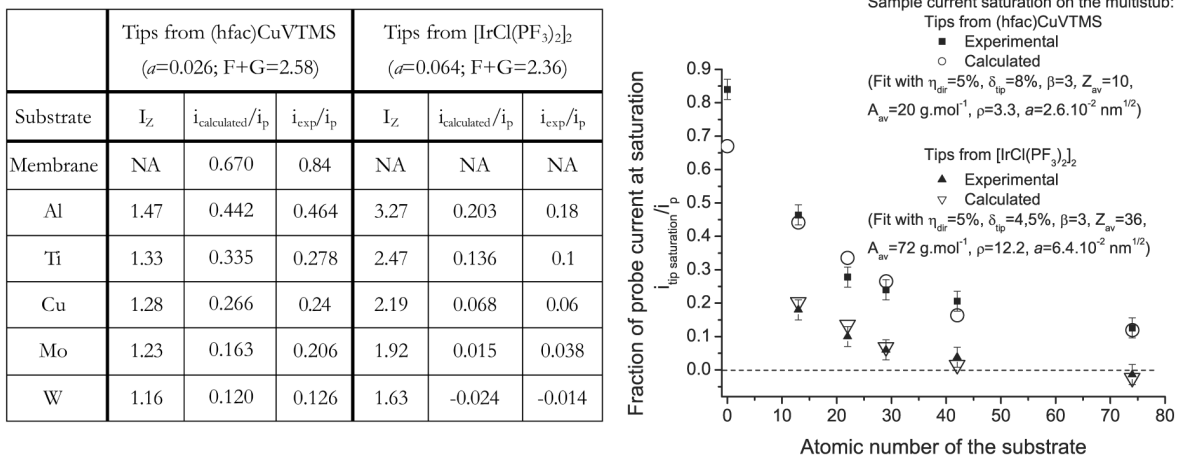
Figure 4-2-33. Comparison of the calculated sample current at tip saturation on several substrates with the experiment.

The analytical model correctly described the experiment. The amount of directly backscattered electrons (η_{dir}) and SE emissions (δ_{tip}) required in the calculations were satisfactory. The results at different energies were also compared to the model (see fig. 4-2-34). The increase in the parameter *a* at lower energies required using the large-angle eq. 4-2-19 below 10 keV. As noticed in the Monte-Carlo simulations, the model was not valid at 2 keV (see above, fig. 4-2-24).

Beam energy	a $(nm^{1/2})$	β (nm^{-3})	γ (nm^{-1})	η_{Si}	$\delta_{deposit}$	η_{dir}	I_Z	F	G
5 keV	0.110	-	5.10^{-3}	0.194	0.12	0.15	3.18	1.68	2.85
10 keV	0.065	-	8.10^{-3}	0.183	0.09	0.1	3.03	0.88	1.48
15 keV	0.048	8.10^{-6}	-	0.177	0.09	0.08	1.72	1.43	1.21
20 keV	0.039	8.10^{-6}	-	0.168	0.08	0.06	1.61	1.59	1.17
30 keV	0.029	8.10^{-6}	-	0.168	0.05	0.05	1.47	1.86	1.12
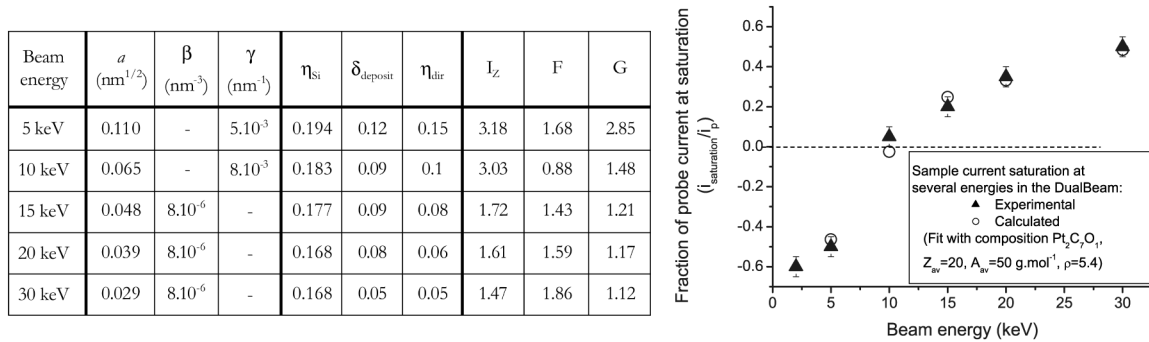
Figure 4-2-34. Comparison of the calculated sample current at tip saturation and at several energies with the experiment.

The calculated and measured values were in good agreement. The fit parameters η, $\delta_{deposit}$ and η_{dir} corresponded to a C-containing material. The physical model in fig. 4-2-26 and the forward scattered electron distributions given by eqs. 4-2-18 and 4-2-19 were confirmed.

4-2-5 Summary

Tip deposition follows three successive growth regimes: base, cone, and cylinder growth. The transition from cone to cylinder growth occurs when all the primary electrons are scattered sideways. The consequence is that the cone adopts a 4th-order polynomial profile. The monitored sample current decreases and saturates, contrary to what has been observed when depositing large-area films. This is an indication of an enhanced BSE yield on the tips. The tip shape is a function of the beam energy and tip chemical composition. The substrate did not influence the growth, but depositing on different substrates led to different monitored sample current curves. An analytical description of the angular distribution of the forward-scattered electrons was proposed by interpreting these curves. A good agreement of the analytical approach, as based on the physical principles of electron scattering, was found with Monte-Carlo simulations and with the results of the experiment.

Monitoring offered not only an immediate indication of the vertical tip deposition rate, but also an integrated information on electron scattering in simple protruding structures. In the next section, information will be gathered on more complex 3D shapes.

4-3 Three-dimensional deposits

In this section, the effects of beam scanning during deposition are described. Electron penetration is shown to be responsible for the deposition of complex periodic structures by simple line scanning. More complex 3D deposits are then described and commented on. The effects of beam scan direction are presented. The scope of the deposition process for the successful design of complex 3D nanostructures is discussed.

4-3-1 Definition

The "three-dimensional deposits" presented here are structures obtained by a lateral displacement of the primary beam during the deposition process.

4-3-2 Linear beam scanning

Large scan speeds (at least 10 nm/s) were chosen so that the effect of occasional beam drifts was comparatively small, requiring the use of precursors with large deposition rates. Unless mentioned otherwise, all experiments were performed from the precursor (hfac)CuVTMS, at 25 keV and 500 pA, on naturally-oxidised silicon. The scan direction was always towards the precursor supply. All side-views are shown with the needle to the right.

4-3-2-A) Construction and observation of the deposits

The results obtained during single scans at constant speed are shown in figure 4-3-1. Walls with increasing thicknesses and heights were deposited when the scan speed was decreased from 50 nm/s to 35 nm/s. During the scan the walls widths and heights increased until constant values were reached. After 4 μm the 40 nm/s line reached a height of 650 ± 50 nm. The cross-section of this line was a rounded triangle, 280 ± 20 nm wide at the base. The triangle base width and the final height increased with decreasing speed. Below 30 nm/s, the deposited lines rose up and a gap periodically appeared between the structures and the substrate. Complex fence-like structures were obtained at lower speeds.
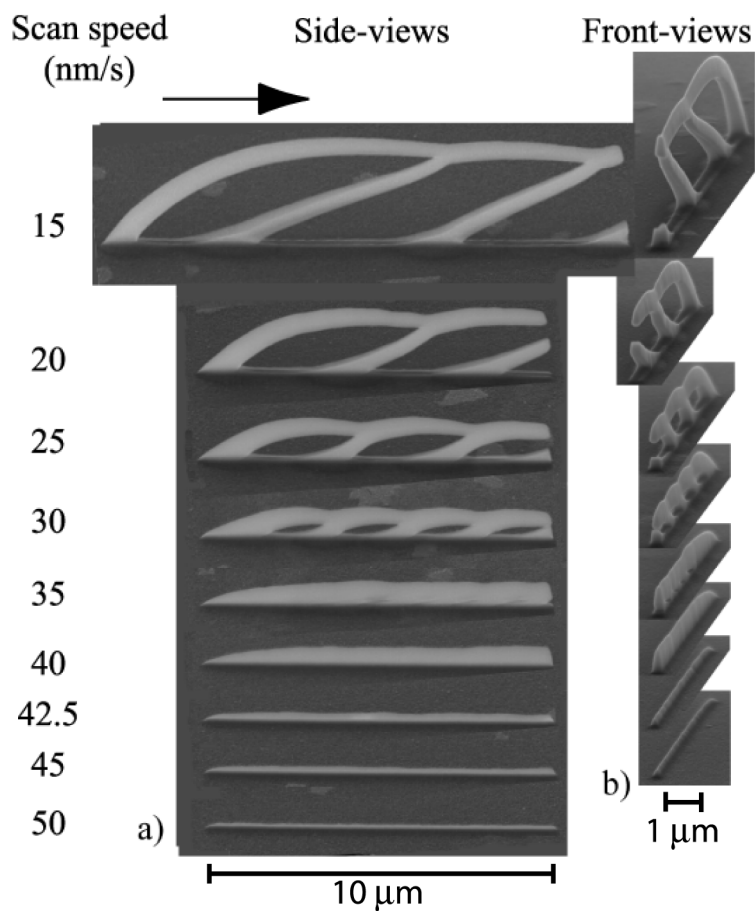
Figure 4-3-1. Deposits obtained by lateral beam scanning at constant speed. Ex-situ SEM views of 10 μm (except the top line, 15-μm) long (hfac)Cu(VTMS) lines written (from left to right on the picture) at 600 pA and constant lateral speeds (as indicated in left column). a) Side views, tilt 73°; b) Front views, tilt 82°.

The periodicity was maintained for long lines (see fig. 4-3-2).
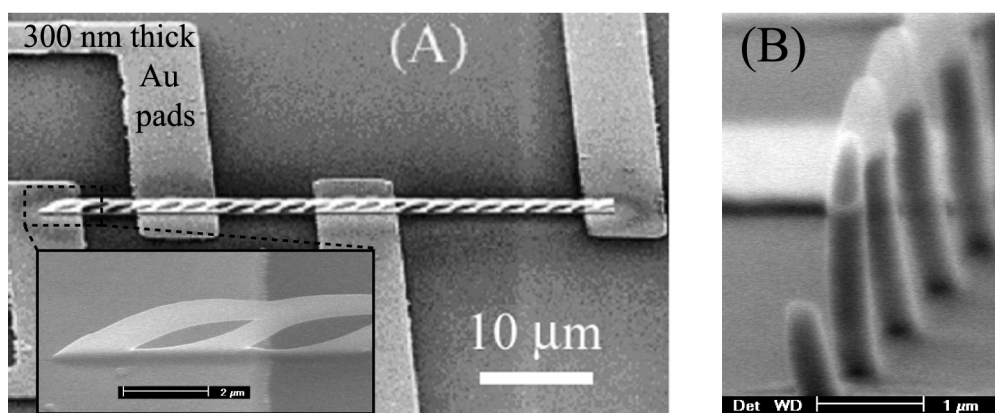
Figure 4-3-2. Long-distance periodicity, even on patterned substrate. A) *Ex-situ* tilted SEM side view, tilt 75°. Inset, starting point. B) SEM front view, tilt 82°.

The deposits remained periodic and followed the height variations of patterned substrates.[33] Other precursor-substrate couples showed the same behaviour on long distances (see fig. 4-3-3).
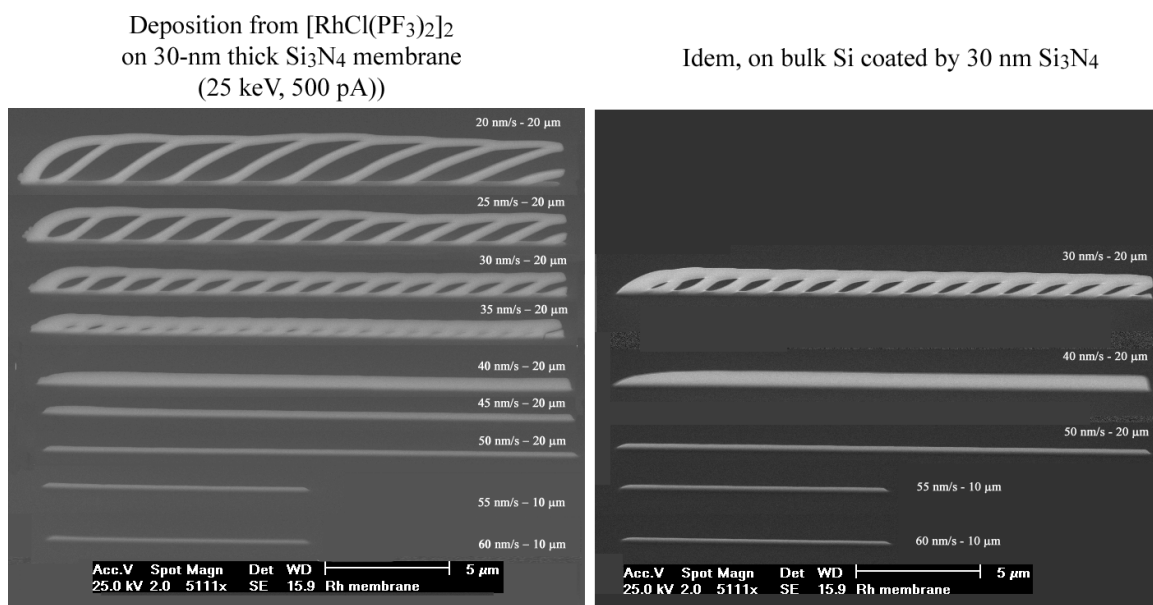
Figure 4-3-3. Periodicity effect from a Rh precursor, on thin film (left) and on bulk Si substrate (right). *Ex-situ* SEM sideviews, tilt 75°, scan speeds and lengths indicated.

Periodic regimes were previously reported during line scans by laser- and FIB-induced CVD.[52-54] The reason why it arises in FEB-induced CVD was investigated. Lines with increasing lengths from (hfac)CuVTMS were deposited at an intermediate scan speed, as shown in the following figure. Marker lines were deposited at the initial and final positions of the primary beam. After the first 1 µm of scanning, the deposit divides. A bottom line continues on the substrate and a pillar rises upwards. This upward pillar is called the primary arch. After 3 µm scan length, the primary arch growth direction progressively becomes parallel to the substrate (see fig. 4-3-4). At 5 µm scan length, the bottom line grows thicker, divides and rises up. This is the "secondary arch." A thin bottom line continues to be deposited on the substrate. At 7-µm scan length, the two arches meet and merge. This is the first "junction." From that point, the growth proceeds from the junction and the bottom line. A new secondary arch forms at 8.5 µm, and the periodicity is continued.
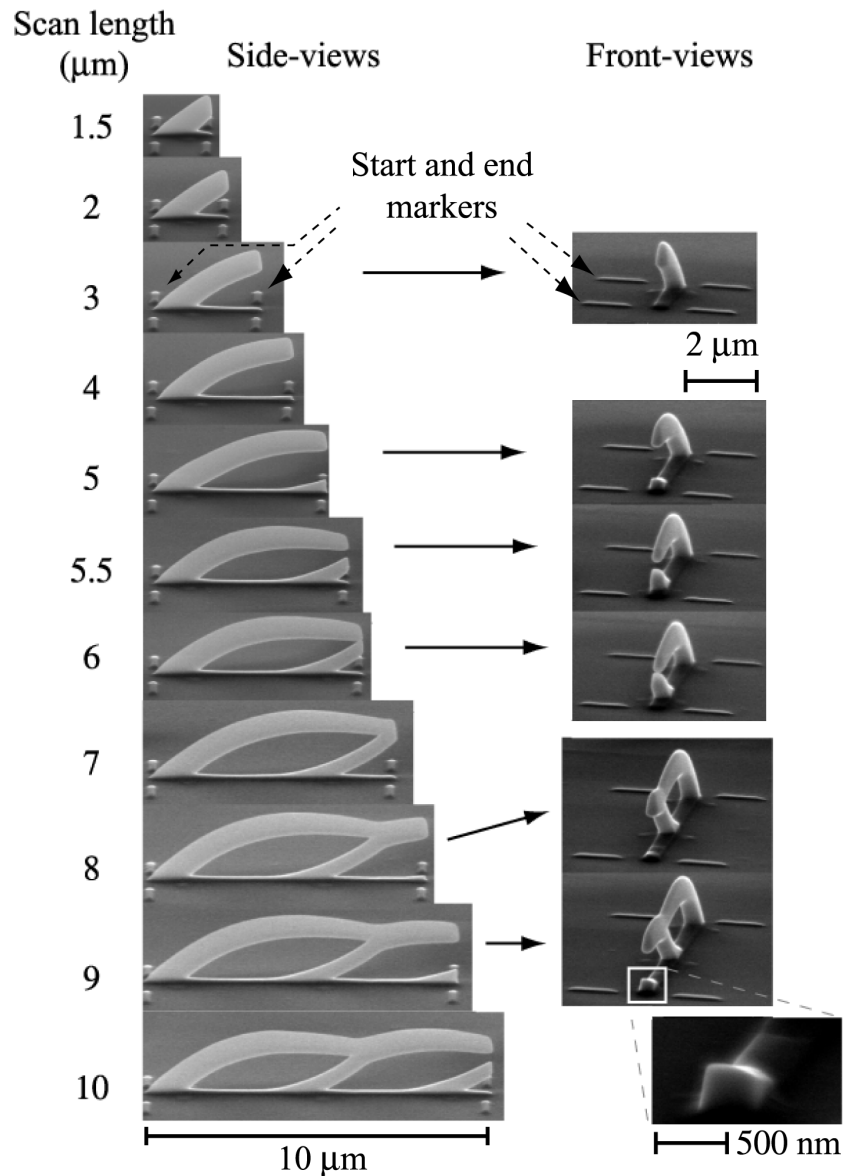
Figure 4-3-4. Periodicity initiation sequence. 25 keV, 500 pA lines deposited at 15 nm/s with increasing scan lengths (1.5 to 10 μm, as indicated in left column). Thin perpendicular lines (1.2 μm long, 50 nm/s) mark the initial and final beam positions. (a) *Ex-situ* SEM side views, tilt 73°. (b) Selected front views, tilt 82°. Inset: detail of the 9 μm secondary arch.

The period was defined as the distance between two successive secondary arches. The 60 μm long periodic line of fig. 4-3-2 has a constant period of 2.9 ± 0.3 μm. According to figs. 4-3-1 and 4-3-3, the period increases with decreasing speed. The primary arch growth angle, and the scan speed at which the periodic growth mode appears, are determined by the ratio of the initial tip vertical growth rate to the lateral scan speed.

The markers in fig. 4-3-4 showed that the final beam position was where the primary arch curvature diameter was smaller (150 ± 20 nm, so close to the probe size of 132 ± 8 nm at $\pm 2 \sigma$, with σ the beam standard deviation). This was confirmed by the following "jumped-line" series:
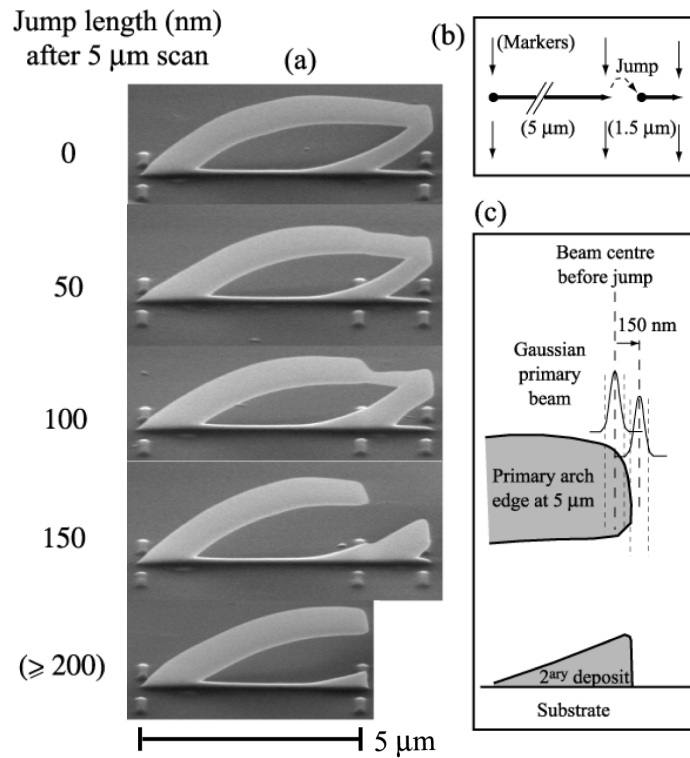
Figure 4-3-5. "Jumped line" series and beam position relatively to the deposits. a) *Ex-situ* SEM sideviews (tilt 73°). 5 µm beam scan (25 keV, 500 pA, 15 nm/s), then forward-shift ("jump"). Scale bar, 5 µm. b) Writing sequence. c) Schematic beam position at jump point. Dash dotted lines: beam diameter at $\pm 2\sigma$ is 132 nm (σ: beam standard deviation).

After a 5 µm long scan at 15 nm/s the beam reached the "jump point", as marked by the middle markers (see fig. 4-3-5b). The beam was then instantaneously shifted forward by a multiple of 50 nm. The point reached after the jump was named the arrival point. From the arrival point, the 15 nm/s scan was continued until the structure was 6.5 µm long. The 5 µm length for the jump point was chosen because it is where the bottom line thickens and the growth of the secondary arch begins. If, after having jumped, the beam still intersected the deposit, then the growth of the primary arch proceeded (see fig. 4-3-5a). This held true for the 50- and 100 nm jumps. The resulting primary arches, however, were thinner at the jump points. A smaller intersection of the beam with the deposit decreased the growth rate. The primary arch was

interrupted shortly after 150-nm jump, but the front edge was sharper than if the jump was 200 nm or more. This result showed that immediately after the jump, the tail of the electron beam was still intersecting the primary arch. At the jump point, the beam was thus centred at least at (150 - 132/2 =) 84 ± 5 nm behind the arch edge, as shown in fig. 4-3-5c. The entire primary beam intersected the primary arch.

The scan speed could also be changed during the process.
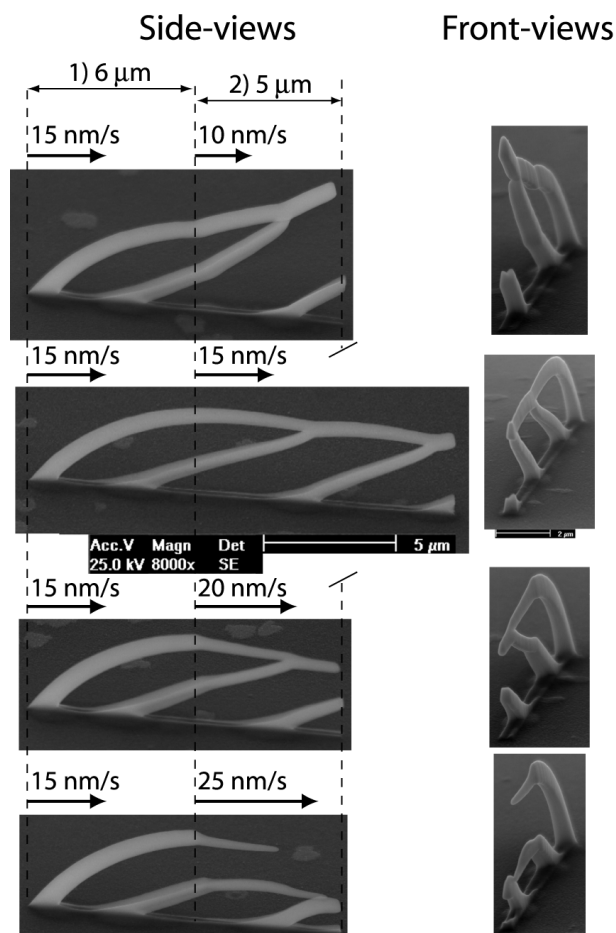
Figure 4-3-6. Speed variation during scan ((hfac)CuVTMS, 25 keV, 700 pA on Si). First 6 μm at scan speed 15 nm/s. Next 5 μm (except the 15 nm/s reference deposit) at 10, 20 or 25 nm/s. SEM micrographs, 25 keV, side- (tilt 57°) and front-views (tilt 83°).

The direction of growth for both primary and secondary arches depended on the scan speed (see fig. 4-3-6). If the scan speed became too fast (see bottom deposit) for the deposit to follow, then the growth of the primary arch was interrupted. This was similar to previous observations on freestanding rods, which were limited in length due to a growth rate decrease.[55]

In order to investigate the structures of the two types of arches, a TEM analysis was performed. A 9-μm-long line was written at 15 nm/s on a thin silicon nitride support film:
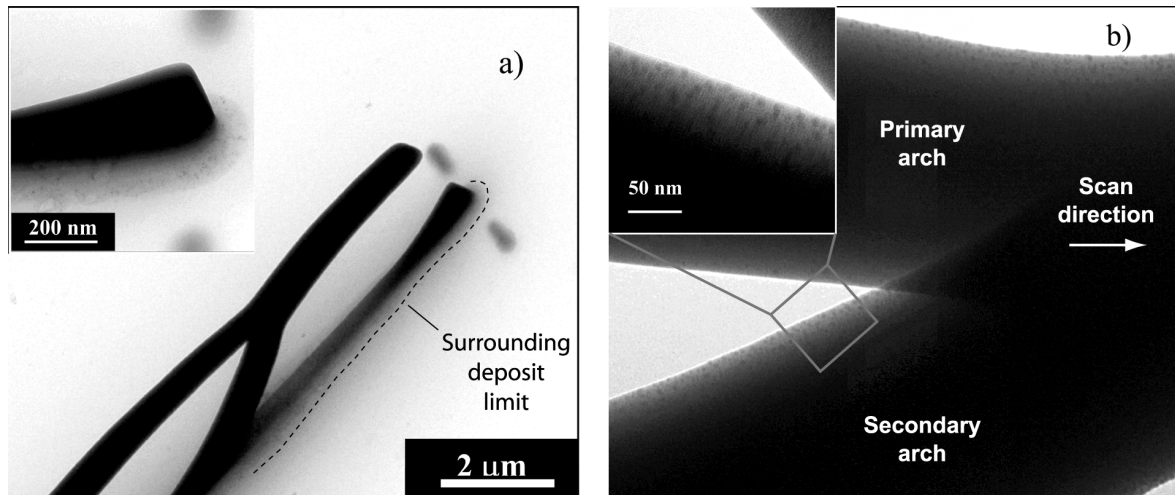
Figure 4-3-7. Surrounding deposits and nano-composite structure of arches. *Ex-situ* TEM sideviews (tilt 30°) of a scanned deposit on a 30-nm-thick Si_3N_4 membrane (500 pA, 9-μm long, 15 nm/s). a) Structure overview. Inset, close-up on the bottom line. b) Junction. Inset, close-up on the nanostructure at the top of the secondary arch.

Around the edge of the bottom line a thin contrasted deposit was observed (see fig. 4-3-7a). It was wider (~2 μm) around the first complete secondary arch and narrower (~1 μm) where the growth of the new secondary arch began. The junction area was smooth on a 10-nm scale. The primary and secondary arches had a similar nano-crystalline structure (see fig. 4-3-7b). Dark grains of up to 10-nm diameter were embedded in an amorphous matrix and were visible on the upper surfaces. On the lower sides of both arches, the grains were less visible. The primary and secondary arches consisted of the same material.

4-3-2-B) *In-situ* monitoring of the signals

Selected *in-situ* monitored signals during the series at varying scan speeds were plotted *vs.* time and compared with the evolutions of a vertical tip (see fig. 4-3-8a). The series of the successive scan lengths (shown in fig. 4-3-4) allowed detailed observation of all the features of the obtained curves, and how these related to successive shape changes (see fig. 4-3-8b).
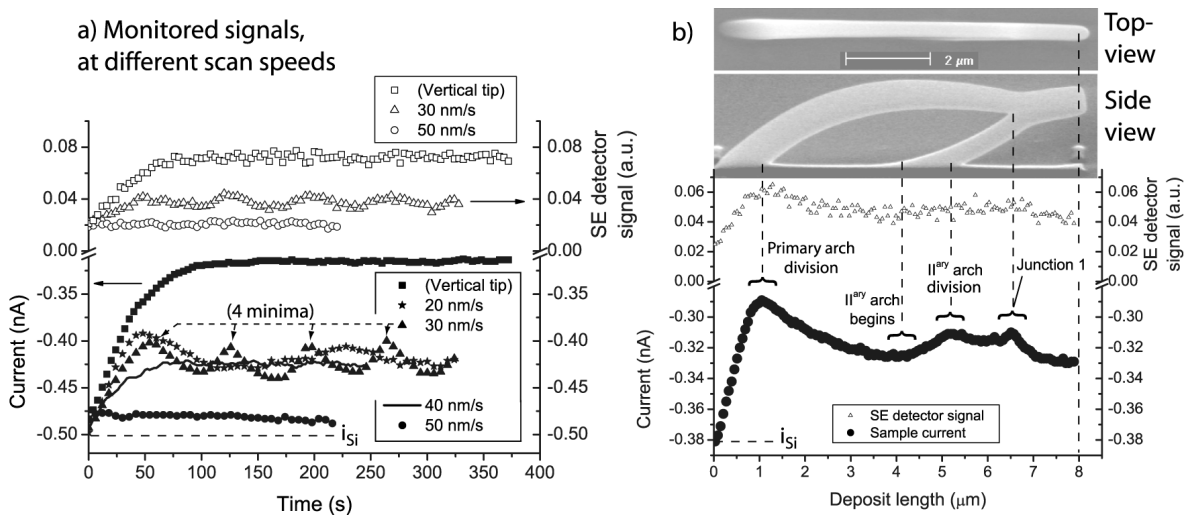
Figure 4-3-8. *In-situ* monitoring during line deposition showed periodicity evidence before tilted observation. a) Selected time evolutions from the fig. 4-3-1, compared to a vertical tip. b) Signals vs. length evolution of the 8-μm line of fig. 4-3-4, correlated to the deposit geometry. Inset, *ex-situ* 25 keV SEM top- and tilted side-views.

On thick walls, the current saturated at constant values, but the periodic line currents had regularly spaced minima (see fig. 4-3-8a). This indicated a periodic structure, without having to tilt the sample, and was clearer than top-view observation. A minimum was reached when the primary arch divided (see fig. 4-3-8b). The current then slowly increased until the secondary arch started to grow. Two local minima corresponded to the secondary arch division and to the junction. The 4 minima of the 30 nm/s line in fig. 4-3-8a thus correspond to the primary arch take-off and to 3 junctions.

To summarize, the larger the local deposit thickness (base, junctions) upon which the beam impinged, the larger the current drop. The result also applied to thick walls like those in fig. 4-3-1. The thicker the wall, the larger the current drop, at a constant height.

4-3-2-C) Interpretation

A physical schematic drawing of electron propagation was compared to Monte-Carlo simulations. The deposited material, with the composition $Cu_1C_3O_1F_1$, was described by its average atomic number $Z_{av} = 11$ and atomic mass $A_{av} = 22$ g/mol. These figures were overestimated because some H from the precursor was probably present, but not detected. The average deposit density ρ was measured as 3.3 ± 0.3 g/cm^3 using a cantilever frequency-shift method. The deposits were similar to Al ($Z = 13$, $\rho = 2.7$). The thicker arch cross-section was 1 μm, representing a mass-thickness of 330 μg/cm^2. All electrons followed a multiple-scattering regime with little absorption (as in Al up to 450 μg/cm^2 at 20 keV).[50]
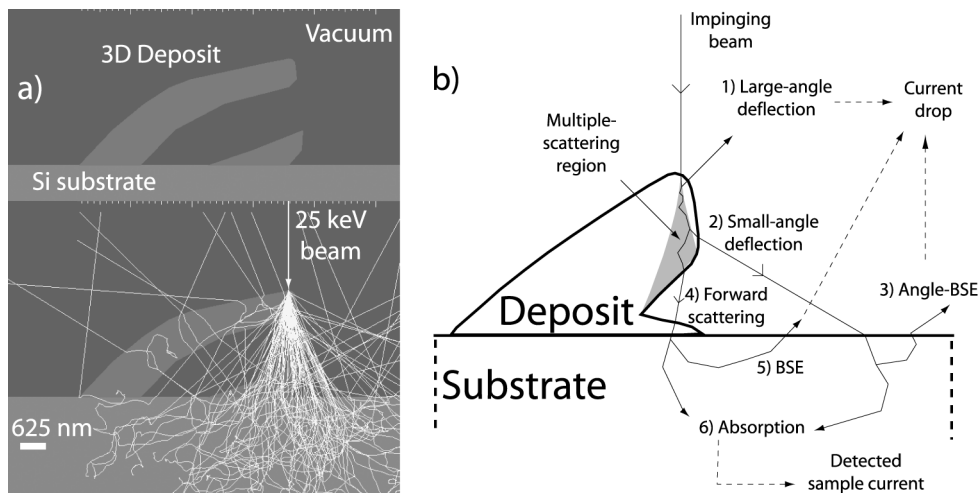
Figure 4-3-9. Electron propagation in 3D deposits. a) Monte-Carlo simulations show quantitative electron transmission through the primary arch. (model structure: planar, $Cu_1C_3O_1F_1$ with density 3.3 on Si, 25 keV). b) Schematic electron paths. The respective contributions of several electrons' trajectories to the measured current are highlighted.

Most electrons were "para-transmitted" through the primary arch (see fig. 4-3-9a).[56] SE were emitted with a cosine law distribution from the lower side of the primary arch, and were collected at the nearest interface.[44] The main contribution to current drop and SE emission came from the deflected electrons (see fig. 4-3-9b). The larger current drops and SE emission measured from the larger interaction volumes were due to more numerous collisions. The resulting incidence angles on the substrate were wider. This is similar to what was observed in the monitoring of tip deposits, where the current drop was larger on bigger tips (see §4-2-4A).

4-3-2-D) Deposited volume *vs*. time – "Efficiency effect"

The instantaneous volume growth rate reached a maximum. Instead of occurring at the cone-cylinder transition as on tips (see fig. 4-2-4), it occurred at primary arch division.
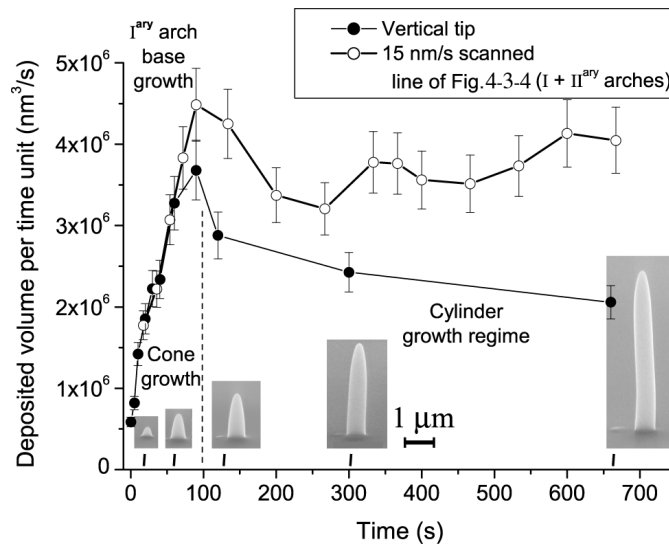
Figure 4-3-10. Maximum deposition efficiency at take-off. Volume deposited per time unit (nm³/s) *vs*. time, compared between 3D structures and tips (inset, SEM 73° tilted side-views; (hfac)CuVTMS, 25 keV, 500 pA on Si; 20, 60, 120, 300, and 660 s; scale bar 1 μm).

The primary electron "efficiency" depended on the geometry of the pre-existing deposit (see fig. 4-3-10). The growth rate decreased with increasing distance from the deposit edge to the substrate. The influence on the primary arch was twofold: firstly, the growth direction was inflected, secondly the arch became thinner and narrower along the scan. The distribution of the electrons transmitted through the primary arch also varied along the scan.

4-3-2-E) Analytical model

As shown in fig. 4-3-5, the secondary arch grew while the electron beam was still entirely intersected by the primary arch. The electrons transmitted through the primary arch deposited the bottom line and the secondary arch. The transmitted distribution through a thin film is Gaussian, with a standard deviation (in cm²) after the thickness t (in cm) given by:[16]

$$x_{rms} = 1.05 \times 10^5 \left(\frac{\rho}{A_{av}} \right)^{1/2} \frac{Z_{av}}{E_0} t^{3/2} \qquad \textbf{(4-3-1)}$$

E_0: beam energy (eV); ρ: density (g/cm³); A_{av} effective atomic weight (g/mol).

The primary arch was modelled as a thin film of homogeneous thickness (t) suspended at height (h) above the next interface (substrate or secondary arch), as shown in fig. 4-3-11.
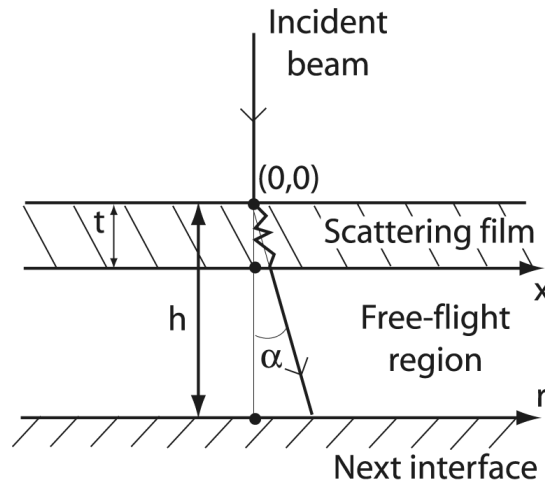
Figure 4-3-11. Transmitted electron distribution schematic model.

The transmitted electrons were projected onto the next interface. For simplicity, it was supposed that they had travelled straight from the incidence, so that x/t = r/h. After convolution by the Gaussian primary beam of standard deviation σ, the electron distribution on the substrate was:

$$N(r) = \frac{1}{2\pi(\sigma^2 + \frac{h^2 x_{rms}^2}{t^2})} \exp\left(-\frac{r^2}{2(\sigma^2 + \frac{h^2 x_{rms}^2}{t^2})}\right) \qquad \textbf{(4-3-2)}$$

After simplification the insertion of (4-3-1) into (4-3-2) gave:

$$N(r) = \frac{1}{2\pi(\sigma^2 + 2.8.10^{-5} h^2 t)} \exp\left(-\frac{r^2}{2(\sigma^2 + 2.8.10^{-5} h^2 t)}\right) \qquad \textbf{(4-3-3)}$$

(r, σ, h, and t in nm; the pre-factor includes the values for the deposit
from (hfac)CuVTMS, given in §4-3-2-C)

The resulting standard deviation of the projected distribution was a function of the product h^2t. The values of t and h *vs.* line length l, measured from the deposits in fig. 4-3-4, at the final beam positions given by the markers, are summarized in table 4-3-I (t, h, l in nm; all values $\pm$ 50 nm).

Deposit length l (nm)	1500	2000	3000	4000	5000	5500
Primary arch thickness t (nm)	825	800	760	685	560	490
I^{ary} arch height above II^{ary} arch h (nm)	1130	1420	1725	1790	1480	740

Table 4-3-I. Geometric parameters of the primary arch.

The arch thickness t decreased linearly with l. The height h first increased, reached a maximum and decreased again. The transmitted electron distributions were calculated.
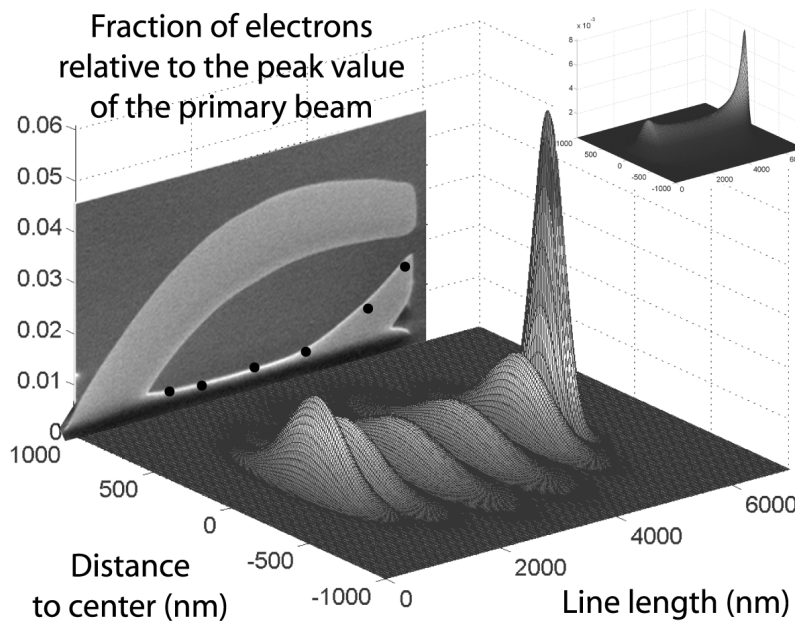
Figure 4-3-12. Calculated distributions of electrons incident on the secondary arch (at the positions marked by the dots). The Gaussian curves appear distorted because of the different scales. Inset, integrated profile.

From 1 to 3 μm, the distribution became flat and widened (see fig. 4-3-12). The primary arch grew higher so the projection was made from an increasing distance. This explained the slight decrease of the bottom-line thickness, and predicted the increasing thickness of the surrounding

deposit seen in fig. 4-3-7. After 3 µm the transmitted distribution narrowed and sharpened due to the growth direction of the primary arch, now parallel to the substrate, and to its decreasing thickness. At 5 µm, the distribution was the same as when the primary arch divided. As the bottom line thickened, the electron efficiency increased through scattering. The secondary arch growth thus started. The distance of the primary arch to the next interface also decreased. As a result, the calculated central intensity was then increased threefold between 5 and 5.5 µm.

This deliberately simple model was sufficient for explaining the formation of the secondary arch. More realistic geometries merely resulted in complex but similar expressions. The integrated point electron dose, as seen in the inset of fig. 4-3-12, showed a parallel evolution. The widths of the obtained distributions were probably overestimated, because the actual Z_{av} was smaller and the eq. (4-3-1) emphasised elastic scattering. Inelastic collisions lead to smaller angles, especially in lower-Z materials. The distribution is mainly controlled by the h^2t term anyway. The secondary arch arises because of the narrowing of the transmitted electron distribution that occurs as the primary arch advances. This result is an indirect consequence of the decrease in the deposited volume per time unit on the primary arch during deposition, combined with the constant electron flux.

4-3-2-F) Summary

A periodic growth regime was obtained by line-scanned FEB deposition. The period was tuned by changing the scan speed. The initiation sequence of periodicity was investigated. The periodicity was interpreted as the result of two main factors: a growth rate decrease when the deposition site gets away from the substrate, and a large electron range at 25 keV compared to the deposits sizes. The electron-induced secondary arch growth must be considered when designing 3D structures. The easy FEB-induced formation of periodic structures could be used in future micro-optical or micro-mechanical devices.

These results have been published in the *Journal of Vacuum Science and Technology*, under the title "Periodic structure formation by focused electron-beam-induced deposition".[57]

4-3-3 Electron scattering in model 3D structures

The evolution of the absorbed sample current on a series of model 3D structures (from (hfac)CuVTMS on Si at 25 keV) summarized the effects of electron scattering during deposition.

4-3-3-A) Thick wall

Instead of a low speed, single scan, a rapid multiple scan was used to deposit a thick wall (see fig. 4-3-13a). The monitored current was compared to that of a vertical tip (see fig. 4-3-13b).
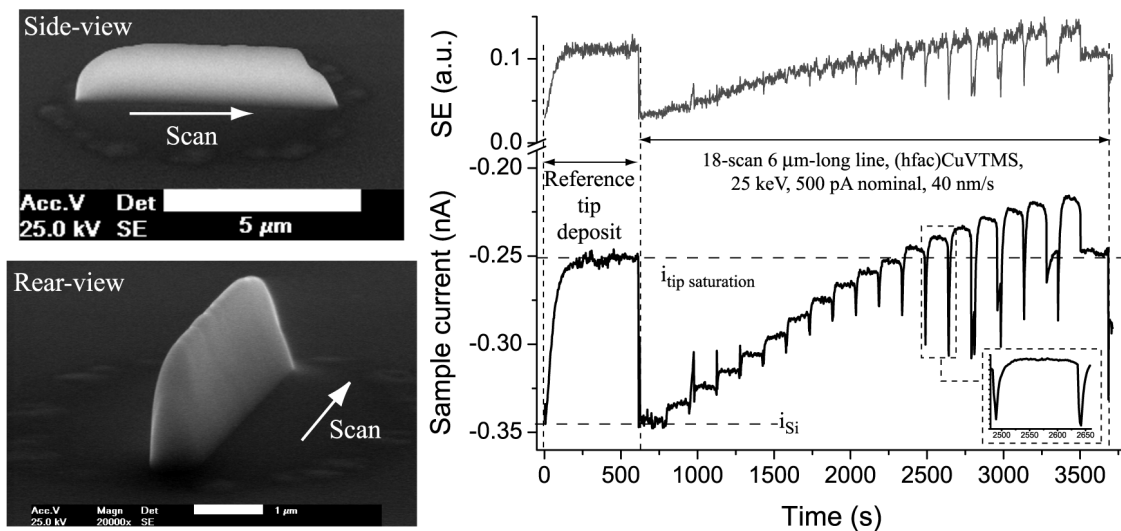
Figure 4-3-13. Thick wall obtained by multiple-scanning, and monitoring. Left, *ex-situ* SEM tilted views. Right, *in-situ* monitoring compared to a reference tip.

The sample current decreased at each new scan. It saturated at a lower value than that of a single tip, indicating a larger interaction volume. The reason is explained schematically in the following figure. In tips, all directions are similar, so laterally scattered electrons rapidly exit the tips (see fig. 4-3-14a). The electrons penetrate deeper in the wall, due to lateral (out-of-plane in the Monte-Carlo simulation) scattering in the deposit (see fig. 4-3-14b). The Monte-Carlo simulations confirm this physical explanation (observe the deeper range of the electrons in the wall as compared to the tip in the simulations of figs. 4-3-14a and b) and indicate a 5 % larger BSE yield from the wall. This value is similar to the measured difference of 30 pA out of 500 pA probe current.
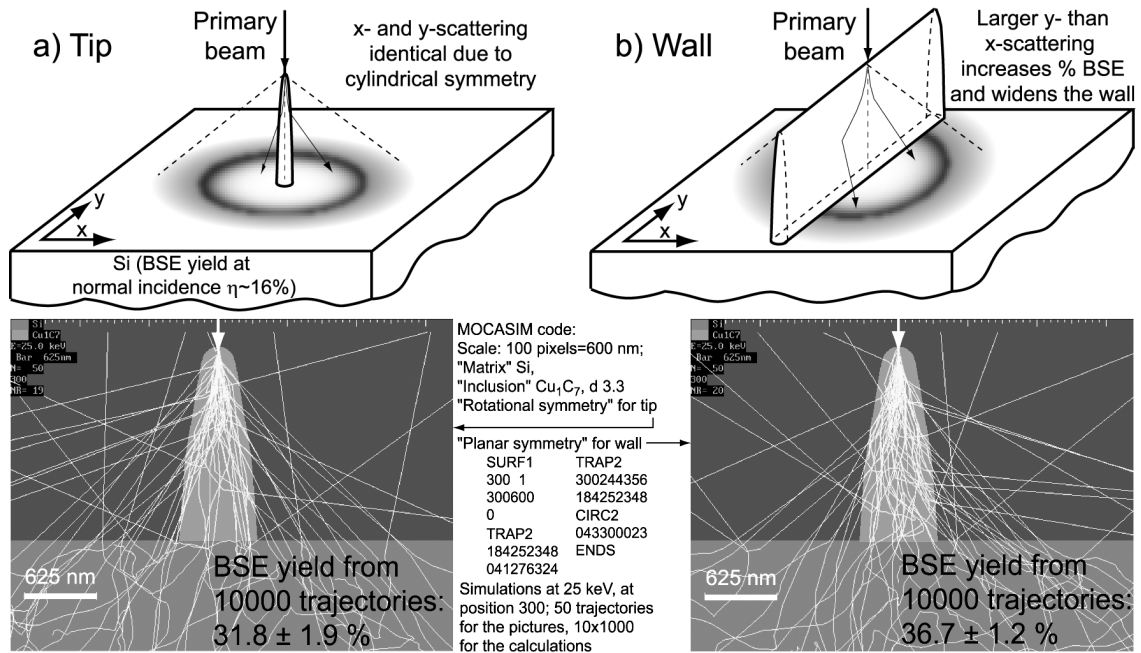
Figure 4-3-14. Comparison of electron propagations in tip and wall. a) Scattering from a tip, and Monte-Carlo simulation with 100 trajectories. b) Idem for a wall. The simulations show the projection of 3D electron trajectories on a cross-section of the protruding shapes.[58]

4-3-3-B) Tip deposits on suspended arch or rod

Tips were deposited by spotting the beam on the edge of high primary arches.
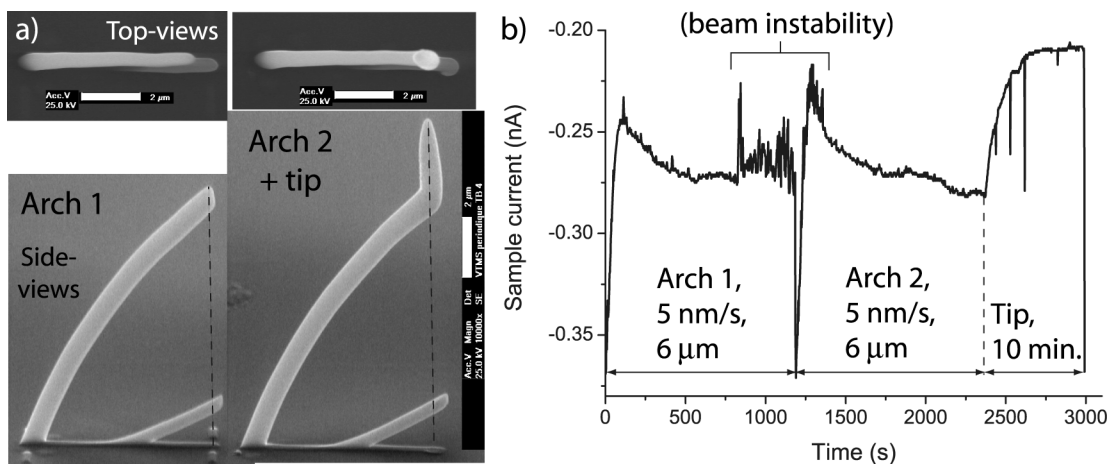
Figure 4-3-15. Tip on arch. a) *Ex-situ* SEM views (top+tilt) of the structures. The dotted lines of the final beam positions, deduced from the markers and tip angle, indicate a slightly non-normal beam incidence during deposition. b) *In-situ* sample current monitoring.

The primary arch could be deposited in a single slow scan (see fig. 4-3-15a). Tip monitoring (see fig. 4-3-15b) saturated more slowly than the current had decreased during the construction of the primary arch base. The tip deposited for 10 minutes was short but with a complete cone.

The primary arch could also be a horizontal rod deposited from a tip (see fig. 4-3-16a).
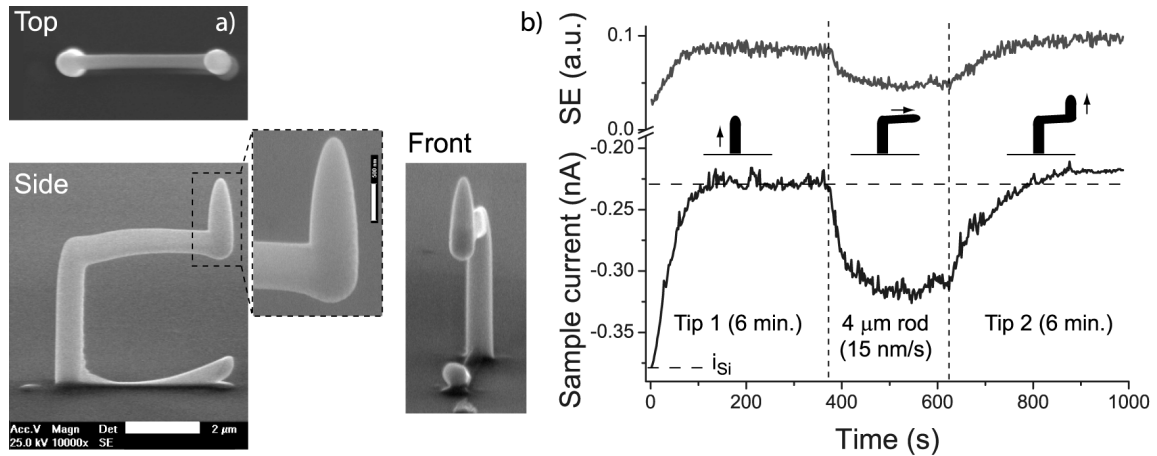
Figure 4-3-16. Tip on horizontal rod. Left, SEM views of the deposited structure. Right, writing sequence used and monitored signals.

The horizontal rod was narrower than the tip diameter, as seen from the top-view. Its thickness slowly decreased, letting a secondary arch grow. On the 3.6 μm high tip 1 deposited in 6 min the sample current saturated (see fig. 4-3-16b). Some deposition took place on the lower side of the rod under tip 2, but no tip appeared on the secondary arch. The transmitted electron distribution widened as the rod thickened with tip 2, so that the current density on the secondary arch quickly decreased. Tip 2 was only 2 μm high, even though the deposition time was the same as for tip 1. The monitored current saturated more slowly and at a slightly lower value than on tip 1 (see fig. 4-3-16b). The interaction volume was larger because the rod occupied part of the cone into which the electrons were forward scattered. For tip 2 the average growth rate was 5.6 nm/s. This was equal to the deposition rate measured on 7 μm-high vertical tips (see fig. 4-2-3), indicating that the distance to the substrate, not the tip height or shape, is the main parameter for the decreasing growth rate.

4-3-3-C) Rods and secondary arches

A series of deposits illustrated how rod height influences secondary arch growth.
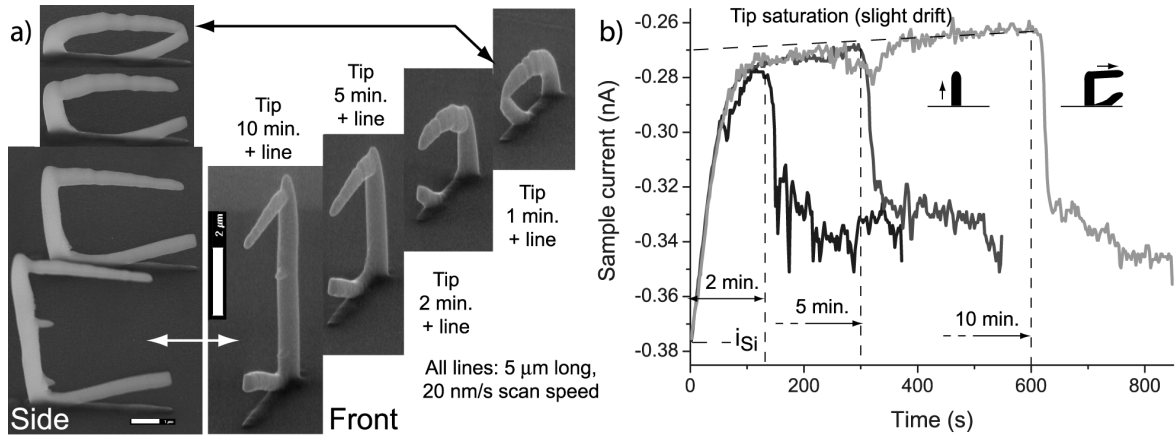
Figure 4-3-17. Rod on tip deposition and monitoring. a) *Ex-situ* SEM views of the resulting structure. b) *In-situ* monitored signals and writing sequence used.

Horizontal rods, initially 300 nm wide and 400 nm thick, grew thinner from higher tips (see fig. 4-3-17). Secondary arches appeared sooner. The thinner rods probably did not intersect the entire beam. The secondary arches may have formed partially under the direct incidence of a fraction of the primary beam. Monitoring indicated when the beam moved away from the tips. The monitored current remained lower on the rods than on the bulk sample (see fig. 4-3-17b).

4-3-3-D) Secondary arch initiation

Several causes were invoked to explain the secondary arch growth: the transmitted electrons, the growth rate reduction with the distance to the substrate, and the larger electron efficiency on protruding deposits. This last point was checked in a series of deposits. A 200 nm thick wall was deposited on the substrate before depositing the main structure (see fig. 4-3-18b). After deposition it was incorporated into the bottom line or the secondary arch (see fig. 4-3-18a). The monitored curves clearly witnessed the geometrical effects (see fig. 4-3-18c). The "efficiency effect" played a clear, but minor role in the formation of the secondary arch.
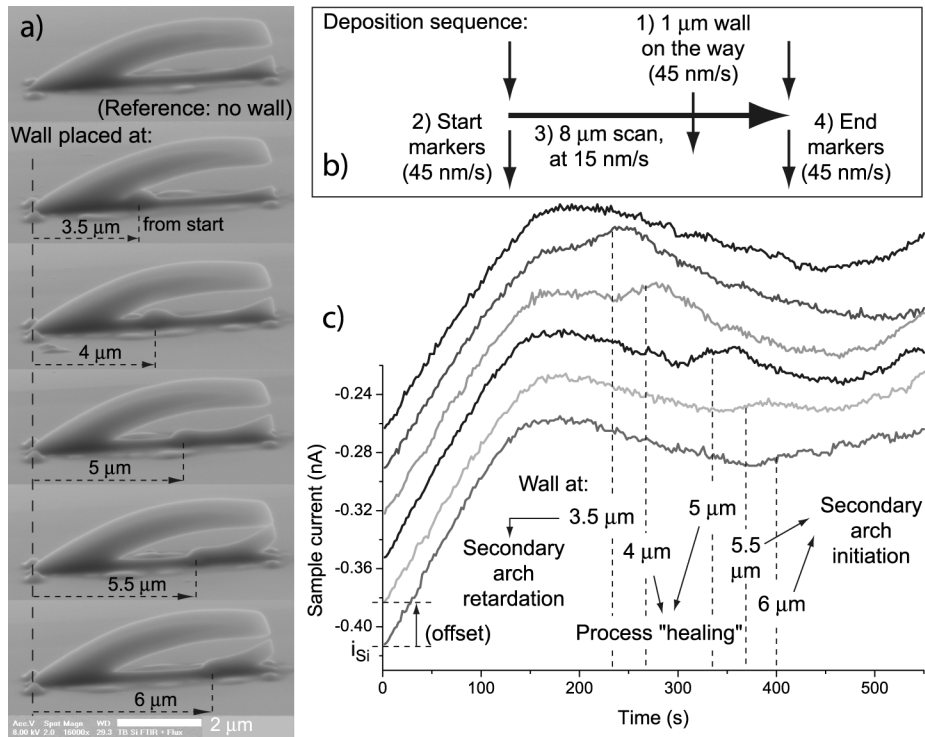
Figure 4-3-18. Secondary arch initiation by a pre-deposited thin wall. a) *Ex-situ* SEM tilted views of the deposits. b) Deposition sequence. c) *In-situ* monitoring (offset for clarity).

When the thick wall was deposited too close to the primary arch division, a higher arch resulted and the secondary arch was delayed (see fig. 4-3-18a). At 4 or 5 μm from start, it created a bump in the bottom line but the process returned to its natural evolution. At 5.5 μm from start the wall initiated the secondary arch growth, which was closer to the junction after the 8 μm scan length than in all the other structures. At 6 μm from start, the secondary arch was already developing, so the wall had a smaller effect.

4-3-3-E) "Stool base" and "Djenné Mosque"

Other simple model structures were realized by adding tips and/or straight scans. The rods grown horizontally (15 nm/s, 2.8 μm-long) to deposit a "stool base" were narrower than their supporting tips (7 min. 20 s), and slightly bent downwards (see fig. 4-3-19a). The monitoring was formally similar to that in figs. 4-3-16 and 4-3-17 (see fig. 4-3-19b).
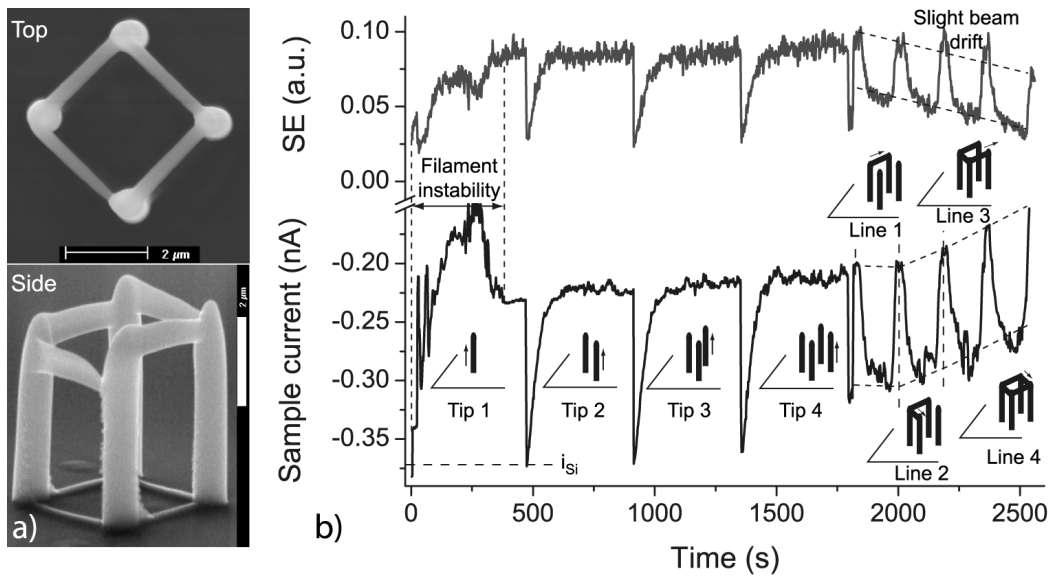
Figure 4-3-19. "Stool base". a) *Ex-situ* SEM views. b) Deposition sequence and *in-situ* monitoring.

A vertical wall could also be constructed of closely spaced tips. The following structure was named the "Djenné Mosque", after a famous earthen building in Mali (Africa):[59]
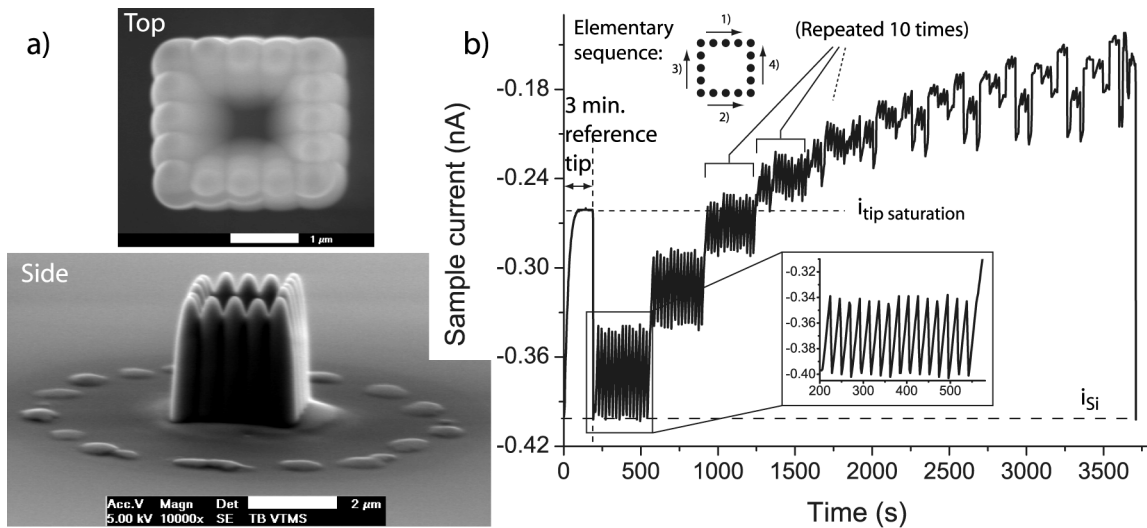
Figure 4-3-20. "Djenné Mosque". a) *Ex-situ* SEM views. b) Writing sequence and *in-situ* monitoring.

The top view revealed that the inside of the walls was thicker than the outside, with respect to the top of the walls (see fig. 4-3-20a). The electrons scattered from each wall exposed the opposite walls. No depth information was available at the centre of the structure in the SEM

picture, but it is highly probable that the "floor" level was above the substrate level, and was not flat. The "outwards" scattering deposited flakes on the nearby substrate. Monitoring indicated a larger interaction volume by saturating at a lower level than on a single tip (see fig. 4-3-20b). It also indicated that the 4 walls had different thicknesses (see the last sequences). This was probably due to different orientations with respect to the precursor flux.

4-3-3-F) "Nanoheart"

The primary beam can move in a curve. Monitoring indicated when successive scans overlapped previously deposited branches (see fig. 4-3-21b). Despite some filament fluctuations, two similar branches were successfully deposited to yield the structure in fig. 4-3-21a.
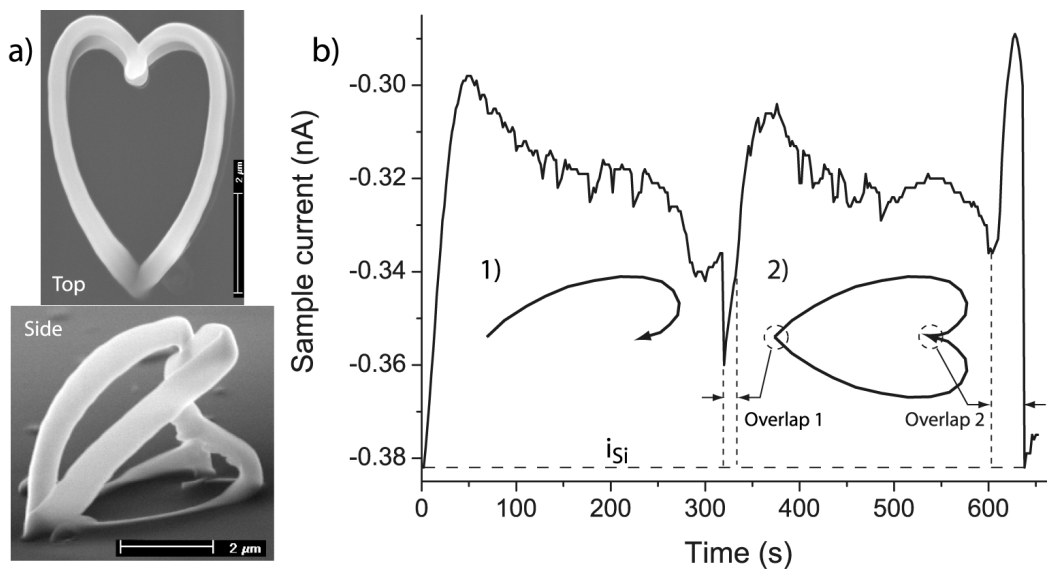
Figure 4-3-21. "Nanoheart". a) *Ex-situ* SEM views. b) Deposition sequence (24 nm/s) and *in-situ* monitoring.

Initially deposited on 2003 Valentine's Day, later it was realized that this "nanoheart" structure was useful for quick demonstration of 3D nanofabrication by FEB-induced deposition. It was subsequently included for pedagogical purposes on the EPFL web site.

4-3-4 Influence of beam scan direction on 3D structure growth

Molecules are brought to the reaction site by a gas-phase transport process, but the actual reactants are adsorbates. The role of surface diffusion is still unclear. I bring here a partial answer by showing that surface diffusion did not have an influence on the deposition of a series of structures when scanning the beam in other directions than towards the needle. Shadowing effects are evidenced and the molecular regime of the gas flow is discussed.

4-3-4-A) Principle of the study

Deposition was performed from the precursor (hfac)CuVTMS on Si, at 25 keV, following a "star-shaped" writing sequence, at three different scan speeds (see fig. 4-3-22a).
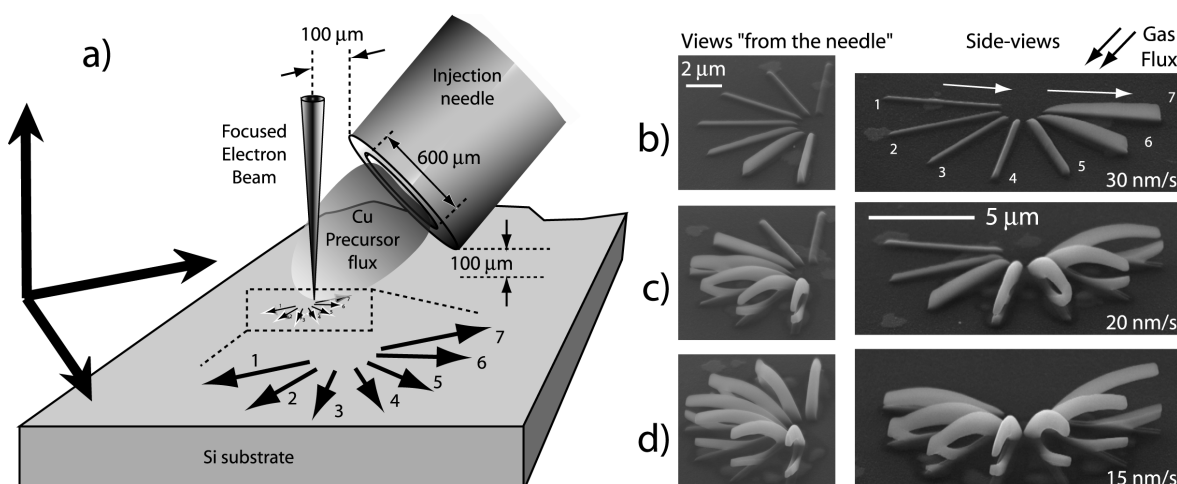
Figure 4-3-22. a) Schematic drawing of the writing sequence. b,c,d) *Ex-situ* SEM tilted views (70°) of the structures deposited at 30, 20, and 15 nm/s. Left, front-views. Right, side-views.

The deposits depended both on scan speed and scan direction (see fig. 4-3-22b,c,d). The writing order was chosen so that the already existing structures would not influence the growth of the following ones. At 30 nm/s only thick walls were deposited (see fig. 4-3-22b), but they were thicker when scanning towards the needle. At 20 nm/s the deposits towards the needle divided, but in the opposite direction thick walls were still obtained (see fig. 4-3-22c). At 15 nm/s all deposits divided, with angles depending on the scan direction (see fig. 4-3-22d). Secondary arches appeared on all divided deposits. Scanning towards constant directions, the effect of decreasing the speed was to grow arches with wider division angles (compare the deposits

named 3 to 5 between fig. 4-3-22b and d). The primary arch growth angles depended on the ratios of scan speed to the vertical growth rates. At constant speed but towards different directions, the arches grew lower when scanning away from the syringe. The line n°1 in fig. 4-3-22d had a slightly larger volume than line n°7 of fig. 4-3-22b. The growth rate varied twofold between these directions. Thus the system was not cylinder-symmetrical. A similar behaviour was qualitatively mentioned in FIB induced deposition.[60]

4-3-4-B) Electron scattering effects

The deposition rate was higher when the beam impinged on larger structures (as shown in figs. 4-2-4 and 4-3-10). To estimate the ratio of growth rates between the two extreme directions only the scan speeds that deposit similar volumes can be compared. The lower growth rates when scanning away from the beam appeared from a new series, where electron scattering effects were initially identical.
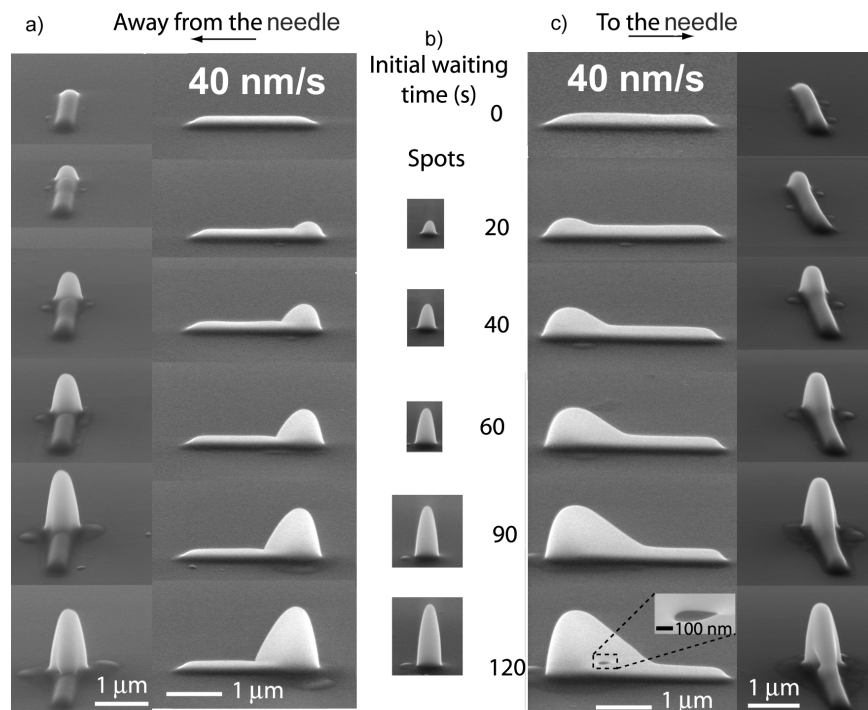
Figure 4-3-23. Lines deposited on pre-existing tips. *Ex-situ* SEM tilted views (75°). Outer columns: front-views. Intermediate columns: side-views. a) Line scan away from the needle, length 2.5 μm. b) Pre-existing tips. c) Line scan towards the needle, length 3 μm).

A spot was first deposited for a given time (0 to 120 s, see fig. 4-3-23b). Then the beam was scanned at constant speed either towards the needle, or away from it. The obtained structures covered the tip (see fig. 4-3-23a,c). Towards one scan direction, after a transitory phase, all lines ended as thick walls. The structures were not linear superpositions of a tip and the line deposited on the bare substrate because of the "efficiency effect". Less volume was deposited and the transitory phase was shorter when scanning the beam away from the needle. The growth rate was smaller when adding deposit overlays on a surface not oriented towards the precursor flux.

The monitoring clearly witnessed the varying interaction volumes:
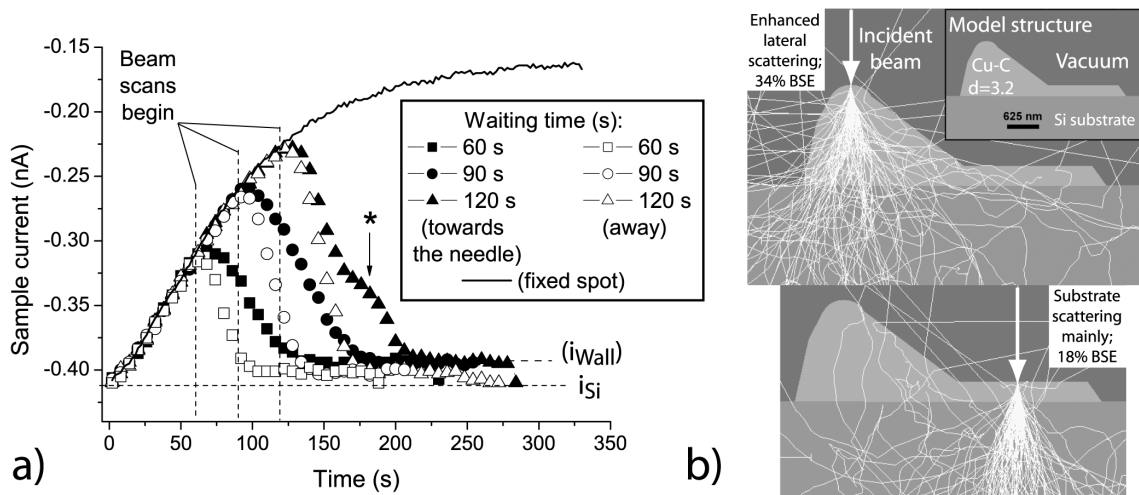
Figure 4-3-24. a) *In-situ* monitoring curves during deposition of the series in fig. 4-3-23. b) Monte-Carlo simulations on a model structure (planar symmetry) of the 90 s - tip deposit.

When the beam scan began, the current increased from a value reached on a partially completed tip cone, to the value on a thin wall (close to that of the bare substrate, see fig. 4-3-24a). The regain was slower when scanning towards the syringe than away from it, indicating that more volume was being deposited. On the 120 s tip + line deposit curve in fig. 4-3-24a, a shoulder (marked by a star) corresponded to the formation of the opening shown as inset in fig. 4-3-23c. Monte-Carlo simulations illustrated the enhanced backscattering on the larger volumes than on the thin walls (see fig. 4-3-24b).

In these conditions (40 nm/s, 400 nm diameter tips, 130 nm beam FWHM), without deposition of the line, the collected current in fig. 4-3-24a would have turned back to the value on the substrate in 7 s. The current curve slopes would have been 16.10^{-3} nA/s. In the transitory phase, the slopes of the signals were 4.10^{-3} nA/s when moving away from the syringe. In the opposite direction, they were $2,1.10^{-3}$ nA/s (see fig. 4-3-24a). The ratio between the slopes was 1.9. At each deposition stage, the beam spent twice as much time in the transitory phase when hitting the side of the tip exposed to the flux, than when hitting the unexposed side. This confirmed the twofold ratio of the growth rates between areas exposed to the flux and "shadowed" areas, measured from fig. 4-3-22. With still one-half the growth rate of the flux-exposed side, the shadowing of the unexposed areas was only partial.

4-3-4-C) Interpretation

The different growth rates were due to the different precursor coverage on differently oriented surfaces against the precursor flux. The flow was in the molecular regime (see fig. 4-3-25a). The number of particles hitting a surface decreases as the cosine of the surface normal with the flux direction. Some surfaces were shadowed. However, precursor molecules did reach them, from several sources, as shown schematically in figure 4-3-25b.
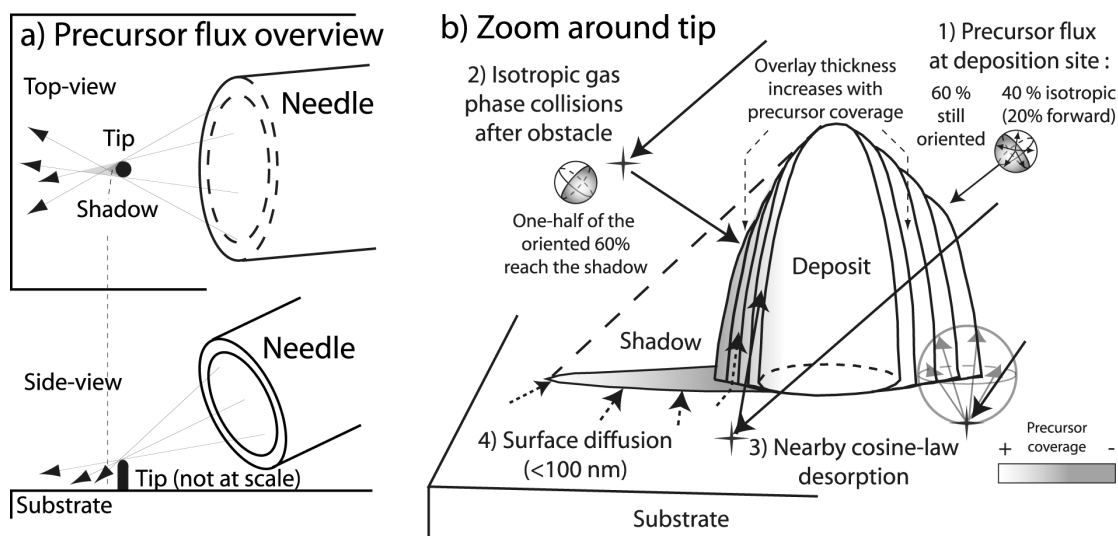
Figure 4-3-25. Schematic summary of the possible reasons for shadowed face coverage. a) Overview of the molecular precursor flux around tip. b) Detailed view around tip.

The precursor flow was in the molecular regime because at the needle exit the precursor flux was $1.4.10^{18}$ molecules/cm^2.s. According to the kinetic theory of gases, the local pressure was 2.10^{-2} mbar, i.e. 1/5 of the precursor vapor pressure of 0.1 mbar.[11, 61] The molecular mean-free path (MFP) was 1 mm. The Knudsen number, as the ratio of the MFP to the needle diameter, was above 1. Assuming a slow pressure drop due to effusion, the pressure 500 μm away from the needle (see fig. 4-3-22a) at the deposition site was 10^{-2} mbar. At equilibrium, the corresponding coverage was 10^5 molecules/μm^2 (i.e. 10% of a monolayer).[62] In molecular flow, the areas behind the deposited tips were shadowed (see fig. 4-3-25a). However, isotropic collisions occurred in the gas. The fraction of molecules traveling without encountering a collision decreased exponentially. The half-life was the MFP of 1 mm. After 500 μm, 40% of the molecules had collided and flew towards random directions (20% to the forward hemisphere, 20% backward), so 80% of the molecules still traveled "forward" (marked (1) in fig. 4-3-25b). The remaining 60% flew beyond the deposit plane, and eventually collided, so that half of them statistically flew towards the shadow (2 in fig. 4-3-25b). The coverage ratio between a surface perpendicular to the flux and a shadowed area thus did not exceed 80 to 30. Second, molecular desorption followed a cosine-law probability.[63] A molecule adsorbed on the substrate desorbed with up to 50% chance towards a vertical surface, depending on its distance (3, in fig. 4-3-25b). The relative substrate coverage around the deposit was 62 (60 x cos(45°) = 42 from the intersected flux + 20 due to isotropic collisions): half of it was 31. This concerned all vertical surfaces equally, so the maximum coverage ratio was then 111 to 61. This was very close to the twofold ratio measured above. Finally, surface diffusion locally homogenized the coverage (4, in fig. 4-3-25b). However, the total path length of an adsorbed organic molecule is 2 μm in random walk, so this effect is short-ranged (<100 nm distance).[64] It contributed to a lesser extent than the gas-phase phenomena. Its effect would probably appear with smaller probe sizes.

This physical approach gave a satisfactory order of magnitude (a precursor coverage ratio of 1.8 between exposed and shadowed areas). More accurate weighing of the contributions would require computational gas flow dynamics. Depositing at different pressures would also influence the coverage ratio by affecting the collision MFP and the isotropic part of the flux at the deposition site. Both these topics are proposed for future studies.

4-3-4-D) Practical consequences on complex structures

Complex shapes appeared from simple scans, as shown in fig. 4-3-26.
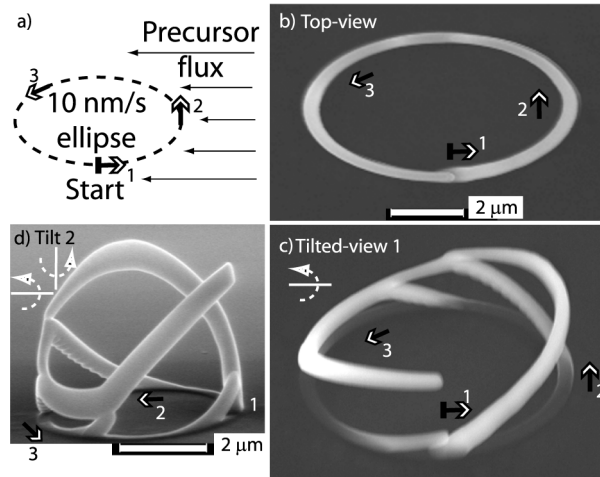
Figure 4-3-26. a) Simple writing sequence. b-d) *Ex-situ* SEM views of the resulting structure.

The expected elliptical corkscrew was not observed in the tilted views. A primary arch divided at arrow 1 but its growth rate decreased, reaching a maximum height at the closest distance to the needle (arrow 2 in fig. 4-3-26d). The growth direction then oriented towards the substrate and secondary arches appeared. As the growth rate increased again, the main arch grew straight (arrow 3). A very different structure was deposited by beginning the scan at another place:
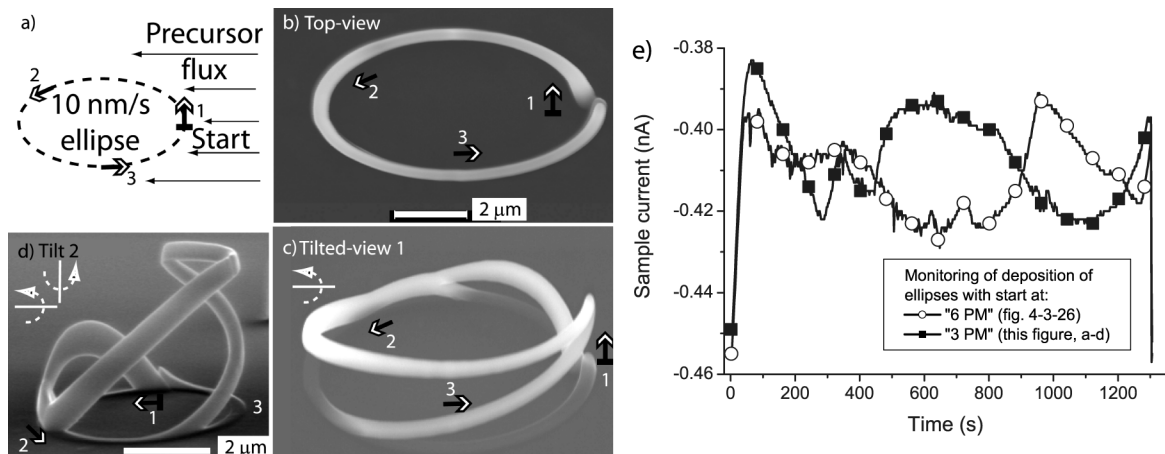
Figure 4-3-27. a-d) The deposit resulting from the elliptical scan depended on the start point. e) *In-situ* monitoring (squares), compared to that of the structure in fig. 4-3-26 (circles).

The same effects as in fig. 4-3-26 took place to build a complex structure (compare the heights at arrows 1 to 3 in fig. 4-3-27 with the corresponding positions in fig. 4-3-26). Monitoring (see fig. 4-3-27e) also clearly indicated that the structures were different. For the successful deposition of a corkscrew, the coverage effects were partially avoided by scanning more slowly (see fig. 4-3-28a).
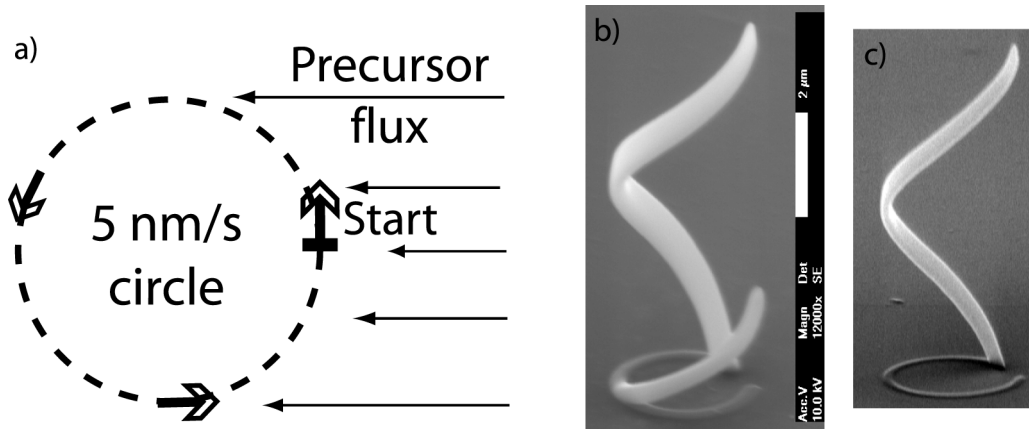
Figure 4-3-28. Successful corkscrew depositions at wider primary arch growth angles. a) Writing sequence. b) 500 pA probe current, c) 100 pA probe current avoids a secondary arch.

These vertical structures developed like bent tips. Hence, the primary beam always impinged at the top of a cone-like shape, which maintained a constant exposure to the flux. A secondary arch appeared at the point where the growth rate increased with the scan direction (see fig. 4-3-28b). By decreasing the probe current the growth of a secondary arch was avoided (although a bottom line was still deposited, see fig. 4-3-28c).

In order to avoid the flux effect and successfully deposit 3D structures, a closed-loop process may help avoid side effects by adapting the instantaneous scan speed to the depositing volume. This could be a useful implementation to the beam scan control software. A micrometric sample positioner with rotational degrees of freedom is another possibility.[65-67] A more symmetrical precursor supply could be another alternative solution.

These results have been published in the scientific journal *Microelectronic Engineering,* under the title "Influence of the beam scan direction during focused electron beam induced deposition of 3D nanostructures".[68]

4-3-5 Summary

When the electron range is larger than the structure sizes, it influences the shapes and sizes of the deposited three-dimensional structures. Secondary arches are formed and cross-deposition is induced between parts of a same structure. Monitoring the sample current summarized the electron scattering phenomena on these complex geometries. Several model structures were deposited and interpreted. The process lacked cylindrical symmetry because of the directionality of the precursor flow. The shape of the 3D structures was affected. By taking this effect into account desired shapes were successfully deposited. Solutions were proposed to overcome this limitation.

4-4 Conclusions

In Section 4-1 the propagation of electrons was shown to change when depositing structures larger than the electron range. The monitoring method was introduced in this simple case. The sample current was shown to evolve mainly in parallel to the BSE yield, with a small contribution from the emitted SE. The deposition rate dependence on deposition parameters was shown to follow Christy's model in the precursor-limited regime. Precursor depletion in 1 μs was observed. Two deposition behaviors were observed: a substrate-independent behavior, which could be due to a radical-assisted mechanism or to autocatalysis, and a substrate-dependent behavior, in which the deposition rate depends on the numbers of PE, BSE and SE.

When reducing the size of the structures below the electron range, tip deposition occurred, as shown in Section 4-2. The tip shape was due to electron scattering from a fixed beam. Systematic monitoring allowed developing a comprehensive model of electron propagation and tip deposition. Several effects observed in the experiments were interpreted. The sample current offered integrated information on the distribution of electronic trajectories in the growing micro- and nanostructures.

By moving the beam during deposition, 3D microstructures were deposited and described in Section 4-3. Their shapes were determined by electron scattering, which took place in the bulk of the structures but resulted in precursor fixation at surfaces. Precursor coverage on complex shapes was shown to influence the deposition rate. The scope and limitations of the deposition method because of scattering appeared through the study of a series of model structures.

A compromise must be found, when choosing parameters for the deposition of a structure, between the lower electron range at lower energy, and the increased forward penetration at higher energy. Sharp tips require high-energy (> 10 keV) electrons but deposition will take place in large areas around the tips due to forward-scattered or transmitted electrons. Secondary arches are avoided in 3D microstructures by using low currents of low energy electrons (< 5 keV) but the obtained shapes are rounded. The design of complex 3D microstructures may include several deposition steps at different electron energies.

Chapter 5 – Chemical analyses of focused electron beam induced deposits

On se persuade mieux, pour l'ordinaire,
par les raisons qu'on a soi-même trouvées,
que par celles qui sont venues dans l'esprit des autres

Pascal, Pensées, 10-737

The previous chapter dealt with the physical effects involved during FEB-induced deposition of structures, now the chemical outcome of the process is examined. If functional structures or applications are to be designed for 3D micro-deposits, then their precise composition must be known. The difficulty lies in the small volume of the deposits, which does not allow usual chemical analysis methods (such as X-ray diffraction analysis, Nuclear Magnetic Resonance Spectroscopy, Chromatography…). Micro-beam characterization methods are required. In Section 5-1 the deposits obtained from volatile organic compounds are described. All the microanalysis methods gave coherent and complementary results. The deposited material is $C_9H_2O_1$, in which the carbon is amorphous and 90% sp^2. The properties of this material (density, refractive index, chemical bonding) were investigated. In Section 5-2 the metal-containing deposits from organometallic precursors are studied. The metal content, which depended on the deposition conditions, could be improved by thermal treatments. Metal-containing carbonaceous mixtures were electrically conductive.

5-1 Deposits from purely organic precursors

5-1-1 Why study the deposition of carbon?

The study of carbon is an immense field of research.[1, 2] Depending on how the element is chemically bonded, it can be used as a hard coating with high chemical inertness and high thermal conductivity, as a wide-bandgap semiconductor, or as a solid lubricant. The study of the amorphous or nanocrystalline phases of carbon has attracted much attention.[3] The discovery of fullerenes and carbon nanotubes has opened the way to new materials and applications.

Most commercially available organometallic CVD precursors contain carbon, as do most of the resulting FEB deposits.[4] Depositing only C and analyzing the deposited material is useful for understanding the properties of the matrix around the metallic grains. It also opens the possibility of locally depositing diamond with the FEB.

Different precursors were screened to investigate the mechanism of deposition. An analysis procedure was defined. It showed that the composition and bonding of the deposits are independent of the precursor used: $C_9H_2O_1$ with 90% sp^2 carbon. The growth rates and deposit morphologies depend on the precursor used. This added knowledge sets the basis for successful future FEB induced deposition of diamond.
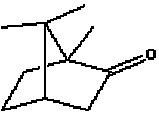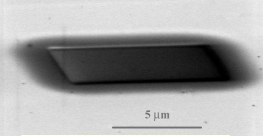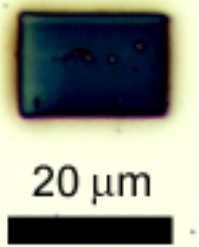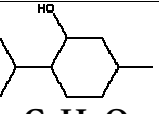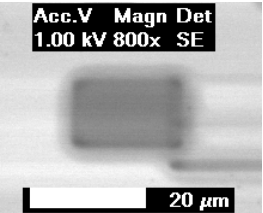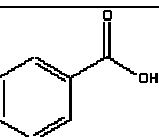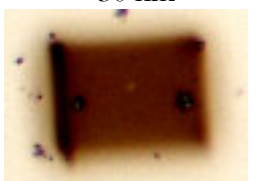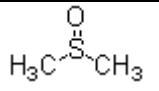
5-1-2 Precursor screening
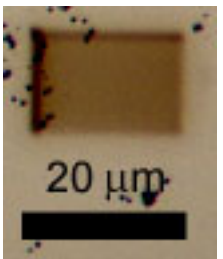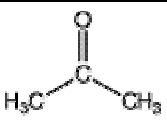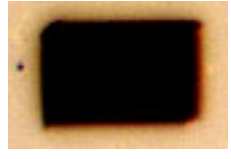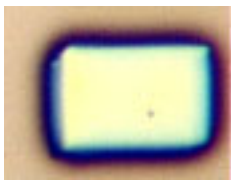
A few volatile organic compounds were previously tested and reported as carbon "precursors", such as styrene, methane, and resist developer solvents.[5-8] The same precursors were used for FIB-induced deposition.[9] A reaction mechanism was proposed based on the experimental observations, but apparently without considering the different adsorption behaviors of the used compounds.[10, 11]

The characterization of deposits requires a few cubic μm as the lower limit of the analysis volume. From the large selection of carbon-containing compounds available, pure compounds with the following properties were tested:

- High vapor pressure. This is the case for most common organic solvents. Volatile solid organic compounds also exist, such as menthol, camphor or naphthalene.

- Stable and easy to handle in normal conditions, non-toxic and commercially available at low cost. Solids and liquids were preferred over gases (such as CO_2 or CH_4…).

- A permanent dipole moment or a possibility of H-bonding. As stated in Christy's model, (see §2-1-2), the deposition rate is proportional to the residence time τ of the adsorbed molecules. Since τ increases exponentially with the adsorption energy,[12] increasing this energy by using molecules that give rise to strong Van der Waals interactions or H bonds should lead to higher growth rates.

- With as few other elements other than C as possible. Since C itself is not volatile, it must be combined with other elements like H, O, N, or F. The relative C content in the precursor was kept as high as possible. The effect of each of the other elements was studied as separately as possible.

- Lack of "condensable" elements else than C. Elements such as S, P, or Si lead to solid compounds at room temperatures.

The following table 5-1-I summarizes the series of tests on molecules selected according to these criteria. Moderate probe currents (5 to 10 nA) were used. No cryo-condensation of the precursor fluxes was used during these experiments.

Compound name	Chemical formula	Physical properties	Supply[a]	Irradiation conditions (all at 25 keV)	Resulting deposit (thickness + SEM and/or optical image, constant magnification)
Camphor	$C_{10}H_{16}O$	Solid (T_m=177°C; T_{eb}=207°C; P_{vap}(RT)= 1.8 mbar)	Int.	P=3.10^{-5} mbar, 5 nA, 1h10	90 nm
Menthol	$C_{10}H_{20}O$	Solid (T_m=122°C; T_{eb}=249°C; P_{vap}(122°C)= 1.3 mbar)	Int.	P=2.10^{-5} mbar, 3 nA, 25 min.	20 nm
Benzoic acid	$C_7H_6O_2$	Solid (T_m=122°C; T_{eb}=249°C; P_{vap}(122°C)= 1.3 mbar)	Int.	P=1.5.10^{-5} mbar 5 nA, 1h	<30 nm
DMSO	C_2H_6SO	Liquid (T_m=18°C; T_{eb}=189°C; P_{vap}(RT)= 0.6 mbar; μ=4.0 D)	Ext.	P=3.10^{-5} mbar 5 nA, 4h30	150 nm
Cyclo-hexane	C_6H_{12}	Liquid (T_m=6.5°C; T_{eb}=81°C; P_{vap}(RT)= 100 mbar)	Ext.	P=7.10^{-4} mbar 3 nA, 1h50	25 nm
Cyclo-hexanone	$C_6H_{10}O$	Liquid (T_m=-31°C; T_{eb}=155°C;	Ext.	P=10^{-4} mbar 5 nA, 1h30	<30 nm

		$P_{vap}(RT)=$ 6.6 mbar; $\mu=2.9$ D)			
Cyano-nonane	**$C_9H_{17}CN$**	Liquid	Ext.	$P=7.10^{-5}$ mbar 5 nA, 1h	<30 nm
Dichloro-methane	**CH_2Cl_2**	Liquid ($T_m=-95°C$; $T_{eb}=40°C$; $P_{vap}(RT)=$ 447 mbar ; $\mu=1.6$ D)	Ext.	$P=7.10^{-4}$ mbar 5 nA, 2h	90 nm
Acetone	**C_3H_6O**	Liquid ($T_m=-95°C$; $T_{eb}=56.5°C$; $P_{vap}(RT)=$ 526 mbar; $\mu=2.9$ D)	Ext.	$P=7.10^{-4}$ mbar 5 nA, 25 min.	40 nm
Methanol	**CH_3OH**	Liquid ($T_m=-98°C$; $T_{eb}=64.5°C$; $P_{vap}(RT)=$ 128 mbar; $\mu=1.7$ D)	Ext.	$P=7.10^{-4}$ mbar 5 nA, 2h40	90 nm
Aceto-nitrile	**CH_3CN**	Liquid ($T_m=-46°C$; $T_{eb}=81.6°C$; $P_{vap}(RT)=$ 96 mbar; $\mu=3.9$ D)	Ext.	$P=7.10^{-4}$ mbar 5 nA, 1h	80 nm
Nitro-methane	**CH_3NO_2**	Liquid ($T_m=-29°C$; $T_{eb}=100°C$; $P_{vap}(RT)=$ 37 mbar; $\mu=3.5$ D)	Ext.	$P=8.10^{-4}$ mbar 5 nA, 1 h.	80 nm
Formic acid	**HCOOH**	Liquid ($T_m=8.4°C$; $T_{eb}=101°C$; $P_{vap}(RT)=$	Ext.	$P=8.10^{-4}$ mbar 5 nA, 100 min.	80 nm

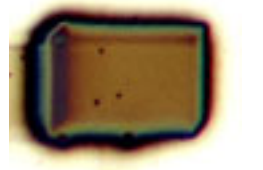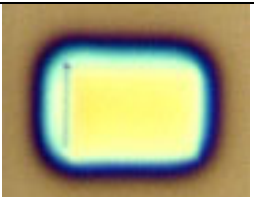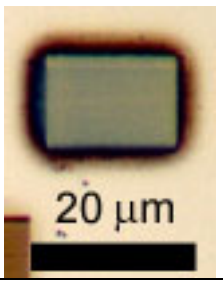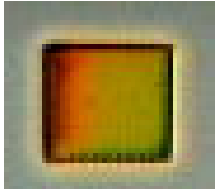|					
		46 mbar ; μ=1.4 D)			
Acetic acid	**CH₃COOH**	Liquid (T_m=17°C; T_{eb}=118°C; P_{vap}(RT)= 15 mbar ; μ=1.7 D)	Ext.	P=8.10⁻⁴ mbar 5 nA, 2 h	100 nm
Acrylic acid	**CH₃CH₂-COOH**	Liquid (T_m=13°C; T_{eb}=141°C; P_{vap}(RT)= 3.8 mbar)	Ext.	P=4.10⁻⁵ mbar 5 nA, 50 min.	150 nm

Table 5-1-I. Precursor screening for deposition of Carbon. Physical properties from the CRC Handbook of Chemistry and Physics, 85th edition.

ᵃ(Int.: internal; Ext. : external)

In figure 5-1-1, a synthetic view of Table 5-1-I is proposed. As the "deposition yield", the volume of the deposits, divided by the deposition time and the probe current, was reported.
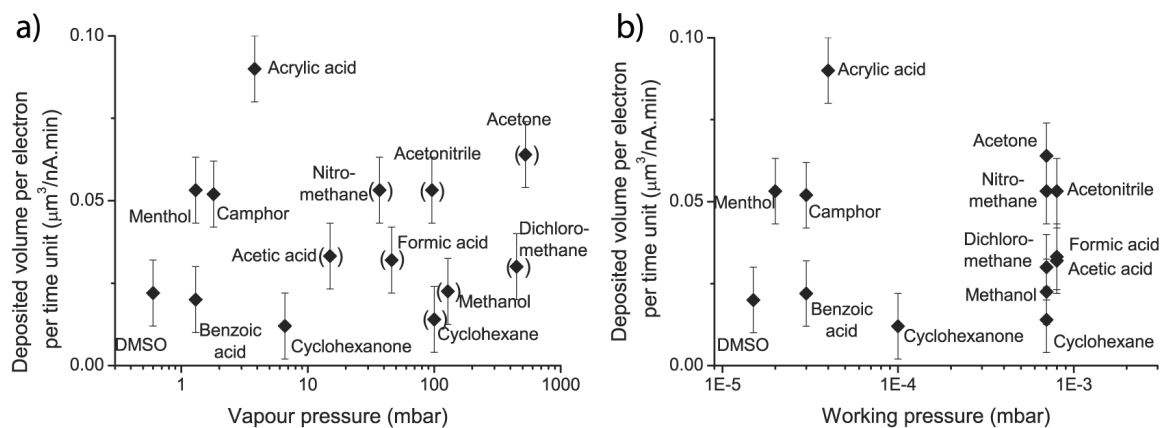
Figure 5-1-1. "Deposition yield" from the data in Table 5-1-I. *vs.* a) precursor vapour pressure, b) Working pressure during deposition. The points around parentheses in (a) indicate precursors for which the leak valve was opened only partially, thus not using as high precursor fluxes as possible.

The more volatile precursors led to higher working pressures, but not to higher growth rates because in most cases the pressure was limited to 7.10^{-4} mbar (see fig. 5-1-1a). If the fluxes and the working pressures were similar, then a difference in growth rate arose between polar and non-polar compounds (compare, for instance, the results from cyclohexane, dichloromethane and acetonitrile in fig. 5-1-1b). The cryo-condensation system shown in fig. 3-1-4 was built to allow using the precursor with the higher vapour pressures.

5-1-3 Chemical micro-analysis of the deposits

Did the different precursors lead to the same material? Was it possible to compare only the growth rates? In order to answer these questions, the deposits from the carboxylic acids were chemically characterized. Styrene was used for comparison. The chemical micro-analysis required deposit volumes of $\sim 100 \ \mu m^3$ (see fig. 5-1-2a,b,c). Large probe currents and long exposure times were chosen. Sharp tips were also deposited (see fig. 5-1-2d) but not analyzed.
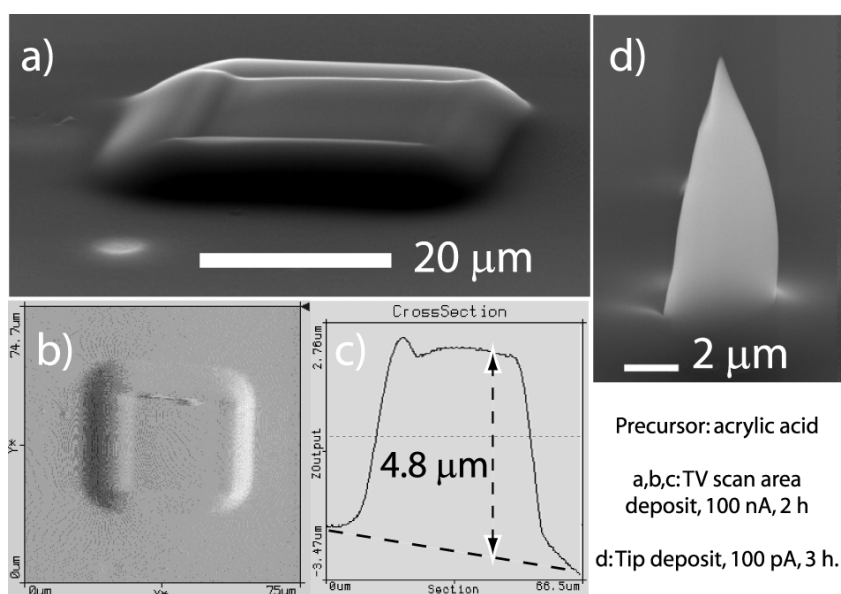
Figure 5-1-2. Examples of C deposits from acrylic acid. a) Thick deposit for micro-analysis. *Ex-situ* SEM tilted view (25 keV, 72°). b) AFM picture (derivative of the height signal, arbitrary units). c) AFM line profile. d) Tip deposit, SEM tilted view (25 keV, 72°).

During deposition of these structures, the monitoring indicated how the growth took place:
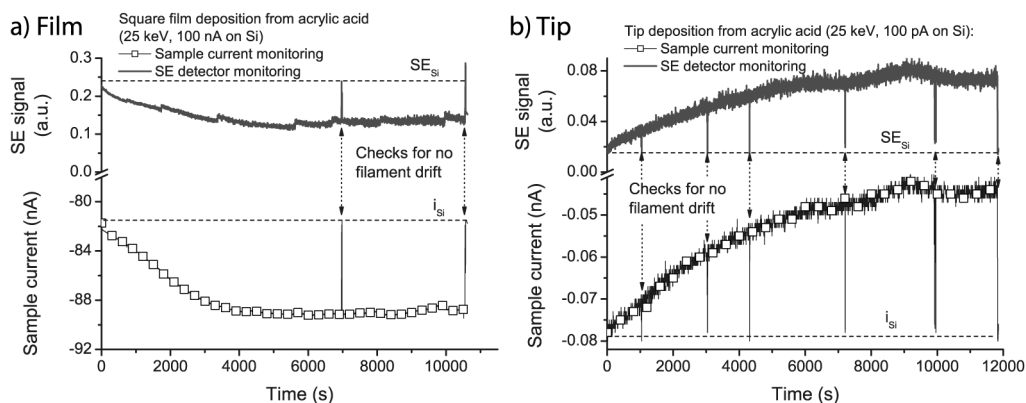
Figure 5-1-3. *In-situ* monitoring of the structures in fig. 5-1-2. a) Thick square deposited at 25 keV, 100 nA. b) Tip deposited at 100 pA, with regular checks for the filament stability.

The collected sample current increased during film deposition (compare figs. 5-1-3a and 4-1-4). During tip growth, the current slowly decreased and saturated (compare figs. 5-1-3b and 4-2-5). The ratio between the apex curvature radius and the cylinder diameter was much larger than in tips from organometallic compounds (described in Section 4-2). The electron penetration is larger in carbonaceous materials as compared to metals or metal-containing composites.[13] The inner tip structure may also contribute to the outer shape (see below, §5-1-3G).

The results of large-area deposition from 5 precursors are compared in table 5-1-II.

Precursor	Molecular formula	Flux (molecules/ cm^2.s)	Working pressure (mbar)	Deposit thickness, TV scan 400 μm^2, 100 nA, 2h	Deposit surface aspect
Styrene	$CH_2=CHC_6H_5$	$3.1 \cdot 10^{19}$	$7 \cdot 10^{-6}$ (a) $4 \cdot 10^{-5}$ (b)	900 nm	Smooth
Acrylic acid	$CH_2=CH-COOH$	$3.5 \cdot 10^{19}$	$8 \cdot 10^{-6}$ (a) $5 \cdot 10^{-5}$ (b)	4.8 μm	Smooth (see fig. 5-1-2)
Propionic acid	CH_3CH_2-COOH	$7 \cdot 10^{18}$	$4 \cdot 10^{-6}$ (a)	800 nm	Rough
Acetic acid	CH_3-COOH	$2 \cdot 10^{20}$	$5 \cdot 10^{-5}$ (a)	(c)	Smooth
Formic acid	$H-COOH$	$6.1 \cdot 10^{20}$	$8 \cdot 10^{-5}$ (a)	(d)	Smooth (e)

Table 5-1-II. Working conditions and deposition output from five carbon precursors
(a) Chamber pressure during effusion using liquid N_2 condensation system.
(b) Working pressure without condensation.
(c) High dose unnecessary: 60 μm^3 spots are obtained in 1 h at 5 nA.
(d) High dose unnecessary: 750 μm^3 spots are obtained in 1 h at 5 nA.
(e) Signs of a non-dense inner structure appear in SEM/TEM, see §5-1-3G.

Although styrene and acrylic acid lead to comparable effusion fluxes, the deposition rate was five times higher when using acrylic acid (see table 5-1-II). Although the flux from propionic acid was smaller than the flux from styrene, the deposit obtained was equally as thick. By reducing the length of the C chain to a methyl group (acetic acid) or to a single H atom (formic acid), the fluxes increased along with the deposition rates.

To analyse the obtained micro-deposits, only micro-characterization techniques could be used. The analyses involved 2 purely elemental particle-microprobe techniques (EDX and ERDA/RBS) and 3 optical micro-spectroscopy techniques (FTIR, Raman, and reflectometry).

5-1-3-A) EDX microanalysis

The volume required for EDX microanalysis is typically $1 \ \mu m^3$. I chose 3keV analysis energy to excite the K peaks of Si, C, N and O. The absence of a Si signal showed that the substrate was below the information depth.
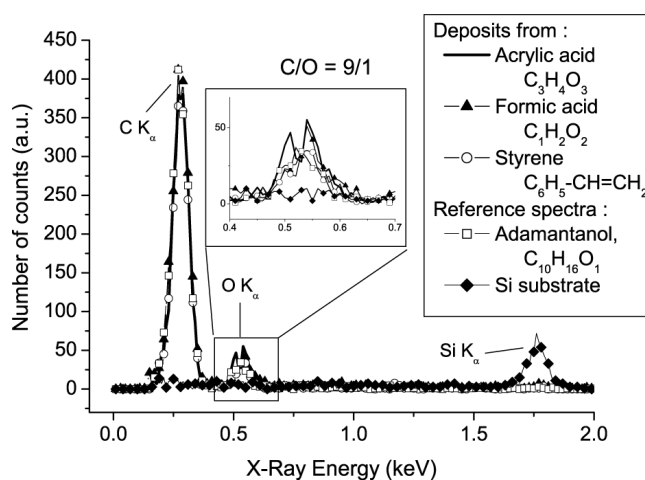
Figure 5-1-4. The C/O ratio is independant on the precursor used. *Ex-situ* EDX spectra (energy 3 keV) of deposits from three precursors (normalization at C K_α peak). The spectra of the bare substrate and of the solid compound adamantanol are included as references.

The substrate reference spectrum showed almost no O (native oxide only), so all the oxygen detected was in the deposit (see fig. 5-1-4). High atomic C/O ratios of 9 to 1 ($\pm$ 10%) were detected in deposits from formic acid, acrylic acid and styrene. The spectrum of the solid compound adamantanol ($C_{10}H_{16}O$, CAS n° [768-98-6], Sigma-Aldrich), used as a reference,

confirmed the quantification. Among the precursors, formic acid had a C/O ratio of 1 to 2, acrylic acid 3 to 2, but styrene had no O at all. A possible mechanism involved, during or after precursor fixation, a quantitative electron-induced O desorption.[14] Losing O by desorbing only CO or CO_2 was less probable since no deposit would have been obtained from HCOOH. Conversely, the deposit from styrene also contained O. Oxygen incorporation occurred, up to 10% of the atomic content, either from the residual background gas during deposition or after breaking the vacuum. This was similar to what was observed when irradiating solid films of organic compounds in the electron microscope.[15, 16]

5-1-3-B) Micro-FTIR analysis

Fourier Transform Infra-red Micro-Spectroscopy (μ-FTIR) gives access to the H content, which is not measurable by EDX. Several chemical bonds, such as C-H or C=O, can be used as IR chromophores since they present intense absorption peaks separate from the absorption of most other functional groups.[17] Crystalline graphite has two weak absorption bands at 1588 and 868 cm^{-1}.[18] Crystalline diamond has no IR-active vibration for symmetry reasons, but some absorption can be due to defects (type I, type II) or impurities.[19-21] Hydrogenated diamond-like carbon phases present a variety of absorption bands.[22-26] IR micro-spectroscopy can be performed on volumes as small as a few μm^3.

The spectra of liquid HCOOH and of the deposit obtained from it are compared in the next figure. In the deposit, several bands disappeared with respect to the liquid formic acid (the huge O-H band and the C-O single bond vibrations), and a new band appeared at 1620 cm^{-1}, indicating C=C double bonds (see fig. 5-1-5). The Si-O peak was due to Si oxide, appearing here because this transmission spectrum was taken across the whole substrate. The C-H band was still present, indicating the presence of H in the deposit. The strong carbonyl band also remained, although shifted (1720 to 1710 cm^{-1}, from a dimerized carboxylic acid to a ketone peak position). This spectrum showed that most of the O present in the deposit was bonded to C by double bonds.
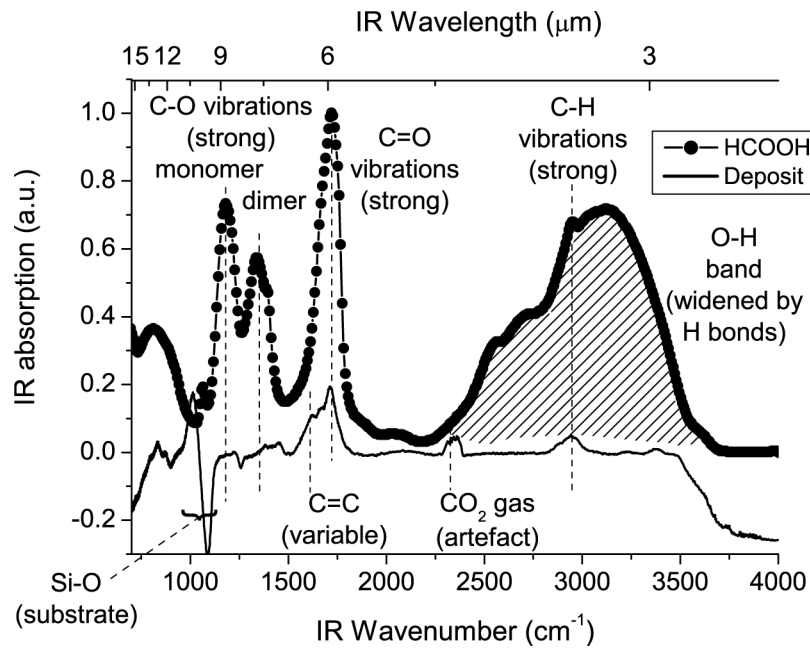
Figure 5-1-5. μ-FTIR absorption spectra of formic acid and of its resulting FEB deposit. Band extinction coefficients shown as strong or variable. Two scales (top: IR wavelength in μm; bottom: IR wavenumber in cm⁻¹).

The very similar spectra of deposits obtained from three precursors were compared in fig. 5-1-6, with a detailed view of the C-H and C=O bands. The spectrum from acetic acid (not shown) was strictly identical to that from acrylic acid, in the 1400-3400 cm⁻¹ region.
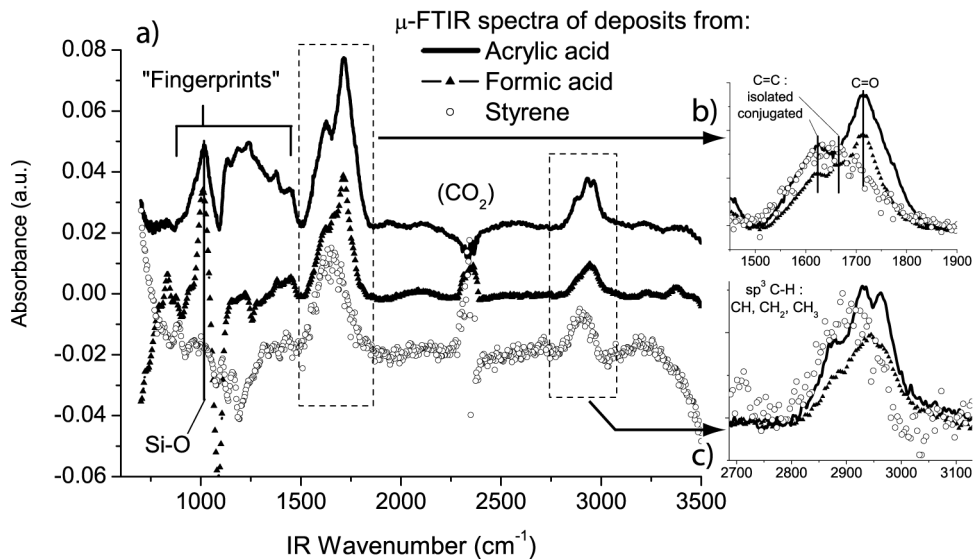
Figure 5-1-6. a) Comparison of μ-FTIR absorption spectra of deposits from three precursors (baseline offset for clarity). b,c) Two characteristic bands magnified (see text).

The spectra had two main features. First, the C-H vibrations band was present from 2800 to 3000 cm^{-1} (see fig. 5-1-6c). This band was typical of amorphous hydrogenated carbon. It indicated that the H present in the deposits was mainly bonded to sp^3 C atoms, less to olefinic sp^2 C atoms, and negligibly to aromatic sp^2 C (which absorb only above 3000 cm^{-1}).[27] The second band, from 1500 to 1800 cm^{-1}, resulted from overlapping C=O (1713 cm^{-1}) and C=C (conjugated, 1660; isolated, 1625 cm^{-1}) vibrations (see fig 5-1-6b). The C=O peak was larger for the carboxylic acids deposits than for styrene, indicating a slightly larger oxygen content. The styrene spectrum was noisier because this precursor led to smaller growth rates than the two others, so the sampled volume was smaller. No C-O peaks were visible. A small band at 3400 cm^{-1}, in the deposit from formic acid, corresponded to the absorption from O-H bonds. As ketones are subject to a rapid equilibrium between a keto and enol form, this did not indicate a quantitative content of alcohol groups in the deposits, so it was not considered here. Difficulties in background correction for this spectral range may also lead to over-interpretation.

The spectra in fig. 5-1-6 allowed for an estimation of the H content in the deposits, using the C/O ratio determined by EDX. Relative IR extinction coefficients of the C-H and C=O vibrators were obtained from the (tabulated[28]) spectra of simpler compounds containing aliphatic C-H bonds, ketone and alkene groups (see fig. 5-1-7).
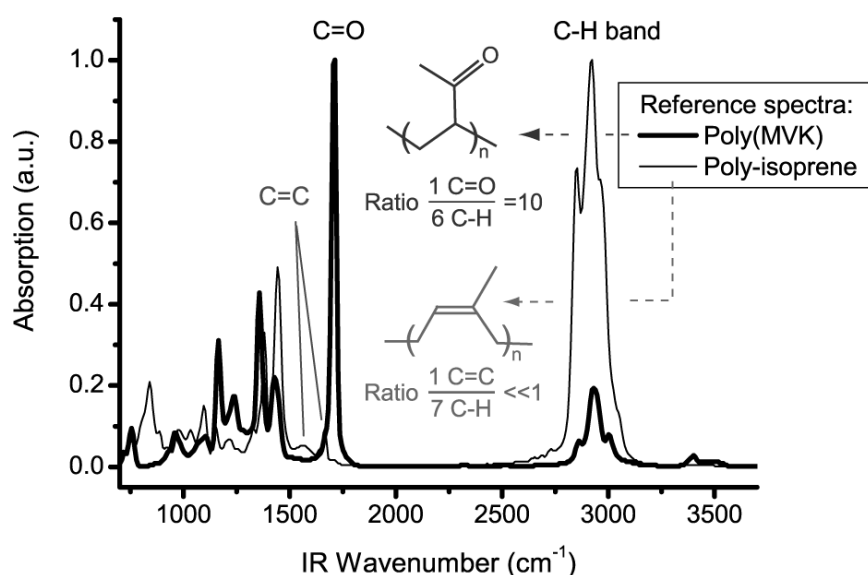
Figure 5-1-7. FTIR spectra of solid reference compounds, used to evaluate the ratio of sensitivity to the C-H, C=O and C=C chromophores. MVK: methyl-vinyl-ketone.

Although, in principle, IR extinction coefficients differ from one compound to another, in the spectra of liquids like *tert*-butyl-methyl-ketone (pinacolone), 3-hexanone, and butanone, the intensity ratio of one C=O vibrator to one C-H vibrator equals 6 (by treating the C-H band as a whole, for simplicity). In the spectra of solid polymers like poly(methyl vinyl ketone) (MVK, see fig. 5-1-7) this ratio equals 10. By deconvoluting the C=O peaks in fig. 5-1-6 with Lorentzians, the intensity ratios of the C=O peak / C-H band were found as 4.3, 4.8 and 2.8 for the deposits from acrylic acid, formic acid and styrene, respectively. The ratio of the numbers of C-H and C=O vibrators in the deposits was thus between 1 and 2, based on the sensitivity ratio obtained on the reference compounds. The H content was at least equal to, and at most twice the oxygen content. Combining these measurements with the EDXS results while considering the precision limits of both techniques, it was concluded that all these deposits have compositions close to $C_9H_2O_1$. The fact that the precursors styrene and acrylic acid had a lower H/C ratio (1/1) than formic acid (2/1) had practically no effect on the H content in the deposits.

In the spectrum of solid poly-isoprene, which contains C-H and C=C vibrators, the absorption by the C-H bonds dominates because the C=C vibrators have much smaller extinction coefficients (see fig. 5-1-7). The relatively intense C=C peak in the spectra of the deposits showed that much of the carbon-carbon bonding consisted of sp^2 bonds, conjugated with olefinic or aromatic units.[29] According to the C-H band position, H-bearing sp^3 C atoms were present. Random network theory indicated that the 15% H and 10% O fractions allowed for only 5 to 10% C sp^3 compared to sp^2, which meant that most sp^3 C were bonded to H atoms.[30] A more precise average deposit composition could be synthetically written as $C(sp^2)_7(C(sp^3)H_2)(C=O)$.

These results agreed with former studies of the effects of electron irradiation. The FTIR spectra obtained from several polymers, irradiated at doses above 0.5 C/cm² (at 70 keV), gave similar results (see fig. 5-1-8a).[31, 32] The electron dose used to obtain the deposits as in fig. 5-1-2 was 80 C/cm². The FTIR spectra of irradiated polymers shown in fig. 5-1-8a have the same structures as those of the deposits (compare fig. 5-1-8a with fig, 5-1-6a), with broad C-H, C=O and C=C bands, a weaker O-H band, and a loss of structure, in comparison to the sharp peaks which correspond to well-defined vibrations. As the polymers were cross-linked, irradiation also removed part of the volatile elements (see fig. 5-1-8b).

a) FTIR of irradiated polystyrene foil (thickness 9.5 μm, 70 keV electrons)

b) Mass loss and compositional changes during irradiation of gelatin
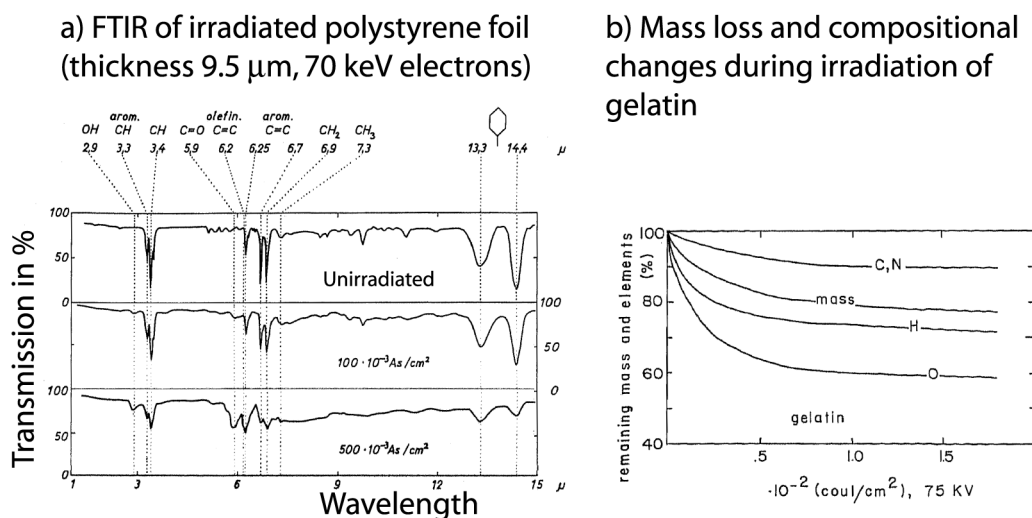
Figure 5-1-8. Former studies of electron irradiation effects on polymers. a) FTIR spectra of irradiated polystyrene.[31] Notice the inverted abscissa scale as compared to the spectra in fig. 5-1-6. b) Irradiation of a long-chain protein, gelatin.[32]

5-1-3-C) Micro-ERDA analysis

Elastic Recoil Detection Analysis (ERDA) and Rutherford Backscattering (RBS) are complementary analysis methods performed with energetic ion beams (typically, H^+ or He^{2+} in the MeV range).[33, 34] ERDA allows for a quantification of the H content. Small areas can be analysed by electromagnetically focusing the ion probe on a 3 μm spot.[35] These non-standard analyses were made at the Centre d'Analyse par Faisceau Ionique, Le Locle, NE. The analysis confirmed the C, H and O content in (120 μm side) square film deposits from acrylic acid.

Individual elements were mapped by these techniques, as shown in the next figure:

H (μ-ERDA)   **Si (μ-RBS)**   **O (μ-RBS)**   **C (μ-RBS)**
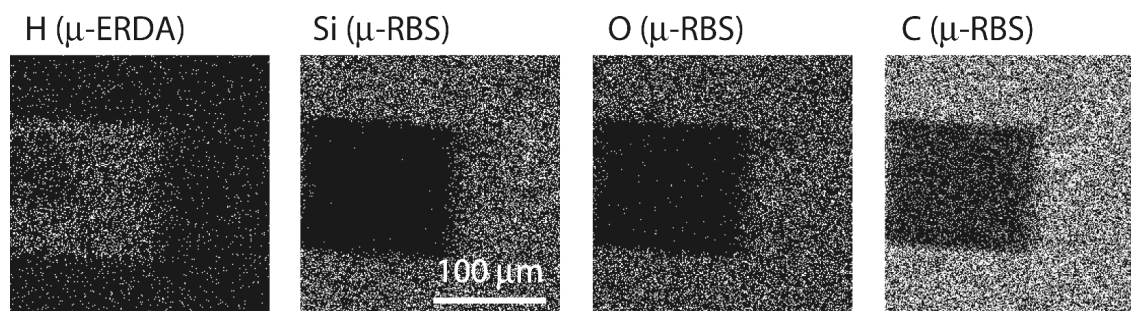
Figure 5-1-9. Element maps by 1.9 MeV He^+ microbeam analysis of a square film deposit from acrylic acid (25 keV on Si, 100 nA, magn. 1 kx, 41 min., thickness 650 nm).

The positive contrast on the H-map confirmed the presence of H in the deposit (see fig. 5-1-9). The Si, C, and O-maps confirmed the presence of more C than O in the deposits. In RBS maps, the signals represented the numbers of ions detected in selected energy ranges. Backscattered ions could have the same energy after hitting either the considered element in a surface layer, or a heavier atom deeper in the film. A Si signal thus appeared as a background around the deposit. The absence of a signal from the film area in the Si map showed that the film was thick enough to avoid ion transmission. If a signal was measured, as was the case on the O and C maps, it was due to backscattering by an atom of the film. The low signal to noise ratios (SNRs) were due to the low ion beam currents and short exposure times used in order to avoid beam damage.

The relative contents were quantified by fitting the experimental energy spectra with reference curves and cross-sections (RBS and ERDA were recorded simultaneously):
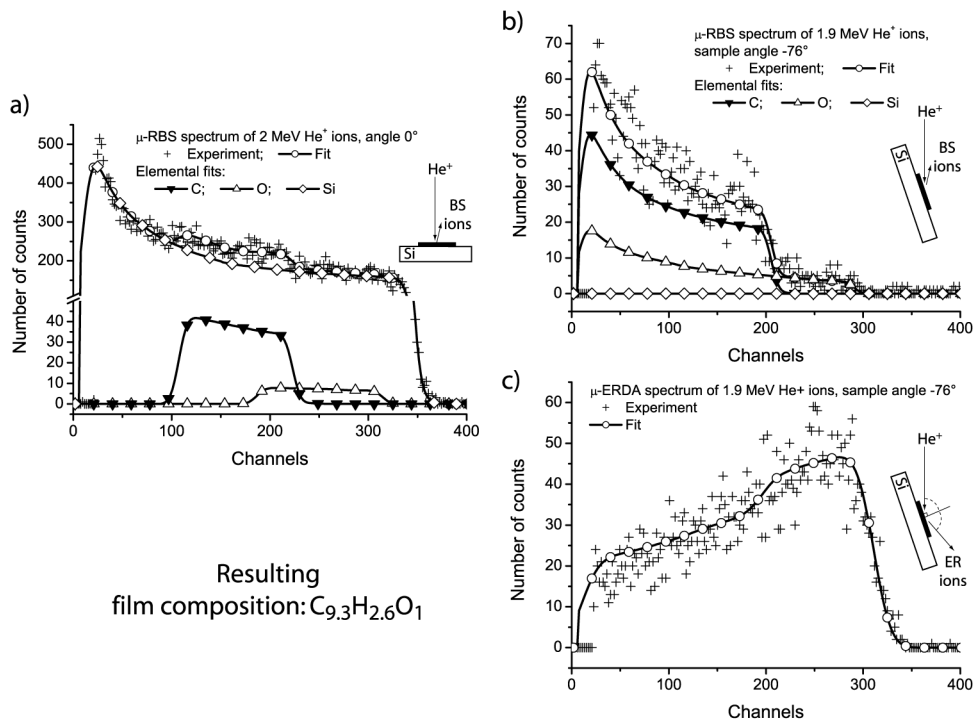
Figure 5-1-10. μ-RBS and μ-ERDA results. a) RBS spectrum at normal incidence gives the C/O ratio. b) and c) The simultaneously acquired spectra of Rutherford Back-Scattered (BS) and Elastic Recoil (ER) ions confirm the C/O ratio and give the H content.

The average composition $C_{9.3}H_{2.6}O_1$ was found. Including the large uncertainties due to the low SNRs, it may rather be written $C_{7-11}H_{2-3.3}O_{0.7-1.3}$ (see fig. 5-1-10a,c). This was in good agreement

with the values found by the EDX and μ-FTIR measurements. The spectra also gave a film thickness of $2.3.10^{18}$ at.cm^{-2}. By comparing this value to the geometric thickness of 230 nm measured by profilometry, a value of 1.7 ±0.2 g.cm^{-3} was obtained as the deposit density. This value corresponded to the density of an amorphous hydrogenated C of medium hardness:

Form of carbon	Density (g.cm^{-3})
Diamond crystal (cubic)	3.52
Graphite single crystal	2.26
Graphite, polygranular	1.57-1.73 (depending on grain texture)
C_{60}	1.72
Glassy C	1.3-1.55
Evaporated C	1.9
Sputtered C	2.2
Amorphous hydrogenated C, hard	1.6-2.2
Amorphous hydrogenated C, soft	1.2-1.6
Polyethylene	0.92

Table 5-1-III: Typical densities of different forms of pure and hydrogenated carbon.[3, 36]

This demonstrated the performances of the ion micro-beam technique. Though only semi-quantitatively because of the low SNRs, it confirmed the deposit composition. The technique is proposed for further H content measurements or as a complementary tool with EDX in the case of ambiguous compositions (overlapping peaks, electron beam effects).

5-1-3-D) Micro-Raman analysis

Raman spectroscopy is an optical technique that uses a monochromatic light beam (usually between 200 and 1000 nm) to excite the sample. The light, re-emitted at slightly different wavelengths due to Raman scattering, can be collected and analysed to give information on the crystalline structure and composition of the sample. A powerful tool for the analysis of carbon phases,[37-41] it can be used in an optical microscope, to analyse volumes down

to 1 μm^3.[42] In the next figure, the micro-Raman spectra obtained on the deposits are compared, after subtraction of a smooth background:
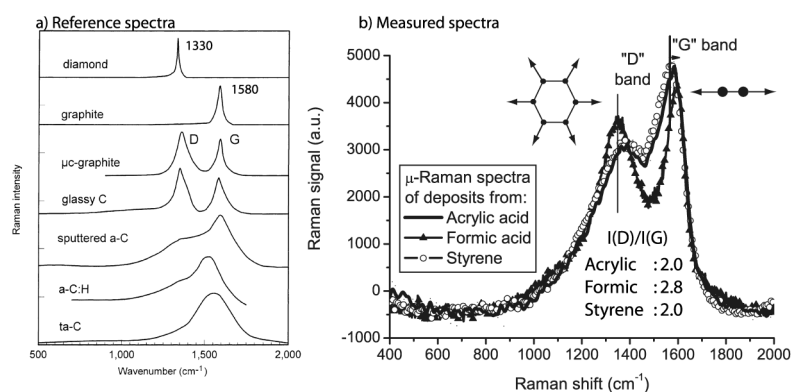
Figure 5-1-11. Comparison of μ-Raman spectra of the deposits from three precursors with reference spectra.[3] The two characteristic bands of amorphous C obtained are highlighted.

The wide signal between 1000 and 1800 cm^{-1} was characteristic of hydrogenated amorphous Carbon (compare figs. 5-1-11a and b). It consisted of two bands, named "D" for "disorder", around 1350 cm^{-1}, and "G" for "graphite", around 1580 cm^{-1}.[43] The involved network vibrations were schematically represented (see fig. 5-1-11b).[44] The spectra of the deposits from acrylic acid and styrene were very similar (as the spectrum from acetic acid, not shown). A previously published spectrum from a contamination deposit had a similar shape.[45] The spectrum from formic acid has a larger D band, with the G band located at a higher Raman shift. The positions and intensity ratios of the D and G bands gave indications on the degree of disorder of amorphized carbon (see fig. 5-1-12). The ratio of D and G bands (by Lorentzian fits) close to 2 in the spectra of fig. 5-1-11b, with a G band at 1580 cm^{-1}, indicated nanocrystalline graphite, with cluster size around 2 nm and sp^2 fraction above 90%,[3] consistent with the FTIR results. The larger values for the G band position and the D/G ratio obtained from formic acid indicated a higher density of small aromatic rings. The volatile element fractions were, respectively, C/(O+H) = ¼ in formic acid, C/(O+H) = 3/5 in acrylic acid, and C/H = 1 in styrene. A larger volatile element fraction was stripped from the formic acid during FEB-induced fixation, than from the other two precursors. The remaining C atoms reorganized better, forming a different nanostructure. The Raman analysis showed that the structure of the deposited material resembled a dense network of small-cluster model structures, like these

shown as the central part of fig. 5-1-12, and less resembled the large polycyclic, graphite-like ribbons or sheets.[46, 47]
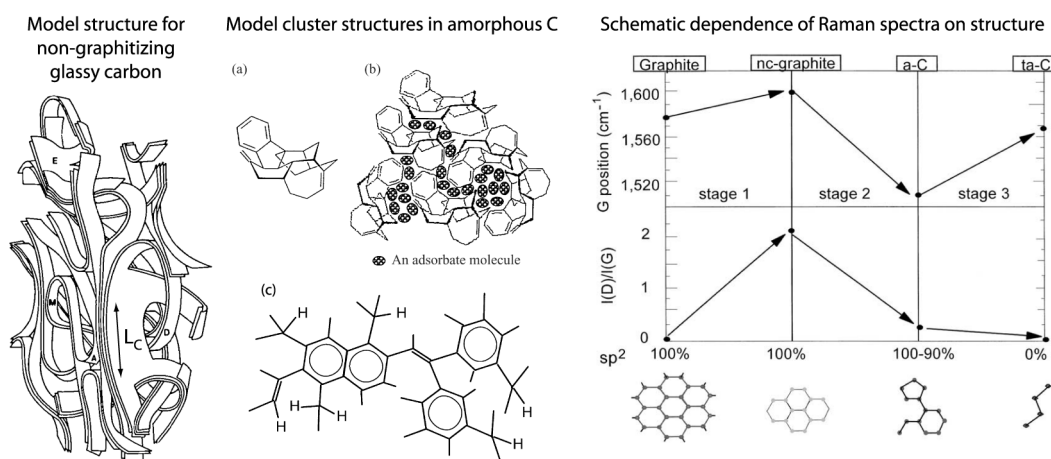
Figure 5-1-12. Model structures for different non-crystalline carbons. Left, graphitic-ribbon structure of a pyrolysed polymer, defining a correlation length L_C.[48, 49] Centre: with smaller L_C, molecular structures were proposed for the clusters, containing both the sp^3 (tetrahedral) and sp^2 (trigonal) forms of C. H can be present in molecules adsorbed in pores,[50] or attached to the backbone.[3] Right, Raman spectra evolve during graphite "tetrahedralization" (nc: nanocrystalline; a-C amorphous C; ta-C tetrahedral amorphous C).[44]

5-1-3-E) Micro-reflectometry

As already noted in Section 4-1, thin carbonaceous films display interferential colours in optical microscopy. Two micro-reflectometry techniques were developed to characterize the optical properties of the deposits in the visible range of the optical spectrum. As the first technique, the intensity of the signal of the co-focused laser beam reflected on the sample was monitored during film growth. This was a new *in-situ* monitoring tool for the large-area film growth rate.[51] Optical interferences take place in thin films (see fig. 5-1-13a). As the film grew the intensity of a reflected monochromatic beam periodically varied and was attenuated. The period of the variation and the attenuation rate depended on the refractive index of the thin film, as shown by the equation in fig. 5-1-13b. The intensity depended on the Fresnel coefficients at the interfaces, which were linked to the refractive index of the film and substrate, but also to the polarization state of the incident beam ([52], pp. 61-70, 281-288 & 615-633). The second technique was *ex-situ* spectral micro-reflectometry, as described in §3-2.

a)

Incident beam
(wavelength λ,
amplitude a₀)

Interferences

ra₀

θ

Vacuum
(index n=1)

t²rr_s a₀
x attenuation
x exp(i.phase shift)

Refraction
in thin film
(ñ=n+ik)

e

Substrate (ñ=n_s+ik_s)

b) Intensity of specularly reflected light:

$$I = r^2 I_0 + \left(t^2 r_s\right)^2 \exp\left(-\frac{4\pi k}{\lambda}\frac{4ne}{\sqrt{1-\frac{1}{n^2}\sin^2(\theta)}}\right) I_0$$

$$+ 2rt^2 r_s \exp\left(-\frac{4\pi k}{\lambda}\frac{2ne}{\sqrt{1-\frac{1}{n^2}\sin^2(\theta)}}\right)\cos\left(\frac{4\pi ne}{\lambda\sqrt{1-\frac{1}{n^2}\sin^2(\theta)}}\right) I_0$$
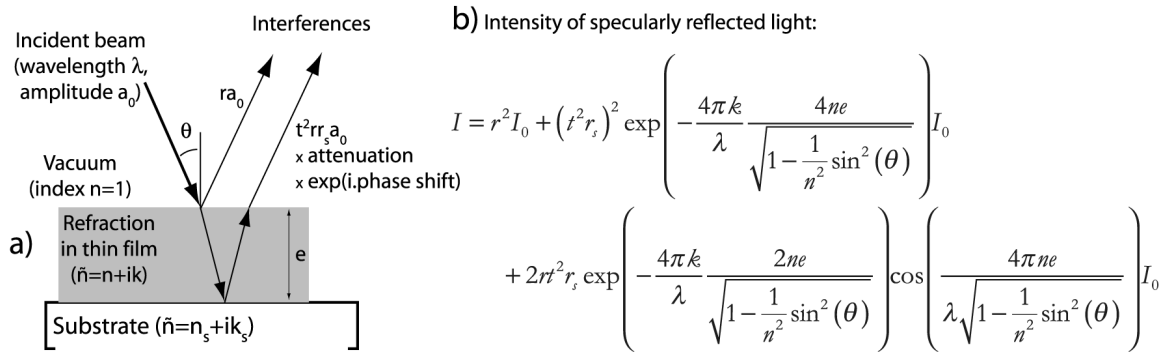
Figure 5-1-13. Interferences on a thin film. a) Schematic principle. *r,t,r_s*: Fresnel reflection and transmission coefficients on the film and substrate, respectively. b) Intensity (with I₀=a₀²) as a function of film thickness e, refractive index n+ik, and incidence angle θ.

The co-focused laser beam at 514 nm was incident at 45° (see fig. 5-1-14a).

a) *In-situ* reflected light monitoring during deposition

FEB

514 nm
Ar+ laser

To photodiode

Sample

Co-focused height

100 µm lower

100 µm

b)

Acrylic acid, 25 keV on Si, 100 nA, 1 kx

200 µm
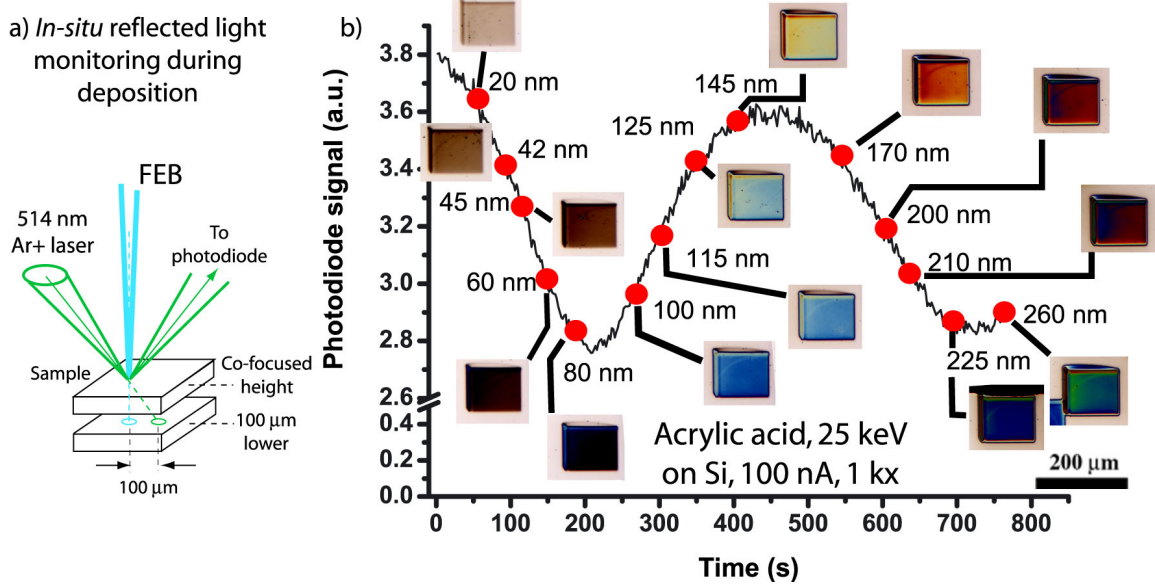
Figure 5-1-14. *In-situ* reflectometry. a) Schematic principle. b) Measured light intensity, with the *ex-situ* optical micrographs (normal incidence, reflection, bright field) of successive films.

The intensity measured at the photodiode varied slowly. It reproducibly reached a minimum at a film thickness of 85 nm, than a maximum a 150 nm, and a second minimum at 230 nm (see fig. 5-1-14b). The values they reached were indicated as red dots in fig. 5-1-14b. Colours were visible under the white light of the optical microscope. As an application, high-resolution multicolour patterns were realized (see fig. 5-1-15a).[53]
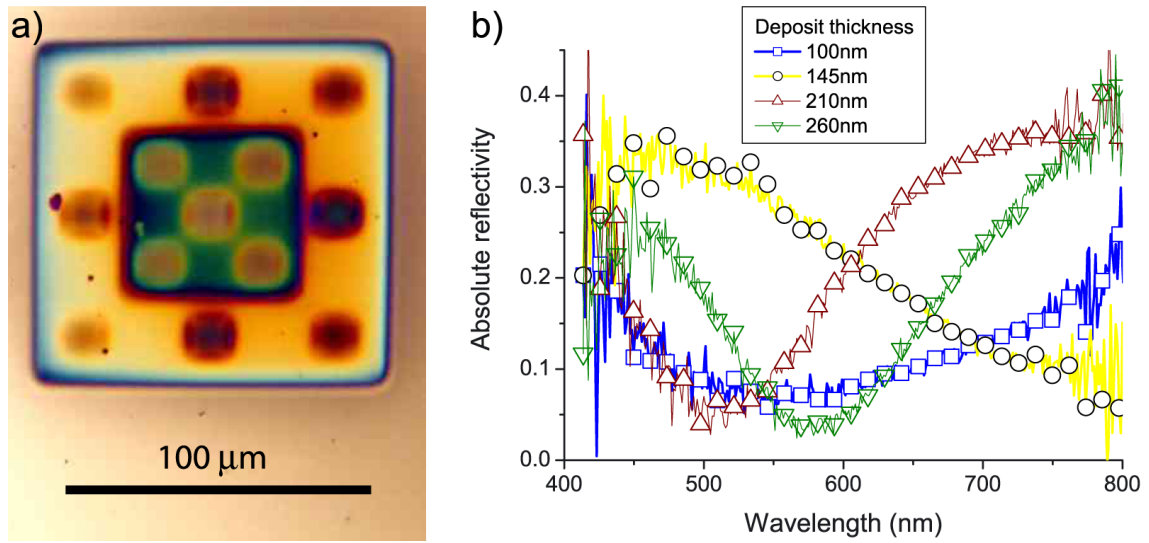
Figure 5-1-15. a) Optical micrograph of multicolour pattern (colour and thickness match). b) *Ex-situ* micro-spectrophotometric measurements on the deposits shown in fig. 5-1-14b.

As expected, the reflectivity spectra showed a broad maximum at wavelengths that increased with the film thickness (see fig. 5-1-15b). The second interferential order was reached at 260 nm thickness, as observed in a second maximum at 460 nm wavelength. The curves were noisy below 450 nm and above 750 nm because of the lower power of the illumination lamp in these spectral ranges. The *ex-situ* spectra of the thinner films were correctly described by the equation shown in fig. 5-1-13a, as shown in fig. 5-1-16a.
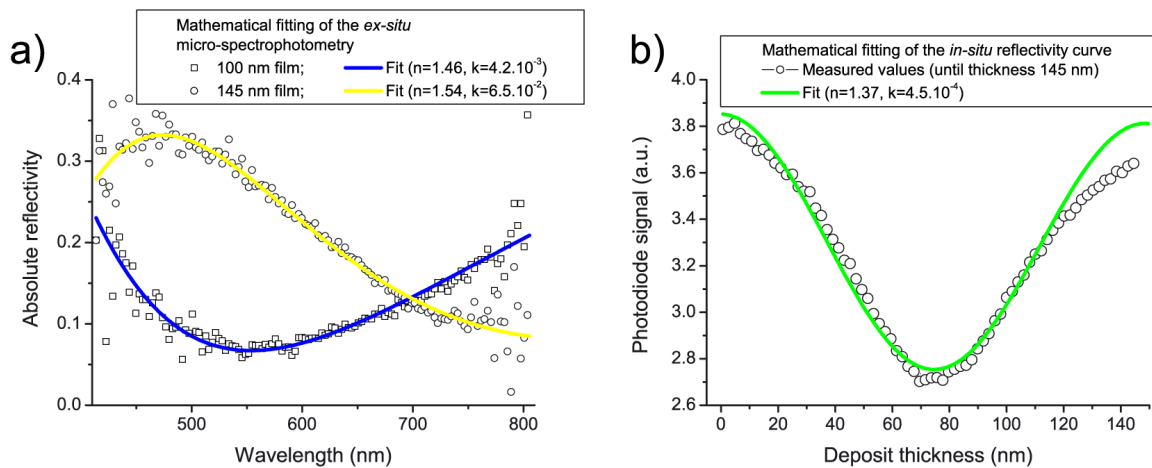
Figure 5-1-16. Mathematical fittings with the equation given in fig. 5-1-13b. a) *Ex-situ* spectra. Variable: λ, at fixed thicknesses. b) *In-situ* curve. Variable: film thickness, at fixed λ.

The initial part of the *in-situ* monitored curves was also fitted by the same equation by keeping all parameters constant including the wavelength, and varying only the film thickness (see fig. 5-1-16b). The films had an index of refraction of 1.45 ± 0.1 according to the good fits. This is lower than the values between 1.65 and 2 usually reported for a-C:H, which vary with the H content.[54] It is also lower than the values for diamond (purely real index, n=2.43 at 2.5 eV) and graphite (1.36+2i parallel to the c-axis, 2.65 + 1.3i perpendicular, at 2.5 eV).[55, 56] Measuring on thin films induced a large dispersion on the absorption coefficient, but the imaginary refractive index of the deposited films was low, between $4.5.10^{-4}$ and $6.5.10^{-2}$. The optical absorption coefficients of the deposits depended on the precursor, as seen in the optical micrographs in Table 5-1-I.

5-1-3-F) Precursors containing Fluorine, Nitrogen and Chlorine

Other polar compounds were used as precursors to investigate how electron-induced fixation affected other elements. Trifluoroacetic acid (CF_3COOH) yielded the following results:
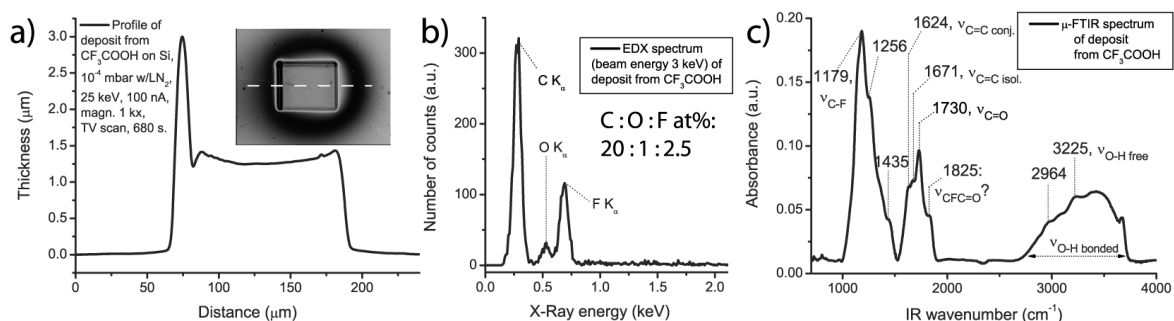
Figure 5-1-17. Analyses of deposits from trifluoroacetic acid. a) Deposition conditions, optical micrograph and cross-sectional profile of a deposited film. b) EDX analysis at 3 keV (notice the absence of signal from the Si substrate). c) μ-FTIR analysis.

A large growth rate was obtained from this strongly polar compound (see fig. 5-1-17a). The C:F ratio was 8:1 in the deposit (see fig. 5-1-17b), as compared to the C:F ratio of 2:3 in the precursor, so more than 90% of the F was lost during deposition. This loss may occur during precursor fixation or by electron-induced desorption during exposure of the already deposited material.[57-60] The O content was slightly lower than what was measured on the hydrogenated series. The possible O incorporation from the residual gas prevents further conclusions.

In the FTIR spectrum, similar bands are obtained for C=O, C=C and C-H vibrations, like from acetic acid (see fig. 5-1-17c). The C-H band is much smaller than the C=O band. New bands appear. The absorption between 2700 and 3700 cm^{-1} is an OH band. The band at 1825 cm^{-1} is most probably the absorption of a C=O vibrator, either in a very strained configuration or bonded to F-bearing C atoms, as compared with reference compounds:
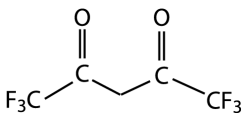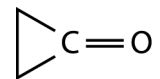
Compound or group	Absorption band (cm^{-1})	Reference	Compound or group	Absorption band (cm^{-1})	Reference
Acyl fluoride R-C(F)=O	1885	[61]	Benzoyl fluoride C_6H_5-CF=O	1812	[62]
Formyl fluoride CH_3-CF=O	1869	[62]	F_2C=O gas	1939 and 1908	[63]
Acetone CH_3-CO-CH_3	1712	[28]	Trifluoro-acetone CF_3-CO-CH_3	1778	[28]
Trifluoro-acetic acid CF_3-COOH	1778	[28]	Hexafluoro-acetylacetone (hfac)	1632, 1693 and 1792	[28]
Perfluoro-alcene R-CF=CF_2	1780	[64]	Cyclo-propanone	1822	[62]

Table 5-1-IV: IR Absorption bands of reference fluorinated and ketone compounds.

The hypothesis of a reactive conjugated acyl fluoride cannot be excluded (see Table 5-1-IV), as this functional group was previously obtained by irradiating fluorinated polymers with electrons.[63] A large absorption peak at 1179 cm^{-1} was due to C-F bonds (the substrate contribution in this area was subtracted as background). Most of the remaining hydrogen was bonded to oxygen: few C-H bonds were created during deposition. The Raman spectrum of this deposit (not shown) revealed a large fluorescence background upon which the amorphous C bands were barely visible. The origin of this fluorescence was not investigated further.

The polar and oxygen-free compound acetonitrile (CH_3CN) yielded the following results:
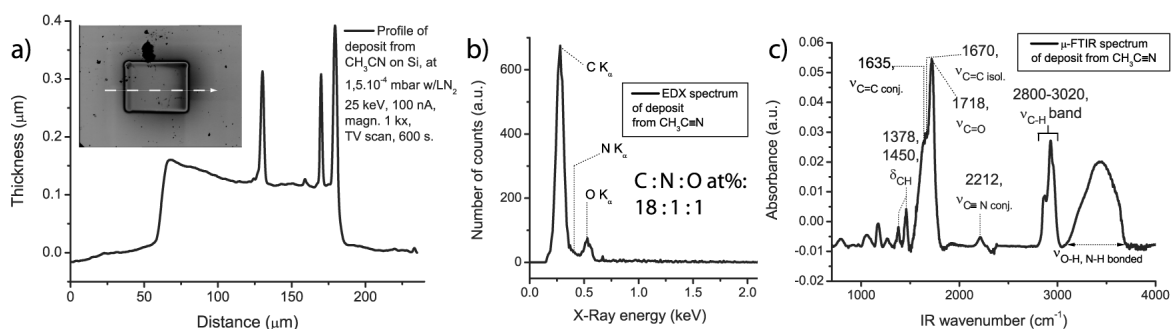
Figure 5-1-18. Analyses of deposits from acetonitrile. a) Deposition conditions, optical micrograph and cross-sectional profile of a deposited film. b) EDX analysis at 3 keV (notice the absence of signal from the Si substrate). c) μ-FTIR analysis.

The growth rate was a little higher than from acetic acid (see fig. 5-1-18a). EDX revealed the oxygen incorporation into the deposit. Nitrogen was present in the deposit, as observed by the small N peak overlapping the bottom of the large C peak (see fig. 5-1-18b). The high C:N ratio of 18:1, as compared to the C:N ratio of 2:1 in the precursor, indicated that at least 90% of the N was lost during deposition. In the FTIR spectrum, the clear C-H, C=O and C=C bands appeared the same as in the previous results (see fig. 5-1-18c). Small deformation (δ_{C-H}) vibration peaks were observed at 1378 and 1450 cm^{-1}. A weak nitrile band at 2212 cm^{-1} indicated that most of the N present was bonded by triple bonds to sp^1 C. These nitrile end groups were bonded to sp^2 C atoms. A large O-H (and possibly N-H) band was present between 3000 and 3700 cm^{-1}, making H quantification difficult.

The Raman spectrum (not shown) presented the same characteristic D and G bands as the spectrum of the deposit from acetic acid. The deposit consisted of hydrogenated amorphous carbon, and did not constitute an exception to the general behaviour discussed in §5-1-3D.

The Chlorine-containing precursor CCl_4 was used. This non-polar compound resulted in much lower deposition rates. The composition measured by EDX (not shown) indicated a C:O:Cl ratio of 12:2:1. Chlorine was also lost during the deposition process. No FTIR or Raman spectrum could be taken on the thin films that were deposited.

5-1-3-G) Morphological (SEM, TEM) and EELS analysis

More detailed SEM, TEM and EELS analyses were made in order to characterize the deposits. Formic acid was chosen as the precursor, at 25 keV and 5 nA probe current, on Si.
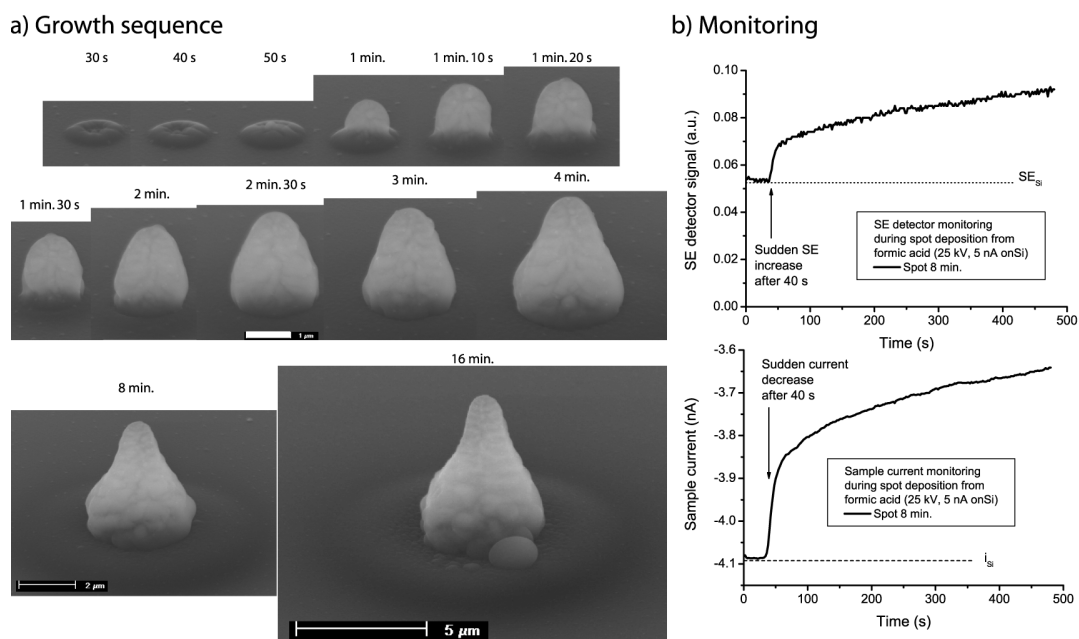
Figure 5-1-19. Preparation of a tip series from formic acid for SEM analysis. a) SEM views (25 keV, tilt 73°) of the successive growth stages of a tip deposited at 5 nA (notice the varying scales in the last row). b) Monitored signals (bottom, sample current; top, SE).

This precursor behaved differently than the organometallics and other organics (compare with the 100 pA tip from acrylic acid, in fig. 5-1-2). Before 50 s, only a doughnut shape was deposited (see fig. 5-1-19a). Spherical growth suddenly began at 50 s and was witnessed in the monitoring (see fig. 5-1-19b). Then, the 3D deposition mode changed from spherical growth to a pear-like growth regime. The pear appeared grainy in the SEM at 25 keV. A round deposit due to forward-scattered electrons was clearly visible on the substrate, around the higher deposit.

This deposition sequence was repeated on a thin membrane for TEM observation. A white contrast in TEM at the centre of the deposits, and a corresponding black contrast in DSTEM, indicated a hollow core surrounded by a denser crust (see fig. 5-1-20). Both were formed from the start, with the first deposits consisting of isolated denser grains, 200 nm in size, which were then covered by further material depositing and appeared to coalesce. Both the deposit outer diameter and the size of the inner structure increased with the deposition time.
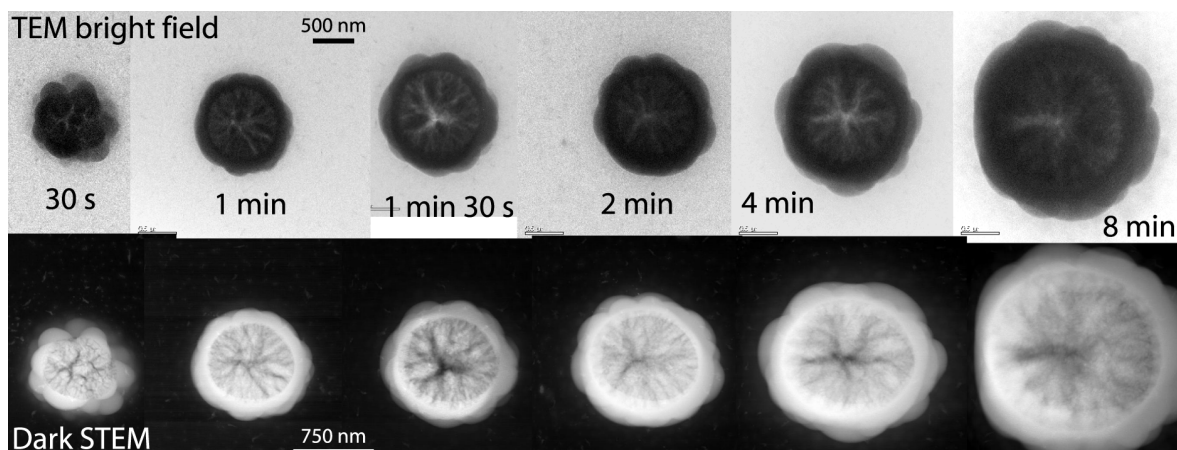
Figure 5-1-20. TEM analysis of a series of deposits from formic acid. Top, transmission bright field topview pictures. Scale bar 500 nm. Bottom, same structures viewed in dark field (SE detector) scanning TEM, at a slightly different magnification. Scale bar 750 nm.

Higher magnification TEM observations revealed only amorphous carbon (see fig. 5-1-21).
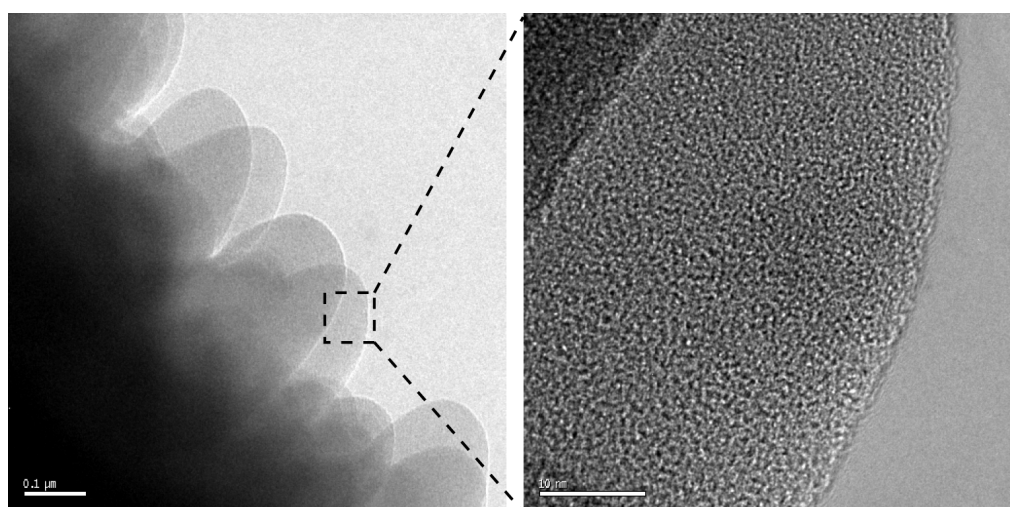
Figure 5-1-21. High-resolution TEM bright-field analysis of carbonaceous deposits. Left, TEM image of the side of a freestanding rod deposited from formic acid, at 25 keV, 100 pA, 5 nm/s on a Cu holding grid. Scale bar 100 nm. Right, higher magnification. Scale bar 10 nm.

EELS analysis was performed on the edges of the deposits. The EELS spectra of the deposits from acetic and formic acid were similar, except above 310 eV, and confirmed the presence of the partially tetrahedral a-C with a $\pi^*(C=C)$ transition at 285 eV (see fig. 5-1-22b). A reference diamond sample graphitized under the beam, showed some $\sigma^*(C=O)$ and did not lead to the expected results (see fig. 5-1-22b): further quantification was not undertaken.
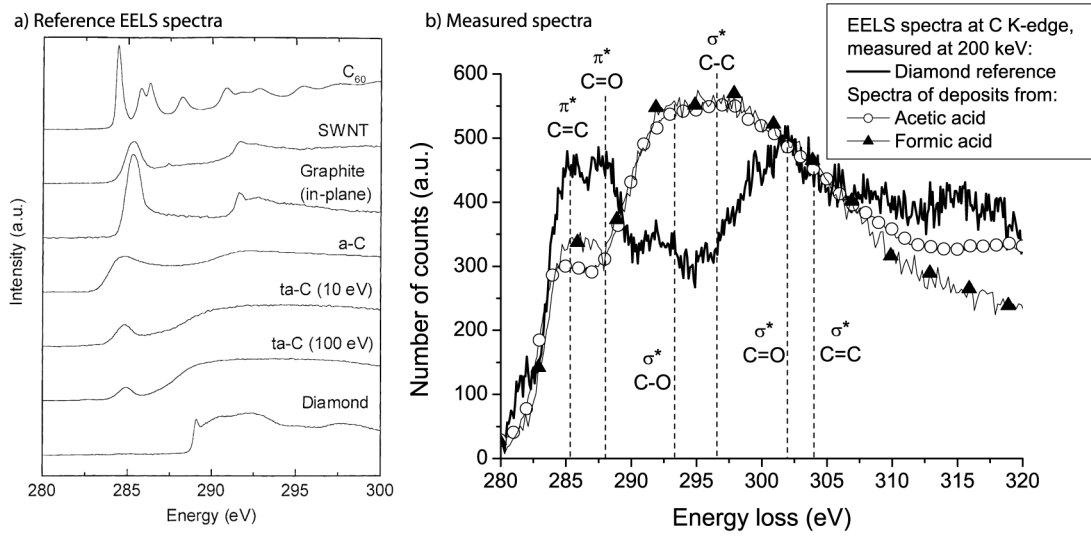
Figure 5-1-22. Comparison of EELS spectra of the deposits from two precursors and a reference sample with reference spectra,[3] with transition assignments.[65]

The core/crust phenomenon influenced the deposition of more complex structures.
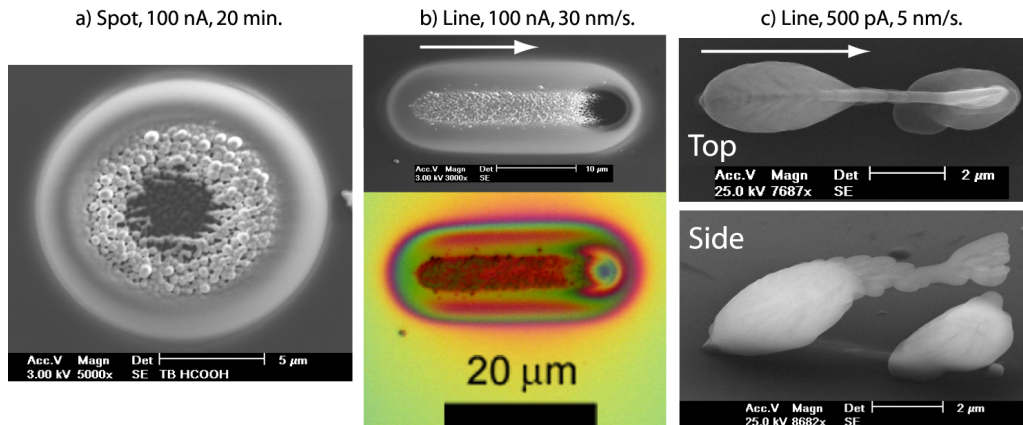
Figure 5-1-23. Influence of the core/crust structure on other deposition sequences. a) SEM top-view of a high current deposit. b) Line deposit in the same conditions. Top, SEM top-view. Bottom, optical micrograph. Thickness differences appear as different colours. c) SEM views (top and 73° tilt) of a taking-off line deposit, scanned at 500 pA and 5 nm/s.

The random positions of the deposited grains made 3D shapes irreproducible. Spots deposited at higher currents remained flat and doughnut-shaped (see fig. 5-1-23a). The scanned line showed that the centre of the beam was responsible for the low height at the centre of the deposit (see fig. 5-1-23b). At lower currents, the primary arches of 3D scanned line deposits showed erratic thickness variations due to the random formation of grains (see fig. 5-1-23c).
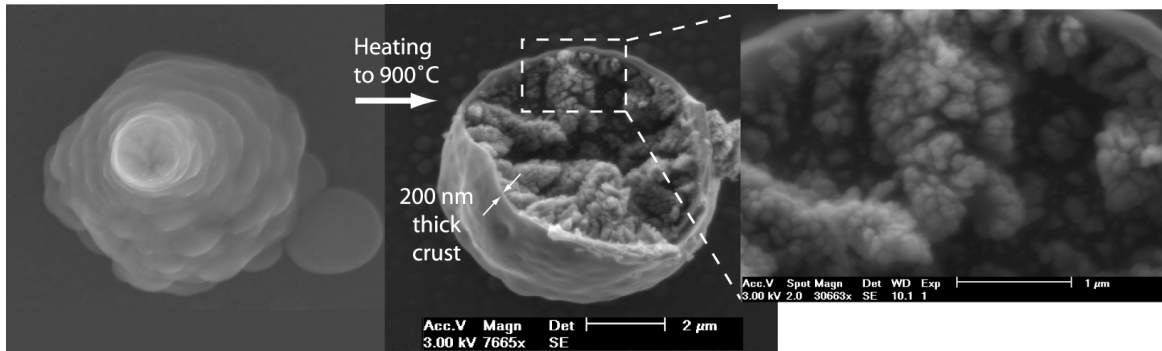
Figure 5-1-24. Temperature-induced deposit breakage. SEM top-views of a 30 min. pear-shaped spot deposit, before and after heating it to 900°C.

Heating pear-shaped spot deposits revealed a hollow interior (see fig. 5-1-24). The protuberances were the outer envelopes of cauliflower-like radial structures formed in the deposits, typically 1 μm long. The deposit boundary was a 200 nm-thick smooth crust, in good agreement with the TEM pictures. The deposit density was clearly inhomogeneous.

5-1-3-H) Effects of temperature

Thin smooth films were deposited from formic acid (see fig. 5-1-25). They had low roughness and showed no trapped bubbles up to at least 600 nm thick. A post-deposition annealing in vacuum reduced their thickness and altered their composition:
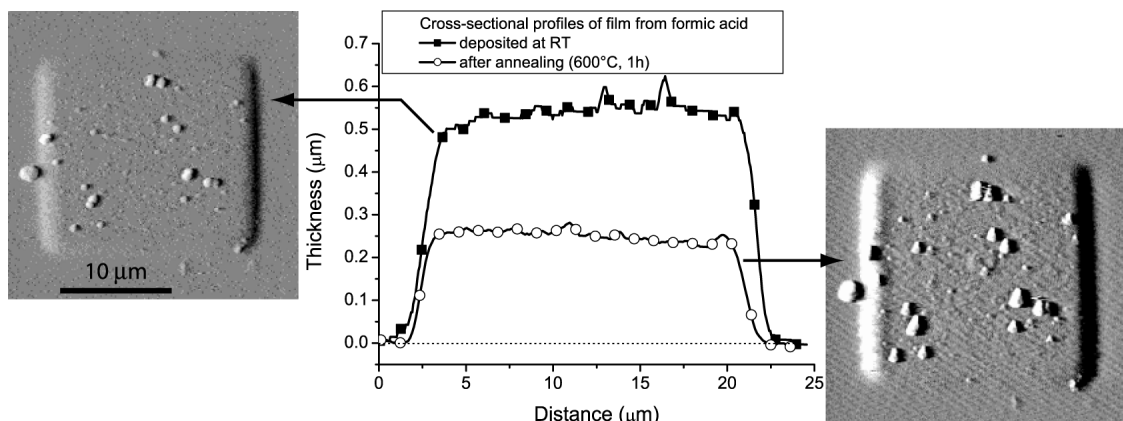
Figure 5-1-25. Thinning of film deposits by annealing. AFM cross-sectional profiles and pictures of the signal derivatives (left, as deposited; right, annealed).

The film remained flat but the thickness was halved (dust particles kept the same heights, see fig. 5-1-25). EDX reveals a loss of O compared to C, down to 98:2 C:O (see fig. 5-1-26a).
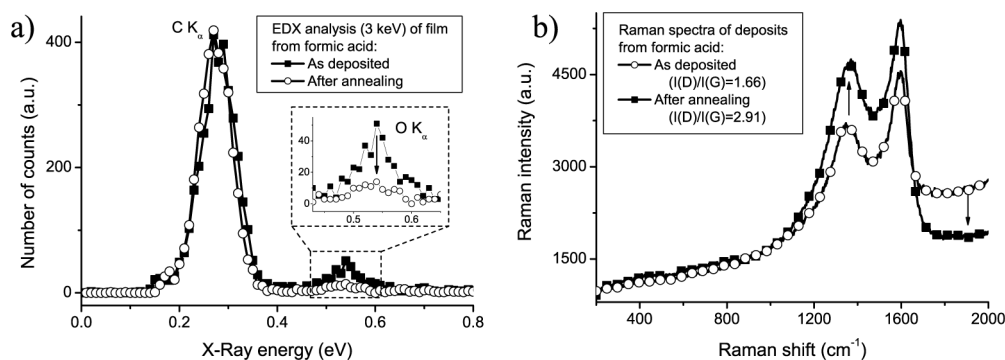
Figure 5-1-26. Chemical analyses of the effects of annealing. a) EDX spectra indicate a quantitative loss of Oxygen. b) Raman spectra indicate a further graphitization.

A featureless FTIR spectrum (not shown) indicated an almost total loss of C-bonded O and H. Raman spectra still correspond to amorphous carbon but with a reduced fluorescence background, an increased Raman intensity of the characteristic D and G bands despite the volume loss, and an increased D/G ratio by Lorentzian 2-peak fitting after background subtraction (see fig. 5-1-26b). The sp^2 fraction increased. Upon annealing, the H-bearing sp^3 C atoms lost H and were inserted into the amorphous material with an sp^2-hybridization.

Depositing on a heated substrate altered the deposition rate and the sp^2 content:

a) Deposition rate vs. substrate temperature

T (°C)	Film deposit thickness (25 keV, 3 nA, 37 min on Si, values in nm)
25	500
40	600
70	470
90	235
120	110
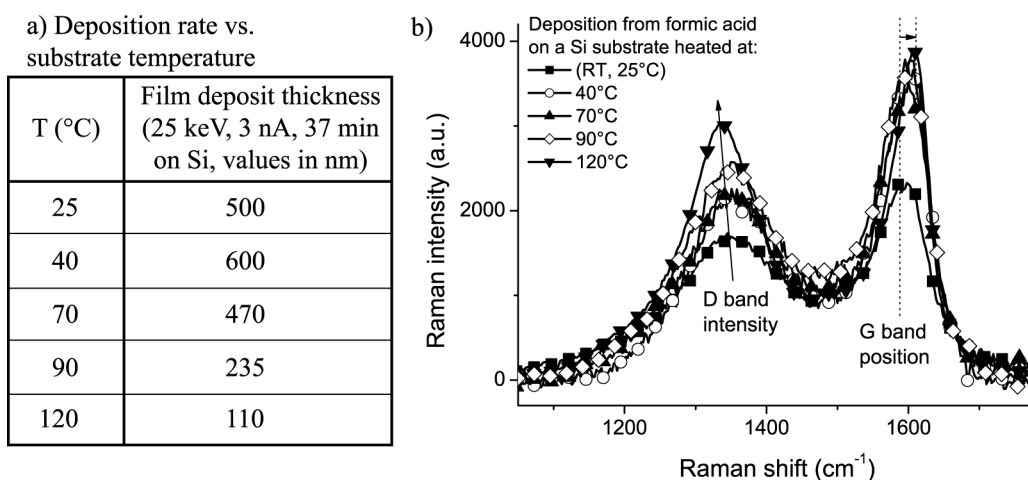
Figure 5-1-27. Deposition on a heated substrate. a) Compared thicknesses of films deposited in the same conditions, at various temperatures. b) Raman spectra of these films.

Raising the substrate temperature to 40°C slightly increased the deposition rate. At higher temperatures the deposition rate was gradually reduced, by a factor of 2 for each additional 20 to 30°C (see fig. 5-1-27a). The films deposited at higher temperatures had more intense Raman signals, indicating an increased optical absorption. The D/G ratio decreased from 1.69 to 1.2 between the films deposited at 25 and 40°C, respectively (see fig. 5-1-27b). At higher temperatures it increased regularly from 1.2 to 1.7. The G band regularly shifted towards higher wavenumbers, from 1592 to 1601 cm^{-1} between 25 and 120°C. These were clear indications that the deposited material had increasing sp^2 content when increasing the temperature (compare with fig. 5-1-26). Optical micrographs (not shown) indicated increasing absorption coefficients.

The chemical vapour deposition of diamond is usually realized at higher temperatures.[66-68] The resistive heating system used here did not allow such high temperatures and made *in-situ* sample current monitoring impossible. Improving the heating system for higher temperatures should bring to new evolutions in the nanostructure of the deposited material, as already indicated by the Raman spectra, and is proposed for further studies.

5-1-4 Discussion

5-1-4-A) Influence of the precursor of the growth rate

All the organic compounds in this family led to deposits with the same compositions. According to the Raman measurements, the nanostructures depended slightly upon the ratio of volatile elements to C in the precursors. As a consequence, the deposition rate depended only on the precursors used.

According to Christy's model (see §2-1-2),[69] the amount of fixed precursor (R) depends on the electron current density (f), the precursor flux (F), the molecular volume (*v*), the electron interaction cross-section (σ), and the surface residence time (τ):

$$R = \frac{v\mathrm{F}}{1 + \dfrac{1}{\sigma\tau\mathrm{f}}}$$

(5-1)

Film growth rate according to Christy's model, in the precursor-limited regime.

The molecular volumes and the electron interaction cross-sections of all the precursors tested stayed within a limited range. The precursor fluxes F of acrylic acid and styrene were similar. Constant current densities f were used. They were high for large growth rates (see §4-1-2D).

Conjugated molecules resist radiation better than aliphatic chains.[70-72] Both styrene and acrylic acid have conjugated electrons, making their resistance to ionizing radiation similar. The difference in growth rate cannot be due to a different resistance to ionizing radiation. The residence time seems to be responsible for the main difference in growth rates between precursors, depending on the adsorption enthalpy:

$$\tau = \tau_0 e^{\frac{\Delta H_{adsorption}}{k_B T}} \qquad (5\text{-}2)$$

τ_0: characteristic vibration time; k_B: Boltzmann's constant; T :temperature

The time τ_0 is a typical vibration time of molecules adsorbed at surfaces. Previous measurements give an estimated range of $10^{-16} < \tau_0 < 10^{-13}$ s.[12] The adsorption enthalpy depends on the adsorbed gas and the surface chemistry. The following table lists typical values:

Adsorption enthalpy	Comments	Typical values of τ at room temperature
24 J/mol	Close to τ_0	$1.2 \cdot 10^{-13}$ s
360 J/mol		$1.3 \cdot 10^{-12}$ s
840 J/mol	Simple gases like Ar, Ne, O_2, N_2, CO…, on surfaces like glass	$4 \cdot 10^{-11}$ s
960 J/mol		$1 \cdot 10^{-10}$ s
2.4 kJ/mol	Many organic substances	$3.2 \cdot 10^{-6}$ s
3.6 kJ/mol		$1.8 \cdot 10^{-2}$ s
4.8 kJ/mol		$1 \cdot 10^{2}$ s
6 kJ/mol		$6 \cdot 10^{5}$ s (~ 1 week)
7.2 kJ/mol		$4 \cdot 10^{9}$ s (~1 century)
35 kJ/mol	Oxygen on W	10^{95} s (~forever)

Table 5-1-V: typical values of adsorption enthalpies and residence times, at RT.[12]

A slight variation in adsorption enthalpy (less than 1 kJ/mol) among the typical values for organic substances (around 2.4 kJ/mol), resulted in changes of the residence times by several orders of magnitude. An increase in the substrate temperature exponentially decreased the growth rate, as observed in fig. 5-1-27a.

Acrylic acid had a permanent dipole moment due to the carboxylic group (its value is not listed in the tables, but it is close to propanoic acid, μ=1.7 D). It also has the ability of forming H-bonds. Styrene lacks both these properties. The specific and non-specific attractive van der Waals forces from the surface are stronger on acrylic acid than on styrene, with larger adsorption enthalpy. These effects, in turn, increase the residence time. Selecting polar molecules with high vapour pressures leads to higher deposition rates.

Some of the results presented in this section were published in the scientific journal *Microelectronic Engineering*, under the title "Characterization of focused electron beam induced carbon deposits from organic precursors", in 2005.[73]

5-1-4-B) Proposed deposition mechanism

H and O were eliminated from the precursors during the deposition process. Two mechanisms may be responsible for the initial precursor fixation step. For the first hypothesis, the beam disintegrates the precursor molecules into their atomic constituents so only non-volatile fragments remain bound at the surface. This interprets deposition as a purely surface level process. As it does not explain the observed crusts, I suggest a second mechanism with a two-step process:

1)   Electron-induced precursor fixation at the surface

The precursor molecules are electronically excited or ionized by inelastic collisions with the primary beam (80% of all the collisions in low-atomic-number materials).[74] Typically, this involves energies between 10 and 40 eV (the C and O outer-shell L levels, known in EELS analysis as the plasmon peaks), and between 300 and 600 eV (the C and O inner-shell K edges).[75-77] Among other desexcitation pathways, the molecules can decay by

cross-linking or ejection of a fragment.[71] In both cases, a non-volatile species is formed at the surface, and further excitation-decay events take place before the next layer is deposited. A small number of bonds are broken in the precursor molecule and a small number of bonds are created with the substrate or the already deposited material.

2)   Electron exposure of the previously deposited material

This is analogous to high-dose electron-beam lithography. Radiation damage transforms the deposited material into a cross-linked, partially dehydrogenated and deoxygenated amorphous carbon.[16, 72, 78-86] This step takes place in the bulk deposit: the newly deposited precursor layers act as a crust or a gas barrier. The stable gases (H_2, O_2, H_2O, and to a lesser extent CO, CO_2, CH_4...) liberated by the exposure remain trapped as bubbles in the deposit (see fig. 5-1-27).[87, 88] These areas of trapped gas create the hollow deposits. By heating, the internal pressure rises, exploding the crust so the trapped gases escape. The quantity of contained gas depends on the ratio between the volatile and solid elements in the precursor. This is why the effect is more pronounced with formic acid, which has only one out of the 5 precursor atoms that is not volatile. The elemental loss during deposition of the main part of the elements that are gaseous at room temperature (H, O, N, F, Cl) is very similar to what is observed during the electron irradiation of polymers.[15, 63, 89-92]
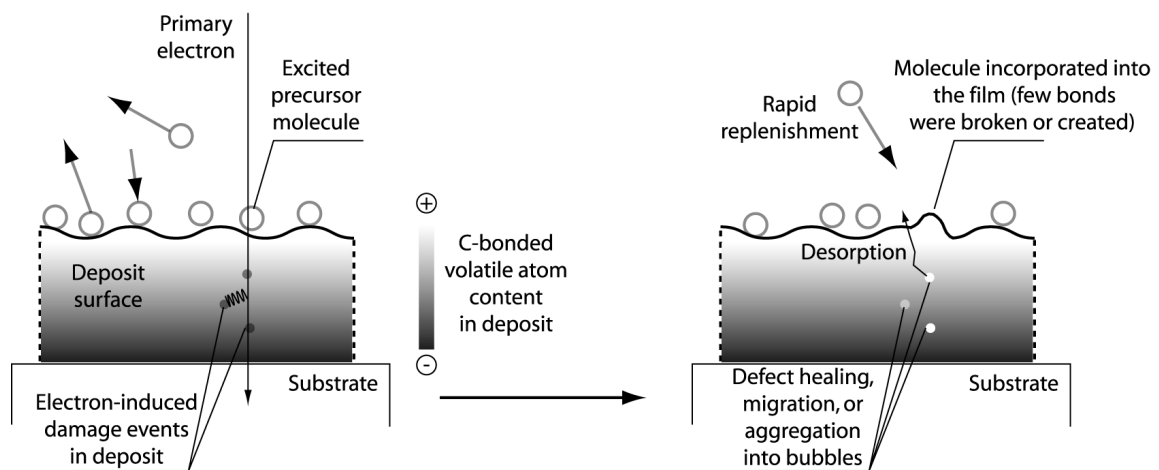
Figure 5-1-27. Schematic two-step mechanism proposed for film formation. Simultaneous precursor fixation and exposure of the deposited film occur.

The chemistry of carbonaceous materials under electron irradiation has been studied in depth. Numerous and complex structures of pure carbon are found at nanoscale.[93] Electron irradiation introduces "structural fluidity". At room temperature, a metastable phase of Carbon under a high-energy (>100 keV), high-density (>10 A/cm^2) electron flux is the "graphitic onion", consisting of successive spherical shells. It can be obtained by irradiating amorphous Carbon,[94, 95] electron-induced contamination deposits,[96] graphite,[97, 98] carbon nanotubes,[99, 100] fullerenes,[101] and diamond nanoparticles.[102, 103] Lower doses disorder and stress the crystalline structures by turning random sp^2 C atoms into sp^3.[104-110]

At higher temperatures (600°C), the trend is reversed because the electron-induced interstitial defects become mobile. Graphitic onions turn into diamond.[111-115] This electron-induced phase transition is due to the local compressive stress inside the carbon onions. The system is slowly driven towards the more stable diamond state.[116, 117] Irradiation drives metal atoms out of graphitic shells.[118] Carbon nanotubes can also be healed,[116, 119] coalesced,[120, 121] and even created under the electron beam by incorporation of C atoms.[122, 123]

Under the irradiation conditions used, the incident electron energy was not high enough to displace carbon atoms by a "knock-on" mechanism. The comparatively low temperature prevents atomic mobility, so the amorphous phase is stable. Diamond crystallites, which would have been occasionally formed in the deposit, rapidly become amorphized under the electron beam. Depositing a diamond-containing material requires higher deposition temperatures for this phase to be stable under irradiation.

5-1-5 Summary

Complementary micro-characterization methods were applied consistently. The material deposited from carbonaceous precursors consisted of amorphous carbon with up to 10% oxygen and 20% hydrogen. The C phase deposited up to 120°C is 90% sp^2. Slight variations in O and H content, as well as in C bonding and nanostructure, appeared between different precursors. The density of deposits obtained from acrylic acid was 1.7 ± 0.2 g.cm^{-3}, and their index of refraction in the visible was 1.45 ± 0.1 with a small imaginary part of 6.10^{-4} to 4.10^{-2}. Oxygen was incorporated from the gas phase, either during deposition or upon exposure of the deposits to air before characterization. Most of the volatile elements (H, O, N, F, Cl) were stripped from the precursors during deposition. The observation of hollow deposits hinted at a two-step mechanism, in which the precursor was first fixed by the electron beam without much elemental change, and then reduced to almost pure C by further electron exposure. The use of polar compounds allowed for higher growth rates because of higher residence times as compared to non-polar compounds.

The analysis showed that the deposition process did not allow for deposition of a diamond phase in the investigated conditions. Increasing the deposition temperature, although it will decrease the growth rate, should allow for increased sp^3 contents. Thanks to the characterization methodology and reproducible conditions described in the present study, FEB-induced deposition of diamond should be possible in the near future.

5-2 Deposits from organometallic precursors

5-2-1 Why depositing from organometallics?

Area-selective deposition of pure metals at the 10 nm scale would be a powerful tool for microcircuit repair. If deposition could be accurately applied in a parallel fashion, it would be a single-step direct-write tool. On the lab scale, easy electrical contact to single nano-objects such as DNA strands or nanotubes may open new opportunities. The miniaturization of 3D electrical devices may also have considerable applications. Magnetic, optical and chemical aspects also make the controlled deposition of pure elements and nanocomposites attractive at the sub-micrometer scale. Many volatile organometallic precursors are available from the field of CVD. How to select or design a precursor for efficient focused electron beam induced metal deposition? Which conditions to use? Which are the parameters involved?

First the effects of temperature are described during and after deposition from a Cu precursor. The outcome of the process was tuned from Cu-containing a-C to a crystalline material with mainly Cu. Applications of electrically conducting FEB deposits are then described.

5-2-2 Thermal effects on Cu-containing deposits

Several Cu precursors used in CVD were screened for the deposition of pure Cu (see fig. 5-2-1). They all had a hexa-fluoro-acetylacetonate (hfac) ligand. The vapor pressures and deposition rates were different but all the similar deposit compositions indicated mainly C. [124]
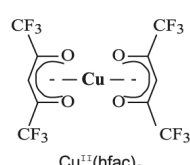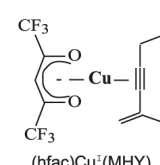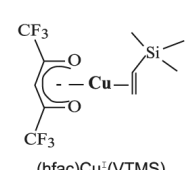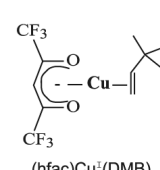
	P_{vap} (mbar)	Growth rate (nm/s)	Composition (Auger spectro., 5 kV, 75 nA)
Cu(hfac)$_2$	4.10^{-3}	4 +/- 1	Cu$_{14}$C$_{75}$O$_5$
(hfac)CuVTMS	0.1	20 +/- 2	Cu$_{20}$C$_{70}$O$_8$Si$_2$
(hfac)CuMHY	0.2	24 +/- 2	Cu$_{13}$C$_{82}$O$_3$
(hfac)CuDMB	1.3	46 +/- 4	Cu$_{25}$C$_{60}$O$_{25}$

Figure 5-2-1. Several Cu precursor at RT leads to similar deposit compositions. The large beam currents used for the Auger electron spectroscopy analyses affected some deposits.

The fixation mechanism at RT polymerized all the C-containing ligands. Probably due to a beam-induced damage, no F was detected in Auger Electron Spectroscopy.

The effect of heat on a rod deposit from (hfac)CuVTMS was observed under a TEM.
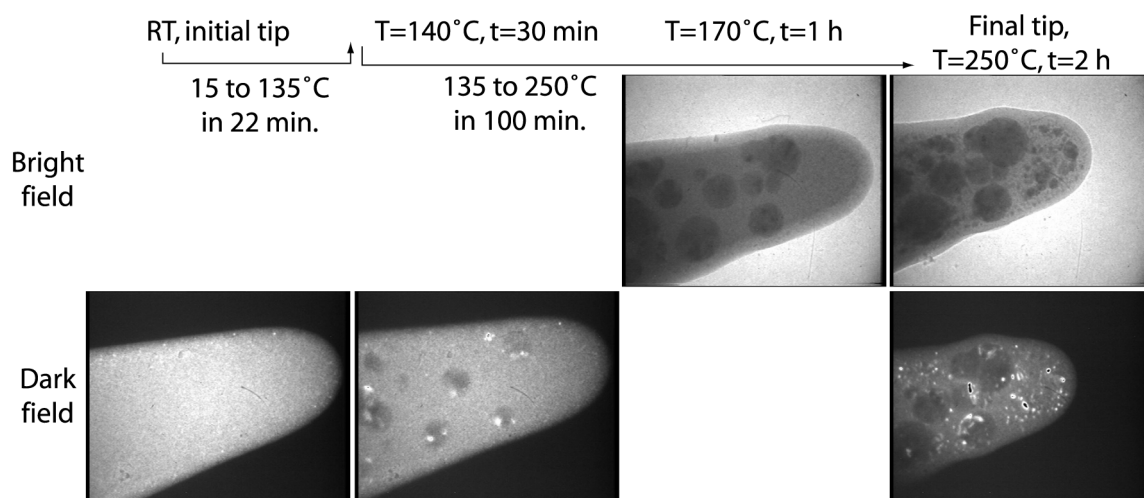
Figure 5-2-2. Heating sequence of a Cu-containing deposit apex in TEM.

Crystallites appeared and grew in the initially smooth tips (see fig. 5-2-2). They had darker contrasts in bright field. Although most of the transformation occurred at 140°C, the final shape was stable at 600°C. The skin observed at the tip apex was not systematically present.
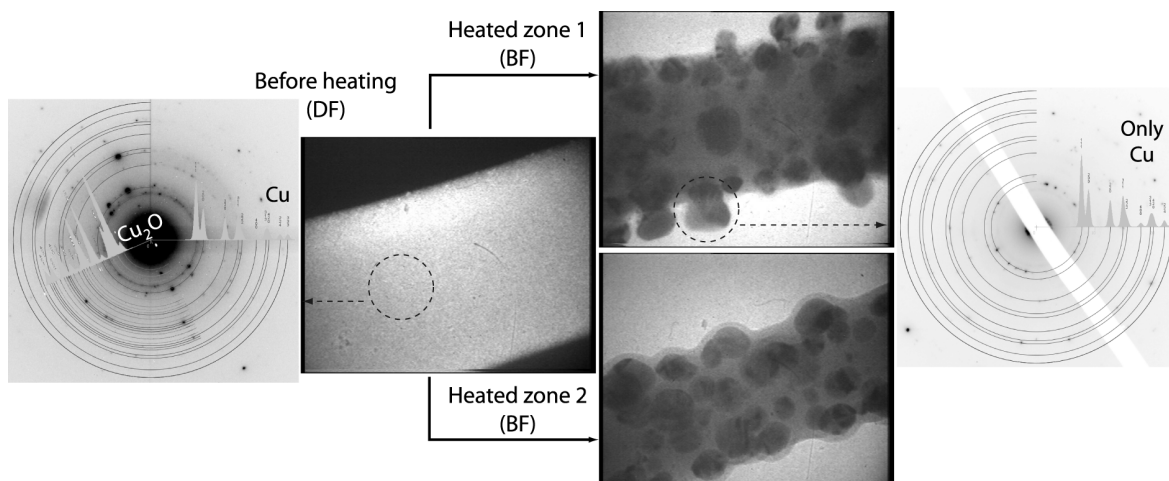
Figure 5-2-3. The cylinder was similarly affected upon heating, but the skin thickness varied. The crystallites were pure Cu. Experimental diffraction patterns compared to simulations from crystallographic data (software JEMS, camera length 829 mm, voltage 300 kV).

In the nanocomposite most of the diffraction spots were from randomly oriented Cu crystallites (see fig. 5-2-3). Some spots, attributed to a copper oxide (cuprite, Cu_2O), disappeared upon heating. The diffraction patterns of the crystallites with geometric shapes indicated pure Cu.

A similar effect was observed under SEM observation of tips at large probe currents.
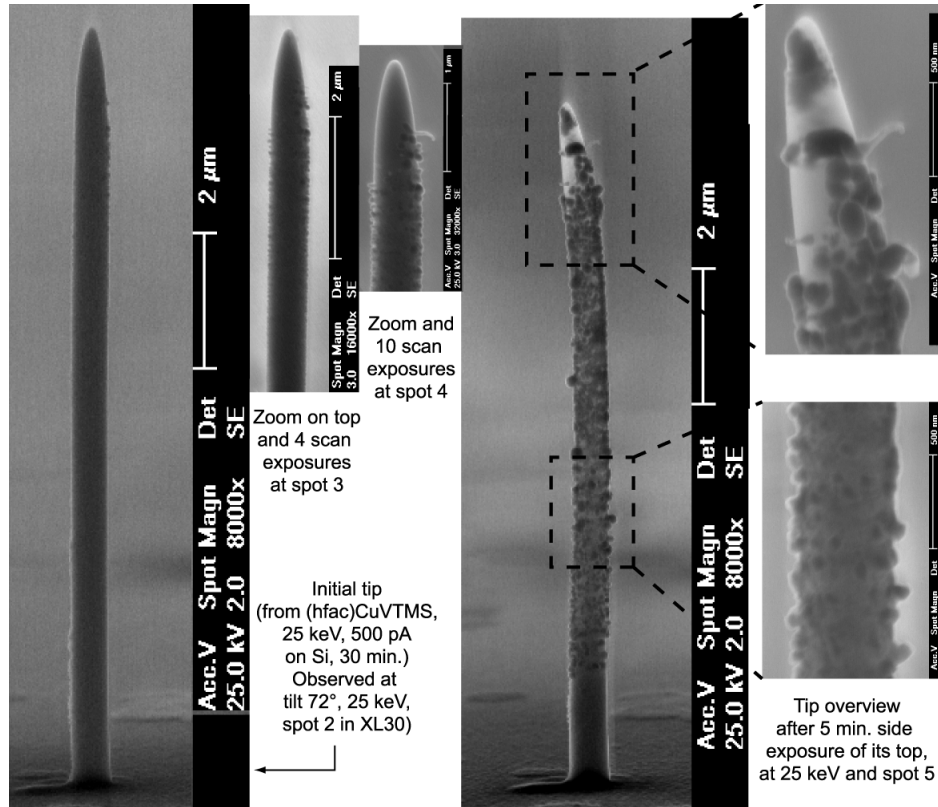
Figure 5-2-4. High vertical tips became rough and shortened under SEM observation.

Under tilted SEM observation at large spot currents, vertical tips roughened and shortened (see fig. 5-2-4). This was either a radiolytic effect or a consequence of electron-induced heating. Only the top was irradiated but the whole tip was affected, so heating was more probable. The energy deposited by the electron probe at the top was not easily dissipated through the narrow carbonaceous tip. A temperature gradient was established along the tip.

The grainy aspects of the tips deposited in longer time frames (see fig. 4-2-3) were explained by this effect. EDX analysis showed a larger Cu content, with respect to the other elements C, O, and F, in the grainy parts than in the smooth parts (see fig. 5-2-5).
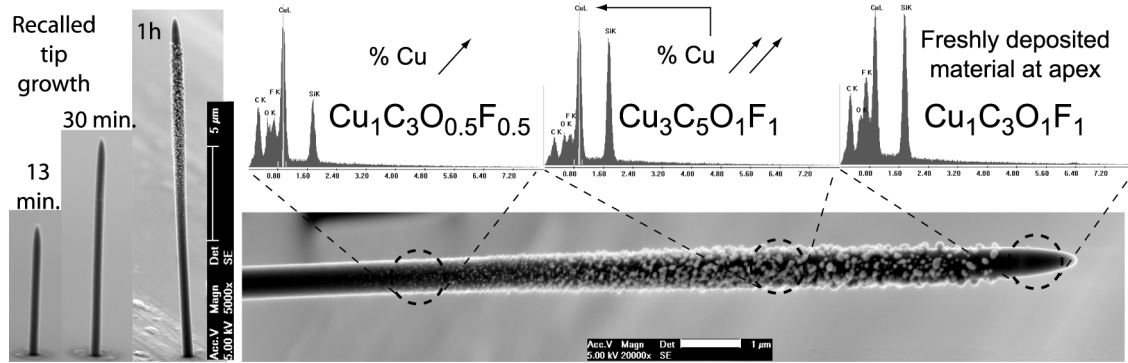
Figure 5-2-5. EDXS-measured Cu content (8 keV excitation) changes with morphology on the 1 h tip from fig. 4-2-3. The Si peak, mainly due to the substrate, was excluded.

Electron scattering and energy deposition in the tip were constant as soon as the tip cone was formed. On higher tips, the resulting temperature gradients between the top of the pillar and the substrate were larger. As a consequence, the precursor residence time decreased on the hot tip, and so did the growth rate. The previously deposited material was affected.

The following temperature estimation was made. In the carbon-rich material, the electron collision mean-free-path was 10 nm. As shown in §4-2, each electron traveled on average 1 μm in the tip cone before being scattered out, so it was submitted to 100 collisions. Approximately 2/3 of these were inelastic and transferred energy to the tip. The average energy losses were considered to be 280 and 40 eV for the C K and L-edges, respectively, and the corresponding collision cross-sections $\sigma_{C,K}=6.10^{-4}$ Å^2 and $\sigma_{C,L}=1.2.10^{-2}$ Å^2.[125] Each electron thus lost 3.3 keV in the tips. From a probe current of 500 pA, this corresponded to an average deposited power P = 1.7 μW. The temperature difference ΔT between the substrate and the top of the tip of surface S, height h, and thermal conductivity κ, was given by:

$$\Delta T = \frac{P.h}{S.\kappa} \qquad\qquad (5\text{-}2\text{-}1)$$

The value for κ was closer to the value for amorphous CVD carbon ($\sim$1 W/m.K) than to the value for pure Cu (395 W/m.K).[126, 127] For a tip diameter of 500 nm, at a height of 12 μm, κ=1 W/m.K led to ΔT=100°K. This explained why the Cu grains grew only on tips higher than 12 μm, after ½ h deposition.

Depositing tips with larger cylinders increased the temperature gradient. Tips deposited at higher probe currents were rough at lower heights and their Cu contents were higher.[128] Thermal effects were seen only after a certain deposit height (see fig. 5-2-6).
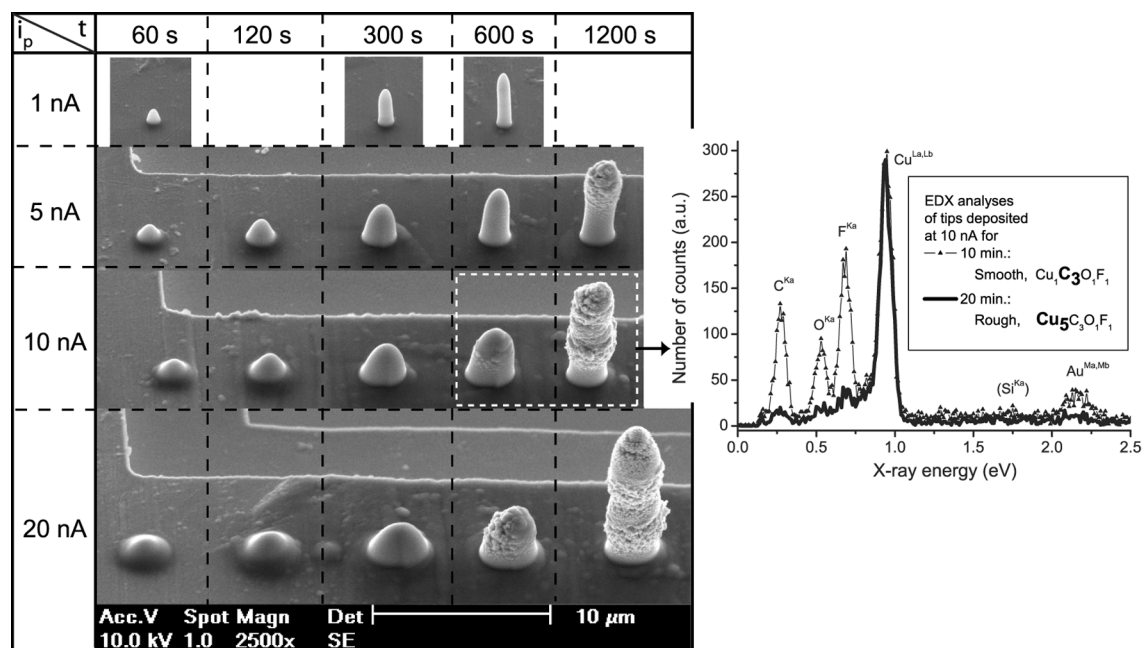
Figure 5-2-6. The transition height from smooth to rough tips depend on the probe current. Left, SEM views (tilt 72°) of tips deposited on an Au-coated TEM grid. Right, EDX analyses.

The Cu content in the deposits depended on the electron beam parameters, as observed with large beams.[129] A similar smooth-to-rough, polymeric-to-metallic transition was observed from $Co_2(CO)_8$.[130] From (hfac)CuVTMS, deposition of facetted Cu crystallites occurred when using as substrate a free-standing rod, which dissipates heat unefficiently.[131, 132]

Local heating thanks to a co-focused laser beam similarly induced the transition. The deposition regime was reversibly modified from smooth to rough (see fig. 5-2-7). The deposited tip diameter was larger when the tip was heated. In the conditions used (~100 mW incident on the substrate, 5 μm diameter spot), the laser-induced temperature increase was estimated to 90 ± 20°C.[133] The current monitoring directly indicated the transition to a larger tip diameter, and then returned to the saturation value reached on smooth tips. Unselective deposition, unnoticed in the S100, then recovered the whole tip and substrate during the rest of the experimental series.
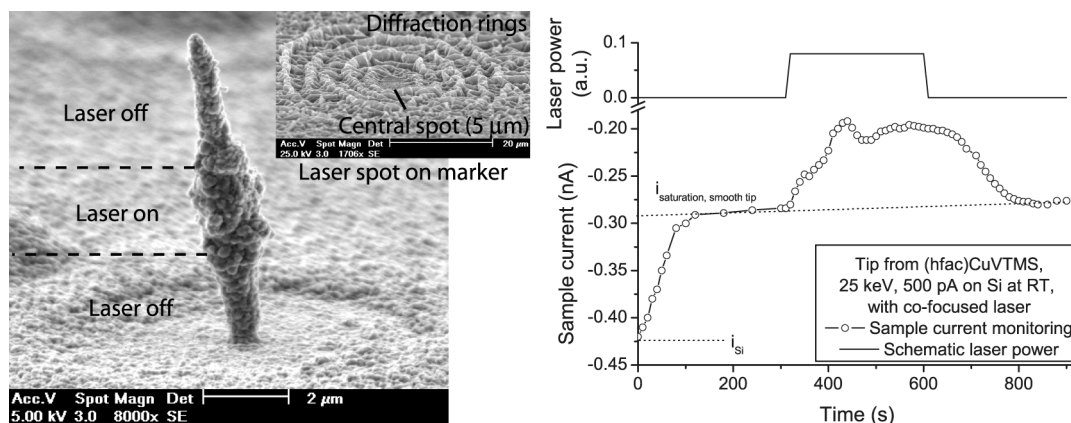
Figure 5-2-7. Reversible smooth-rough transition induced by a co-focused laser beam. Laser output 200 mW, direct injection into the vacuum chamber (no optical fibre). Left, SEM view (tilt 75°) of tip aspect when the laser is switched on or off. Right, sample current monitoring.

5-2-3 Electrical conduction in metal-containing deposits

Functional electrical nanodevices were created thanks to the FEB-induced deposition of metal-containing materials. As an example, single-wall C nanotubes were electrically contacted with the use of the inorganic gold precursor described in §4-1-4 (see fig. 5-2-8).
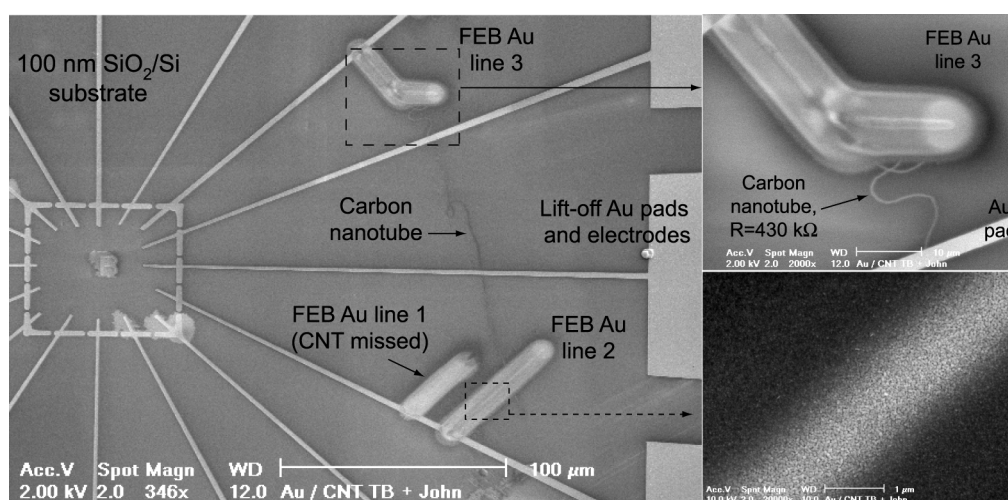
Figure 5-2-8. FEB line contacts to a single-wall C nanotube. SEM top views (2 and 10 kV). Deposition from $AuPF_3Cl$, at 25 keV, 100 nA, magn. 1kx, ½ h multiple line-scans.

The FEB line resistivities were measured as 43 ±8 μΩ.cm. This was 20 times larger than the value for bulk Au, probably because the conduction between percolating grains in the deposits was not as good as in bulk Au. Electrostatic force microscopy measured the resistance of the nanotube portion shown in inset as 430 kΩ (i.e. 10-15 kΩ/μm). The contact resistances were small in comparison. Nanoelectrical applications were envisioned.[134]

Co-containing FEB deposits were used to realize a miniaturized Hall sensor.[135, 136]
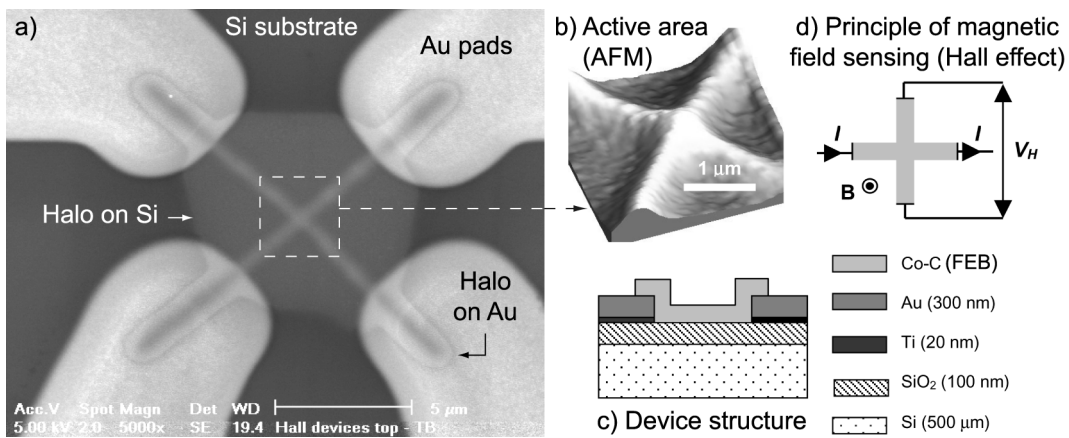
Figure 5-2-9. Sub-μm Hall device by FEB-induced deposition from $Co_2(CO)_8$. a) SEM top view (5 keV, scale bar 5 μm). b) AFM profile of the active area. c,d) Schematic principles.

The main thick lines were continuous thanks to the carbonaceous matrix (see fig. 5-2-9a). A thin halo was deposited around them. It was wider on Si than on Au. Since a thin probe (500 pA, 132 nm at 4σ, 25 keV) was used for deposition, the halo resulted from the BSE exposure. Other authors observed it but its origin had been misinterpreted.[137] Its contribution to electrical conduction was measured to be negligible. The active area was restricted to the overlap between the two lines and was 500x500 nm^2 (see fig. 5-2-9b). The electrical resistance of each of the lines was 2 kΩ, which corresponded to a resistivity of 7 μΩ.m (100 times the resistivity of pure Co, 6.2 μΩ.cm). Their composition was $Co_3C_6O_1$. The Co was present as nanocrystals.[130] The deposited material had a non-zero magnetic susceptibility.[138] The effect of a magnetic field was to induce a Hall voltage when a current flew through the device (see fig. 5-2-9d). The sensitivity was 0.9 V/AT. The active area thickness being 50 nm, the Hall coefficient was calculated as R_H=5.10^{-8} Ω.m/T, similar to that reported for Fe-Pt or Fe-Si thin films. This device was among

the smaller magnetic field sensors. Using a deposition machine with a smaller probe diameter could almost certainly increase its resolution further.

As the lines fused at currents above 1 mA, many devices were damaged between the FEB deposition and the electrical measurements, even by careful handling. More reliable measurements were obtained by monitoring *in-situ* the resistances (R) of depositing lines.
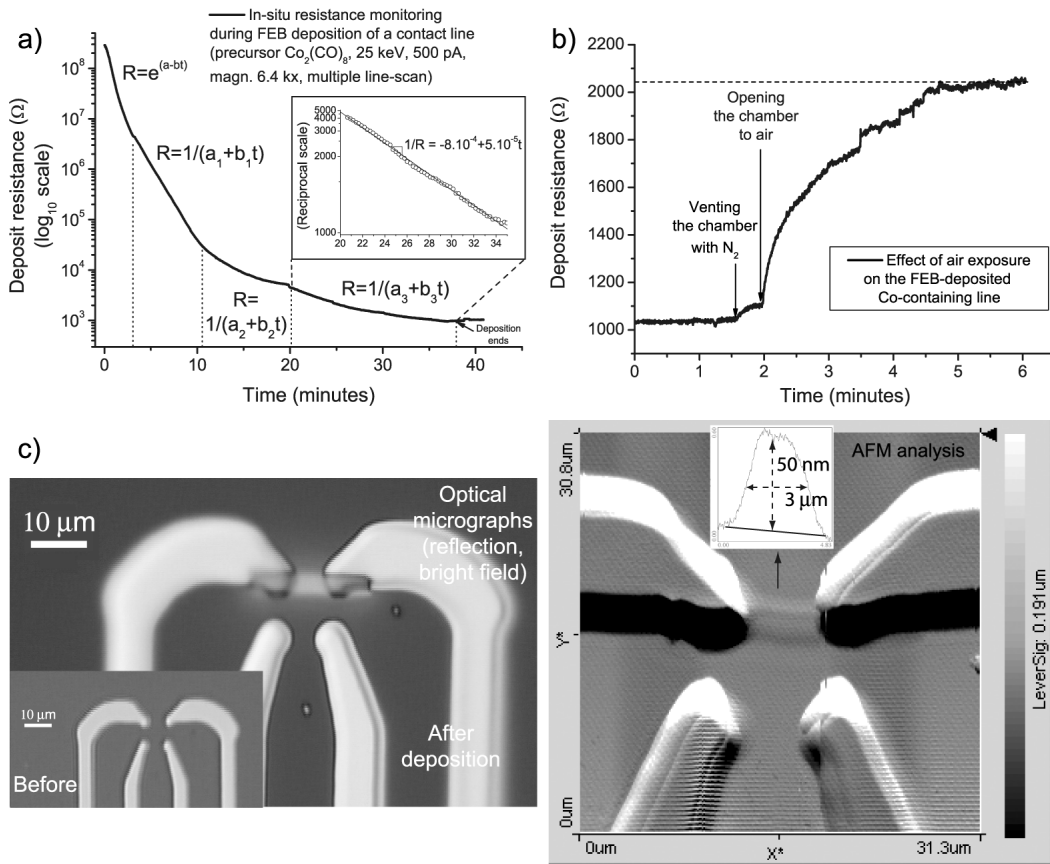
Figure 5-2-10. *In-situ* monitoring of the resistance of a depositing line. a) Line deposition. b) Resistance monitoring upon exposure to air. c) *Ex-situ* characterization of the deposit.

The resistance decreased over 5 decades during deposition (see fig. 5-2-10a). The measurement started at 300 MΩ and the final resistance of the 60 nm thick line (see fig. 5-2-10d) was 1.18 kΩ. The line was 5 μm long and 3 μm wide because of a slow but continuous beam drift (see fig. 5-2-10c). After an initially exponential decrease, the measured resistance decreased as the inverse power of the deposition time. The three successive decrease rates were due to

experimental realignments on the electrodes because of the drift. Supposing an ohmic conduction, the deposit resistance ($R_{deposit}$) and thickness (h_{dep}) were linked by:

$$R_{deposit} = \frac{\rho_{dep} l_{contact}}{S_{dep}} = \frac{\rho_{dep} l_{contact}}{w_{dep} h_{dep}} \qquad \textbf{(5-2-2)}$$

with ρ_{dep}: deposit resistivity; $l_{contact}$: effective resistor length between the electrodes; S_{dep}: deposit cross-sectional surface; w_{dep}: deposit width; h_{dep}: deposit thickness.

The line had a constant width and was deposited between two fixed electrodes. Only its thicknesses increased with time. A linear thickness increase ($h=h_0+\alpha t$) from a couple of values (R, h_0) explained the observed dependence:

$$R_{deposit} = \frac{\rho_{dep} l_{contact}}{w_{dep} h_0 + w_{dep} \alpha t} := \frac{1}{a + bt} \qquad \textbf{(5-2-3)}$$

In the last deposited section in fig. 5-2-10a, the deduced resistivity was $\rho_{dep}=14\,\mu\Omega.m$. It was similar but slightly larger than the value calculated on the whole device. The resistance was constant when deposition ceased. Opening the chamber to air increased the deposit resistance by a factor 2 (see fig. 5-2-10b). As the venting with N_2 had no effect, it was either an effect of O_2 or of moisture. Two mechanisms were imagined. The resistance increase was either due to an oxidation of the Co nanocrystals or to the O_2-induced quenching of free radicals in the carbonaceous matrix.

To study the role of the Co content, the experiment was repeated on a line containing only the carbonaceous matrix, as deposited from acrylic acid (see fig. 5-2-11c). The 700 nm thick resulting film had a resistance of 180 kΩ after deposition (see fig. 5-2-11a). Its resistivity was 0.94 Ω.m. In the former case, the conduction was thus mainly due to the Co nanocrystals and not to the C matrix. Interestingly, the resistance of the C-containing line increased every time that the beam was switched off (see fig. 5-2-11a). The 180 kΩ resistance of the deposited line increased overnight up to 430 kΩ.
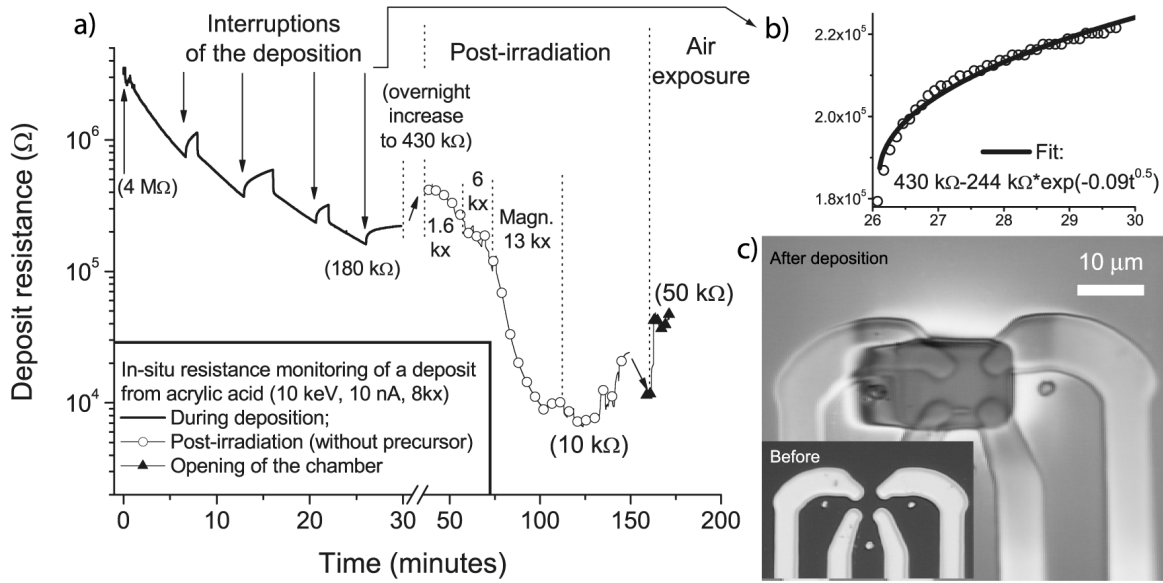
Figure 5-2-11. a) *In-situ* resistance monitoring during deposition, post-irradiation, and exposure to air of a C deposit. b) Detailed view and fit of a resistance increase when irradiation is interrupted. c) Optical micrographs, bright-field (an initial beam drift occurred).

The resistance increase was fitted by an exponential of the square root of the time (see fig. 5-2-11b). This indicated a diffusion-limited charge carrier recombination pathway (see fig. 5-2-12).
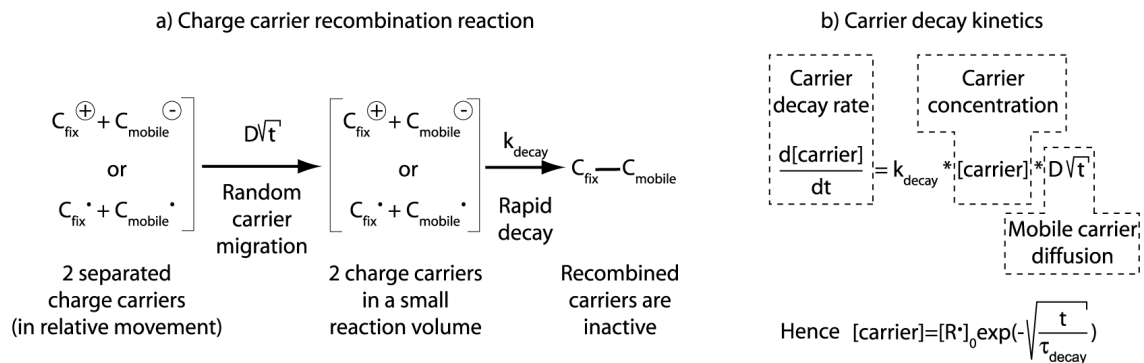
Figure 5-2-12. Charge carrier recombination model in carbonaceous materials, based on the decay rate observed in fig. 5-2-11. a) Proposed carrier recombination mechanism. b) The kinetics of reaction describes the experiment correctly.

When irradiating this line again without precursor, its resistance dropped down to 10 kΩ (see fig. 5-2-11a). The resistivity under irradiation was only 6.10^{-3} Ω.m. This was attributed to the breakage of C-C bonds under irradiation. The generated free radicals increased the low

concentration of charge carriers in the deposited amorphous carbon, as observed previously on silicone films.[139] Comparatively, the effect of turning off the beam from the Co-containing deposits was weak. As a conclusion, upon exposure to air, the oxidation of the Co nanocrystals was more probable to explain the decrease in conductivity.

5-2-4 Summary

At room temperature carbon-containing deposits were obtained from most of the C-containing organometallic precursors. Electron-induced polymerization appeared as the most probable mechanism. The deposited nanocomposites were unstable upon heating. Depositing on locally heated substrates, either by the electron beam or by a co-focused laser beam, yielded materials with higher metal contents. They had rougher aspects. Electrical applications of the metal-containing deposits were presented. Contacting single-wall carbon nanotubes was realized with the inorganic Au precursor. Sub-micrometric Hall sensors were realized with the polymeric Co-C mixture deposited from a cobalt carbonyl. The C matrix around the Co clusters contributed negligibly to conduction but prevented their complete oxidation.

Chapter 6 – Conclusion and future research

Les yeux d'une lumière invisible noyés,
Pensif, vous souhaitez déjà la bienvenue,
Dans notre gouffre d'ombre à l'immense inconnue !
Vous savez le total quand Dieu jette les dés !

Victor Hugo, la Légende des Siècles, XLVI, 106

The main results obtained during this study are summarized in Section 6-1. In Section 6-2, future research directions are proposed.

6-1 Conclusion

The Focused Electron Beam induced deposition process was successfully applied and studied in a dedicated setup.

6-1-A) Electron scattering in solids was demonstrated to have a profound effect on the outcome of the process.

- Carbon films were deposited from acrylic acid on Si and Au. At 10 keV with 100 nA probe current, the deposition rate of 67 nm/min over an exposed area of 3000 μm^2 was substrate-independent. Monitoring the sample current allowed for controlling *in-situ* the deposition rate at 5 and 10 keV, with increased sensitivity in the first nanometers due to a change in SE yield. The sample current continuously increased, mainly because of a decreasing BSE yield, and reached saturation when the film was thicker than 60% of the electron range. The deposition rate

depended on the power 0.58 of the probe current and on the power -0.32 of the exposed area. Christy's static deposition model was then adapted to fit a scanning deposition model. A radical-assisted mechanism is probable.

- Films with a composition $Cu_1C_3O_1F_1$ were deposited from (hfac)CuVTMS, at 3 to 25 keV and 10 nA, with different growth rates on different substrates, typically 2 nm/min over an exposed area of 3000 μm^2. The different growth rates were attributed to the differences in BSE yield and SE emission from the substrates, but the relative rôles of the high-energy electrons and the low-energy SE in the precursor fixation process could not be determined.

- Pure Au films were deposited from $AuPF_3Cl$ with a constant growth rate of 1 nm/min. over an exposed area of 3000 μm^2 on Si, at 5 and 10 keV. Monitoring indicated a decrease in the absorbed sample current, consistent with the increasing BSE and SE yields on heavier elements.

6-1-B) With a fixed beam, vertical tips were deposited from several organometallic compounds.

- Tips show three successive growth regimes: base, cone, and cylinder.

- Electron scattering is responsible for the tip shape and growth rate, which depend upon the precursor, but are independent of the substrate.

- The sample current monitors the tip growth rates from all the precursors, at all acceleration voltages, at all beam sizes and focusing conditions, and on all substrates, including patterned substrates. The obtained results were used to create a model of the forward scattered electron distribution.

6-1-C) By slowly moving the beam, 3D microstructures were built.

- When the structures were smaller than the electron range, the scattered electrons fixed the adsorbed precursor at each of interface crossed.

- The transmitted electrons were responsible for the deposition of secondary structures or caused nearby existing shapes to become thickened.

- The precursor flux was in the molecular flow regime. Deposition occurred symmetrically on both sides of the plane, which was defined by the direction of the needle and the vertical axis of the FEB.

- Surface diffusion was so small, as compared to gas-phase effects, that it could not be observed at the investigated scales.

6-1-D) The FEB-induced deposits were chemically analysed by micro-beam techniques (EDX, μ-ERDA, μ-FTIR, μ-Raman, μ-Reflectometry, and EELS).

- All organic compounds containing only C, H and/or O, deposited an amorphous material with a composition of $C_9H_{2\pm x}O_{1\pm x}$ (x<1). The C phase was 90% sp^2.

- Almost all of the volatile atoms (H, N, O, F, Cl), which were present in the precursor, were removed during deposition. An electron-induced desorption mechanism is probable.

- The deposits from acrylic acid had a density of 1.7 ± 0.2 g.cm^{-3} and an index of refraction of 1.45 ± 0.1, with an imaginary part of 6.10^{-4} to 4.10^{-2}.

- The growth rate was higher when using compounds with higher dipole moments because of the longer residence time of adsorbed molecules on surfaces.

- The C sp^2 fraction and the growth rate depended on the deposition temperature.

6-1-E) The metal content in deposits from organometallic compounds varied with the precursor composition and the deposition conditions.

- The atomic Cu content in deposits from (hfac)CuVTMS was increased from 16% to 50% by depositing on substrates locally heated to 100°C.

- The tip growth rate decreased during deposition because of beam-induced heating of the cone. High tips were annealed up to 100°C during deposition.

- Electrical micro-devices were built with Au- and Co-containing deposits.

6-2 Future research

Focused electron beam induced deposition of diamond should be possible at higher temperatures. For high deposition rates, the precursor needs to be acrylic, formic, or trifluoroacetic acid. Heating with the co-focused laser beam has two advantages. The non-resistive heating allows for sample current monitoring, making certain enough material is deposited for analysis. The *in-situ* reflectometry offers a second simultaneous measurement of the growth rate. With a 1W Ar^+ laser power in a 10 μm diameter spot on an Au substrate, it should be possible to investigate the effect of temperature up to 1000°C. Micro-Raman spectroscopy is the best analysis technique for measuring the sp^3 fraction. A possible application for the deposits could be wear-resistant coatings or tips.

The optical properties of the obtained nanocomposites (in particular the Rh-containing deposits, which have a non-absorbing P matrix) could be examined in depth with the *in-situ* reflectometry and the micro-spectrophotometric setup. Bright colours were seen in a series of deposits, indicating a large index of refraction and a small absorption coefficient. This is probably due to the high metal content (60% Rh) in this material.

The effects of metal content on the electrical conductivity of the deposits can be studied with the help of the *in-situ* resistance measurements. A rapid optimization of the deposition conditions, including co-focused laser heating for depositing pure metals, should be possible.

The electron-induced stripping of volatile elements was seen on simple compounds. Precursor polarity played an important role in the surface residence time of the adsorbed species. The choice of the precursors for future focused electron beam induced processes, such as area-selective particle beam-assisted metal etching, will need to consider these factors for increased efficiency.

Several chemical compounds may prove to be interesting for deposition. Among the options, samarium compounds could be used for strong magnetic deposits. Titanium and nickel compounds may prove useful for memory shape alloy deposits. Doped alumina garnets could be deposited from mixtures of rare-earth CVD precursors. The methodology developed in this study will hopefully contribute to future practical nanofabrication tools.

A n n e x e s

ANNEX 1: PRINCIPLES OF ELECTRON SCATTERING

The principles of electron scattering by atoms are briefly recalled. Consider that a single electron impinges on a solid material: scattering begins as the electron crosses the surface. The average deflection angle at each collision depends on the deposit composition and on the electron energy according to the following laws.[1] Most of the electrons are scattered inside the characteristic angles θ_0 (by elastic scattering) or θ_E (by inelastic scattering):

Elastic scattering:

$$\frac{d\sigma_{\acute{e}l}}{d\Omega} = \frac{e^4 Z^2}{4(4\pi\varepsilon_0)^2 m^2 v^4} \frac{1}{\left[\sin^2\left(\frac{\theta}{2}\right) + \sin^2\left(\frac{\theta_0}{2}\right)\right]^2}$$

with $\quad \sin\left(\frac{\theta_0}{2}\right) = \dfrac{h}{4\pi m v a_H Z^{-\frac{1}{3}}}$
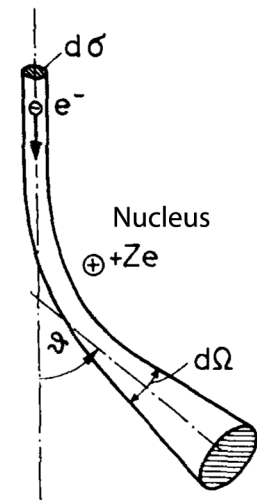
Inelastic scattering:

$$\frac{d\sigma_{in\acute{e}l}}{d\Omega} = \frac{4e^4 Z}{(4\pi\varepsilon_0)^2 m^2 v^4} \frac{1 - \dfrac{1}{\left[1 + \dfrac{\theta^2 + \theta_E^2}{\theta_0^2}\right]^2}}{\left(\theta^2 + \theta_E^2\right)^2}$$

with $\quad \theta_E = \dfrac{J}{4E}$

Figure A-1. Screened Rutherford scattering of electrons by atoms. $\sigma_{\acute{e}l,\ in\acute{e}l}$: cross-sections for elastic and inelastic scattering, respectively; Ω: solid angle corresponding to the angle θ; e, electron charge; Z, atomic number of the scattering atom; ε_0, electrical permittivity of vacuum; m, electron mass; v, electron speed; a_H the Bohr radius; J, mean ionization energy of the scattering atom; E, kinetic energy of the incident electron.

For instance, for 10 keV electrons scattered by C atoms $\theta_0 = 3.57°$, and by Au atoms $\theta_0 = 8.44°$. Inelastic scattering concerns narrower angles: $\theta_E = 0.08°$ on C and $\theta_E = 1.14°$ on Au.[1]

The incoming electron occasionally escapes the solid directly by experiencing a large-angle single-scattering event. In the most probable contrary case, it penetrates further and rapidly (≤ 30 nm) enters a multiple-scattering regime with a succession of collisions.[2] Typical mean-free-path (MFP) lengths are recalled in the following table ([3], p. 83):

Element		Energy (keV)			
		5	10	25	
C (Z=6, $v=\sigma_{inél}/\sigma_{él} \sim 3$)	$\sigma_{él}$	0.11	0.055	0.022	x 10^{-16} cm^2
	$\Lambda_{él}$	9	18	45	nm
	Λ_t	2.3	4.5	12	
Al (Z=13, $v=\sigma_{inél}/\sigma_{él} \sim 1.5$)	$\sigma_{él}$	0.31	0.16	0.065	x 10^{-16} cm^2
	$\Lambda_{él}$	5	10	25	nm
	Λ_t	2	4	10	
Cu (Z=29, $v=\sigma_{inél}/\sigma_{él} \sim 0.6$)	$\sigma_{él}$	0.64	0.37	0.18	x 10^{-16} cm^2
	$\Lambda_{él}$	1.8	3.2	6.5	nm
	Λ_t	1.1	2.0	4.2	
Ag (Z=47, $v=\sigma_{inél}/\sigma_{él} \sim 0.4$)	$\sigma_{él}$	1.15	0.71	0.36	x 10^{-16} cm^2
	$\Lambda_{él}$	1.5	2.4	4.5	nm
	Λ_t	1.0	1.7	3.3	
Au (Z=79, $v=\sigma_{inél}/\sigma_{él} \sim 0.2$)	$\sigma_{él}$	1.6	1.05	0.59	x 10^{-16} cm^2
	$\Lambda_{él}$	1.0	1.6	2.9	nm
	Λ_t	0.9	1.3	2.4	

Table A-I. Elastic cross-sections $\sigma_{él}$, elastic mean-free-path lengths $\Lambda_{él}$, and total MFP lengths including inelastic collisions Λ_t, for different elements and electron energies.

The collision MFP decreases with the increasing atomic number of the material and with the decreasing electron energy. Inelastic collisions dominate in light elements. Elastic collisions are dominant in heavy elements.

ANNEX 2: ELECTRON RANGE AND BACKSCATTERING RANGE

The backscattering range r_B is the larger distance from the incidence point at which a backscattered electron (BSE) can exit. It obeys the following relation:[4]

$$r_B = \frac{CR_m\gamma}{1+\gamma}$$ (A-2-1)

Backscattering range r_B (in nm) as a function of maximum range R, a constant C empirically fixed as 1.1, and the parameter $\gamma = 0.19 \cdot Z^{\frac{2}{3}}$.

The maximum range R_m is the larger depth down to which a PE can travel. It is given by:

$$R_m = 2.76 \cdot 10^{-4} \frac{A \cdot E_0^{\frac{5}{3}}}{Z^{\frac{8}{9}} \cdot \rho}$$ (A-2-2)

Maximum electron range R_m (in nm) as a function of primary beam energy E_0 (in eV), substrate atomic mass A (g), atomic number Z, and density ρ (in g/cm^3).

Element				Energy				
Symbol	Z	A (g.mol^{-1})	ρ (g.cm^{-3})	3 keV	5 keV	10 keV	15 keV	25 keV
C	6	12.0	2.26	179	418	1322	2591	6050
Al	13	27.0	2.70	171	399	1261	2471	5771
Si	14	28.1	2.33	193	451	1425	2792	6520
Cu	29	63.5	8.96	60	140	441	865	2019
Ag	47	107.9	10.50	57	132	418	820	1914
Au	79	197.0	19.30	36	83	263	515	1204

Table A-2-I. Maximum ranges R_m (in nm) calculated from eq. **(A-2-2)**, *vs.* beam energy.

With the values shown in the above table, the following BSE ranges were calculated:

Energy Element	3 keV	5 keV	10 keV	15 keV	25 keV
C	75	176	556	1091	2547
Al	95	223	705	1381	3225
Si	110	258	815	1598	3731
Cu	42	98	309	606	1414
Ag	44	103	325	637	1488
Au	30	71	223	438	1023

Table A-2-II. Corresponding backscattering ranges r_B (in nm) calculated from eq. **(A-2-1)**.

For a single element, both R_m and r_B increase with energy. No simple evolution is seen between different elements because of the number of parameters involved. r_B is always smaller than R_m. They have closer values in heavier elements, due to the reducting "diffusion depth" (x_D in fig. 4-1-1a, the depth at which all electrons propagate isotropically in the solid) with increasing Z.

ANNEX 3: BACKSCATTERING YIELDS

The following table summarizes the dependence of the BSE yields at several energies on usual materials. The values were compiled from D.C. Joy's "Database of Electron-Solid interactions".[5] This database compiles results published until 2001.[1]

Element		Energy				
Symbol	Z	3 keV	5 keV	10 keV	15 keV	25 keV
C	6	7.4 ±1.6	7.8 ±1.1	7.0 ±0.3	6.3 ±0.5	5.6 ±0.5
Si	14	20.3 ±1.0	19.4 ±1.0	18.3 ±1.1	17.7 ±1.3	16.8 ±1.4
Ti	22	28.7 ±1.0	25.9 ±1.0	25.6 ±1.3	25.8 ±1.0	24.7 ±1.6
Cu	29	35.4 ±4.1	34.3 ±3.6	32.7 ±2.4	31.8 ±1.4	31.4 ±1.1
Ag	47	39.1 ±3.9	39.4 ±2.7	40.7 ±2.1	41.0 ±1.0	41.0 ±1.0
Au	79	43.9 ±2.3	45.5 ±2.1	48.0 ±1.1	49.0 ±1.3	49.8 ±1.4
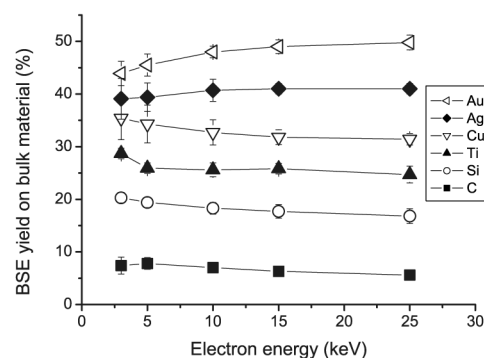
Table A-3. Average values and standard deviations of BSE yield data (in %).

The BSE yield η increases monotonically with the atomic number Z at all energies. Under normal incidence at 20 keV it obeys the following empirical relation:

$$\eta = -0.0254 + 0.016Z - 1.8.10^{-4}Z^2 + 8.3.10^{-7}Z^3 \qquad \textbf{(A-3)}$$

Several authors have studied the BSE yields in dedicated setups (see fig. A-3a), on evaporated films with increasing thicknesses and at various acceleration energies (see fig. A-3c,d).[2, 6, 7]

---

[1] It was also available on the Internet at http://web.utk.edu/~srcutk/htm/interact.htm or graphically at http://www.napchan.com/bse/mat_list.htm#TOC1.
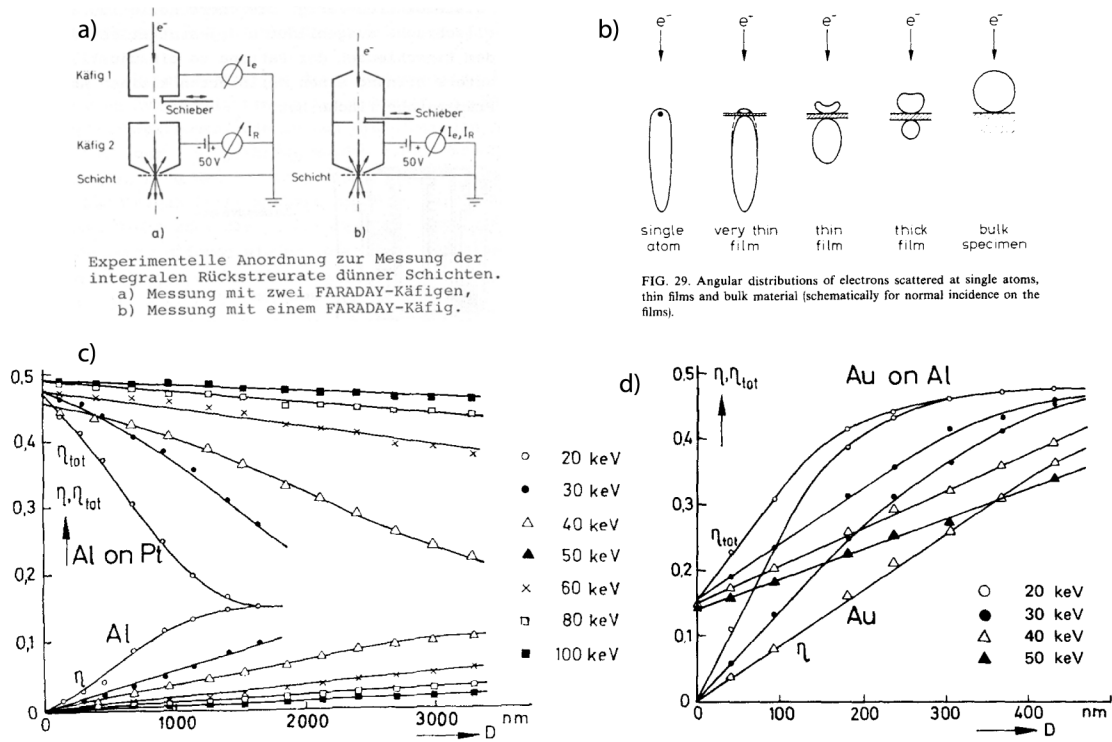
Figure A-3. BSE yields of evaporated films on substrates. a) Experimental setup.[6] b) Schematic evolution of scattering. c) BSE results for Al films (free-standing, bottom; on Pt, top) at several energies. d) *Idem* for Au films (free-standing, bottom; on Al, top).[2]

The BSE yield of thin films increases with increasing thickness, until reaching saturation at a thickness that depends on the electron energy (see fig. A-3c,d). The angular distribution of BSE also varies (see fig. A-3b). When deposited on a substrate, the BSE yield of the layered structure evolves with increasing film thickness from the BSE yield of the substrate to that of the bulk film, with the same characteristic thickness as on the free-standing films.

A good review of the physical models and practical consequences of electron backscattering can be found in [2].

ANNEX 4: SECONDARY ELECTRON EMISSION YIELDS

The absolute SE yield is difficult to measure accurately. Due to the influence of a number of poorly-controlled effects (surface contamination, oxidation, charging, second- or third generation SE emission…), values available from the literature show considerable dispersion.[5, 8] But on such different materials as C (or Si) and Au, the SE yield is higher on the heavier element whatever the energy. Above 3 keV, the SE yield decreases with the increasing electron energy.

Element		Energy				
Symbol	Z	3 keV	5 keV	10 keV	15 keV	25 keV
C	6	31 ±10	27 ±14	14	11.5 ±1.3	5.9 ±1.0
Si	14	42 ±30	36 ±18	28 ±9	20 ±9.4	12.5 ±6.3
Ti	22	36 ±22	34 ±6.5	29	NA	13
Cu	29	68 ±21	49 ±17	33 ±16	22	16
Ag	47	75 ±13	50 ±14	34 ±7	28.7 ±3.5	21.2 ±2.8
Au	79	86 ±22	54 ±18	39 ±15	32 ±13	20 ±10
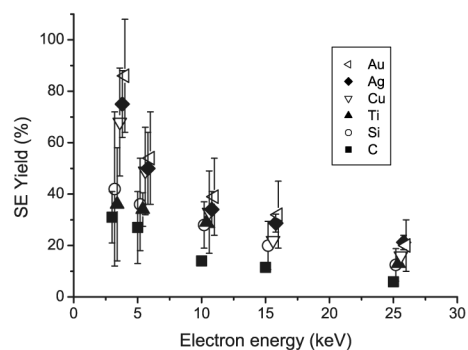
Table A-4. Average values and standard deviations of SE yield data (in %). NA: not available. Numbers without error margin are from a single experimental result. The plotted points were offset for readability.

SE are emitted only from the topmost layers of the sample, but they are released both by PE and BSE. Good reviews of the physics of SE emission can be found in [9, 10].

ANNEX 5: X-RAY TRANSITION ENERGIES

The excitation of heavier elements requires higher primary beam energies ([11], p. 276).
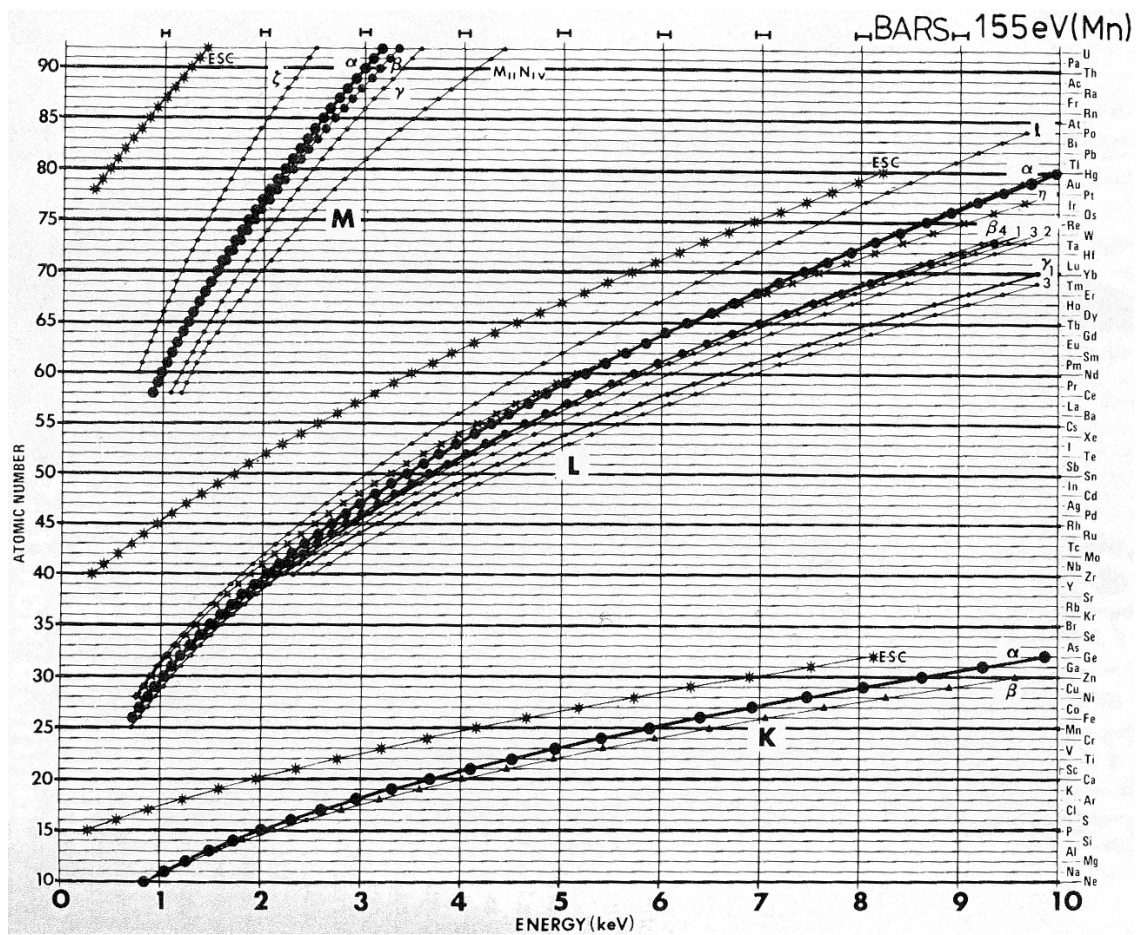
Figure A-5. X-Ray edge energies of the elements in the 0-10 keV range.

ANNEX 6: MOLECULAR STRUCTURES OF THE PRECURSORS USED

The precursors used in this study have the following molecular formulae.

Bis-hexafluoroacetylacetonato-
Copper(II)
Cu(hfac)$_2$
CAS 14781-45-4

hexafluoroacetylacetonato-
Copper(I)-methylhexenyl
(hfac)CuMHY

di-µ-chloro-tetrakis-
trifluorophosphine-di-Rhodium,
CAS 14876-98-3

hexafluoroacetylacetonato-
Copper(I)-Vinyltrimethylsilane
(hfac)CuVTMS
CAS 139566-53-3

hexafluoroacetylacetonato-
Copper(I)-dimethylbutene
(hfac)CuDMB

di-µ-chloro-tetrakis-
(phosphorous trifluoride-κP)-di-Iridium
CAS 28237-90-3

dimethyl-Gold(III)-
trifluoroacetylacetonate
Me$_2$Au(tfac)
CAS 63470-53-1

chloro-Gold(I)-
trifluorophosphine,
CAS 141845-34-3

(Trimethyl)methylcyclo-
pentadienylplatinum
CAS 94442-22-5

Acrylic acid
CAS 79-10-7

Figure A-6-1. Cu, Rh, Ir, Au, Pt precursors and a carbon precursor used.

ANNEX 7: LIST OF ABBREVIATIONS USED

The following abbreviations were used.

Acac	Acetylacetonate ligand
a-C:H	Hydrogenated amorphous Carbon
AES	Auger electron spectroscopy
AFM	Atomic force microscopy
BSE	Backscattered electron
Cp	Cyclopentadienyl ligand
CVD	Chemical vapour deposition
EBL	Electron-beam lithography
EDX	Electron-dispersive X-ray spectroscopy
EELS	Electron energy loss spectroscopy
EM	Electron Microscopy
ERDA	Elastic recoil detection analysis
FEB	Focused electron beam
FEG	Field-emission gun
FIB	Focused ion beam
FTIR	Fourier transform infrared
hfac	Hexafluoroacetylacetonate
HRTEM	High-resolution TEM
Me	Methyl group

NPGS	Nanometer pattern generating system
PE	Primary Electron
RBS	Rutherford backscattering
RHEED	Reflection high-energy electron diffraction
RT	Room Temperature
SE	Secondary Electron
SEM	Scanning electron microscope
STM	Scanning tunneling microscopy
TEM	Transmission Electron Microscope
TEOS	Tetraethyl orthosilicate
tfac	Trifluoroacetylacetonate
VTMS	Vinyl-trimethylsilane

Bibliography

References of Chapter 1

[1] U. F. W. Behringer and P. Vettiger, *Repair techniques for Si transmission masks used for submicron lithography*, **J. Vac. Sci. Technol. B 4**, 94-99 (1986)

[2] T. Bret *et al.*, *Beam-induced etching*, Pat. n°(submitted) (2005).

[3] W. Fritzsche *et al.*, *Making electrical contact to single molecules*, **Nanotechnology. 9**, 177-83 (1998)

[4] K. Mølhave *et al.*, *Constructing, connecting and soldering nanostructures by environmental electron beam deposition*, **Nanotechnology 15**, 1047-1053 (2004)

[5] F. Floreani *et al.*, *Operation of high power field emitters fabricated with electron beam deposition and concept of a miniaturised free electron laser*, **Microelectron. Eng. 57-8**, 1009-1016 (2001)

[6] K. I. Schiffmann, *Investigation of fabrication parameters for the electron beam induced deposition of contamination tips used in AFM*, **Nanotechnology 4**, 163-169 (1993)

References of Chapter 2

[1] E. Gehrcke and R. Seeliger, *Über Oberflächenladungen auf Leitern im Vakuum*, **Verhandlungen der Deutschen Physikalische Gesellschaft 15**, 438-450 (1913)

[2] J. E. Henderson, *A pseudo photographic effect of slow electrons*, **Phys. Rev. 29**, 360 (1927)

[3] P. H. Carr, *A new method of recording electrons*, **Phys. Rev. 33**, 1068 (1929)

[4] O. Goche *et al.*, *Sur une méthode d'enregistrement des électrons*, **Bulletin de la Classe des Sciences/Académie Royale de Belgique 20**, 447-456 (1934)

[5] M. A. Dauvillier, *La spectrographie des Rayons X de grande longueur d'onde*, **J. Phys. Rad. VIII**, 1-10 (1927)

[6] D. L. Webster *et al.*, *The measurement of X-ray intensities as functions of voltage, up to 180 kV*, **Rev. Sci. Instrum. 3**, 729-749 (1932)

[7] J. J. Trillat and R. Mérigoux, *Sur les effets produits par le bombardement d'une surface métallique par des électrons rapides*, **J. Phys. Rad. 10**, 245-249 (1939)

[8] G. F. Bahr *et al.*, *High-voltage electron microscopy*, **J. Appl. Phys. 37**, 2900-2907 (1966)

[9] A. Kumao *et al.*, *Studies on specimen contamination by TEM*, **J. Electron. Microsc. 30**, 161-170 (1981)

[10] E. H. Hirsch, *Image formation by electron bombardment of metal targets*, **Brit. J. Appl. Phys. 11**, 547-550 (1960)

[11] T. Djenizian *et al.*, *Electron-beam induced carbon deposition used as a mask for CdS deposition on Si(100)*, **Electrochimica Acta 47**, 891-897 (2001)

[12] A. E. Shaw, *Electron orbits in crossed electric and magnetic fields*, **Phys. Rev. 44**, 1006-1011 (1933)

[13] R. Lariviere Stewart, *Insulating films formed under electron and ion bombardment*, **Phys. Rev. 45**, 488-490 (1934)

[14] C. W. Oatley, *The early history of the scanning electron microscope*, **J. Appl. Phys. 53**, R1-R13 (1982)

[15] D. McMullan, *Scanning Electron Microscopy 1928-1962*, **Scanning 17**, 175-185 (1995)

[16] J. H. L. Watson, *An effect of electron bombardment upon carbon black*, **J. Appl. Phys. 18**, 153-161 (1947)

[17] E. F. Burton *et al.*, *Specimen changes due to electron bombardment in the electron microscope*, **Nature 160**, 565-567 (1947)

[18] H. König, *Die Rolle der Kohle bei elektronenmikroskopischen Abbildungen*, **Naturwissenschaften 9**, 261-265 (1948)

[19] Y. Mizushima *et al.*, *Specimen contamination in electron microscope*, **J. Phys. Soc. Japan 11**, 463-464 (1956)

[20] J. H. L. Watson, *Specimen contamination in Electron Microscopes*, **J. Appl. Phys. 19**, 110-111 (1948)

[21] J. Hillier, *On the investigation of specimen contamination in the electron microscope*, **J. Appl. Phys. 19**, 226-230 (1948)

[22] K. M. Poole, *Electrode contamination in an electron optical system*, **Proc. Phys. Soc. London B 66**, 542-547 (1953)

[23] A. E. Ennos, *The origin of specimen contamination in the electron microscope*, **Brit. J. Appl. Phys. 4**, 101-106 (1953)

[24] A. E. Ennos, *The sources of electron-induced contamination in kinetic vacuum systems*, **Brit. J. Appl. Phys. 5**, 27-31 (1954)

[25] H. Akahori, *Contamination dependence on the electron beam irradiation*, **J. Electron. Microsc. 12**, 269-270 (1963)

[26] R. L. Patterson and C. M. Wayman, *Study of contamination rates in an electron microscope*, **Rev. Sci. Instrum. 34**, 1213-1215 (1963)

[27] G. V. T. Ranzetta and V. D. Scott, *Specimen contamination in Electron-Probe Microanalysis and its reduction using a cold trap*, **J. Sci. Instrum. 43**, 816-819 (1966)

[28] D. R. Beaman and J. A. Isasi, *Electron Beam Microanalysis - Part 2*, **Materials Research and Standards 11**, 12-56 (1971)

[29] H. König, *Verkohlung organischer Objekte durch Elektronen*, **Z. Phys. 129**, 483-490 (1951)

[30] A. Lempicki, *A demountable vacuum system for secondary emission studies*, **J. Sci. Instrum. 32**, 221-223 (1955)

[31] G. A. Harrower, *Dependence of electron reflection on contamination of the reflecting surface*, **Phys. Rev. 102**, 1288-1289 (1956)

[32] C. J. Powell *et al.*, *Effects of contamination on the characteristic loss spectrum of W*, **Phys. Rev. 110**, 657-660 (1958)

[33] U. Decker, *Kontrastumkehr im Elektronen-Emissions-Mikroskop*, **Z. Phys. 174**, 460-463 (1963)

[34] Y. Uchikawa *et al.*, *The Ion-induced Emission Electron Microscope and an image contrast due to specimen contamination*, **Jpn. J. Appl. Phys. 8**, 436-442 (1969)

[35] R. Speidel, *Kornlose und höchstauflösende Fixierung von Ionen- und Elektronenbildern mittels lichtoptischer Interferenzfilter*, **Z. Phys. 154**, 238-263 (1959)

[36] G. Möllenstedt and H. Düker, *Emissionsmikroskopische Oberflächenabbildung mit Elektronen, die durch schrägen Ionenbeschubb ausgelöst wurden*, **Optik 10**, 192-203 (1953)

[37] G. Möllenstedt and W. Hubig, *Substanzdifferenzierung im Elektronen-Emissionsmikroskop*, **Optik 11**, 528-539 (1954)

[38] E.-L. Huguenin, *Sur le microscope électronique à photoémission*, **Ann. Phys. 13**, 214-266 (1957)

[39] U. Decker, *Kontrasterhöhung im SE-emissionsmikroskop durch Beseitigung der Objekt-Kontamination mittels Ionenbeschuss*, **Z. Phys. 172**, 556-562 (1963)

[40] L. Mayer, *Photocontrol of growth rate of thin polymer films formed by electron bombardment*, **J. Appl. Phys. 34**, 2088-2093 (1963)

[41] M. Wendt, *The role of contamination layers in Electron Probe Microanalysis*, **Kristall u. Technik 15**, 1367-1375 (1980)

[42] H. G. Heide, *Elektronenmikroskopie von Objekten unter Atmosphärendruck oder unter Drucken, welche ihre Austrocknung verhindern*, **Naturwissenschaften 47**, 313-317 (1960)

[43] G. Dupouy *et al.*, *L'observation des objets en milieu gazeux. Application à l'étude de la contamination dans le microscope électronique*, **C. R. Acad. Sci. (Paris) 254**, 3786-3791 (1962)

[44] J. S. Duerr and R. E. Ogilvie, *Electron Probe Microdetermination of C in Fe alloys*, **Analytical Chemistry 44**, 2361-2367 (1972)

[45] H. Konuma, *Rate of C contamination on Cu, Fe and Al targets in gas flows by an electron microprobe*, **Mikrochimica Acta II**, 99-108 (1983)

[46] M. T. Postek, *An approach to the reduction of hydrocarbon contamination in the SEM*, **Scanning 18**, 269-274 (1996)

[47] D. Wang *et al.*, *Lithography using electron beam induced etching of a C film*, **J. Vac. Sci. Technol. B 13**, 1984-1987 (1995)

[48] E. Zehender, *Die Bildung von Kohleschichten auf elektronenmikroskopischen Präparaten*, **Optik 16**, 522-526 (1959)

[49] T. Komoda and N. Morito, *Experimental study of the specimen contamination in the electron microscope*, **J. Electron. Microsc. 9**, 77-80 (1960)

[50] E. Yoda and B. Siegel, *Reduction of contamination in reflection electron diffraction*, **J. Appl. Phys. 33**, 1419-1422 (1962)

[51] M. Baker *et al.*, *Etude de la contamination dans un système de pompage*, **Le Vide 127**, 22-27 (1967)

[52] E. K. Brandis *et al.*, *Reduction of C contamination in the SEM*, **SEM** 505-510 (1971)

[53] J. T. Fourie, *The controlling parameter in contamination of specimens in electron microscopes*, **Optik 44**, 111-114 (1975)

[54] H. G. Heide, *Die Restgas-zusammensetzung im Elektronenmikroskop*, **Z. Angew. Phys. XVII**, 70-72 (1963)

[55] R. K. Hart *et al.*, *The contamination of surfaces during high-energy electron irradiation*, **Phil. Mag. 21**, 453-467 (1970)

[56] A. T. Marshall, *Residual gas analysis in a SEM*, **J. Microsc. 133**, 119-120 (1984)

[57] R. Buhl, *Verringerung der Kontamination durch Ionen-Bombardement der das Präparat umgebenden Wände*, **Optik 19**, 122-131 (1962)

[58] U. R. Bance *et al.*, *Hydrocarbon contamination in vacuum dependent scientific instruments*, **Vacuum 28**, 489-496 (1978)

[59] G. Love *et al.*, *Sources of contamination in electron optical equipment*, **Scanning 4**, 32-39 (1981)

[60] N. Davidson and J. Hillier, *Single crystal electron diffraction by micro-crystalline materials*, **J. Appl. Phys. 18**, 499-511 (1947)

[61] G. M. Rackham and J. A. Eades, *Specimen contamination in the electron microscope when small probes are used*, **Optik 47**, 227-232 (1977)

[62] B. Bauer and R. Speidel, *Herabsetzung der Kontaminationsrate im STEM bei Druck von 10^{-5} Torr*, **Optik 48**, 237-246 (1977)

[63] J. S. Wall, *Contamination in the STEM at ultra high vacuum*, **SEM 1**, 99-106 (1980)

[64] N. Yoshimura *et al.*, *Mechanism of contamination build-up induced by fine electron probe irradiation*, **Vacuum 33**, 391-395 (1983)

[65] P. Charalambous, Ph. D. Thesis: *Image data collection, contamination and beam writing in STEM*, University of London, Queen Elizabeth College, (1982).

[66] H. Konuma, *Rate of C contamination on Al targets in a high vacuum electron excitation X-ray tube*, **Jpn. J. Appl. Phys. 18**, 357-362 (1979)

[67] G. Möllenstedt and C. Jönsson, *Elektronen-Mehrfachinterferenzen an regelmässig hergestellten Feinspalten*, **Z. Phys. 155**, 472-474 (1959)

[68] A. N. Broers, *Combined electron and ion beam processes for microelectronics*, **Microelectron. Reliab. 4**, 103-105 (1965)

[69] R. W. Christy, *Formation of thin polymer films by electron bombardment*, **J. Appl. Phys. 31**, 1680-1683 (1960)

[70] P. White, *Electron-beam initiated polymerization of an organic vapour adsorbed on a metal surface*, **J. Phys. Chem. 67**, 2493-2494 (1963)

[71] I. Haller and P. White, *Polymerization of butadiene gas on surfaces under low energy electron bombardment*, **J. Phys. Chem. 67**, 1784-1788 (1963)

[72] H. T. Mann, *Electrical properties of thin polymer films. I. Thickness 500-2500 Å*, **J. Appl. Phys. 35**, 2173-2179 (1964)

[73] R. W. Christy, *Electrical properties of thin polymer films. II. Thickness 50-150 Å*, **J. Appl. Phys. 35**, 2179-2184 (1964)

[74] L. Holland and L. Laurenson, *The electrical properties of silicone films polymerized by electron bombardment*, **Vacuum 14**, 325-332 (1964)

[75] L. E. Babcock and R. W. Christy, *Electron-beam-deposited thin polymer film - electrical properties vs. bombarding current*, **J. Appl. Phys. 43**, 1423-1432 (1972)

[76] B. H. Choi *et al.*, *Electrical properties of electron-beam exposed Si dioxides and their applications to nano-devices*, **Jpn. J. Appl. Phys. Part 1 37**, 6996-6997 (1998)

[77] D. Kunze *et al.*, *Polymerization adsorbierter Kohlenwasserstoffe bei Elektronenbeschuss*, **Z. Angew. Phys. 22**, 69-75 (1967)

[78] R. Angelova *et al.*, *On the controlled deposition of conducting films by means of an electron beam*, **Radio Engineering and Electronic Physics 13**, 161-163 (1968)

[79] R. Castaing and J. Descamps, *Sur la contamination des échantillons dans le microanalyseur à sonde électronique*, **C. R. Acad. Sci. (Paris) 238**, 1506-1508 (1954)

[80] L. Reimer and M. Wächter, *Contribution to the contamination problem in TEM*, **Ultramicroscopy 3**, 169-174 (1978)

[81] M. Amman *et al.*, *AFM study of EB written contamination structures*, **J. Vac. Sci. Technol. B 14**, 54-62 (1996)

[82] K. H. Müller, *Speed-controlled electron-microrecorder. Part 1*, **Optik 33**, 296-311 (1971)

[83] K. H. Müller, *Speed-controlled electron-microrecorder. Part 2*, **Optik 33**, 331-343 (1971)

[84] G. S. Zhdanov and B. N. Vedstner, *Mechanism behind formation of hydrocarbon impurities upon surfaces irradiated by a narrow electron beam*, **Doklady Akademii Nauk SSSR 176**, 1040-1043 (1967)

[85] J. H. De Boer, *The dynamical character of adsorption*, 2nd ed., Clarendon Press, Oxford 1968.

[86] A. N. Broers *et al.*, *Electron-beam fabrication of 80-Å metal structures*, **Appl. Phys. Lett. 29**, 596-598 (1976)

[87] R. Voss *et al.*, *Nb nanobridge dc SQUID*, **Appl. Phys. Lett. 37**, 656-658 (1980)

[88] W. Fritzsche *et al.*, *Wiring of metallized microtubules by electron beam-induced structuring*, **Nanotechnology 10**, 331-335 (1999)

[89] W. Simon and M. Eden, *3D measurements from SEM micrographs by electron scribing*, **Rev. Sci. Instrum. 47**, 443-444 (1976)

[90] W. W. Molzen *et al.*, *Materials and techniques used in nanostructure fabrication*, **J. Vac. Sci. Technol. 16**, 269-272 (1979)

[91] E. I. Rau, *Microrecording and Information reproduction with SEM*, **Scanning 10**, 207-209 (1988)

[92] T. Takahashi *et al.*, *In situ patterning of contamination resists in metalorganic chemical vapor deposition for fabrication of quantum wires*, **Appl. Phys. Lett. 58**, 2372-2374 (1991)

[93] Y. Ochiai *et al.*, *Nanometer-scale direct carbon mask fabrication using electron-beam-assisted deposition*, **Jpn. J. Appl. Phys. 32**, 6147-6152 (1993)

[94] H. W. P. Koops *et al.*, *Combined lithographies for the reduction of stitching errors in lithography*, **J. Vac. Sci. Technol. B 12**, 3265-3269 (1994)

[95] U. F. W. Behringer and P. Vettiger, *Repair techniques for Si transmission masks used for submicron lithography*, **J. Vac. Sci. Technol. B 4**, 94-99 (1986)

[96] H. G. Heide, *Die Objektverschmutzung im Elektronenmikroskop und das Problem der Strahlenschädigung durch Kohlenstoffabbau*, **Z. Angew. Phys. XV**, 116-128 (1963)

[97] P. Hirsch *et al.*, *Contamination in a SEM and the influence of specimen cooling*, **Scanning 16**, 101-110 (1994)

[98] K.-H. Löffler, Ph. D. Thesis: *Erzeugung freitragender Mikroobjekte durch elektronenstrahlaktivierten Kohlefolienabbau*, Technische Universität, Fakultät für Allgemeine Ingenieurwissenschaften, (1964).

[99] Hren, *Specimen contamination in Analytical Electron Microscopy: sources and solutions*, **Ultramicroscopy 3**, 375-380 (1979)

[100] J. J. Hren, "Chapter 18 - Barriers to AEM: contamination and etching", in *Introduction to Analytical Electron Microscopy*, pp. J.J. Hren, J.I. Goldstein and D. C. Joy, Plenum Press 1979.

[101] K. Kanaya *et al.*, *A contamination reducing method by ion-beam bombardment of the specimen in high-resolution electron-microscopy*, **Micron Microsc. Acta 19**, 163-173 (1988)

[102] K. Kanaya *et al.*, *A cone formation theory of contamination in high-resolution TEM*, **J. Electron. Microsc. 39**, 322-322 (1990)

[103] V. Harada *et al.*, *Reduction of contamination in analytical electron microscopy*, **SEM** 103-110 (1979)

[104] H. W. Conru and P. C. Laberge, *Oil contamination with the SEM operated in the spot scanning mode*, **J. Phys. E-Sci. Instrum. 8**, 136-138 (1975)

[105] W. A. Knox, *Contamination formed around a very narrow electron beam*, **Ultramicroscopy 1**, 175-180 (1976)

[106] R. F. W. Pease and W. C. Nixon, Microformation of filaments, *in* Proceedings of *1st Int. Conf. Electron Ion Beam Sci. Tech.*, 1965).

[107] J. P. Martin and R. Speidel, *Herstellung freitragender Mikrogitter im REM*, **Optik 1**, 13-18 (1972)

[108] P. Kreuzer, *Formation and examination of self-supporting contamination filaments*, **Optik 78**, 158-164 (1988)

[109] G. Möllenstedt, *Die Entstehung einer Vielzahl von Kontaminationsfäden unter der Elektronen-mikrosonde*, **Optik 78**, 132-134 (1988)

[110] V. V. Aristov *et al.*, *Direct electron-beam-induced formation of nanometer-scale carbon structures in STEM. 1. Nature of long-range growth outside the substrate*, **Microsc. Microanal. Microstruct. 3**, 313-322 (1992)

[111] V. V. Aristov *et al.*, *A new approach to fabrication of nanostructures*, **Nanotechnology 6**, 35-39 (1995)

[112] N. A. Kislov, *Formation and testing of self-sustaining nanometer carbon structures by STEM*, **Bulletin of the Russian Academy of Sciences 57**, 1513-1518 (1993)

[113] N. A. Kislov, *Direct STEM fabrication and characterization of self-supporting structures for nanoelectronics*, **Scanning 15**, 212-218 (1993)

[114] A. Bezryadin and C. Dekker, *Nanofabrication of electrodes with sub-5 nm spacing for transport experiments on single molecules and metal-clusters*, **J. Vac. Sci. Technol. B 15**, 793-799 (1997)

[115] T. Fujii *et al.*, *Micropattern measurement with an atomic force microscope*, **J. Vac. Sci. Technol. B 9**, 666-669 (1991)

[116] M. Yamaki *et al.*, *Efficient microtip fabrication with carbon coating and electron beam deposition for atomic force microscopy*, **J. Vac. Sci. Technol. B 10**, 2447-2450 (1992)

[117] H. Ximen and P. E. Russell, *Microfabrication of AFM tips using FIB and FEB*, **Ultramicroscopy 42-44**, 1526-1532 (1992)

[118] M. Castagné *et al.*, *Near field optical behaviour of C supertips*, **Ultramicroscopy 76**, 187-194 (1999)

[119] D. J. Keller and C. Chih-Chung, *Imaging steep, high structures by SFM with electron-beam deposited tips*, **Surf. Sci. 268**, 333-339 (1992)

[120] D. Keller *et al.*, *Sharp, vertical-walled tips for SFM imaging of steep or soft samples*, **Ultramicroscopy 42-44**, 1481-1489 (1992)

[121] M. Weber *et al.*, *Scanning probe microscopy of deposits employed to image the current-density distribution of electron beams*, **J. Vac. Sci. Technol. B 10**, 3116-3119 (1992)

[122] K. I. Schiffmann, *Investigation of fabrication parameters for the electron beam induced deposition of contamination tips used in AFM*, **Nanotechnology 4**, 163-169 (1993)

[123] M. Wendel *et al.*, *Sharpened electron beam deposited tips for high resolution AFM lithography and imaging*, **Appl. Phys. Lett. 67**, 3732-3734 (1995)

[124] Y. Akama *et al.*, *New scanning tunnelling microscopy tip for measuring surface topography*, **J. Vac. Sci. Technol. A 8**, 429-433 (1990)

[125] S. Matsui *et al.*, *Electron beam induced selective etching and deposition technology*, **Superlatt. Microstruct. 7**, 295-301 (1990)

[126] B. Hübner *et al.*, *Tips for STM Produced by electron-beam-induced deposition*, **Ultramicroscopy 42**, 1519-1525 (1992)

[127] H. G. Frey *et al.*, *Enhancing the resolution of Scanning near-field optical microscopy by a metal tip grown on an aperture probe*, **Appl. Phys. Lett. 81**, 5030-5032 (2002)

[128] M. Wendel *et al.*, *Nanolithography with an atomic force microscope*, **Superlatt. Microstruct. 20**, 349-356 (1996)

[129] B. Irmer *et al.*, *Josephson junctions defined by a nanoplough*, **Appl. Phys. Lett. 73**, 2051-2053 (1998)

[130] Y. Matsuzaki *et al.*, *Improvement of nanoscale patterning of heavily doped p-type GaAs by AFM-based surface oxidation process*, **J. Cryst. Growth 209**, 509-512 (2000)

[131] T. Mühl, Ph. D. Thesis: *Elektroneninduzierte Oxidation von dünnen Schichten aus a-C - eine neue Lithographiemethode und ihre Anwendungen*, TU Dresden, (2000).

[132] M. Antognozzi *et al.*, *Fabrication of nano-tips by C contamination in a SEM for use in scanning probe microscopy and field emission*, **Microsc. Microanal. Microstruct. 8**, 355-368 (1997)

[133] W. Ding *et al.*, *Mechanics of hydrogenated amorphous carbon deposits from electron-beam-induced deposition of a paraffin precursor*, **J. Appl. Phys. 98**, 014905 (2005)

[134] M. Plaschke *et al.*, *Alignment of in situ AFM images using microstructured reference points*, **Ultramicroscopy 75**, 77-83 (1998)

[135] J. Römer *et al.*, *Alignment of AFM images using an iterative mathematical procedure*, **Ultramicroscopy 85**, 99-105 (2000)

[136] F. Banhart, *The formation of a connection between C nanotubes in an electron beam*, **Nano Lett. 1**, 329-332 (2001)

[137] H. Adachi *et al.*, *Field emission characteristics of a carbon needle made by use of EB assisted decomposition of methane*, **Appl. Surf. Sci. 76/77**, 11-15 (1994)

[138] N. Miura *et al.*, *Fabrication of sub-micron tungsten carbide (WC$_x$)/ amorphous carbon (a-C) stacked junction by beam-induced reaction processes*, **Jpn. J. Appl. Phys. Part 2 36**, L1275-8 (1997)

[139] N. Miura *et al.*, *Electron beam induced deposition of carbonaceous microstructures using SEM*, **Appl. Surf. Sci. 113-114**, 269-273 (1997)

[140] N. Miura *et al.*, *RT operation of amorphous carbon-based single-electron transistors fabricated by beam-induced deposition techniques*, **Jpn. J. Appl. Phys. Part 2 37**, L423-L425 (1998)

[141] N. Miura *et al.*, *Fabrication of sub-μm gap structures using directly-deposited amorphous C wires*, **Jpn. J. Appl. Phys. Part 1 37**, 2072-2073 (1998)

[142] F. C. Sze *et al.*, *Investigation of impurity deposition on plasma facing component using electron beam technique*, **J. Nucl. Mat. 246**, 165-170 (1997)

[143] S. Kiyohara *et al.*, *Microfabrication of diamond films by localized electron beam CVD*, **Semicond. Sci. Technol. 17**, 1096-1100 (2002)

[144] J. T. Fourie, *Electric effects in contamination and electron beam etching*, **SEM 1**, 127-134 (1981)

[145] F. Banhart, *Fractal C filaments grown on insulators under irradiation in an electron microscope*, **Phil. Mag. Lett. 69**, 45-51 (1994)

[146] F. Banhart, *Laplacian growth of amorphous filaments in a non-diffusion-limited experiment*, **Phys. Rev. E 52**, 5156-5160 (1995)

[147] H. Z. Wang *et al.*, *Fractal C trees on polymer and metal substrates in TEM observation*, **Journal of Materials Science Letters 19**, 2225-2226 (2000)

[148] H. Z. Wang *et al.*, *Intergrowth of a C layer and fractal-like trees on 3Y-TZP in TEM observations*, **Mater. Sci. Eng. A 311**, 180-184 (2001)

[149] H. Z. Wang *et al.*, *In situ electron microscope study on the formation and morphological evolution of carbon aggregates*, **Carbon 40**, 2117-2124 (2002)

[150] M. Song *et al.*, *Fabrication of self-standing nanowires, nanodendrites, and nanofractal-like trees on insulator substrates with an electron-beam-induced deposition*, **Appl. Phys. A 80**, 1431-1436 (2005)

[151] A. G. Baker, *Deposition of metallic films by electron impact decomposition of organometallic vapors*, **Rev. Sci. Instrum. 32**, 458 (1961)

[152] R. W. Christy, *Conducting thin films Formed by electron bombardment of substrate*, **J. Appl. Phys. 33**, 1884-& (1962)

[153] H. T. Mann, *Method for the deposition of thin films by electron bombardment*, US Pat. n°3,132,046 (1964).

[154] O. G. Fritz, *Conducting film formed by electron bombardment of tungsten hexacarbonyl vapor in vacuum*, **J. Appl. Phys. 35**, 2272 (1964)

[155] H. W. P. Koops *et al.*, *High-resolution electron-beam induced deposition*, **J. Vac. Sci. Technol. B 6**, 477-481 (1988)

[156] P. D. Rack *et al.*, *Nanoscale electron-beam-stimulated processing*, **Appl. Phys. Lett. 82**, 2326-2328 (2003)

[157] B. A. Vishnyakov and K. A. Osipov, *Production of thin films of chemical compounds by electron beam bombardment*, Freund, Israel 1972.

[158] R. W. Bigelow *et al.*, *Analysis of thin films arising from electron-, ion- and photon-beam-induced decomposition of $Cr(CO)_6$ and $Al(CH_3)_3$*, **Thin Solid Films 94**, 233-247 (1982)

[159] J. S. Foord and R. B. Jackman, *Chemical vapour deposition on Si: in situ surface studies*, **Chem. Phys. Lett. 112**, 190-194 (1984)

[160] J. S. Foord and R. B. Jackman, *Studies of adsorption and electron-induced dissociation of $Fe(CO)_5$ on Si(100)*, **Surf. Sci. 171**, 197-207 (1986)

[161] D. Welipitiya *et al.*, *Ultraviolet and electron radiation induced fragmentation of adsorbed ferrocene*, **J. Appl. Phys. 79**, 8730-8734 (1996)

[162] H. Jiang *et al.*, *Fabrication of 2- and 3-dimensional nanostructures*, **Int. J. Mod. Phys. B 15**, 3207-3213 (2001)

[163] M. Takeguchi *et al.*, *Nanostructures fabricated by electron beam induced chemical vapor deposition*, **Superlatt. Microstruct. 36**, 255-264 (2004)

[164] R. R. Kunz and T. M. Mayer, *Catalytic growth rate enhancement of electron beam deposited iron films*, **Appl. Phys. Lett. 50**, 962-964 (1987)

[165] R. R. Kunz *et al.*, *Selective area deposition of metals using low-energy electron-beams*, **J. Vac. Sci. Technol. B 5**, 1427-1431 (1987)

[166] R. R. Kunz and T. M. Mayer, *Electron-beam induced surface nucleation and low-temperature decomposition of metal-carbonyls*, **J. Vac. Sci. Technol. B 6**, 1557-1564 (1988)

[167] R. E. Winters and R. W. Kiser, *Mass spectrometric studies of Cr, Mo, and W hexacarbonyls*, **Inorg. Chem. 4**, 157-161 (1964)

[168] S. Pignataro *et al.*, *Negative ions from metal carbonyls by electron impact*, **Z. Phys. Chem. (N.F.) 47**, 106-113 (1965)

[169] B. Cantone *et al.*, *Decomposition processes and fragmentation probabilities of $W(CO)_6$ by electron impact*, **J. Chem. Phys. 14**, 3115-3120 (1966)

[170] D. R. Bidinosti and N. S. McIntyre, *Electron-impact study of some binary metal carbonyls*, **Can. J. Chem. 45**, 614-648 (1967)

[171] R. W. Kiser *et al.*, *Mass spectrometric study of $Ni(PF_3)_4$*, **J. Am. Chem. Soc. 89**, 3653-3654 (1967)

[172] R. B. King, *Mass spectra of organometallic compounds. II. Some cyclopentadienyl carbonyl derivatives*, **J. Am. Chem. Soc. 90**, 1417-1428 (1967)

[173] S. M. Schildcrout *et al.*, *Ionization potentials of tris(β-diketonate)metal(III) complexes and Koopmans' theorem*, **J. Am. Chem. Soc. 90**, 4006-4010 (1968)

[174] J. Lewis and B. F. G. Johnson, *Mass spectra of some organometallic molecules*, **Acc. Chem. Res. 1**, 245-256 (1968)

[175] D. F. Torgerson and J. B. Westmore, *Energetics of the Ionization and Fragmentation of PF_3 by electron impact*, **Can. J. Chem. 53**, 933-938 (1975)

[176] J. Müller, *Decomposition of organometallic complexes in the mass spectrometer*, **Angew. Chem. Int. Ed. 11**, 653-665 (1972)

[177] J. R. Swanson *et al.*, *Low energy electron induced decomposition on surfaces: $W(CO)_6$ on Si(111)-(7x7)*, **Surf. Sci. 215**, L293-L296 (1989)

[178] D. Rapp *et al.*, *Cross sections for dissociative ionization of molecules by electron impact*, **J. Chem. Phys. 42**, 4081-4085 (1965)

[179] B. G. Lindsay *et al.*, *Absolute partial cross-section for electron-impact ionization of NO and NO_2 from threshold to 1000 eV*, **J. Chem. Phys. 112**, 9404-9410 (2000)

[180] B. G. Lindsay *et al.*, *Absolute cross-section for electron-impact ionization of N_2O, H_2S, and CS_2 from threshold to 1000 eV*, **J. Chem. Phys. 118**, 5894-5900 (2003)

[181] B. G. Lindsay *et al.*, *Electron-impact ionization of CCl_4 and CCl_2F_2*, **J. Chem. Phys. 121**, 1350-1356 (2004)

[182] S. Matsui and K. Mori, *New selective deposition technology by electron beam induced surface reaction*, **J. Vac. Sci. Technol. B 4**, 299-304 (1986)

[183] V. Scheuer *et al.*, *Electron beam decomposition of carbonyls on Si*, **Microelectron. Eng. 5**, 423-430 (1986)

[184] K. T. Kohlmann *et al.*, *E-beam induced X-ray mask repair with optimized gas nozzle geometry*, **Microelectron. Eng. 13**, 279-282 (1991)

[185] K. T. Kohlmann von Platen *et al.*, *Electron-beam induced etching of resist with water vapor as the etching medium*, **J. Vac. Sci. Technol. B 14**, 4262-4265 (1996)

[186] K. L. Lee and M. Hatzakis, *Direct electron-beam patterning for nanolithography*, **J. Vac. Sci. Technol. B 7**, 1941-1946 (1989)

[187] J. H. Kindt *et al.*, *Automated wafer-scale fabrication of electron beam deposited tips for atomic force microscopes using pattern recognition*, **Nanotechnology 15**, 1131-1134 (2004)

[188] S. Matsui and T. Ichihashi, *In situ observation on electron-beam-induced chemical vapor deposition by transmission electron microscopy*, **Appl. Phys. Lett. 53**, 842-844 (1988)

[189] S. Matsui *et al.*, *Electron beam induced selective etching and deposition technology*, **J. Vac. Sci. Technol. B 7**, 1182-1190 (1989)

[190] D. A. Bell *et al.*, *Electron beam-induced deposition of tungsten*, **J. Vac. Sci. Technol. B 12**, 2976-9 (1994)

[191] R. B. Jackman and J. S. Foord, *Electron beam stimulated chemical vapor deposition of patterned tungsten films on Si(100)*, **Appl. Phys. Lett. 49**, 196-198 (1986)

[192] S. Matsui and M. Mito, *Si deposition by electron beam induced surface reaction*, **Appl. Phys. Lett. 53**, 1492-1494 (1988)

[193] H. O. Funsten *et al.*, *Low-temperature beam-induced deposition of thin tin films*, **J. Appl. Phys. 71**, 1475-84 (1992)

[194] S. H. Kim and G. A. Somorjai, *Stereospecific Ziegler-Natta model catalysts produced by electron beam-induced deposition of $TiCl_4$: deposition kinetics, film structure, and surface structure*, **J. Phys. Chem. B 106**, 1386-1391 (2002)

[195] M. Shimojo *et al.*, *Selective growth and characterization of nanostructures with transmission electron microscopes*, **Appl. Surf. Sci. 241**, 56-60 (2005)

[196] S. H. Kim *et al.*, *Surface characterization of the TiCl$_x$/MgCl$_2$ model Ziegler-Natta polymerization catalysts: adsorption site studies using mesitylene thermal desorption*, **Langmuir 16**, 9414-9420 (2000)

[197] M. Rüb *et al.*, *Electron beam induced deposition in a reducing image projector*, **Microelectron. Eng. 9**, 251-254 (1989)

[198] A. Ishibashi *et al.*, *Electron-beam induced resist and aluminum formation*, **J. Vac. Sci. Technol. B 9**, 169-172 (1991)

[199] T. Takahashi *et al.*, *Selective growth of GaAs wire structures by electron beam induced metalorganic chemical vapor deposition*, **Appl. Phys. Lett. 60**, 68-70 (1992)

[200] T. Takahashi *et al.*, *MOCVD selective growth of GaAs:C wire and dot structure by electron beam irradiation*, **J. Cryst. Growth 124**, 213-219 (1992)

[201] K. Watanabe *et al.*, *Inducement of GaAs growth by electron beam irradiation on GaAs covered by native oxide*, **J. Cryst. Growth 150**, 612-615 (1995)

[202] K. T. Kohlmann *et al.*, *Repair of open stencil masks for ion projection lithography by e-beam induced metal deposition*, **Microelectron. Eng. 17**, 427-430 (1992)

[203] K. L. Lee *et al.*, *Submicron Si trench profiling with an electron beam fabricated AFM tip*, **J. Vac. Sci. Technol. B 9**, 3562-3568 (1991)

[204] J. G. Clabes *et al.*, *Nanometer scale probe for an atomic force microscope, and method for making the same*, US Pat. n°5,171,992 (1992).

[205] W. Görtz *et al.*, *Resolution enhanced scanning force microscopy measurements for characterizating dry etching methods applied to titanium masked InP*, **J. Vac. Sci. Technol. B 13**, 34-39 (1995)

[206] C. Schoessler *et al.*, *Conductive supertips for scanning probe applications*, **J. Vac. Sci. Technol. B 15**, 1535-1538 (1997)

[207] K. T. Kohlmann-von Platen *et al.*, *Electron-beam induced tungsten deposition: Growth rate enhancement and applications in microelectronics*, **J. Vac. Sci. Technol. B 10**, 2690-2694 (1992)

[208] K. T. Kohlmann-von Platen *et al.*, *Resolution limits in electron-beam induced tungsten deposition*, **J. Vac. Sci. Technol. B 11**, 2219-2223 (1993)

[209] H. W. P. Koops *et al.*, *Constructive three-dimensional lithography with electron-beam induced deposition for quantum effect devices*, **J. Vac. Sci. Technol. B 11**, 2386-2389 (1993)

[210] H. W. P. Koops *et al.*, "Nano-lithography in 3 dimensions with electron beam induced deposition", in *Nanolithography: A borderland between STM, EB, IB, and X-ray lithographies*, pp. 87-93, M. Gentili, Kluwer Academic Publishers, The Netherlands 1994.

[211] M. Weber, *Scattering of non-relativistic electrons in tip structures*, **J. Phys. D-Appl. Phys. 27**, 1363-1369 (1994)

[212] M. Weber, Ph. D. Thesis: *Der Prozess der elektronenstrahlinduzierte Deposition*, Technische Hochschule Darmstadt, Fachbereich Physik, (1995).

[213] H. W. P. Koops *et al.*, *Fabrication and characterization of platinum nanocrystalline material grown by electron-beam-induced deposition*, **J. Vac. Sci. Technol. B 13**, 2400-2403 (1995)

[214] P. C. Hoyle *et al.*, *Ultralow-energy focused electron beam induced deposition*, **Appl. Phys. Lett. 64**, 1448-1450 (1994)

[215] H. Hiroshima *et al.*, *Conditions for fabrication of highly conductive wires by electron-beam-induced deposition*, **Jpn. J. Appl. Phys. 38**, 7135-7139 (1999)

[216] Y. Ochiai *et al.*, *Electron-beam-induced deposition of copper compound with low resistivity*, **J. Vac. Sci. Technol. B 14**, 3887-3891 (1996)

[217] M. Komuro and H. Hiroshima, *Fabrication and properties of dot array using electron-beam-induced deposition*, **Microelectron. Eng. 35**, 273-276 (1997)

[218] M. Komuro and H. Hiroshima, *Lateral tunnel junction produced by electron-beam-induced deposition*, **J. Vac. Sci. Technol. B 15**, 2809-2815 (1997)

[219] M. Komuro *et al.*, *Miniature tunnel junction by electron-beam-induced deposition*, **Nanotechnology 9**, 104-107 (1998)

[220] H. Hiroshima and M. Komuro, *High growth rate for slow scanning in electron-beam-induced deposition*, **Jpn. J. Appl. Phys. 36**, 7686-7690 (1997)

[221] H. Hiroshima and M. Komuro, *Fabrication of conductive wires by electron-beam-induced deposition*, **Nanotechnology 9**, 108-12 (1998)

[222] H. W. P. Koops *et al.*, *Characterization and application of materials grown by electron-beam-induced deposition*, **Jpn. J. Appl. Phys. 33**, 7099-7107 (1994)

[223] F. Floreani *et al.*, *Operation of high power field emitters fabricated with electron beam deposition and concept of a miniaturised free electron laser*, **Microelectron. Eng. 57-8**, 1009-1016 (2001)

[224] J. Kretz *et al.*, *Three-dimensional structurization by additive lithography, analysis of deposits using TEM and EDX, and application to field-emitter tips*, **Microelectron. Eng. 23**, 477-481 (1994)

[225] S.-Y. Lin and H. W. P. Koops, *Photonic crystal devices formed by a charged-particle beam*, **US Patent n° 6,093,246** (2000)

[226] H. W. P. Koops *et al.*, *Two-dimensional photonic crystals produced by additive nanolithography with electron beam-induced deposition act as filters in the infrared*, **Microelectron. Eng. 57-8**, 995-1001 (2001)

[227] M. Weber *et al.*, *Electron-beam induced deposition for fabrication of vacuum field emitter devices*, **J. Vac. Sci. Technol. B 13**, 461-464 (1995)

[228] H. W. P. Koops *et al.*, *Conductive dots, wires, and supertips for field electron emitters produced by electron-beam-induced deposition on samples having increased temperature*, **J. Vac. Sci. Technol. B 14**, 4105-4109 (1996)

[229] A. Folch *et al.*, *Electron-beam deposition of Au nanostructures in a reactive environment*, **Appl. Phys. Lett. 66**, 2080-2082 (1995)

[230] A. Folch *et al.*, *High-Vacuum versus environmental electron-beam deposition*, **J. Vac. Sci. Technol. B 14**, 2609-2614 (1996)

[231] M. Weber *et al.*, *New compound quantum dot materials produced by electron-beam induced deposition*, **J. Vac. Sci. Technol. B 13**, 1364-1368 (1995)

[232] C. Schoessler *et al.*, *Electrical and field emission properties of nanocrystalline materials fabricated by electron-beam induced deposition*, **Microelectron. Eng. 30**, 471-474 (1996)

[233] N. A. Kislov *et al.*, *Electron-beam-induced fabrication of metal-containing nanostructures*, **Scanning 18**, 114-118 (1996)

[234] C. Schoessler and H. W. P. Koops, *Nanostructured integrated electron source*, **J. Vac. Sci. Technol. B 16**, 862-865 (1998)

[235] H. W. P. Koops *et al.*, *Miniature low-voltage beam systems producable by combined lithographies*, **Nucl. Instr. Meth. A 363**, 1-9 (1995)

[236] H. W. P. Koops *et al.*, *Novel lithography and signal processing with water vapor ions*, **J. Vac. Sci. Technol. B 15**, 1369-1372 (1997)

[237] M. Takai *et al.*, *Fabrication of field emitter array using focused ion and electron beam induced reaction*, **Microelectron. Eng. 41-42**, 453-456 (1998)

[238] O. Yavas *et al.*, *Maskless fabrication of field-emitter array by FIB and FEB*, **Appl. Phys. Lett. 76**, 3319-3321 (2000)

[239] I. W. Rangelow *et al.*, *Thermal nano-probe*, **Microelectron. Eng. 57-58**, 737-748 (2001)

[240] C. Lehrer *et al.*, *Integration of field emitters into scanning probe microscopy sensors using focused ion and electron beams*, **J. Vac. Sci. Technol. B 22**, 1402-1406 (2004)

[241] K. Murakami and M. Takai, *Characteristics of nano electron source fabricated using beam assisted process*, **J. Vac. Sci. Technol. B 22**, 1266-1268 (2004)

[242] X. Yang *et al.*, *Intregrated tungsten nanofiber field emission cathodes selectively grown by nanoscale electron beam-induced deposition*, **Appl. Phys. Lett. 86**, 183106 (2005)

[243] F. Hirose and H. Sakamoto, *Low-temperature Si selective epitaxial growth using electron-beam-induced reaction*, **Jpn. J. Appl. Phys. 34**, 5904-5907 (1995)

[244] J. H. Campbell *et al.*, *Electron irradiation effects on digermane adsorbed on Si(100) surfaces*, **Appl. Surf. Sci. 180**, 345-350 (1997)

[245] J. Lozano *et al.*, *A TPD, HREELS, and XPS study of electron-induced deposition of germanium on Si(100)*, **Appl. Surf. Sci. 137**, 197-203 (1999)

[246] K. Nakano *et al.*, *Low-temperature growth of SiO_2 films by Electron-Induced ultrahigh vacuum Chemical Vapor Deposition*, **Jpn. J. Appl. Phys. 35**, 6570-6573 (1996)

[247] J. Kouvetakis *et al.*, Electron beam assisted chemical vapor deposition of gold in an environmental TEM, *in* Proceedings of *Mat. Res. Soc. Symp.*, Materials Research Society 1995).

[248] I. Utke *et al.*, *Focused electron beam induced deposition of gold*, **J. Vac. Sci. Technol. B 18**, 3168-3171 (2000)

[249] P. Hoffmann *et al.*, Focused Electron Beam Induced Deposition of Gold and Rhodium, *in* Proceedings of *Mat. Res. Soc. Symp.*, (San Francisco, 2000).

[250] I. Utke *et al.*, *Electron beam induced deposition of metallic tips and wires for microelectronics applications*, **Microelectron. Eng. 53**, 261-264 (2000)

[251] O. Sqalli *et al.*, *Gold elliptical nanoantennas as probes for near field optical microscopy*, **J. Appl. Phys. 92**, 1078-1083 (2002)

[252] K. Mølhave *et al.*, *Solid gold nanostructures fabricated by electron beam deposition*, **Nano Lett. 3**, 1499-1503 (2003)

[253] D. N. Madsen *et al.*, *Soldering of nanotubes onto microelectrodes*, **Nano Lett. 3**, 47-49 (2003)

[254] K. Mølhave *et al.*, *Constructing, connecting and soldering nanostructures by environmental electron beam deposition*, **Nanotechnology 15**, 1047-1053 (2004)

[255] F. Cicoira, Ph. D. Thesis: *Electron Beam Induced Deposition of Rhodium Nanostructures*, EPFL, Département de Microtechnique, n°2528 (2002).

[256] F. Cicoira, *Electron Beam Induced Deposition of rhodium from the precursor [RhCl(PF₃)₂]₂: morphology, structure and chemical composition.*, **J. Cryst. Growth 265**, 619-626 (2004)

[257] F. Cicoira *et al.*, *Auger electron spectroscopy analysis of high metal content micro-structures grown by electron beam induced deposition*, **Appl. Surf. Sci. 242**, 107-113 (2005)

[258] I. Utke *et al.*, *High resolution magnetic Co supertips grown by a focused electron beam*, **Appl. Phys. Lett. 80**, 4792-4794 (2002)

[259] Y. M. Lau *et al.*, *Properties and applications of cobalt-based material produced by electron-beam-induced deposition*, **J. Vac. Sci. Technol. A 20**, 1295-1302 (2002)

[260] M. R. Koblischka and U. Hartmann, *Recent advances in magnetic force microscopy*, **Ultramicroscopy 97**, 103-112 (2003)

[261] P. E. Batson *et al.*, *Sub-angstrom resolution using aberration corrected electron optics*, **Nature 418**, 617-620 (2002)

[262] N. Silvis-Cividjian *et al.*, *The role of secondary electrons in electron-beam-induced-deposition spatial resolution*, **Microelectron. Eng. 61-62**, 693-699 (2002)

[263] N. Silvis-Cividjian *et al.*, *Direct fabrication of nanowires in an electron microscope*, **Appl. Phys. Lett. 82**, 3514-3516 (2003)

[264] K. Mitsuishi *et al.*, *Electron-beam-induced deposition using a subnanometer-sized probe of high-energy electrons*, **Appl. Phys. Lett. 83**, 2064-2066 (2003)

[265] M. Shimojo *et al.*, *Electron induced nanodeposition of tungsten using field emission scanning and transmission electron microscopes*, **J. Vac. Sci. Technol. B 22**, 742-746 (2004)

[266] M. Tanaka *et al.*, *Ultimate sized nano-dots formed by electron beam-induced deposition using an ultrahigh vacuum transmission electron microscope*, **Surf. Interface Anal. 37**, 261-264 (2005)

[267] W. F. van Dorp *et al.*, *Approaching the resolution limit of nanometer-scale electron beam-induced deposition*, **Nano Lett. 5**, 1303-1307 (2005)

[268] M. Tanaka *et al.*, *Position- and size-controlled fabrication of iron silicide nanorods by electron-beam-induced deposition using an ultrahigh-vacuum transmission electron microscope*, **Appl. Phys. Lett. 86**, 183104 (2005)

[269] C. G. Pantano and T. E. Madey, *Electron beam damage in Auger electron spectroscopy*, **Appl. Surf. Sci. 7**, 115-141 (1981)

[270] M. Isaacson, "Specimen damage in the electron microscope", in *Principles and Techniques of Electron Microscopy*, pp. Vol. 7, ed. by M.A. Hayat, Van Nostrand Reinhold co.

[271] C. G. Pantano *et al.*, "Electron Beam Damage at Solid Surfaces", in *Beam Effects, Surface Topography, and Depth Profiling in Surface Analysis*, pp. 39-95, 1, A. W. Czanderna, T. Madey and C. Powell, Plenum Press 1998.

[272] L. W. Hobbs, "Chapter 17 - Radiation effects in analysis of inorganic specimens by TEM", in *Introduction to Analytical Electron Microscopy*, pp. J.J. Hren, J.I. Goldstein and D. C. Joy, Plenum Press 1979.

[273] R. Sharma *et al.*, *Electron-induced decomposition of RbCrF₃*, **Ultramicroscopy 23**, 453-462 (1987)

[274] R. F. Egerton *et al.*, *Radiation damage in the TEM and SEM*, **Micron 35**, 399-409 (2004)

[275] J. A. Venables, *Developments in Electron Microscopy and Analysis*, Academic Press, London 1976.

[276] R. D. Ramsier and J. T. Yates, *Electron-stimulated desorption: principles and applications*, **Surf. Sci. Rep. 12**, 243-378 (1991)

[277] D. Cherns *et al.*, *Sputtering in the high voltage electron microscope*, **Nucl. Instr. Meth. 132**, 369-376 (1976)

[278] L. E. Thomas, *Light-element analysis with electrons and X-rays in a HR-STEM*, **Ultramicroscopy 18**, 173-184 (1985)

[279] W. E. King *et al.*, *Damage effects of high energy electrons on metals*, **Ultramicroscopy 23**, 345-354 (1987)

[280] C. R. Bradley and N. J. Zaluzec, *Atomic sputtering in the analytical electron microscope*, **Ultramicroscopy 28**, 335-338 (1989)

[281] H. Hiraoka, *Radiation chemistry of Poly(methacrylates)*, **Radiation Chemistry - IBM J. Res. Dev.** 121-130 (March 1977)

[282] J. Pacansky and H. Coufal, *Electron-beam-induced Wolff rearrangement*, **J. Am. Chem. Soc. 102**, 410-412 (1980)

[283] W. Schnabel and H. Sotobayashi, *Polymers in electron beam and X-ray lithography*, **Prog. Polym. Sci. 9**, 297-365 (1983)

[284] A. N. Broers, *Resolution limits for electron-beam lithography*, **IBM J. Res. & Dev. 32**, 502-513 (1988)

[285] M. I. Lutwyche, *The resolution of electron beam lithography*, **Microelectron. Eng. 17**, 17-20 (1992)

[286] G. M. Wallraff and W. D. Hinsberg, *Lithographic imaging techniques for the formation of nanoscopic features*, **Chem. Rev. 99**, 1801-1821 (1999)

[287] D. R. Medeiros *et al.*, *Recent progress in electron beam resists for advanced mask-making*, **IBM J. Res. & Dev. 45**, 639-650 (2001)

[288] A. Barraud *et al.*, *Monomolecular resists-A new approach to high resolution electron beam microlithography*, **J. Vac. Sci. Technol. 16**, 2003-2007 (1979)

[289] C. Xu and B. E. Koel, *Electron-induced dissociation of hydrocarbon multilayers*, **Surf. Sci. Lett. 292**, L803-L809 (1993)

[290] M. J. Lercel *et al.*, *Electron beam nanofabrication with self-assembled monolayers of alkylthiols and alkylsiloxanes*, **Microelectron. Eng. 27**, 43-46 (1995)

[291] F. Y. C. Hui *et al.*, *Factors affecting resolution in scanning electron beam induced patterning of surface adsorption layers*, **Appl. Phys. Lett. 72**, 341-343 (1998)

[292] W. Geyer *et al.*, *Electron-induced crosslinking of aromatic self-assembled monolayers: negative resists for nanolithography*, **Appl. Phys. Lett. 75**, 2401-2403 (1999)

[293] M. N. Kozicki *et al.*, *Electron-beam exposure of self-assembled monolayers of 10-undecenoic acid*, **Superlatt. Microstruct. 27**, 481-484 (2000)

[294] X. Wang *et al.*, *Formation, characterization and sub-50-nm patterning of organosilane monolayers with embedded disulfide bonds: an engineered self-assembled monolayer resist for electron-beam lithography*, **Langmuir 19**, 9748-9758 (2003)

[295] T. P. Woodman, *The formation of thin films of silica by the electron bombardment of triphenylsilanol*, **Brit. J. Appl. Phys. 16**, 359-364 (1965)

[296] M. Hatzakis *et al.*, *Organometallic materials in lithography: a review*, **J. Vac. Sci. Technol. B 6**, 2224-2228 (1988)

[297] H. W. P. Koops *et al.*, *Evaluation of the dry resist octavinylsilsesquioxan and its application to three-dimensional electron-beam lithography*, **Microelectron. Eng. 30**, 539-42 (1996)

[298] M. E. Mochel *et al.*, *Electron beam cutting in amorphous alumina sheets*, **Appl. Phys. Lett. 44**, 502-504 (1984)

[299] J. L. Hollenbeck and R. C. Buchanan, *Oxide thin films for nanometer scale electron beam lithography*, **J. Mater. Res. 5**, 1058-1072 (1990)

[300] S. Matsui *et al.*, *Electron beam irradiation effects for high-T_c superconducting thin films*, **J. Vac. Sci. Technol. B 8**, 1771-1774 (1990)

[301] X. Pan and A. N. Broers, *Nanometer scale pattern generation in deposited SiO_2 with electron beam irradiation*, **J. Appl. Phys. 71**, 6189-6191 (1992)

[302] H. Hiroshima and M. Komuro, *Characteristics of SiO_2 as a high-resolution electron beam resist*, **Jpn. J. Appl. Phys. 32**, 6153-6157 (1993)

[303] G. S. Chen *et al.*, *Novel fabrication method for nanometer-scale silicon dots and wires*, **Appl. Phys. Lett. 62**, 1949-1951 (1993)

[304] F. Carcenac *et al.*, *High voltage electron beam nanolithography on WO_3*, **J. Vac. Sci. Technol. B 14**, 4283-4287 (1996)

[305] S. Fujita *et al.*, *Nanostructure fabrication using the selective thermal desorption of SiO_2 induced by electron beams*, **Appl. Phys. Lett. 69**, 638-640 (1996)

[306] H. Watanabe *et al.*, *Selective thermal decomposition of ultrathin silicon oxide layers induced by electron-stimulated oxygen desorption*, **Appl. Phys. Lett. 71**, 1038-1040 (1997)

[307] T. Kizuka and N. Tanaka, *Atomic desorption process in nanometre-scale electron-beam drilling of MgO in high-resolution TEM*, **Phil. Mag. Lett. 76**, 289-297 (1997)

[308] G. S. Chen *et al.*, *Electron-beam-induced damage in amorphous SiO_2 and the direct fabrication of silicon nanostructures*, **Phil. Mag. A 78**, 491-506 (1998)

[309] T. Kizuka and T. Yanaka, *Atomic-scale electron beam processing*, **Jpn. J. Appl. Phys. 38**, 1595 (1999)

[310] M. Isaacson and A. Muray, *In situ vaporization of very low molecular weigth resists using 1/2 nm diameter electron beams*, **J. Vac. Sci. Technol. 19**, 1117-1120 (1981)

[311] A. Muray *et al.*, *Fabrication of apertures, slots, and grooves at the 8-80 nm scale in silicon and metal films*, **J. Vac. Sci. Technol. B 1**, 1091-1095 (1983)

[312] A. Muray *et al.*, *AlF_3-A new very high resolution electron beam resist*, **Appl. Phys. Lett. 45**, 589-591 (1984)

[313] I. G. Salisbury *et al.*, *Nanometer scale electron beam lithography in inorganic materials*, **Appl. Phys. Lett. 45**, 1289-1291 (1984)

[314] A. Muray *et al.*, *Radiolysis and resolution limits of inorganic halide resists*, **J. Vac. Sci. Technol. B 3**, 367-372 (1985)

[315] E. Kratschmer and M. Isaacson, *Nanostructure fabrication in metals, insulators, and semiconductors using sel-developing metal inorganic resist*, **J. Vac. Sci. Technol. B 4**, 361-364 (1985)

[316] J. M. Macaulay and S. D. Berger, *Characterization of hte lithographic properties of inorganic resists with nanometre resolution on bulk substrates*, **Microelectron. Eng. 6**, 527-532 (1987)

[317] W. Langheinrich *et al.*, *Homogeneous lithium fluoride films as a high resolution electron beam resist*, **Microelectron. Eng. 17**, 287-290 (1992)

[318] V. I. Nikolaichik, *Self-developing processes in metal fluorides under a focused electron beam*, **Phil. Mag. A 68**, 227-236 (1993)

[319] W. Langheinrich and H. Beneking, *Fabrication of metallic structures in the 10 nm region usign an inorganic electron beam resist*, **Jpn. J. Appl. Phys. 32**, 6218-6223 (1993)

[320] D. Streblechenko and M. R. Scheinfein, *Magnetic nanostructures produced by electron beam patterning of direct write transition metal fluoride resists*, **J. Vac. Sci. Technol. A 16**, 1374-1379 (1998)

[321] M. Malac *et al.*, *Exposure characteristics of cobalt fluoride (CoF_2) self-devloping electron-beam resist on sub-100 nm scale*, **J. Appl. Phys. 92**, 1112-1121 (2002)

[322] J. P. Ballantyne and W. C. Nixon, *Selectve area metallization by electron-beam controlled direct metallic deposition*, **J. Vac. Sci. Technol. 10**, 1094-1097 (1973)

[323] M. Green *et al.*, *Electron beam decomposition of CdCl₂*, **J. Appl. Phys. 57**, 631-633 (1985)

[324] Q. Dou *et al.*, *Electron-irradiation-induced structural and compositional changes on alkali halide surfaces*, **Surf. Sci. 219**, L623-L627 (1989)

[325] H. Watanabe *et al.*, *Electron-stimulated desorption and in situ SEM study on self-developing reaction of high-resolution inorganic electron beam resist*, **Jpn. J. Appl. Phys. 34**, L948-L950 (1995)

[326] J. Fujita *et al.*, *Sub-10 nm lithography and development properties of inorganic resist by scanning electron beam*, **Appl. Phys. Lett. 66**, 3065-3067 (1995)

[327] J. Fujita *et al.*, *Sub-10 nm lithography and development properties of inorganic resist by scanning electron beams*, **J. Vac. Sci. Technol. B 13**, 2757-2761 (1995)

[328] K. Tsutsui *et al.*, *Fabrication of site-controlled metal dot array by electron beam surface modification*, **Microelectron. Eng. 35**, 245-248 (1997)

[329] R. Bennewitz *et al.*, *Bulk and surface processes in low-energy-electron-induced decomposition of CaF₂*, **Phys. Rev. B 59**, 8237-8246 (1999)

[330] W. Jones *et al.*, *Evidence for the formation of single crystals of Na metal during the decomposition of NaAlH₄: an electron microscopic study*, **Mat. Lett. 2**, 377-379 (1984)

[331] P. J. Herley and W. Jones, *Transmission electron microscopy of beam-sensitive metal hydrides*, **Z. Phys. Chem. (N.F.) 147**, 147-159 (1986)

[332] P. J. Herley *et al.*, *Ultra-fine particles of aluminium formed by electron-beam-induced decomposition of aluminium hydride*, **Mat. Lett. 7**, 441-444 (1989)

[333] P. J. Herley *et al.*, *Electron beam decomposition of CuH and the generation of ultra-fine particles of Cu*, **Journal of Materials Science Letters 8**, 1013-1015 (1989)

[334] P. J. Herley and W. Jones, *Electron microscopic study of fine particles of beryllium*, **J. Mater. Sci. 28**, 1874-1878 (1993)

[335] T. Takahagi *et al.*, *Control of the chemical reactivity of a Si single-crystal surface using the chemical modification technique*, **J. Appl. Phys. 68**, 2187-2191 (1990)

[336] K. Okamoto *et al.*, *Sub-half-micron silicon pattern generation by electron beam direct writing on polysilane films*, **Jpn. J. Appl. Phys. 31**, 4441-4443 (1992)

[337] K. Tsubouchi and K. Masu, *Area-selective CVD of metals*, **Thin Solid Films 228**, 312-318 (1993)

[338] X. Chen *et al.*, *Electron-beam-induced nucleation centers and selective deposition of thin Zinc films*, **Jpn. J. Appl. Phys. 41**, 775-777 (2002)

[339] C. Goeden and G. Dollinger, *Electron-stimulated hydrogen desorption from diamond surfaces and its influence on the low-pressure synthesis of diamond*, **Appl. Phys. Lett. 81**, 5027-5029 (2002)

[340] G. M. King *et al.*, *Nanometer patterning with ice*, **Nano Lett. 5**, 1157-1160 (2005)

[341] J. V. Mantese *et al.*, *Use of electron beam lithography to selectively decompose metalorganics into patterned thin-film superconductors*, **Appl. Phys. Lett. 53**, 526-528 (1988)

[342] T. J. Stark *et al.*, *Electron beam induced metalization of palladium acetate*, **J. Vac. Sci. Technol. B 9**, 3475-3478 (1991)

[343] T. J. Stark *et al.*, *Formation of complex features using electron beam direct-write decomposition of Pd(OAc)₂*, **J. Vac. Sci. Technol. B 10**, 2685-2689 (1992)

[344] S. Okamura *et al.*, *Micropatterning of ferroelectric Bi₄Ti₃O₁₂ using electron-beam-induced reaction of metal octylate films*, **Jpn. J. Appl. Phys. 35**, 6579-6583 (1996)

[345] M. S. M. Saifullah *et al.*, *Effect of chelating agents on high-resolution electron beam nanolithography of spin-coatable Al₂O₃ gel films*, **Jpn. J. Appl. Phys. 38**, 7052-7058 (1999)

[346] W. J. Mitchell and E. L. Hu, *In situ electron-beam lithography on GaAs substrates using a metal alkoxide resist*, **Appl. Phys. Lett. 74**, 1916-18 (1999)

[347] M. Alexe *et al.*, *Patterning and switching of nanosize ferroelectric memory cells*, **Appl. Phys. Lett. 75**, 1793-1795 (1999)

[348] M. Alexe *et al.*, *100-nm lateral size ferroelectric memory cells fabricated by electron-beam direct writing*, **Appl. Phys. A 70**, 247-251 (2000)

[349] M. S. M. Saifullah *et al.*, *Comparative study of sputtered and spin-coatable aluminum oxide electron beam resists*, **J. Vac. Sci. Technol. B 18**, 2737-2744 (2000)

[350] W. J. Mitchell and E. L. Hu, *High-resolution in situ electron bea patterning using Ti(OC₃H₇)₄ as a negative-type resist*, **J. Vac. Sci. Technol. B 20**, 596-603 (2002)

[351] M. S. M. Saifullah *et al.*, *Sub-10 nm electron beam nanolithography using spin-coatable TiO₂ resists*, **Nano Lett. 3**, 1587-1591 (2003)

[352] S. Kiyohara *et al.*, *Nanopatterning of diamond films with composite oxide mask of metal octylates in electron beam lithography*, **Journal of Materials Science: Materials in Electronics 15**, 99-102 (2004)

[353] P. Hoffmann, Ph. D. Thesis: *Untersuchung zum Direkt-Schreiben von Metallinien mit fokussierten Licht- und Teilchenstrahlen aus festen metallorganischen Schichten*, EPFL, (1992).

[354] G. J. Berry *et al.*, *The production of fine metal tracks from a new range of organometallic compounds*, **Sensors and Actuators A 51**, 47-50 (1995)

[355] M. D. R. Thomas *et al.*, *Electron-beam-induced conduction in a ruthenium carbonyl nanoparticle polymer*, **Appl. Phys. Lett. 76**, 1773-1775 (2000)

[356] B. F. G. Johnson *et al.*, *Electron-beam induced formation of nanoparticle chains and wires from a ruthenium cluster polymer*, **Chem. Commun.** 1317-1318 (2000)

[357] S. B. Clendenning *et al.*, *Direct writing of patterned ceramics using electron-beam lithography and metallopolymer resists*, **Adv. Mater. 16**, 215-219 (2004)

[358] H. G. Craighead and L. M. Schiavone, *Metal deposition by electron beam exposure of an organometallic film*, **Appl. Phys. Lett. 48**, 1748-1750 (1986)

[359] M. T. Reetz and M. Winter, *Fabricatio of metallic and bimetallic nanostructures by electron beam induced metallization of surfactant stabilized Pd and Pd/Pt clusters*, **J. Am. Chem. Soc. 119**, 4539-4540 (1997)

[360] J. Lohau *et al.*, *Electron-beam lithography with metal colloids: direct writing of metallic nanostructures*, **J. Vac. Sci. Technol. B 16**, 77-79 (1998)

[361] T. R. Bedson *et al.*, *Quantitative evaluation of electron beam writing in passivated gold nanoclusters*, **Appl. Phys. Lett. 78**, 1921-1923 (2001)

[362] T. R. Bedson *et al.*, *Mechanism of electron-beam writing in passivated gold nanoclusters*, **Appl. Phys. Lett. 78**, 2061-2063 (2001)

[363] M. H. V. Werts *et al.*, *Nanometer scale patterning of Langmuir-Blodgett films of gold nanoparticles by electron beam lithography*, **Nano Lett. 2**, 43-47 (2002)

[364] P. A. Dowben *et al.*, *Deposition of thin metal and metal silicide films from the decomposition of organometallic compounds*, **Mater. Sci. Eng. B 2**, 297-323 (1989)

[365] D. Bäuerle, *Laser processing and chemistry*, 3rd ed., Springer Verlag, Berlin 2000.

[366] O. Lehmann and M. Stuke, *Generation of 3-dimensional freestanding metal micro-objects by laser chemical-processing*, **Appl. Phys. A 53**, 343-345 (1991)

[367] O. Lehmann and M. Stuke, *3-dimensional laser direct writing of electrically conducting and isolating microstructures*, **Mat. Lett. 21**, 131-136 (1994)

[368] F. T. Wallenberger, *Rapid prototyping directly from the gas phase*, **Science 267**, 1274-1275 (1995)

[369] E. Halary-Wagner *et al.*, *Light induced chemical vapour deposition painting with titanium dioxide*, **Appl. Surf. Sci. 208-209**, 663-668 (2003)

[370] E. Halary-Wagner, Ph. D. Thesis: *Selective light induced chemical vapour deposition of titanium dioxide thin films*, EPFL, Faculté STI, n°2650 (2003).

[371] V. Kadekar *et al.*, *Deposition technologies for micromanufacturing: a review*, **Journal of Manufacturing Science and Engineering 126**, 787-795 (2004)

[372] K. Boller *et al.*, *Investigation of carbon contamination of mirror surfaces exposed to synchrotron radiation*, **Nucl. Instr. Meth. Phys. 208**, 273-279 (1983)

[373] R. Zanoni *et al.*, *Synchrotron radiation induced metal deposition on semiconductors: Mo(CO)₆ on Si(111)*, **Appl. Phys. Lett. 55**, 1020-1022 (1989)

[374] D. C. Mancini *et al.*, *Synchrotron radiation induced chemical vapor deposition of thin films from metal hexacarbonyls*, **J. Vac. Sci. Technol. B 8**, 1804-1807 (1990)

[375] F. K. Perkins *et al.*, *Synchrotron-radiation-induced deposition of boron and boron carbide films from borane and carboranes: Decaborane*, **J. Appl. Phys. 69**, 4103-4109 (1991)

[376] R. Zanoni *et al.*, *Synchrotron-radiation-stimulated tungsten deposition on silicon from W(CO)₆*, **J. Vac. Sci. Technol. A 9**, 931-934 (1991)

[377] D. C. Mancini *et al.*, *Chemical vapour deposition of Cr, Mo and W thin films induced by synchrotron radiation*, **Vacuum 46**, 1165-1169 (1995)

[378] R. A. Rosenberg and D. C. Mancini, *Deposition of carbon on gold using synchrotron radiation*, **Nucl. Instr. Meth. A 291**, 101-106 (1990)

[379] H. Kyuragi, *Role of low-energy secondary electrons in synchrotron radiation-excited chemical vapor deposition of silicon nitride films*, **J. Vac. Sci. Technol. A 15**, 2644-2652 (1997)

[380] R. M. Silver *et al.*, *Direct writing of submicron metallic features with a scanning tunneling microscope*, **Appl. Phys. Lett. 51**, 247-249 (1987)

[381] M. A. McCord *et al.*, *Direct deposition of 10-nm metallic features with the STM*, **J. Vac. Sci. Technol. B 6**, 1877-1880 (1988)

[382] D. S. Saulys *et al.*, *Electron-beam-induced patterned deposition of allylcyclopentadienyl palladium using scanning tunneling microscopy*, **J. Appl. Phys. 76**, 7639-41 (1994)

[383] W. W. Pai *et al.*, *Magnetic nanostructures fabricated by scanning tunneling microscope-assisted chemical vapor deposition*, **J. Vac. Sci. Technol. B 15**, 785-787 (1997)

[384] H. Brückl *et al.*, *Low energy electron beam decomposition of metalorganic precursors with a scanning tunneling microscope at ambient atmosphere*, **J. Vac. Sci. Technol. B 17**, 1350-1353 (1999)

[385] F. Marchi *et al.*, *Direct patterning of noble metal nanostructures with a scanning tunneling microscope*, **J. Vac. Sci. Technol. B 18**, 1171-1176 (2000)

[386] S. Mezhenny *et al.*, *Field-induced growth of a quantum dot from Ge_2H_6 precursor gas using the scanning tunneling microscope*, **J. Vac. Sci. Technol. B 19**, 567-568 (2001)

[387] U. R. Schöffel *et al.*, *Nanostructure formation by localized decomposition of $Mo(CO)_6$ on Si(111)-(7x7) surfaces*, **J. Appl. Phys. 91**, 2853-2858 (2002)

[388] I. Lyubinetsky *et al.*, *Scanning tunneling microscope assisted nanostructure formation: Two excitation mechanisms for precursor molecules*, **J. Appl. Phys. 86**, 4949-4953 (1999)

[389] I. Lyubinetsky *et al.*, *STM-assisted nanostructure formation: field-induced excitation and diffusion of precursor molecules*, **Surf. Sci. 459**, L451-L456 (2000)

[390] A. D. Kent *et al.*, *Growth of high aspect ratio nanometer-scale magnets with CVD and STM*, **Science 262**, 1249-1252 (1993)

[391] C. H. Oon *et al.*, *High-resolution atomic force microscope nanotip grown by self-field emission*, **Appl. Phys. Lett. 81**, 3037-3039 (2002)

[392] R. M. Nyffenegger and R. M. Penner, *Nanometer-scale surface modification using the Scanning Probe Microscope - Progress since 1991*, **Chem. Rev. 97**, 1195-1230 (1997)

[393] K. Gamo *et al.*, *Maskless ion beam assisted deposition of W and Ta films*, **Microelectron. Eng. 5**, 163-170 (1986)

[394] J. Melngailis, *Critical Review: Focused ion beam technology and applications*, **J. Vac. Sci. Technol. B 5**, 469-495 (1987)

[395] J. Orloff, *High-resolution focused ion beams*, **Rev. Sci. Instrum. 64**, 1105-1130 (1993)

[396] I. Adesida *et al.*, *Ion beam lithography at nanometer dimensions*, **J. Vac. Sci. Technol. B 3**, 45-49 (1985)

[397] S. Matsui and Y. Ochiai, *Focused ion beam applications to solid state devices*, **Nanotechnology 7**, 247-258 (1996)

[398] S. Matsui *et al.*, *Three-dimensional nanostructure fabrication by focused-ion-beam chemical vapor deposition*, **J. Vac. Sci. Technol. B 18**, 3181-3184 (2000)

[399] P. G. Blauner *et al.*, *Focused ion beam fabrication of submicron gold structures*, **J. Vac. Sci. Technol. B 7**, 609-617 (1989)

[400] T. Tao *et al.*, *Focused ion beam induced deposition of platinum*, **J. Vac. Sci. Technol. B 8**, 1826-1829 (1990)

[401] T. Tao *et al.*, *Focused ion beam induced deposition of platinum for repair processes*, **J. Vac. Sci. Technol. B 9**, 162-164 (1991)

[402] A. J. DeMarco and J. Melngailis, *Lateral growth of focused ion beam deposited platinum for stencil mask repair*, **J. Vac. Sci. Technol. B 17**, 3154-3157 (1999)

[403] J. S. Ro *et al.*, *Mechanism of ion beam induced deposition of gold*, **J. Vac. Sci. Technol. B 12**, 73-77 (1993)

[404] A. D. Della Ratta *et al.*, *Focused-ion beam-induced deposition of copper*, **J. Vac. Sci. Technol. B 11**, 2195-2199 (1993)

[405] J. Funatsu *et al.*, *Laser assisted focused-ion-beam-induced deposition of copper*, **J. Vac. Sci. Technol. B 14**, 179-180 (1996)

[406] T. P. Chiang *et al.*, *Surface kinetic studies of ion-induced chemical vapor deposition of copper for FIB apllications*, **J. Vac. Sci. Technol. A 15**, 3104-3114 (1997)

[407] J.-F. Lin *et al.*, *Classical and quantum transport in FIB deposited Pt interconnects*, **Appl. Phys. Lett. 82**, 802-804 (2003)

[408] K. Shimizu *et al.*, *Contamination layers formed by argon ion bombardment*, **J. Phys. D-Appl. Phys. 8**, 1453-1459 (1975)

[409] L. R. Harriott and M. J. Vasile, *FIB induced deposition of opaque C films*, **J. Vac. Sci. Technol. B 6**, 1035-1038 (1988)

[410] M. J. Vasile and L. R. Harriott, *FIB stimulated deposition of organic compounds*, **J. Vac. Sci. Technol. B 7**, 1954-1958 (1989)

[411] S. J. Kirch and D. E. Seeger, *Importance of adsorption in ion beam induced deposition of C*, **Appl. Phys. Lett. 57**, 49-51 (1990)

[412] J. Fujita *et al.*, *Observation and characteristics of mechanical vibration in 3D nanostructures and pillars grown by FIB-CVD*, **J. Vac. Sci. Technol. B 19**, 2834-2837 (2001)

[413] M. Ishida *et al.*, *Density estimation for amorphous carbon nanopillars grown by focused ion beam assisted chemical vapor deposition*, **J. Vac. Sci. Technol. B 20**, 2784-2787 (2002)

[414] M. Geissler and Y. Xia, *Patterning: Principls and some new developments*, **Adv. Mater. 16**, 1249-1269 (2004)

[415] B. D. Gates *et al.*, *New approaches to nanofabrication: molding, printing, and other techniques*, **Chem. Rev. 105**, 1171-1196 (2005)

References of Chapter 3

[1] F. Cicoira, Ph. D. Thesis: *Electron Beam Induced Deposition of Rhodium Nanostructures*, EPFL, Département de Microtechnique, n°2528 (2002).

[2] P. Doppelt and M. Abourida, dedicated lab-scale synthesis, ESPCI, Paris (2002).

[3] J.-M. Breguet, Ph. D. Thesis: *Actionneurs "stick and slip" pour micro-manipulateurs*, EPFL, n°1756 (1998).

[4] R. Dominik, *Student's semester project: Fabrication d'un positionneur micrométrique pour microscope électronique à balayage*, IOA/LSRO-EPFL (2004).

[5] Y. Suzaki and A. Tachibana, *Measurement of μm sized radius of Gaussian laser beam using the scanning knife-edge*, **Appl. Optics 14**, 2809 (1975)

[6] P. Hoffmann, Ph. D. Thesis: *Untersuchung zum Direkt-Schreiben von Metallinien mit fokussierten Licht- und Teilchenstrahlen aus festen metallorganischen Schichten*, EPFL, (1992).

[7] A. Dysli, *Student's semester project: Réalisation et test d'un dispositif de mesure in situ de la résistance électrique d'une déposition de cobalt induite par faisceau d'électrons focalisé*, IOA/LMIS3-EPFL (2005).

[8] M. Geissbühler, *Student's semester project: Conception, réalisation et application d'un système de micro-spectrophotométrie*, IOA-EPFL (2005).

References of Chapter 4

[1] K. Kanaya and S. Ono, Interaction of electron beam with the target in SEM, *in* Proceedings of *Electron beam interactions with solids for microscopy, microanalysis & microlithography*, D.F. Kyser, SEM Inc., AMF O'Hare 1982).

[2] H. Seiler, *Einige aktuelle Probleme der Sekundärelektronemission*, **Z. Angew. Phys. 22**, 249-263 (1967)

[3] J. Schaefer and J. Hoelzl, *A contribution to the dependence of secondary electron emission from the work function and Fermi energy*, **Thin Solid Films 13**, 81-86 (1972)

[4] M. S. Chung and T. E. Everhart, *Simple calculation of energy distribution of low-energy secondary electrons emitted from metals under electron bombardment*, **J. Appl. Phys. 45**, 707-709 (1974)

[5] H. Seiler, *Secondary electron emission in the electron microscope*, **J. Appl. Phys. 54**, R1-R18 (1983)

[6] H. Seiler, *Electron spectroscopy in the scanning electron microscope*, **Ultramicroscopy 17**, 1-8 (1985)

[7] M. Cailler and J.-P. Ganachaud, *Secondary electron emission from solids. I. Secondar Electron Spectroscopy*, **Scanning Microscopy Supplement 4** 57-79 (1990)

[8] D. C. Joy *et al.*, *Experimental secondary electron spectra under SEM conditions*, **J. Microsc. 215**, 77-85 (2004)

[9] P. G. Blauner *et al.*, *Focused ion beam fabrication of submicron gold structures*, **J. Vac. Sci. Technol. B 7**, 609-617 (1989)

[10] K. T. Kohlmann *et al.*, *E-beam induced X-ray mask repair with optimized gas nozzle geometry*, **Microelectron. Eng. 13**, 279-282 (1991)

[11] S. Dushman, *Scientific Foundations of Vacuum Technique*, J. Wiley & Sons, New York 1962.

[12] A. Luisier, *Student's diploma work: Dépôt de nanostructures de cuivre par faisceau d'électrons focalisé*, EPFL (2002).

[13] D. R. Beaman and J. A. Isasi, *Electron Beam Microanalysis - Part 2*, **Materials Research and Standards 11**, 12-56 (1971)

[14] I. Utke *et al.*, *Focused electron beam induced deposition of gold*, **J. Vac. Sci. Technol. B 18**, 3168-3171 (2000)

[15] T. Matsukawa *et al.*, *Measurement of the energy distribution of backscattered kilovolt electrons with a spherical retarding-field energy analyser*, **J. Phys. D-Appl. Phys. 7**, 695-702 (1974)

[16] L. Reimer, *Scanning Electron Microscopy*, Springer, Berlin 1985.

[17] M. Kindt, Ph. D. Thesis: *Messungen zur Elektronenrückstreuung an polykristallinen und einkristallinen Schichten im Elektronenmikroskop*, TU Berlin, (1976).

[18] H. Niedrig, *Electron backscattering from thin films*, **J. Appl. Phys. 53**, R15-R49 (1982)

[19] K. L. Hunter *et al.*, *Enhanced secondary electron emission from multilayer surfaces: experiment and Monte Carlo simulation*, **J. Phys. D-Appl. Phys. 27**, 1769-1773 (1994)

[20] H. Seiler and M. Stärk, *Bestimmung der mittleren Laufwege von Sekundärelektronen in einer Polymerisatschicht*, **Z. Phys. 183**, 527-531 (1965)

[21] H. Kanter, *Contribution of backscattered electrons to secondary electron formation*, **Phys. Rev. 121**, 681-684 (1960)

[22] V. E. Cosslett and R. N. Thomas, *Multiple scattering of 5-30 keV electrons in evaporated metal films II-Range-energy relations*, **Brit. J. Appl. Phys. 15**, 1283-1300 (1964)

[23] J. Robertson, *Diamond-like amorphous carbon*, **Mater. Sci. Eng. R 37**, 129-281 (2002)

[24] R. W. Christy, *Formation of thin polymer films by electron bombardment*, **J. Appl. Phys. 31**, 1680-1683 (1960)

[25] I. Haller and P. White, *Polymerization of butadiene gas on surfaces under low energy electron bombardment*, **J. Phys. Chem. 67**, 1784-1788 (1963)

[26] C. R. Fritzsche, *Deposition of thin films by beam induced polymerization of divinyl benzene*, **J. Appl. Phys. 53**, 9053-9057 (1982)

[27] D. E. Newbury, *The utility of specimen current imaging in the SEM*, **SEM** 111-120 (1976)

[28] C. Donolato, *On the theory of SEM charge-collection imaging of localized defects in semiconductors*, **Optik 52**, 19-36 (1978/79)

[29] H. J. Leamy, *Charge collection scanning electron microscopy*, **J. Appl. Phys. 53**, R51-R80 (1982)

[30] D. B. Holt and E. Napchan, *Quantitation of SEM EBIC and CL signals using Monte Carlo electron-trajectory simulations*, **Scanning 16**, 78-86 (1994)

[31] K. Kanaya *et al.*, *A cone formation theory of contamination in high-resolution TEM*, **J. Electron. Microsc. 39**, 322-322 (1990)

[32] H. W. P. Koops *et al.*, *Constructive three-dimensional lithography with electron-beam induced deposition for quantum effect devices*, **J. Vac. Sci. Technol. B 11**, 2386-2389 (1993)

[33] A. Luisier *et al.*, *Comparative Study of Cu-precursors for 3-D focused electron beam induced deposition*, **J. Electrochem. Soc. 151**, C535-C537 (2004)

[34] K. Kanaya *et al.*, *A contamination reducing method by ion-beam bombardment of the specimen in high-resolution electron-microscopy*, **Micron Microsc. Acta 19**, 163-173 (1988)

[35] K. T. Kohlmann-von Platen *et al.*, *Resolution limits in electron-beam induced tungsten deposition*, **J. Vac. Sci. Technol. B 11**, 2219-2223 (1993)

[36] P. Doppelt and M. Abourida, dedicated lab-scale synthesis, ESPCI, Paris (2002).

[37] F. Cicoira, Ph. D. Thesis: *Electron Beam Induced Deposition of Rhodium Nanostructures*, EPFL, Département de Microtechnique, n°2528 (2002).

[38] F. Cicoira, *Electron Beam Induced Deposition of rhodium from the precursor [RhCl(PF$_3$)$_2$]$_2$: morphology, structure and chemical composition.*, **J. Cryst. Growth 265**, 619-626 (2004)

[39] T. Bret *et al.*, In-situ control of the focused-electron-beam induced deposition process, *in* Proceedings of *Electron, Ion and Photon Beams nanofabrication (EIPBN)*, (Tampa, Florida, 2003).

[40] T. Bret *et al.*, *In situ control of the focused-electron-beam-induced deposition process*, **Appl. Phys. Lett. 83**, 4005-7 (2003)

[41] N. Thivolle, *Student's semester project: Etude expérimentale d'une méthode de contrôle in-situ du procédé de croissance assistée par faisceau focalisé d'électrons*, EPFL (2004).

[42] M. Weber *et al.*, *Electron-beam induced deposition for fabrication of vacuum field emitter devices*, **J. Vac. Sci. Technol. B 13**, 461-464 (1995)

[43] F. Arnal *et al.*, *Coefficient de rétrodiffusion dans le cas d'électrons monocinétiques arrivant sur la cible sous une incidence oblique*, **C. R. Acad. Sci. B 268**, 1526-1529 (1969)

[44] W. Oppel and H. Jahrreiss, *Messungen der Winkelverteilung von SE an dünnen freitragender Al- und Au-schichten*, **Z. Phys. 252**, 107-117 (1972)

[45] H. Hiroshima and M. Komuro, *Fabrication of conductive wires by electron-beam-induced deposition*, **Nanotechnology 9**, 108-12 (1998)

[46] V. E. Cosslett and R. N. Thomas, *Multiple scattering of 5-30 keV electrons in evaporated metal films I-Total transmission and angular distribution*, **Brit. J. Appl. Phys. 15**, 883-907 (1964)

[47] W. Bothe, *Die Streuabsorption der Elektronenstrahlen*, **Z. Phys. 54**, 161-178 (1929)

[48] E. J. Williams, *Multiple scattering of Fast electrons and alpha-particles, and "curvature" of cloud tracks due to scattering*, **Phys. Rev. 58**, 292-306 (1940)

[49] V. E. Cosslett and D. C. Thomas, *Multiple scattering of 5-30 keV electrons in evaporated metal films III: backscattering and absorption*, **Brit. J. Appl. Phys. 16**, 779-796 (1965)

[50] L. Reimer and H. Drescher, *SE emission of 10-100 keV electrons from transparent films of Al and Au*, **J. Phys. D-Appl. Phys. 10**, 805-815 (1977)

[51] B. Rossi and K. Greisen, *Cosmic-Ray Theory*, **Rev. Mod. Phys. 13**, 240-309 (1941)

[52] P. B. Kargl *et al.*, *Bistable growth in laser CVD*, **Appl. Phys. A 57**, 577 (1993)

[53] T. Tao *et al.*, *Focused ion beam induced deposition of platinum*, **J. Vac. Sci. Technol. B 8**, 1826-1829 (1990)

[54] X. Xu and J. Melngailis, *Quasiperiodic nanostructures in FIB deposited tungsten at high angles of incidence*, **J. Vac. Sci. Technol. B 11**, 2436-2440 (1993)

[55] I. Utke *et al.*, *Focused-electron-beam-induced deposition of freestanding three-dimensional nanostructures of pure coalesced copper crystals*, **Appl. Phys. Lett. 81**, 3245-3247 (2002)

[56] F. Arnal *et al.*, *Calcul de l'intensité transmise par des objets minces*, **C. R. Acad. Sci. B 278**, 759-762 (1974)

[57] T. Bret *et al.*, *Periodic structure formation by Focused-Electron-Beam induced deposition*, **J. Vac. Sci. Technol. B 22**, 2504-2510 (2004)

[58] L. Reimer, MOCASIM software Manual, Plano GmbH (1995).

[59] R. Snelder, *The Great Mosque at Djenné*, **MIMAR: Architecture in Development 12**, 66-74 (1984)

[60] A. J. DeMarco and J. Melngailis, *Lateral growth of focused ion beam deposited platinum for stencil mask repair*, **J. Vac. Sci. Technol. B 17**, 3154-3157 (1999)

[61] S.-W. Rhee *et al.*, *Property of Hexafluoroacetylacetonate Cu(I) (3,3-Dimethyl-1-butene) as a Liquid Precursor for Chemical Vapor Deposition of Copper Films*, **Electrochem. Solid. St. Lett. 3**, 135-137 (2000)

[62] T. P. Chiang *et al.*, *Surface kinetic studies of ion-induced chemical vapor deposition of copper for FIB apllications*, **J. Vac. Sci. Technol. A 15**, 3104-3114 (1997)

[63] J. Hillier, *On the investigation of specimen contamination in the electron microscope*, **J. Appl. Phys. 19**, 226-230 (1948)

[64] J. H. De Boer, *The dynamical character of adsorption*, 2nd ed., Clarendon Press, Oxford 1968.

[65] M. Nakao *et al.*, *DNA extraction from cell nuclei and DNA fishing using a 3D nano-probe*, **ASPE (American Society for Precision Engineering) Proceedings 20**, 41-44 (1999)

[66] T. Ooi *et al.*, *3D Nano wire-frame for handling and observing a single DNA fiber*, **Proc. IEEE** 580-583 (2000)

[67] M. Nakao *et al.*, *Micro handling with rotational Needle-type tools under real-time observation*, **Annals of the CIRP 50**, 9-12 (2001)

[68] T. Bret *et al.*, *Influence of the beam scan direction during focused electron beam induced deposition of 3D nanostructures*, **Microelectron. Eng. 78-79**, 307-313 (2005)

References of Chapter 5

[1] A. Grill, *Diamond-like carbon: state of the art*, **Diam. Relat. Mat. 8**, 428-434 (1999)

[2] R. Hauert, *A review of modified DLC coatings for biological applications*, **Diam. Relat. Mat. 12**, 583-589 (2003)

[3] J. Robertson, *Diamond-like amorphous carbon*, **Mater. Sci. Eng. R 37**, 129-281 (2002)

[4] H. W. P. Koops *et al.*, *Characterization and application of materials grown by electron-beam-induced deposition*, **Jpn. J. Appl. Phys. 33**, 7099-7107 (1994)

[5] Y. Ochiai *et al.*, *Nanometer-scale direct carbon mask fabrication using electron-beam-assisted deposition*, **Jpn. J. Appl. Phys. 32**, 6147-6152 (1993)

[6] H. Adachi *et al.*, *Field emission characteristics of a carbon needle made by use of EB assisted decomposition of methane*, **Appl. Surf. Sci. 76/77**, 11-15 (1994)

[7] S. Kiyohara *et al.*, *Microfabrication of diamond films by localized electron beam CVD*, **Semicond. Sci. Technol. 17**, 1096-1100 (2002)

[8] H. W. P. Koops *et al.*, *Combined lithographies for the reduction of stitching errors in lithography*, **J. Vac. Sci. Technol. B 12**, 3265-3269 (1994)

[9] M. J. Vasile and L. R. Harriott, *FIB stimulated deposition of organic compounds*, **J. Vac. Sci. Technol. B 7**, 1954-1958 (1989)

[10] L. R. Harriott and M. J. Vasile, *FIB induced deposition of opaque C films*, **J. Vac. Sci. Technol. B 6**, 1035-1038 (1988)

[11] S. J. Kirch and D. E. Seeger, *Importance of adsorption in ion beam induced deposition of C*, **Appl. Phys. Lett. 57**, 49-51 (1990)

[12] J. H. De Boer, *The dynamical character of adsorption*, 2nd ed., Clarendon Press, Oxford 1968.

[13] M. Weber *et al.*, *Electron-beam induced deposition for fabrication of vacuum field emitter devices*, **J. Vac. Sci. Technol. B 13**, 461-464 (1995)

[14] M. L. Knotek and P. J. Feibelman, *Ion desorption by Core-Hole Auger decay*, **Phys. Rev. Lett. 40**, 964-967 (1978)

[15] D. Vesely, *Electron beam damage of amorphous synthetic polymers*, **Ultramicroscopy 14**, 279-290 (1984)

[16] R. F. Egerton, *Measurement of radiation damage by EELS*, **J. Microsc. 118**, 389-399 (1980)

[17] B. Wojtkowiak and M. Chabanel, *Spectrochimie moléculaire*, Technique et Documentation, Paris 1977.

[18] R. J. Nemanich *et al.*, *Infrared active optical vibrations of graphite*, **Solid State Communications 23**, 117-120 (1977)

[19] M. Lax and E. Burstein, *Infrared Lattic Absorption in Ionic and Homopolar Crystals*, **Phys. Rev. 97**, 39-52 (1955)

[20] C. P. Kealey *et al.*, *Fluorination of polycrystalline diamond films and powders. An investigation using FTIR spectroscopy, SEM, energy-filtered TEM, XPS and fluorine-18 radiotracer methods*, **J. Mater. Chem. 11**, 879-886 (2001)

[21] T. Nakamura *et al.*, *Photochemical Modification of Diamond Films: Introduction of Perfluorooctyl Functional Groups on Their Surface*, **Langmuir 20**, 5846-5849 (2004)

[22] B. Dischler *et al.*, *Bonding in hydrogenated hard C studied by optical spectroscopy*, **Solid State Communications 48**, 105-108 (1983)

[23] J. Ristein *et al.*, *A comparative analysis of a-C:H by IR and mass selected thermal effusion*, **J. Appl. Phys. 84**, 3836-3847 (1998)

[24] M. Zarrabian, Ph. D. Thesis: *Dépôt de couches minces de carbone adamantin dans un plasma magnétron micro-onde*, Université de Nantes, IMN-ISITEM, (1998).

[25] V. Paret *et al.*, *Optical investigations of the microstructure of hydrogenated amorphous carbon films*, **Journal of Non-Crystalline Solids 227-230**, 583-587 (1998)

[26] C. J. Tang *et al.*, *Infrared absorption study of hydrogen incorporation in thick nanocrystalline diamond films*, **Appl. Phys. Lett. 86**, 223107 (2005)

[27] Hudgins, *Infra-Red spectroscopy of Matrix Isolated Polycyclic Aromatic Hydrocarbons (parts II and III)*, **J. Phys. Chem. A 102**, 344-360 (1998)

[28] *Aldrich FTIR Atlas*,

[29] F. Piazza *et al.*, *Transpolyacetylene chains in a-C:H free of nanocrystalline diamond*, **Appl. Phys. Lett. 82**, 358-360 (2003)

[30] J. C. Angus and F. Jansen, *Dense "diamondlike" hydrocarbons as random covalent networks*, **J. Vac. Sci. Technol. A 6**, 1778-1782 (1988)

[31] A. Brockes, *Uber Veränderungen des aufbaus organischer Folien durch EB*, **Z. Phys. 149**, 353-369 (1957)

[32] G. F. Bahr *et al.*, *The elementary composition of organic objects after electron irradiation*, **Lab. Invest. 14**, 377-395 (1965)

[33] W.-K. Chu *et al.*, *Backscattering spectrometry*, Academie Press, New York 1978.

[34] J. R. Tesmer and M. Nastasi, *Handbook of modern ion beam materials analysis*, Materials Research Society, Pittsburgh, Pennsylvania 1995.

[35] C. Y. Yang *et al.*, *Hydrogen 3D distribution in solids by ERDA imaging*, **Nucl. Instr. Meth. B 158**, 706-712 (1999)

[36] B. McEnaney, "Carbons and Graphites, Mechanical Properties of", in *Encyclopedia of Materials: Science and Technology*, pp. 967-975, Elsevier 2001.

[37] M. Nakamizo *et al.*, *Laser Raman studies on Carbons*, **Carbon 12**, 259-267 (1974)

[38] R. J. Nemanich *et al.*, *Raman scattering characterization of carbon bonding in diamond and diamondlike thin films*, **J. Vac. Sci. Technol. A 6**, 1783-1787 (1988)

[39] D. S. Knight and W. B. White, *Characterization of diamond films by Raman spectroscopy*, **J. Mater. Res. 4**, 385-393 (1989)

[40] J. Wagner *et al.*, *Resonant Raman scattering of amorphous Carbon and polycrystalline diamond films*, **Phys. Rev. B 40**, 1817-1824 (1989)

[41] A. C. Ferrari, *Determination of bonding in diamond-like carbon by Raman spectroscopy*, **Diam. Relat. Mat. 11**, 1053-1061 (2002)

[42] B. Schrader, *Infrared and Raman Spectroscopy-Methods and applications*, VCH, Weinheim 1995.

[43] F. Tuinstra and J. L. Koenig, *Raman spectrum of Graphite*, **J. Chem. Phys. 53**, 1126-1130 (1970)

[44] A. C. Ferrari and J. Robertson, *Interpretation of Raman spectra of disordered and amorphous C*, **Phys. Rev. B 61**, 14095-14107 (2000)

[45] N. Miura *et al.*, *Fabrication of sub-micron tungsten carbide (WC$_x$)/amorphous carbon (a-C) stacked junction by beam-induced reaction processes*, **Jpn. J. Appl. Phys. Part 2 36**, L1275-8 (1997)

[46] C. Mapelli *et al.*, *Graphite and graphitic compounds: vibrational spectra from oligomers to real materials*, **J. Mol. Struct. 480-481**, 615-620 (1999)

[47] F. Negri *et al.*, *A Computational Study of the Raman SPectra of Large Polycyclic Aromatic Hydrocarbons: Toward Molecularly Defined Subunits of Graphite*, **J. Phys. Chem. A 106**, 3306-3317 (2002)

[48] L. L. Ban *et al.*, *Lattice-resolution Electron Microscopy in Structural Studies of Non-graphitizing Carbons from Polyvinylidene Chloride (PVDC)*, **Journal of Applied Crystallography 8**, 415-420 (1975)

[49] G. M. Jenkins *et al.*, *Formation and Structure of Polymeric Carbons*, **Proceedings of the Royal Society of London. Series A, Mathematical and Physical Sciences 327**, 501-517 (1972)

[50] P. J. F. Harris, "Non-graphitizing Carbons", in *Encyclopedia of Materials: Science and Technology*, pp. Elsevier 2001.

[51] A. Perentes *et al.*, Real-time reflectometry controlled focused electron beam induced deposition of transparent materials, *in* Proceedings of *Electron, Ion and Photon-beam nanofabrication (EIPBN)*, (Orlando, 2005).

[52] M. Born and E. Wolf, *Principles of optics*, 6th ed., Pergamon Press, Oxford 1980.

[53] E. Halary-Wagner *et al.*, *Light induced chemical vapour deposition painting with titanium dioxide*, **Appl. Surf. Sci. 208-209**, 663-668 (2003)

[54] P. Koidl *et al.*, *Plasma deposition, properties and structure of amorphous hydrogenated carbon films*, **Materials Science Forum 52 & 53**, 41-70 (1989)

[55] D. F. Edwards and H. R. Philipp, "Cubic Carbon (Diamond)", in *Handbook of optical constants of solids*, pp. 665-673, Academic Press, 1985.

[56] A. Borghesi and G. Guizzetti, "Graphite (C)", in *Handbook of optical constants of solids II*, pp. 449-460, Academic Press, 1991.

[57] J. A. Kelber and M. L. Knotek, *Electron-stimulated desorption in organic molecular solids*, **J. Vac. Sci. Technol. A 1**, 1149-1153 (1983)

[58] J. A. Kelber and M. L. Knotek, *Electron-stimulated desorption fro partially fluorinated hydrocarbon thin films: Molecules with common versus separate hydrogen and fluorine bonding sites*, **Phys. Rev. B 30**, 400-403 (1984)

[59] M. De Moraes and D. Lichtman, *Fluorine detection sensitivity in electron stimulated desorption*, **J. Vac. Sci. Technol. A 2**, 1595-1596 (1984)

[60] R. D. Ramsier and J. T. Yates, *Electron-stimulated desorption: principles and applications*, **Surf. Sci. Rep. 12**, 243-378 (1991)

[61] J. Pacansky *et al.*, *Irradiation of poly(perfluoropropylene oxide) by a 175 kV electron beam: the formation and hydrolysis of acid fluoride groups*, **J. Fluor. Chem. 32**, 283-297 (1986)

[62] N. B. Colthup *et al.*, *Introduction to infrared and Raman spectroscopy*, 3th ed., Academic Press, Boston 1990.

[63] J. Pacansky and R. J. Waltman, *Electron Beam irradiation of Poly(perfluoro ethers): Identification of Gaseous Products as a Result of Main Chain Scission*, **J. Phys. Chem. 95**, 1512-1518 (1991)

[64] U. Lappan *et al.*, *Identification of new chemical structures in PTFE-co-PFPVE irradiated in vacuum at different temperatures*, **Rad. Phys. Chem. 67**, 447-451 (2003)

[65] K. Varlot *et al.*, *Towards sub-nanometer scale EELS analysis of polymers in the TEM*, **Ultramicroscopy 68**, 123-133 (1997)

[66] B. V. Spitsyn *et al.*, *Vapor growth of diamond on diamond and other surfaces*, **J. Cryst. Growth 52**, 219-226 (1981)

[67] P. K. Bachmann *et al.*, *Towards a general concept of diamond chemical vapour deposition*, **Diam. Relat. Mat. 1**, 1-12 (1991)

[68] K. Fabisiak *et al.*, *A laser-induced chemical transport reaction method for diamond deposition*, **Surface and Coatings Technology 47**, (1991)

[69] R. W. Christy, *Formation of thin polymer films by electron bombardment*, **J. Appl. Phys. 31**, 1680-1683 (1960)

[70] K. S. Stenn and G. F. Bahr, *A study of mass loss and product formation after irradiation of some dry amino acids, peptides, polypeptides and proteins with an electron beam of low current density*, **Journal of Histochemistry and Cytochemistry 18**, 574-580 (1970)

[71] S. D. Lin, *Electron radiation damage of thin films of Glycine, Diglycine, and Aromatic Amino Acids*, **Rad. Res. 59**, 521-536 (1974)

[72] P. Bernsen *et al.*, *Investigation of electron irradiation damage of evaporated films by laser microprobe mass analysis*, **Ultramicroscopy 7**, 197-202 (1981)

[73] T. Bret *et al.*, *Characterization of focused electron beam induced carbon deposits from organic precursors*, **Microelectron. Eng. 78-79**, 300-306 (2005)

[74] D. E. Johnson, *The interactions of 25 keV electrons with Guanine and Cytosine*, **Rad. Res. 49**, 63-84 (1972)

[75] M. Isaacson, *Interaction of 25 keV electron swith the Nucleic Acid bases Adenine, Thymine, and Uracil. I. Outer shell excitation*, **J. Chem. Phys. 56**, 1803-1812 (1972)

[76] M. Isaacson, *Interaction of 25 keV electron with the Nucleic Acid Bases, Adenine, Thymine, and Uracil. II. Inner shell excitation and inelastic scattering cross sections*, **J. Chem. Phys. 56**, 1813-1818 (1972)

[77] M. Isaacson *et al.*, *Electron beam Excitation and Damage of Biological Molecules; Its implications for Specimen Damage in Electron Microscopy*, **Rad. Res. 55**, 205-224 (1973)

[78] L. Reimer, *Irradiation changes in Organic and Inorganic objects*, **Lab. Invest. 14**, 344-358 (1965)

[79] W. Baumeister *et al.*, *Radiation damage in tripalmitin layers studied by means of IR and electron microscopy*, **Biophysical Journal 16**, 791-810 (1976)

[80] D. G. Howitt and G. Thomas, *Electron damage in organic crystals*, **Radiation Effects 34**, 209-215 (1977)

[81] M. Isaacson, *Electron beam induced damage of organic solids: Implications for analytical electron microscopy*, **Ultramicroscopy 4**, 193-199 (1979)

[82] M. Isaacson, "Specimen damage in the electron microscope", in *Principles and Techniques of Electron Microscopy*, pp. Vol. 7, ed. by M.A. Hayat, Van Nostrand Reinhold co.

[83] R. F. Egerton, *Organic mass loss ot 100 K and 300 K*, **J. Microsc. 126**, 95-100 (1982)

[84] L. Reimer and J. Spruth, *Interpretation of the fading of diffraction patterns from organic substances irradiated with 100 keV electrons at 10-300 K*, **Ultramicroscopy 10**, 199-210 (1982)

[85] J. R. Fryer, *Radiation damage in organic crystal films*, **Ultramicroscopy 14**, 227-236 (1984)

[86] C. G. Pantano *et al.*, "Electron Beam Damage at Solid Surfaces", in *Beam Effects, Surface Topography, and Depth Profiling in Surface Analysis*, pp. 39-95, 1, A. W. Czanderna, T. Madey and C. Powell, Plenum Press 1998.

[87] L. Reimer and A. Schmidt, *The shrinkage of bulk polymers by radiation damage in an SEM*, **Scanning 7**, 47-53 (1985)

[88] J. Pacansky and M. Maier, *Irradiation of small molecules isolated in rare gas matrices by high energy electron beams*, **J. Mol. Struct. 222**, 33-75 (1990)

[89] M. I. Bro *et al.*, *Reactions of Irradiated Polytetrafluoroethylene Resin*, **Journal of Applied Polymer Science 7**, 2121-2133 (1963)

[90] K. A. H. Lindberg *et al.*, *Chlorine loss and mass loss from polyvinylchloride and polyvinylidenchloride under the electron beam*, **J. Mater. Sci. 20**, 2225-2232 (1985)

[91] D. Vesely and D. S. Finch, *Chemical changes in electron-beam-irradiated polymers*, **Ultramicroscopy 23**, 329-338 (1987)

[92] B. J. Ciliax *et al.*, *Radiation damage of fluorinated organic compounds measured by parallel electron energy loss spectroscopy*, **Ultramicroscopy 48**, 13-25 (1993)

[93] O. A. Shenderova *et al.*, *Carbon nanostructures*, **Critical reviews in Solid State and Material Sciences 27**, 227-356 (2002)

[94] D. Ugarte, *Curling and closure of graphitic networks under electron-beam irradiation*, **Nature 359**, 707-709 (1992)

[95] D. Ugarte, *Formation mechanism of quasi-spherical carbon particles induced by electron bombardment*, **Chem. Phys. Lett. 207**, 473-479 (1993)

[96] M. S. Zwanger *et al.*, *Formation and decay of spherical concentric-shell carbon clusters*, **J. Cryst. Growth 163**, 445-454 (1996)

[97] G. Lulli *et al.*, *Influence of electron-beam parameters on the radiation-induced formation fo graphitic onions*, **Ultramicroscopy 60**, 187-194 (1995)

[98] S. Muto and T. Tanabe, *Temperature effect of electron-irradiation-induced structural modification in graphite*, **J. Nucl. Mat. 283-287**, 917-921 (2000)

[99] Y. Zhang and S. Iijima, *Microstructural evolution of single-walled carbon nanotubes under electron irradiation*, **Phil. Mag. Lett. 80**, 427-433 (2000)

[100] J. Li and F. Banhart, *The Engineering of Hot Carbon Nanotubes with a Focused Electron Beam*, **Nano Lett. 4**, 1143-1146 (2004)

[101] S. Seraphin and D. Zhou, *Electron-beam-induced structural changes in crystalline C₆₀ and C₇₀*, **J. Mater. Res. 8**, 1895-1899 (1993)

[102] L.-C. Qin and S. Iijima, *Onion-like graphitic particles produced from diamond*, **Chem. Phys. Lett. 262**, 252-258 (1996)

[103] J. Hiraki *et al.*, *Transformation of diamond nanoparticles into onion-like carbon by electron irradiation studied directly inside an ultrahigh-vacuum transmission electron microscope*, **Appl. Phys. Lett. 86**, 223101 (2005)

[104] W. Jones, *The electron-beam induced monomerization of di-p-anthracene*, **J. Microsc. 107**, 151-154 (1976)

[105] S. G. Burnay, *Radiation induced changes in the structure of cis-1,4-polybutadiene*, **Rad. Phys. Chem. 13**, 171-180 (1979)

[106] P. Fedorko *et al.*, *Carbon onions: Optical investigations of Electron Beam Irradiated Carbon materials*, **Materials Science Forum 191**, 171-176 (1995)

[107] M. Takeuchi *et al.*, *Structural change in graphite under electron irradiation at low temperatures*, **J. Nucl. Mat. 271&272**, 280-284 (1999)

[108] S. Muto *et al.*, *Change in Chemical Bonding states in Electron-Irradiated Graphite*, **Jpn. J. Appl. Phys. 38**, 1514-1515 (1999)

[109] B. W. Smith and D. E. Luzzi, *Electron irradiation effects in single wall carbon nanotubes*, **J. Appl. Phys. 90**, 3509-3515 (2001)

[110] R. F. Egerton *et al.*, *Radiation damage in the TEM and SEM*, **Micron 35**, 399-409 (2004)

[111] T. Füller and F. Banhart, *In situ observation of the formation and stability of singla fullerene molecules under electron irradiation*, **Chem. Phys. Lett. 254**, 372-378 (1996)

[112] F. Banhart and P. M. Ajayan, *Carbon onions as nanoscopic pressure cells for diamond formation*, **Nature 382**, 433-435 (1996)

[113] F. Banhart *et al.*, *The formation, annealing and self-compression of carbon onions under electron irradiation*, **Chem. Phys. Lett. 269**, 349-355 (1997)

[114] F. Banhart, *The transformation of graphitic onions to diamond under electron irradiation*, **J. Appl. Phys. 81**, 3440-3445 (1997)

[115] M. Zaiser and F. Banhart, *Radiation-induced transformation of graphite to diamond*, **Phys. Rev. Lett. 79**, 3680-3683 (1997)

[116] F. Banhart, *Irradiation effects in carbon nanostructures*, **Rep. Prog. Phys. 62**, 1181-1221 (1999)

[117] I. V. Ponomareva and L. A. Chernozatonskii, *How can carbon onion transform into diamond-like structure*, **Microelectron. Eng. 69**, 625-628 (2003)

[118] F. Banhart *et al.*, *The migration of metal atoms through carbon onions*, **Chem. Phys. Lett. 292**, 554-560 (1998)

[119] A. Yasuda *et al.*, *Graphitization Mechanism during the Carbon-Nanotube formation based on the in-situ HRTEM Observation*, **J. Phys. Chem. B 106**, 1849-1852 (2002)

[120] M. Terrones *et al.*, *Coalescence of Single-Walled Carbon nanotubes*, **Science 288**, 1226-1229 (2000)

[121] M. Terrones *et al.*, *Molecular junctions by joining Single-Walled Carbon Nanotubes*, **Phys. Rev. Lett. 89**, 075505-1-4 (2002)

[122] A. Yasuda *et al.*, *Carbon-nanotube formation directly on a substrate by an electron-beam*, **Surf. Sci. 514**, 216-221 (2002)

[123] A. Yasuda and W. Mizutani, *Carbon nanotube formation by an electron beam: elignment- and space-effect of the precursor*, **Thin Solid Films 464-465**, 282-285 (2004)

[124] A. Luisier *et al.*, *Comparative Study of Cu-precursors for 3-D focused electron beam induced deposition*, **J. Electrochem. Soc. 151**, C535-C537 (2004)

[125] C. J. Powell, *Cross sections for ionization of inner-shell electrons by electrons*, **Rev. Mod. Phys. 48**, 33-47 (1976)

[126] A. J. Bullen *et al.*, *Thermal conductivity of amorphous carbon thin films*, **J. Appl. Phys. 88**, 6317-6320 (2000)

[127] D. Bäuerle, *Laser processing and chemistry*, 3rd ed., Springer Verlag, Berlin 2000.

[128] V. Callegari, *Student's semester project: Etude expérimentale du procédé de dépôt de cuivre induit par faisceau d'électrons focalisé*, EPFL (2003).

[129] M. Rüb *et al.*, *Electron beam induced deposition in a reducing image projector*, **Microelectron. Eng. 9**, 251-254 (1989)

[130] I. Utke *et al.*, *Thermal effects during FEBID of nanocomposite magnetic-Co-containing tips*, **Microelectron. Eng. 73-74**, 553-558 (2004)

[131] I. Utke *et al.*, *Focused-electron-beam-induced deposition of freestanding three-dimensional nanostructures of pure coalesced copper crystals*, **Appl. Phys. Lett. 81**, 3245-3247 (2002)

[132] A. Luisier, *Student's diploma work: Dépôt de nanostructures de cuivre par faisceau d'électrons focalisé*, EPFL (2002).

[133] P. Hoffmann, Ph. D. Thesis: *Untersuchung zum Direkt-Schreiben von Metallinien mit fokussierten Licht- und Teilchenstrahlen aus festen metallorganischen Schichten*, EPFL, (1992).

[134] T. Brintlinger *et al.*, *Electrodes for Carbon Nanotube Devices by Focused Electron Beam Induced Deposition of Gold*, **J. Vac. Sci. Technol. B** presented at the EIPBN conference (Orlando, 2005)

[135] N. Quack, *Student's semester project: Réalisation d'un capteur Hall par dépôt de cobalt induit par faisceau d'électrons focalisé*, (2004).

[136] G. Boero *et al.*, *Submicrometer Hall devices fabricated by FEB-induced deposition*, **Appl. Phys. Lett. 86**, 042503 (2005)

[137] V. Gopal *et al.*, *Metal delocalization and surface decoration in direct-write nanolithography by electron beam induced deposition*, **Appl. Phys. Lett. 85**, 49-51 (2004)

[138] I. Utke *et al.*, *High resolution magnetic Co supertips grown by a focused electron beam*, **Appl. Phys. Lett. 80**, 4792-4794 (2002)

[139] L. E. Babcock and R. W. Christy, *Electron-beam-deposited thin polymer film - electrical properties vs. bombarding current*, **J. Appl. Phys. 43**, 1423-1432 (1972)

References of Annexes

[1] M. Weber, Ph. D. Thesis: *Der Prozess der elektronenstrahlinduzierte Deposition*, Technische Hochschule Darmstadt, Fachbereich Physik, (1995).

[2] H. Niedrig, *Electron backscattering from thin films*, **J. Appl. Phys. 53**, R15-R49 (1982)

[3] L. Reimer, *Scanning Electron Microscopy*, Springer, Berlin 1985.

[4] K. Kanaya and S. Okayama, *Penetration and energy-loss theory of electrons in solid targets*, **J. Phys. D-Appl. Phys. 5**, 43-58 (1972)

[5] D. C. Joy, *A database on Electron-Solid interactions*, **Scanning 17**, 270-275 (1995)

[6] M. Kindt, Ph. D. Thesis: *Messungen zur Elektronenrückstreuung an polykristallinen und einkristallinen Schichten im Elektronenmikroskop*, TU Berlin, (1976).

[7] K. L. Hunter *et al.*, *Enhanced secondary electron emission from multilayer surfaces: experiment and Monte Carlo simulation*, **J. Phys. D-Appl. Phys. 27**, 1769-1773 (1994)

[8] K. S. Sim and J. D. White, *New technique for in-situ measurement of backscattered and secondary electron yields for the calculation of signal-to-noise ratio in a SEM*, **J. Microsc. 217**, 235-240 (2005)

[9] H. Seiler, *Einige aktuelle Probleme der Sekundärelektronenemission*, **Z. Angew. Phys. 22**, 249-263 (1967)

[10] H. Seiler, *Secondary electron emission in the electron microscope*, **J. Appl. Phys. 54**, R1-R18 (1983)

[11] J. I. Goldstein *et al.*, *Scanning Electron Microscopy and X-Ray Microanalysis*, 2nd ed., Plenum Press, New-York and London 1984.

Tristan Bret

Born in Paris (France), on September 30th, 1976

French nationality, single;

Free from military duty

Education :

1993 : **Baccalauréat** scientifique (C), mention Assez Bien. (High School Graduation Diploma with specialization in Mathematics, Physics, and Chemistry)

(Lycée Fénelon, Paris, France)

1993-1995 : **Classes Préparatoires :** Math. Sup., Math. Spé. P' (2 year selective preparatory classes leading to entrance at French Engineering Schools, studying mainly mathematics, physics, and chemistry)

(Lycée Fénelon, Paris, France)

1995-1997 : **1ère et 2ème année d'ingéniorat à l'Ecole Supérieure de Physique et Chimie Industrielles de Paris** (1st and 2nd year student studying physics and chemistry)

(Ecole Supérieure de Physique et Chimie Industrielles, Paris, France)

Academic and industrial placements :

July-August 1996: Laboratoire de Chimie, Ecole Normale Supérieure, Paris (France)

August-December 1997 : Institut de recherches Servier, Suresnes (France)

1997-1998 : **3ème année d'ingéniorat à l'ESPCI**, spécialité chimie. (3rd year studying chemistry at ESPCI)

Academic placement:

July-September 1998: Institut d'Optique Appliquée, EPFL, Lausanne (Suisse)

1998-1999 : **Diplôme d'Etudes Approfondies** (DEA) de Chimie organique et bioorganique, Université Pierre-et-Marie-Curie, Paris VI, France. (Master's diploma in Organic and Bioorganic Chemistry)

Mémoire de DEA: « Synthèse de pyrrolidines substituées »

(Diploma thesis : « Organic synthesis of substituted pyrrolidines »)

December 1999 : **Engineering Diploma** from the Ecole Supérieure de Physique et Chimie Industrielles

2001-2005 : **Assistant-doctorant,** Institut d'Optique Appliquée, Ecole Polytechnique Fédérale de Lausanne, Lausanne (Suisse). (Ph. D. student)

Civil service:

November 1999 – March 2001 : **Coopérant du Service National - Chargé de mission auprès du Conseiller pour la Science et la Technologie près l'Ambassadeur de France à Rome** (Civil servant**,** scientific office of the French Embassy, Rome, Italy.)

(In charge of environmental, academic and industrial topics in the relations between France and Italy)

Publications :

Patents :

- P. Hoffmann, T. Bret, V. Moreau, *Process for providing marking on security papers,* **Patent** PCT 03405576.4-, (2003).

- T. Bret, P. Hoffmann, M. Rossi, X. Multone, *Cr lithographic mask repair by Focused Electron Beam assisted etching,* **Patent submitted**, (2005).

Scientific articles :

1- T. Bret *et al., A study of GaN laser lift-off*, **Physica Status Solidi A** 194, 559-562 (2002).

2- E. Halary-Wagner, T. Bret, P. Hoffmann, *Laser-Induced Chemical Vapour Deposition painting with TiO_2*, **Applied Surface Science** 208, 663-668 (2003).

3- T. Bret *et al.*, *In-situ growth control of the focused-electron-beam-induced deposition process*, **Applied Physics Letters** 83(19), 4005-4007 (2003).

4- I. Utke, T. Bret *et al.*, *Thermal effects during focused electron beam induced deposition of nanocomposite magnetic-cobalt-containing tips*, **Microelectronic Engineering** 73-74, 553-558 (2004).

5- E. Halary-Wagner, T. Bret, *et al., Resist-free patterned deposition of titanium dioxide thin films by light-induced chemical vapour deposition*, **Microelectronic Engineering** 73-74, 289-294 (2004).

6- A. Luisier *et al.*, *Comparative study of Cu precursors for 3D focused electron beam induced deposition*, **Journal of the Electrochemical Society**, 151(8), C535-C537 (2004).

7- T. Bret *et al.*, *Periodic structure formation by focused electron beam induced deposition*, **Journal of Vacuum Science and Technology B** 22(5), 2504-2510 (2004).

8- G. Boero, I. Utke, T. Bret *et al*, *Submicrometer Hall devices fabricated by focused electron-beam-induced deposition*, **Applied Physics Letters** 86, 042503 (2005).

9- T. Bret *et al.*, *Influence of beam scan direction during focused electron beam induced deposition of 3D nanostructures*, **Microelectronic Engineering**, 78-79, 307-313 (2005).

10- T. Bret *et al.*, *Characterization of C deposits obtained by focused electron beam induced deposition from organic precursors,* **Microelectronic Engineering**, 78-79, 300-306 (2005).

R e m e r c i e m e n t s